Structural and Functional Characterization of Lipid-based mRNA Delivery Systems

Dissertation
zur Erlangung des Grades
„Doktor der Naturwissenschaften“
im Promotionsfach Pharmazie

am Fachbereich Chemie, Pharmazie, Geographie und Geowissenschaften
der Johannes Gutenberg-Universität Mainz

Lukas Christian Jürgen Uebbing
geb. in Witten

Mainz, 2022

1. Berichterstatter:

2. Berichterstatter:

Tag der mündlichen Prüfung: 05.12.2022

D77

Für Stella

Acknowledgement

Eidesstattliche Erklärung / Affidavit

Hiermit versichere ich, dass ich die vorliegende Dissertation selbst angefertigt und alle benutzten Hilfsmittel und Quellen in der Arbeit angegeben habe. Ich habe weder die jetzt als Dissertation vorgelegte Arbeit noch Teile davon bei einer anderen Fakultät bzw. einem anderen Fachbereich als Dissertation eingereicht.

Ort, Datum Lukas Christian Jürgen Uebbing

With this statement I declare that the thesis presented here was written only by me and all the resources and sources used are clearly marked within the text. I have never submitted this thesis – or parts thereof – as a dissertation at another faculty or department.

Place, Date Lukas Christian Jürgen Uebbing

Uncharted territory is a good place to be in.
- Bo Burnham

Abstract

Pharmaceutical research has progressed in rapid manner over the last century. It has seen a shift from small molecule drugs to so called biologicals, which comprise macromolecules (such as proteins or nucleic acids) and have led to significant advantages in some therapeutic fields, such as several forms of cancer, by enabling the possibility of cancer immunotherapy. This therapeutical concept is based on utilizing the body's own defense mechanisms to combat the mutated cancer cells by training the immune system to recognize tumor antigens, which can for example be achieved through transfection of antigen presenting cells with the tumor antigen by delivering nucleic acids coding for this antigen into these cells. Traditionally, viral vectors have often been used to transfect target cells with genetic information. However, several problems (such as antiviral immune responses against the vector) come with the use of these delivery systems. Therefore, several approaches have been developed to mimic viral vectors while trying to reduce their downsides. One of these approaches is the use of lipid-based nanosized delivery systems, which are called lipoplexes or lipid nanoparticles (LNPs).

Recent years have seen the first approvals of lipid-based delivery systems delivering nucleic acid drug molecules. However, while a lot of effort has been spent on efficacy studies – be it *in vitro* or *in vivo* – and on general physicochemical characterization of lipid-based nanomedicines for mRNA delivery in cancer immunotherapy or other applications, a lack of insight into the internal structures, their transformation in relation to environmental changes, and the implications thereof still remains. This thesis therefore gives accurate *in situ* insights into the structural organization of lipid-based mRNA delivery systems – be it lipoplexes or LNPs – by utilizing potent and seldom applied characterization methods in the form of small angle scattering techniques, as well as traditional nanoparticle and nucleic acid characterization tools such as dynamic light scattering, fluorescence-based pK_a determination, microscopy, zeta potential measurements, nucleic acid encapsulation assays, and *in vitro* transfection efficacy. This enables the confirmation and optimization of previously established models to describe the internal structures and changes thereof more accurately in terms of both formulation and environmental parameters. New models are developed describing the pH-responsiveness of both lipoplexes and lipid nanoparticles, as well as the differences between these kinds of RNA delivery systems. Additionally, a first attempt to draw conclusions about a structure-function relationship is made.

Overall, the results described within this thesis should therefore provide better understanding of the functional and structural coherencies inside lipid-based mRNA delivery systems, which will help in the intelligent design and fine-tuning of the next generation of delivery systems during this just beginning new era of nucleic acid drug products.

Zusammenfassung

Im Laufe des letzten Jahrhunderts hat sich die pharmazeutische Forschung in hohem Tempo weiterentwickelt. Dabei wurde eine Verschiebung weg von traditionellen Produkten, mit kleinen Molekülen als Wirkstoffen, hin zu sogenannten Biologicals, welche Makromoleküle wie beispielsweise Proteine oder Nukleinsäuren enthalten, offensichtlich. Diese Produkte führten zu signifikanten Verbesserungen in mehreren Therapiegebieten, wie beispielsweise verschiedenen Krebsformen, indem sie das Prinzip der Krebs-Immuntherapie ermöglichten. Dieses therapeutische Konzept basiert darauf, körpereigene Abwehrmechanismen bei der Bekämpfung der mutierten Krebszellen zu nutzen, indem das Immunsystem auf die Erkennung von Tumorantigenen trainiert wird. Dies kann beispielsweise durch die Transfektion von antigenpräsentierenden Zellen mit dem Tumorantigen erfolgen, indem antigencodierende Nukleinsäuren in die Zielzellen eingebracht werden. Traditionell wurden hierfür virale Vektoren genutzt, allerdings bringen diese verschiedene Problematiken (wie beispielsweise antivirale Immunreaktionen gegen den Vektor) mit sich. Aufgrund dessen wurden verschiedene Ansätze entwickelt, um die viralen Vektoren nachzuahmen und deren Nachteile zu umgehen. Einen dieser Ansätze stellt die Nutzung von lipidbasierten nanopartikulären Freigabesystemen dar. Diese Systeme werden auch Lipoplexe oder Lipidnanopartikel (LNP) genannt.

Die ersten lipidbasierten Nukleinsäure-Freigabesysteme wurden im Verlauf der letzten Jahre zugelassen. Obwohl dabei ein großes Augenmerk auf Effektivitätsstudien – egal ob *in vitro* oder *in vivo* – und auf generelle physikochemische Charakterisierung der lipidbasierten mRNA Freigabesysteme für die Krebstherapie (oder andere Applikationen) gelegt wurde, blieben die internen Strukturen, deren Veränderungen als Reaktion auf Umwelteinflüsse und die Folgen dieser Strukturen und Reaktivitäten relativ wenig erforscht und sind daher häufig noch unzureichend erklärt. Daher beschäftigt sich diese Arbeit mit *in situ* Einblicken in den strukturellen Aufbau von lipidbasierten mRNA-Freigabesystemen (Lipoplexe und LNPs), indem sowohl potente und selten genutzte Charakterisierungsmethoden in Form von Kleinwinkelstreumethoden als auch traditionelle Nanopartikel- und Nukleinsäure-Charakterisierungsexperimente wie beispielsweise dynamische Lichtstreuung (DLS), fluoreszenzbasierte pK_a-Bestimmung, Mikroskopie, Zeta-Potential Messung, Bestimmung der Nukleinsäuren-Einschlussrate und Transfektionsexperimente angewendet werden. Dies ermöglicht die Bestätigung und Optimierung eines bereits beschriebenen Modells zur Beschreibung der internen Struktur von Lipoplexen und ihrer Veränderung in Abhängigkeit von Formulierungs- und Umweltparametern. Des Weiteren werden neue Modelle erarbeitet, die die pH-Responsivität von Lipoplexen und Lipidnanopartikeln sowie die Unterschiede zwischen diesen beiden Arten von mRNA-Freigabesystemen beschreiben. Außerdem wird versucht, erste Struktur-Wirkungszusammenhänge zu erörtern.

Zusammengefasst ermöglichen die Ergebnisse, die in dieser Dissertation erarbeitet werden, die funktionellen und strukturellen Zusammenhänge in lipidbasierten mRNA-Freigabesystemen besser zu verstehen, was beim intelligenten Design und der Verbesserung der nächsten Generationen von Freigabesystemen in diesem neuen Zeitalter der nukleinsäurebasierten Arzneimittel eine wichtige und hilfreiche Rolle spielen wird.

Disclaimer

Some of the results presented in this thesis (as shown in chapter 4.2.2 pH-Responsive Structural Changes of Lipoplexes) were previously published in an article in the research journal "Langmuir". A license was granted by the publisher for up to full reproduction, including adaptions. The following represents the required credit statement:
Reprinted (adapted) with permission from Uebbing, L.; Ziller, A.; Siewert, C.; Schroer, M. A.; Blanchet, C. E.; Svergun, D. I.; Ramishetti, S.; Peer, D.; Sahin, U.; Haas, H.; Langguth, P. Investigation of pH-Responsiveness inside Lipid Nanoparticles for Parenteral mRNA Application Using Small-Angle X-ray Scattering. Langmuir 2020, 36 (44), 13331–13341. DOI: 10.1021/acs.langmuir.0c02446. Copyright 2020 American Chemical Society.

Cell culture and FACS (fluorescence-activated cell sorting) experiments were performed by Isabell Sofia Keil at TRON (Translational Oncology at the University Medical Center of Johannes Gutenberg University) gGMBH, Freiligrathstraße 12, 55131 Mainz, Germany.

Contents

Abbreviations

a.u.	arbitrary units
ABC	accelerated blood clearance
APC	antigen presenting cell
API	active pharmaceutical ingredient
aRNA	antisense ribonucleic acid
ASAXS	anomalous small angle X-ray scattering
C16-PEG-2000-Ceramide	N-palmitoyl-sphingosine-1-70 {succinyl[methoxy(polyethylene glycol)2000]}
CAR	chimeric antigen receptor
CARPA	complement activation-related pseudoallergy
CMV	cytomegalovirus
DALY	disability adjusted life-year
DAC	dual asymmetric centrifuge
DNA	deoxyribonucleic acid
DLin-MC3-DMA	dilinoleylmethyl-4-dimethylaminobutyrate
DLS	dynamic light scattering
DODAP	1,2-dioleoyl-3-dimethylammonium-propane
DODMA	1,2-dioleyloxy-3-dimethylamino-propane
DOPC	1,2-dioleoyl-sn-glycero-3-phosphocholine
DOPE	1,2-dioleoyl-sn-glycero-3-phosphoethanolamine
DOPG	1,2-dioleoyl-sn-glycero-3-phospho-(1'-rac-glycerol)
DOTAP	1,2-dioleoyl-3-trimethylammonium-propane
DOTMA	1,2-di-O-octadecenyl-3-trimethylammonium propane
DPBS	Dulbecco's phosphate-buffered saline
DPL-14	[bis[(9Z,12Z)-octadeca-9,12-dienyl]amino]4-(dimethylamino)butanoate
DPPE	1,2-dipalmitoyl-sn-glycero-3-phosphoethanolamine
dsDNA	double stranded deoxyribonucleic acid
DSPC	1,2-distearoyl-sn-glycero-3-phosphocholine
EDL	electric double layer
EDTA	ethylenediaminetetraacetic acid
ELS	electrophoretic light scattering
EMA	European Medicines Agency
EPC	egg phosphatidylcholine
EPR	enhanced permeability and retention
FACS	fluorescence activated cell sorting
FDA	Food and Drug Administration
FWHM	full width at half maximum
GG	glycylglycine
gRNA	guide ribonucleic acid
HEPES	(4-(2-hydroxyethyl)-1-piperazineethanesulfonic acid)
IM	Intermediate
LDV	laser doppler velocimetry
LNP	lipid nanoparticle
LPX	lipoplex
MFI	mean fluorescence intensity
miRNA	micro ribonucleic acid
MP	manual protocol
MRI	magnetic resonance imaging
mRNA	messenger ribonucleic acid
nt	nucleotide
PBMC	peripheral blood mononuclear cell
PCS	photon correlation spectroscopy
PDI	polydispersity index
pDNA	plasmid deoxyribonucleic acid
PC	polycarbonate
PEG	polyethylene glycol
PMT	photomultiplier tube
pSar	polysarcosine
pSar BA12-100	didodecyl amine initiated polysarcosine with a pSar chain length of 77, as determined by ^{1}H NMR
pSar BA12-25	didodecyl amine initiated polysarcosine with a pSar chain length of 26, as determined by ^{1}H NMR
pSar BA12-50	didodecyl amine initiated polysarcosine with a pSar chain length of 44, as determined by ^{1}H NMR
pSar BA12-75	didodecyl amine initiated polysarcosine with a pSar chain length of 61, as determined by ^{1}H NMR

RNA	ribonucleic acid
SANS	small angle neutron scattering
SAS	small angle scattering
SAXS	small angle X-ray scattering
siRNA	small interfering ribonucleic acid
SLD	scattering length density
ssDNA	single stranded deoxyribonucleic acid
TBE	TRIS borate EDTA
TEM	transmission electron microscopy
TNS	6-(p-toluidino)-2-naphthalenesulfonic acid
TRIS	tris(hydroxymethyl)aminomethane
VEGF	vascular endothelial growth factor
WFI	water for injections
WHO	World Health Organization
Z-Ave	Z-Average

1 | Introduction

1.1 General Introduction

Pharmaceutical research has progressed in rapid manner over the last century. While traditional pharmacological approaches often involved the use of medicinal plants or extracts of their active ingredients, most pharmaceutical products approved today utilize purified or chemically synthesized and often modified active ingredients in the shape of so-called small molecules.[1] One example of this would be acetylsalicylic acid, better known as Aspirin®, which is a molecule that was chemically derived from salicylic acid, the active ingredient in willow bark extracts. The mechanism of action of these drugs often originates from their ability to function better (or deliberately worse) than physiologically occurring molecules such as neurotransmitters. However, pharmaceutical development in recent years has seen the start of a shift away from these small molecules to the field of so-called biologicals. This class of drugs consists of macromolecules such as proteins or nucleic acids and has led to significant advantages in some therapeutic fields, such as several forms of cancer.[2,3]

1.2 Cancer Immunotherapy

According to a recent report by the World Health Organization (WHO), cancer in its different forms places the highest burden in terms of disability adjusted life-years (DALYs) on the worldwide population.[4] While some forms of cancer display promising prospects in terms of survivability, many other types still remain without a cure or even an adequate life-prolonging therapy. One of the most recent developments in this respect is the rise of a concept called cancer immunotherapy. The general idea behind this concept is utilizing the body's own defense mechanisms to combat the mutated cancer cells – a physiological process that is often suppressed in patients by pathophysiological mechanisms such as cancer immunoediting and immune escape.[5] This can be achieved in several ways, such as administering monoclonal antibodies or antibody fragments which were synthesized ex-vivo, through the use of so-called small molecule immunomodulators, or by training the body to recognize neoplastic cells through antigen presentation.[6] Most of the time, these approaches are not used exclusively, but rather in a synergistic manner to try to exclude the possibility of the cancer developing immune escape mechanisms and in order to achieve the three known distinct steps needed to activate an effective antitumor immunity: antigen presentation in dendritic cells, T cell response, and overcoming local immunosuppression at the tumor site (see **Figure 1**).[7] Failure to achieve any one of these three steps could even result in counteracting effects, such as the development of immune tolerance through regulatory T cells.

Training the immune system into recognizing tumor antigens, a concept also called therapeutic cancer vaccination, has been the focus of many research groups over the years, as it opens the theoretic possibilities of personalized and ubiquitous cancer therapies. In short, the idea involves transfecting antigen presenting cells (APCs) with antigens specific to the patient's cancer cells and therefore activating cytotoxic T cell responses against those cells.[6,7] This can either be done *in vivo* – using peptides, proteins, viral vectors, or lipoplexes – or *ex vivo*. In the latter case, the patient's dendritic cells are isolated, transfected, activated, and then reapplied into the system. Recently, approaches trying to bypass the problematic T cell activation step by directly transfecting T cells with the appropriate tumor-antigen-recognizing T cell receptor have been proposed as well. These types of T cells are called CAR-T cells, as they carry a chimeric antigen receptor (CAR) if the transfection was successful. The first two CAR-T cell therapies, tisagenlecleucel-T (Novartis) and axicabtagene ciloleucel (Kite Pharma / Gilead), were approved in short order in 2017, marking a major step forward in cancer immunotherapy.[8] However, while most of these approaches have carried out the transfection step *ex vivo*, direct transfection *in vivo* would be even more preferred, as it eliminates the isolation and cell culture steps.

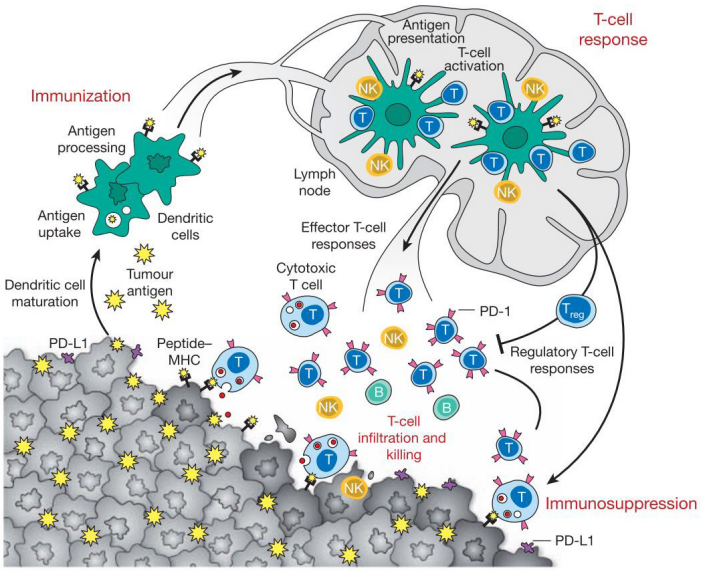

Figure 1. Generation and regulation of antitumor immunity. Tumor antigens are presented by dendritic cells after either uptake or transfection with tumor vaccines and presented or cross-presented on MHC molecules to activate effector T cell responses against the tumor. This is only possible in the presence of an immunogenic maturation stimulus, otherwise immune tolerance will be achieved instead. After successful antigen-education, T cells, along with B and NK cells, enter the tumor bed and execute the antitumor immune response, which can be hampered by tumor-derived immunosuppressive defense mechanisms, such as PD-L1 upregulation on the tumor cell surface, amongst others.
(Reprinted by permission from Springer Nature: Springer *Nature*. Cancer immunotherapy comes of age. Mellman I, Coukos G, Dranoff G. © 2011.[7])

Therefore, from an ease-of-use standpoint, *in vivo* transfection is targeted for both dendritic cell and T cell transfection approaches. Traditionally, viral vectors have often been used for these approaches, but in recent years, other non-viral transfection systems have increased in popularity. These transfection systems are often polymer- or lipid-based and contain either DNA or – more recently – mRNA coding for the tumor antigen (in the case of vaccinations) or the T cell receptor (in the case of CAR-T cell therapy).[6,9] While first major breakthroughs came early, such as the first vaccination of mice with mRNA encoding cancer antigens in 1995, no therapy based on the concept of tumor vaccination has been approved to this date.[9,10] However, several products have been developed to the clinical trial stage, with the notable recent announcements of mRNA cancer vaccine products starting phase II clinical trials in 2019 and 2021.[11–16]

1.3 Lipid-based, Nanosized Delivery Systems

1.3.1 Basic Concept

As mentioned above, viral vectors are often used to transfect target cells with genetic information, such as DNA or RNA. Two very recent examples of this being done *in vivo* are the Covid-19 vaccines Vaxzevria (Astra Zeneca) and Covid-19 Vaccine Janssen (Johnson & Johnson), which utilize adenoviruses as a delivery system to transport antigen-encoding DNA.[17,18] However, several problems come with the use of viral vectors, such as safety concerns due to incomplete inactivation of the viral vector, problematic splicing products, or immune responses against the vector itself.[19–22] Therefore, several approaches have been developed to mimic viral vectors while trying to reduce their downsides. One of these approaches is the use of nanosized delivery systems, such as liposomes or polymersomes. Liposomes are vesicles which can range from the low nanometer scale to several micrometers in size, comprising – as the name suggests – lipids. The term lipid itself is a very generalized one, basically describing molecules which are soluble in nonpolar solvents. Most of the time however, it is used to

describe lipids such as phospho- or sphingolipids, which consist of an aliphatic lipid "tail" and a polar linker or headgroup, such as glycerol, sphingosine, or a modified phosphate group including groups like choline or ethanolamine. In excess of water, these lipids tend to assemble themselves into ordered arrangements, such as bilayer structured liposomes, in order to minimize hydrophilic-hydrophobic interaction (see Figure 2).[23]

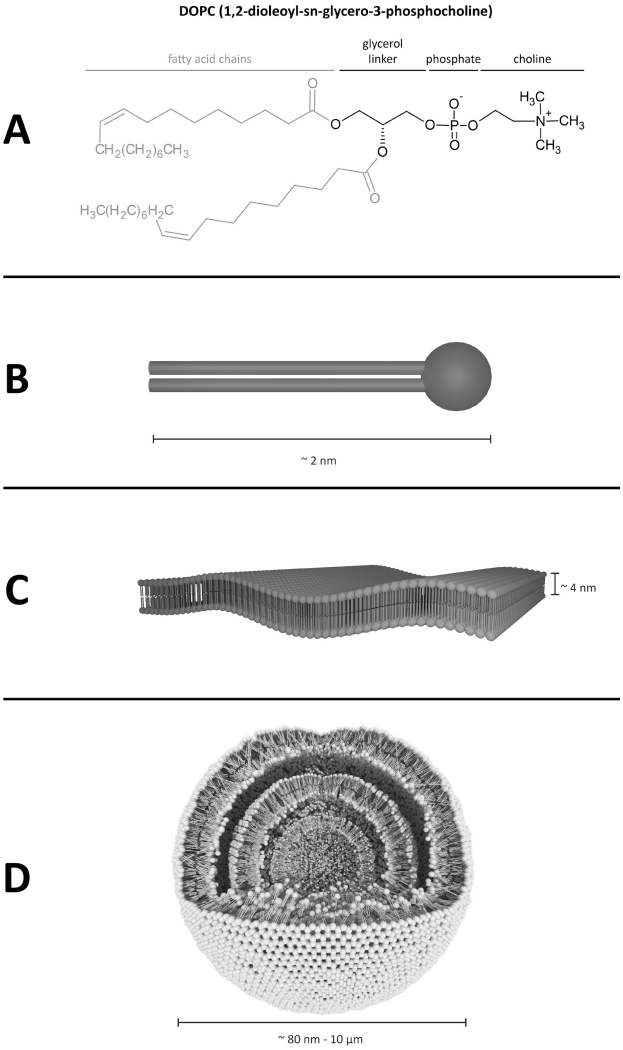

Figure 2. A. 1,2-dioleoyl-sn-glycero-3-phosphocholine (DOPC) as an example for a typical phospholipid, comprising hydrophobic chains (or "tails") and a modular polar headgroup. B-D: Schematic representations of a single lipid molecule (B), lipid molecules forming a lipid bilayer (C), and lipid molecules forming a multilamellar liposome (D).

1.3.2 History of Lipid-based Nanomedicines

It is widely accepted that liposomes were first described by Bangham and colleagues in the 1960s.[24–27] Following this discovery, their potential for different therapeutical and cosmetical applications was rapidly recognized and a vast amount of research was performed on their development, physicochemical and biological characterization, and translation into clinical products. In parallel, pioneer work by Abuchowski and colleagues in the 1970s led to the discovery of the effects of conjugating polyethylene glycol onto drug molecules – the so-called PEGylation.[28,29] The principles from these combined efforts finally led to Doxil®, a liposomal formulation of doxorubicin, becoming the first nanoscale drug product to attain approval by the United States Food and Drug Administration (FDA) in 1995.[30,31] Since then, more than a dozen liposomal drug products have been approved, covering a wide field of therapeutic areas such as cancer, fungal diseases, analgesics,

photodynamic therapy, and antiviral vaccines. [27,32] Even more are undergoing investigation in clinical studies at the time of writing this thesis. While most of these products contain small molecules as the active pharmaceutical ingredient (API), advances have also been made in the field of non-viral transfection reagents. Since their development in the 1990s lipid-based *in vitro* transfection reagents, such as Lipofectamine®, have become the gold-standard for transfecting cells with exogenous DNA or RNA in the laboratory scale.[33] For these principles to reach in-human use however, it took a few years longer, until in 2018, the first clinical trial of an mRNA-based vaccine was reported, where the mRNA included in the lipid-based delivery system encoded two proteins of the Zika virus ZIKV.[34] In 2020, the Covid-19 pandemic led to the rapid clinical testing and subsequent authorizations of the first two mRNA based drug products in the shape of Comirnaty (formerly known as BNT162b2, BioNTech SE, Mainz, Germany) and Spikevax (formerly known as Covid-19 Vaccine Moderna, Moderna, Inc., Cambridge, MA, USA).[35,36] Now that this hurdle has been tackled, many hopes and expectations are set into mRNA and DNA based therapies due to their possible uses in a wide field of applications, including the already mentioned cancer immunotherapy, but also fields like cardiovascular diseases or autoimmune diseases, such as multiple sclerosis.[37,38]

1.3.3 Important Aspects of Lipid-based Nanomedicines

When it comes to lipid-based nanosized delivery systems, there are many important factors to consider both in terms of regulatory requirements, but also in other quality- and efficacy-defining terms. Regulatory agencies such as the European Medicines Agency (EMA) or the FDA have published a number of guidelines and reflection papers defining terms such as “nanomedicine” and regulating their requirements.[39–45] Specifically, the EMA requires the following parameters to be defined for liposomal products: chemical composition and quality (including stability and impurities), morphology and size, encapsulation, *in vitro* release and methods of testing therefore, leakage tests, storage stability, and robustness of the reconstitution process.[42] However, for pharmaceutical drug products, flexibility is given in the regulatory framework and therefore evaluation on a case-by-case basis is possible when it comes to the authorization and approval of lipid-based nanomedicines.[39] Therefore, a best-practice approach should be taken when it comes to the characterization and definition of a drug product candidate.

Independent of regulatory aspects, several important characteristics of lipid-based nanomedicines can be defined. Two of the most obvious parameters are lipid purity and particle size. Lipid purity can be achieved by using synthetic GMP-grade materials. Historically, phospholipid products such as egg phosphatidylcholine (EPC) have been used to prepare liposomes due to their low production costs. However, EPC is not a defined molecule, but rather a mixture of different phospholipids, such as 1,2-dioleoyl-sn-glycero-3-phosphocholine (DOPC). Therefore, moving to substances such as synthetic and pure DOPC should be considered when it comes to reproducible production processes and drug products. Particle size is important both in terms of dosage reproducibility and in terms of applicability, especially when it comes to parenteral applications, where embolic risks have to be taken into account. Additionally, particle size also plays an important role in different uptake processes from the gastrointestinal tract, e.g. transparacellular uptake via the so-called Peyer’s patches or endocytosis by enterocytes.[46] Intestinal particle uptake however is not quantitatively significant and mainly plays a role in immunological processes. Appropriate absolute particle sizes depend on the desired application route, but a general requirement of low polydispersity (polydispersity index PDI < 0.3) can be stated nonetheless.[47] For example, lipoplexes within a size-range of 400 - 1400 nm have shown more efficient transfection in cell culture experiments than both those of a smaller or larger diameter (with 1 µm being the approximate cut-off for endosomal uptake), while particles with a diameter below approximately 500 nm are needed to take advantage of the enhanced permeability and retention (EPR) effect for local accumulation in tumors, and even smaller sizes are targeted when liposomes are used

as contrasting agents in magnetic resonance imaging (MRI).[48–51] Two other important physicochemical parameters are the encapsulation efficacy and the surface charge. While the former is mainly important in terms of reproducible dosing and also reducing the costs of raw materials in the production process, the latter is important in terms of long term colloidal stability in liquid drug products, can influence biodistribution patterns, and has been linked to systemic toxicity effects.[13,39,52,53]

While the physicochemical properties described above can be easily monitored during quality control testing through established assays such as liquid chromatography (lipid purity) or dynamic light scattering (DLS; particle size), other physicochemical properties that are harder to monitor can also play a role in lipid-based nanomedicines. One example of these would be the lipid order as defined by the different lipid mesophases, such as the lipid bilayer phase, the inverse hexagonal H_{II} phase, or a bicontinuous cubic phase such as the Im3m phase (see an illustration of the first two in **Figure 3**).[54] Typical liposomes containing small molecule drugs are usually considered to be bilayer structured vesicles that comprise at least one bilayer (as illustrated in **Figure 2, D**). However, when it comes to lipid-based transfection reagents, such as lipoplexes or lipid nanoparticles, other lipid mesophases have been observed and the ability to undergo phase transitions, such as the transition from the lamellar L_α to the inverse hexagonal H_{II} phase, has been proposed to play an important role in cellular uptake and endosomal escape processes. Lipids that facilitate an easier transition, such as 1,2-dioleoyl-sn-glycero-3-phosphoethanolamine (DOPE), are therefore being called fusogenic lipids and their exact influence on the different steps of cell transfection are still a subject of investigation.[54–57]

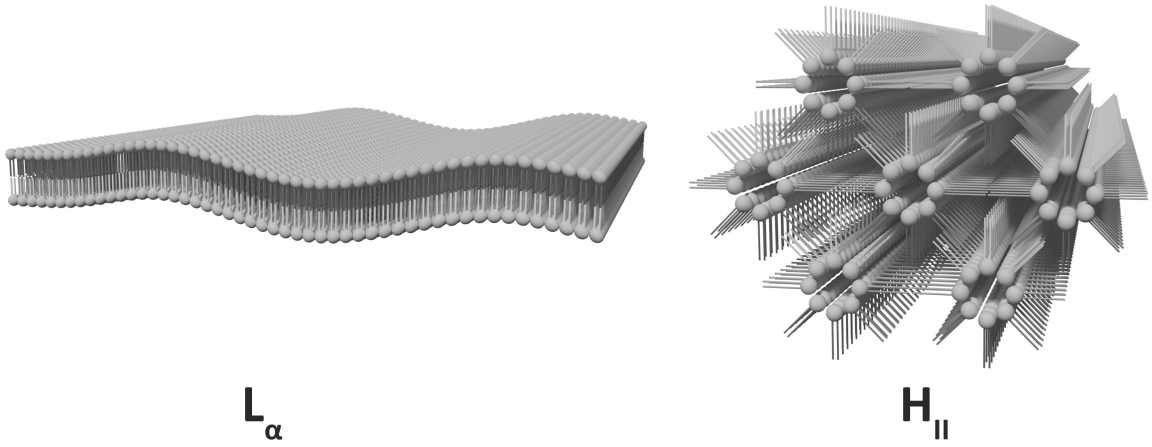

Figure 3. Illustration of the lamellar L_α and the inverse hexagonal H_{II} phases.

In addition to physicochemical properties of lipid-based nanomedicines, biological and clinical implications also need to be taken into account when designing a suitable delivery vehicle. Ideally, the lipid components used should be non-toxic and without another pharmacodynamic effect, easily biodegradable, and their degradation products or the molecules themselves easily excreted after transfection of the cell. Also, unwanted immunogenicity of components, such as the complement activation-related pseudoallergy (CARPA) reaction known for PEGylated nanoparticles, need to be considered, and alternatives to PEGylation have been the focus of several research groups over the last years.[58–60] The importance of PEGylation (or its alternatives) can be observed when looking at studies investigating the so-called protein corona – a term for the accumulated plasma proteins that get bound to the particle surface during circulation *in vivo* and that can have a strong influence on the systemic distribution and particle uptake into the target cells.[61–63] The coupling of active targeting moieties, such as antibody fragments, to target specific cell types has also been a goal that has been worked towards, in order to minimize unwanted off-target cell transfection.[64,65]

As can be seen from this short elaboration, many important aspects have to be considered in parallel when designing lipid-based nanomedicines. While some aspects, such as the impact of particle size and surface charge have been studied extensively, other fields, such as the endosomal escape mechanism, which is needed for successful transfection of target cells, are still very much debated.[48,66] Therefore, gaining as many insights as possible into the structural implications of different particle properties is important for designing the next generations of lipid-based nanomedicines.

1.3.4 Possible Therapeutical Applications, Nucleic Acid Therapies, and Current Level

Lipid-based nanomedicines offer many possible therapeutical applications. Next to their classical application profile – encapsulating small molecule drugs to combat solubility and absorption problems or facilitate delivery across the blood-brain barrier (see Table 1 for a list of approved drug products) – lipid nanomedicines can also be used to deliver biological drugs, such as peptides or nucleic acids, with the latter group comprising both deoxyribonucleic acids (DNA) and ribonucleic acids (RNA). As proteins and peptides can perform a variety of functions, both physiologically and therapeutically, lipid nanomedicines carrying this class of biologicals can also be used for a variety of therapeutic applications. For example, they can carry antigens for vaccination purposes, prolong insulin activity, or deliver enzymes such as asparaginase (for the treatment of asparagine-dependent P1534 tumors).[65] Two examples of already authorized drug products consisting of lipid-based nanoparticles encapsulating viral proteins – so called virosomes – are the vaccines Epaxal® and Inflexal® V (both Crucell / Janssen) against Hepatitis A and influenza, respectively. Unfortunately, both of these products were discontinued.[67] However, a new Covid-19 vaccine (NVX-CoV2373/Nuvaxovid®, Novavax) comprising an antigen protein encapsulated in a lipid nanoparticle has recently shown satisfactory results in the clinical trial stages and was consequently granted a conditional marketing authorization by the EMA in 2021.[68,69]

Drug Product	API	Company	Approval Year	Indication
Doxil / Caelyx	Doxorubicin	Janssen	1995 (FDA), 1996 (EMA)	- Ovarian Cancer - HIV-associated Kaposi's sarcoma - Multiple myeloma
DaunoXome	Daunorubicin	Galen	1996 (FDA)	- HIV-associated Kaposi's sarcoma
AmBiosome	Amphotericin B	Gilead Sciences	1997 (FDA)	- Fungal/protozoal infections
Myocet	Doxorubicin	Teva UK	2000 (EMA)	- Metastatic breast cancer
Visudyne	Verteporfin	Bausch and Lomb	2000 (FDA & EMA)	- Wet age-related macular degeneration - Myopia - Ocular histoplasmosis
MEPACT	Mifamurtide	Millennium	2009 (EMA)	- Osteosarcoma
Marqibo	Vincristine	Spectrum	2012 (FDA)	- Acute lymphoblastic leukemia
Onivyde	Irinotecan	Merrimack	2015 (FDA)	- Metastatic pancreatic cancer
Vyxeos	Cytarabine & Daunorubicin	Jazz Pharmaceuticals	2017 (FDA), 2018 (EMA)	- Acute myeloid leukemia

Table 1. List of FDA- or EMA- approved liposomal drug products containing small molecule APIs.[67,70]

While often consolidated into a single group of pharmaceuticals, nucleic acids can also cover a vast variety of therapeutical applications. This is particularly true for RNA medicines, as different types of RNA have been demonstrated to play central parts in many different physiological and pathophysiological processes. For example, microRNAs (miRNA) such as let-7e play an important part

in regulating gene expression in leukemic stem cells and can themselves be influenced by many factors, such as inflammatory processes.[71] Both small-interfering RNA (siRNA) and antisense nucleotides (aRNA or aDNA) can be used to knock down protein expression via a process called RNA interference or direct mRNA binding, respectively, while mRNA itself can be used to generate expression of the encoded protein.[9,61,72] RNA and DNA can also form aptamers – small molecules that can bind target structures such as proteins.[73] Recently the CRISPR-Cas9 method for gene editing, which utilizes a so-called guide RNA (gRNA) to guide the Cas9-nuclease to the cutting location in the genome, has been at the center of public attention, as the possibilities opened up by this method seem endless.[74–76]

Nucleic Acid Type	Drug Name Brand Name	Company	Approval Year	Indication
ssDNA	*Alipogene tiparvovec* *Glybera*	uniQure	- (FDA) 2012-2017 (EMA)	Lipoprotein lipase deficiency
	Voretigene neparvovec-rzyl *Luxturna*	Spark Therapeutics	2017 (FDA) 2018 (EMA)	Leber congenital amaurosis
	Onasemnogene abeparvovec *Zolgensma*	AveXis / Novartis	2019 (FDA) 2020 (EMA)	Spinal muscular atrophy
	AZD1222 *Vaxzevria*	AstraZeneca	- (FDA) 2021 (EMA)	Vaccine against the SARS-CoV-2 virus
	Ad26.COV2.S *Covid-19 Vaccine Janssen*	Johnson & Johnson	2021 (FDA, EMA)	Vaccine against the SARS-CoV-2 virus
Antisense oligo-nucleotide	Fomivirsen Vitravene	Ionis Pharmaceuticals	1998 - 2006 (FDA) 1999 - 2002 (EMA)	CMV retinitis
	Mipomersen Kynamro	Ionis Pharmaceuticals	2013 (FDA) - (EMA)	Familial hypercholesterolemia
	Nusinersen Spinraza	Ionis Pharmaceuticals	2016 (FDA, EMA)	Spinal muscular dystrophy
	Eteplirsen Exondys 51	Sarepta Therapeutics	2016 (FDA) - (EMA)	Duchenne muscular dystrophy
	Inotersen Tegsedi	Ionis Pharmaceuticals	2018 (FDA, EMA)	Hereditary transthyretin amyloidosis
	Golodirsen Armondys 45	Sarepta Therapeutics	2019 (FDA) - (EMA)	Duchenne muscular dystrophy
	Casimersen Vyondys 53	Sarepta Therapeutics	2021 (FDA) - (EMA)	Duchenne muscular dystrophy
RNA aptamer	Pegaptanib Macugen	Gilead Sciences / OSI Pharmaceuticals	2004 (FDA) 2005 (EMA)	Age-related macular degeneration
siRNA	**Patisiran** **Onpattro**	Alnylam Pharmaceuticals	2018 (FDA, EMA)	Hereditary transthyretin amyloidosis
	Givosiran Givlaari	Alnylam Pharmaceuticals	2019 (FDA) 2020 (EMA)	Acute hepatic porphyria
	Inclisiran Leqvio	Novartis / Alnylam Pharmaceuticals	- (FDA) 2020 (EMA)	Hypercholesterolamia
	Lumasiran Oxlumo	Alnylam Pharmaceuticals	2020 (FDA, EMA)	Primary hyperoxaluria type 1
mRNA	**Tozinameran** **Comirnaty**	Biontech SE	2020 (FDA, EMA)	Vaccine against the SARS-CoV-2 virus
	Elasomeran **Spikevax**	Moderna, Inc.	2020 (FDA) 2021 (EMA)	Vaccine against the SARS-CoV-2 virus

Table 2. List of FDA- or EMA-approved or authorized drug products (including orphan drugs and emergency use authorizations) containing nucleic acids. Therapies using lipid-based delivery systems are printed bold, viral vectors are printed in italics, and modified or conjugated nucleic acids without a delivery vesicle are printed normally. [77,78]

In theory, nucleic acids that promote protein expression, such as ssDNA (single stranded DNA), pDNA (plasmid DNA), or mRNA, can be used for vaccinations (when coding for the antigen), for CAR-T cell therapies (when coding for the T cell receptor), or for all other diseases which are caused by the absence or low levels of a specific protein (protein replacement therapy), such as vascular endothelial growth factor (VEGF) in ischemic heart disease or blood factors in haemophilia.[9,79,80] Nucleic acids

whose mechanism of action induces the silencing or knock-down of protein expression in target cells – such as siRNA or antisense nucleotides (both RNA and DNA) – can be used in therapeutic fields where the overexpression of a given gene is causing the disease (such as hereditary transthyretin amyloidosis or oncogenes in different forms of cancer). Lipid nanomedicine delivered CRISPS-Cas9 technology could in theory do both.[52,76,81] However, ethical questions remain for the *in human* use of the latter.

Table 2 displays a list of all FDA- and or EMA- approved or authorized drug products containing nucleic acids. The first nucleic acid drug – fomivirsen (Isis Pharmaceuticals / Novartis), an antisense oligonucleotide for the treatment of cytomegalovirus (CMV) retinitis – was already approved in 1998, followed six years later by the first RNA aptamer drug pegaptanib (Gilead Sciences / OSI Pharmaceuticals).[77] However, even though nucleic acid therapies have been heavily researched for more than two decades, major breakthroughs were only accomplished within the last few years, both with the approval of the first siRNA drug product Onpattro® (Patisiran, Alnylam Pharmaceuticals) – an siRNA lipid nanoparticle for the treatment of polyneuropathies induced by hereditary transthyretin amyloidosis – in 2018 and with the approval of the first two mRNA drugs in the shape of the aforementioned Covid-19 vaccines Comirnaty® and Spikevax® in 2020 and 2021, respectively. However, with these recent approvals, the general principles behind lipid-based nucleic acid delivery systems have proven to be effective in a clinical setting. Therefore, one can look into an exciting future with many prospects regarding new and potentially groundbreaking steps in cancer immunotherapy through lipid-based nanomedicines.

1.3.5 Lipoplexes and Lipid Nanoparticles for Nucleic Acid Delivery

Typically, lipid nanomedicines for nucleic acid delivery are based on a very simple principle. Nucleic acids represent polyanions due to their phosphate backbone, where each phosphate group is carrying a net negative charge. Therefore, lipid molecules carrying a net positive charge, such as 1,2-dioleoyl-3-trimethylammonium-propane (DOTAP) are used to electrostatically bind the nucleic acid molecules and form so-called lipoplexes. The term lipoplex is universally applicable to both DNA- and RNA-complexing lipid vesicles. The molar ratio of positive to negative charges is called the N/P-ratio, since the cationic charges are most often generated by an amine group (N), which complexes the phosphate group (P). While the employment of the cationic lipid alone is in theory sufficient for lipoplex formation, the addition of a so-called helper lipid (such as the already mentioned phospholipid DOPE or its phosphatidylcholine-homologue DOPC), which carries no net charge, has been proven beneficial for the particle formation process and for cellular uptake. It is therefore used in almost every practical approach (see Figure 4).[55,82]

In recent years, some major observations on the improvement of this basic principle have been made. For one, the permanently positive charged cationic lipids have been shown to cause systemic toxicity effects due to unspecific binding to the overwhelmingly negatively charged biological membranes and plasma proteins within the human body.[48,53] Therefore, pH-dependently charged (so-called ionizable) lipids, which only carry a positive charge at pH levels below the physiological pH of 7.4, have been developed.[83] Since this charge is important for encapsulating the nucleic acid during the preparation process, lipoplexes comprising these kinds of molecules are prepared at slightly acidic pH levels, before being dialyzed against physiological buffers prior to *in vivo* application, reducing the positive charge and leading to an overall neutral or net negative charge of the lipoplex for lower toxicity effects. In addition to these benefits, the pH-sensitivity also facilitates a reaction to the endosomal uptake.[84,85] For example, the ability to generate osmotic pressure within the endosome by continuous lipid protonation via endosomal ATPases (the so-called proton sponge effect) has been proposed as a possible endosomal escape mechanism – a further argument for using pH-dependently charged cationic lipids.[66] Another major step forward was the inclusion of cholesterol or cholesterol-analogues, as well as the addition of so-called stealth-lipids such as PEGylated lipids into the formulation, as these

more complex compositions seem to lead to higher efficacy.[86] Since the inclusion of these components into lipoplexes has shown to lead to a condensed non-aqueous core, formulations following this pattern of components are often called solid lipid nanoparticles, or just lipid nanoparticles (LNPs).[57]

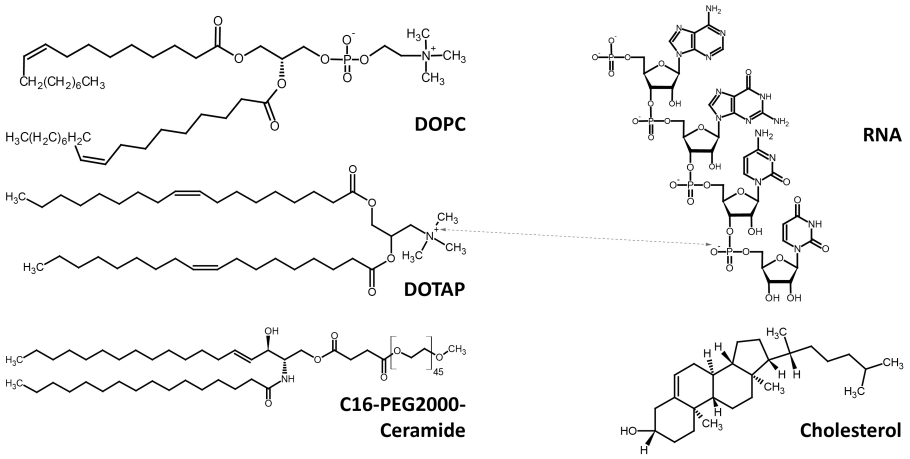

Figure 4. Lipoplexes comprise a helper lipid (e.g., DOPC), a cationic lipid (e.g., DOTAP), and the nucleic acid (e.g., RNA). The positive charge of the cationic lipid is needed to electrostatically bind the phosphate backbone of the anionic nucleic acid (dotted grey arrow). Improvements in colloidal stability and transfection efficacy have been made by the introduction of PEGylated stealth-lipids (e.g., C16-PEG2000-Ceramide) and cholesterol(-analogues).

1.4 Aim of this Thesis

While a lot of effort has been spent on efficacy studies – be it *in vitro* or *in vivo* – and on general physicochemical characterization of lipid-based nanomedicines for mRNA delivery in cancer immunotherapy or other applications, a lack of insight into the internal structures, their transformation in relation to environmental changes, and the implications thereof still remains. This thesis aims to alleviate some of these deficiencies in the understanding of lipoplexes and LNPs by studying their internal structure in dependency of formulation parameters and environmental changes. A special focus is set on pH-dependent changes in particle structure, a process which is known to play an important role in endosomal escape mechanisms. Additionally, parts of this work are dedicated to confirming a previously established structural model for lipoplexes comprising permanently charged cationic lipids and to the optimization of the lipoplex preparation process in terms of reproducibility and influences on the particle structure. For this, potent and rarely applied characterization tools in the form of small angle X-ray and neutron scattering (SAXS and SANS) are used to study the particle structure and its changes *in situ*, alongside more traditional lipoplex characterization methods. The findings gained therein are used to further develop structural models and gain an understanding of the underlying structural process during lipoplex and LNP formation and endosomal processing. This understanding could then be critical for the intelligent design of the next generation of nucleic acid delivery systems.

2 | Materials & Methods

2.1 Materials

The following materials, instruments, and software were used during the experimental portion of this thesis:

2.1.1 Chemicals and Reagents

Name (Short Name)	Supplied by
(4-(2-hydroxyethyl)-1-piperazineethanesulfonic acid) (HEPES)	Carl Roth GmbH + Co. KG (Karlsruhe, Germany)
[bis[(9Z,12Z)-octadeca-9,12-dienyl]amino] 4-(dimethylamino)butanoate (Lipid 14, DPL-14)	either synthesized by the Dan Peer Lab (University of Tel Aviv, Israel) or purchased from NucleoSyn (Olivet, France).
1,2-dioleoyl-3-dimethylammonium-propane (DODAP)	Avanti Polar Lipids (Alabaster, AL, USA)
1,2-dioleoyl-3-trimethylammonium-propane (chloride salt) (DOTAP-Cl)	Avanti Polar Lipids (Alabaster, AL, USA)
1,2-dioleoyl-sn-glycero-3-phospho-(1'-rac-glycerol) (sodium salt) (DOPG-Na)	Lipoid GmbH (Ludwigshafen, Germany)
1,2-dioleoyl-sn-glycero-3-phosphocholine (DOPC)	Avanti Polar Lipids (Alabaster, AL, USA) and Merck & Cie (Schaffhausen, Switzerland)
1,2-dioleoyl-sn-glycero-3-phosphoethanolamine (DOPE)	Avanti Polar Lipids (Alabaster, AL, USA)
1,2-dioleyloxy-3-dimethylaminopropane (DODMA)	Avanti Polar Lipids (Alabaster, AL, USA)
1,2-di-O-octadecenyl-3-trimethylammonium propane (chloride salt) (DOTMA-Cl)	Avanti Polar Lipids (Alabaster, AL, USA)
1,2-distearoyl-sn-glycero-3-phosphocholine (DSPC)	Lipoid GmbH (Ludwigshafen, Germany)
10x Tris-borate-EDTA buffer (10x TBE buffer)	Carl Roth GmbH + Co. KG (Karlsruhe, Germany)
2-mercaptoethanol	Life technologies (San Diego, CA, USA)
3',3'',5',5''-Tetrabromophenolsulfonephthalein (bromophenol blue)	Sigma-Aldrich (Saint Louis, MO, USA)
6-(p-toluidino)-2-naphthalenesulfonic acid (TNS)	Sigma-Aldrich (Saint Louis, MO, USA)
Agarose (LE Agarose)	Biozym Scientific GmbH (Hessisch Oldendorf, Germany)
Bright-Glo™ Luciferase Assay System	Promega GmbH (Walldorf, Germany)
CD14-BV510 monoclonal antibody (clone: MφP9)	BD Biosciences (San Jose, CA, USA)
CD19-PerCP-Cy5.5 monoclonal antibody (clone: SJ25C1)	eBioscience Inc. (San Diego, CA, USA)
CD3-BV421 monocolonal antibody (clone: UCHT1)	BD Biosciences (San Jose, CA, USA)
CD4-PE monoclonal antibody (clone: SK3)	BioLegend (San Diego, CA, USA)
CD56-PE-Cy7 monoclonal antibody (clone:B-159)	BD Biosciences (San Jose, CA, USA)
CD8-APC monoclonal antibody (clone: SK1)	BD Biosciences (San Jose, CA, USA)
CD90.1 encoding mRNA (Thy1.1 RNA)	BioNTech SE (Mainz, Germany)
CD90.1-BB515 monoclonal antibody (clone: OX7)	BD Biosciences (San Jose, CA, USA)
Chloroform	Sigma-Aldrich (Saint Louis, MO, USA)
Cholesterol (plant based)	Avanti Polar Lipids (Alabaster, AL, USA)
D-(+)-trehalose dihydrate from Saccharomyces cerevisiae, BioReagent	Sigma-Aldrich (Saint Louis, MO, USA)
Didodecyl amine initiated polysarcosine with a pSar chain length of 26, as determined by 1H NMR (pSar BA12-25)	synthetized by Christian Muhl as previously described (Muhl et al European Polymer Journal 2019)[87]
Didodecyl amine initiated polysarcosine with a pSar chain length of 44, as determined by 1H NMR (pSar BA12-50)	synthetized by Christian Muhl as previously described (Muhl et al European Polymer Journal 2019)[87]
Didodecyl amine initiated polysarcosine with a pSar chain length of 61, as determined by 1H NMR (pSar BA12-75)	synthetized by Christian Muhl as previously described (Muhl et al European Polymer Journal 2019)[87]
Didodecyl amine initiated polysarcosine with a pSar chain length of 77, as determined by 1H NMR (pSar BA12-100)	synthetized by Christian Muhl as previously described (Muhl et al European Polymer Journal 2019)[87]
Dilinoleylmethyl-4-dimethylaminobutyrate (DLin-MC3-DMA)	synthetized by the lab of Prof. Dan Peer (Tel Aviv, Israel)
Disodium hydrogen phosphate (Na2HPO4)	Sigma-Aldrich (Saint Louis, MO, USA)
Dulbecco's phosphate-buffered saline (Gibco DPBS)	Fisher Scientific GmbH (Schwerte, Germany)

Ethanol, absolute (200 proof), molecular biology grade, Fisher BioReagents™	Fisher Scientific GmbH (Schwerte, Germany)
Ethylenediaminetetraacetic acid (EDTA)	Carl Roth GmbH + Co. KG (Karlsruhe, Germany)
Ethylenediaminetetraacetic acid (EDTA)	Life technologies (San Diego, CA, USA)
Fetal bovine serum (FBS)	
Gel-Red® nucleic acid gel stain, 3X in water	Biotium (Fremont, CA, USA)
GlutaMAX-I	Life technologies (San Diego, CA, USA)
Glycylglycine (PUFFERAN® ≥ 98.5% Buffer Grade)	Carl Roth GmbH + Co. KG (Karlsruhe, Germany)
Luciferase encoding mRNA (iVT-Luc RNA)	BioNTech SE (Mainz, Germany)
MEM NEAA	Life technologies (San Diego, CA, USA)
N1-methylpseudouridine-5'-triphosphate (m1ΨTP)	TriLink Biotechnologies (San Diego, CA, USA)
Non-coding mRNA ~1670 nucleotides (R159)	BioNTech SE (Mainz, Germany)
Non-coding mRNA ~1900 nucleotides (R18)	BioNTech SE (Mainz, Germany)
N-palmitoyl-sphingosine-1-70 {succinyl[methoxy(polyethylene glycol)2000]} (C16-PEG2000-Ceramide)	Avanti Polar Lipids (Alabaster, AL, USA)
Nuclease-free water (DEPC-treated)	Carl Roth GmbH + Co. KG (Karlsruhe, Germany)
Octylphenoxypolyethoxyethanol (Triton™ X-100)	Sigma-Aldrich (Saint Louis, MO, USA)
Pen Strep	Life technologies (San Diego, CA, USA)
Pooled human serum (PHS)	Life technologies (San Diego, CA, USA)
Potassium dihydrogenphosphate (KH2PO4)	Sigma-Aldrich (Saint Louis, MO, USA)
Quant-IT™ RiboGreen™ RNA reagent	Fisher Scientific GmbH (Schwerte, Germany)
RNaseZAP™	Sigma-Aldrich (Saint Louis, MO, USA)
RPMI medium 1640	Life technologies (San Diego, CA, USA)
Sodium pyruvate	Life technologies (San Diego, CA, USA)
Stabilizing fixative	BD Biosciences (San Jose, CA, USA)
Thermo Scientific™ RiboRuler High Range RNA ladder	Fisher Scientific GmbH (Schwerte, Germany)
Viability dye	eBioscience Inc. (San Diego, CA, USA)
Water for injections (Ampuwa)	Fresenius Kabi Deutschland GmbH (Bad Homburg vor der Höhe, Germany)

2.1.2 Labware and Disposables

Name	Supplied by
15 mL Cellstar™ conical bottom tubes	Greiner Bio-One GmbH (Kremsmünster, Austria)
50 mL freestanding centrifuge tubes, sterile	VWR International GmbH (Darmstadt, Germany)
CellStar™ 96-well, cell culture-treated, flat-bottom microplates (black)	Greiner Bio-One GmbH (Kremsmünster, Austria)
Combitips Advanced™ 0.1 dispensing pipette tips PCR clean	Eppendorf AG (Hamburg, Germany)
Combitips Advanced™ 1.0 mL dispensing pipette tips PCR clean	Eppendorf AG (Hamburg, Germany)
Copper electron microscopy grid 300 µm mesh	Plano GmbH (Wetzlar, Germany)
Discovery Comfort 0.5-10 µL single channel pipette	Kinesis GmbH (Langenfeld, Germany)
Discovery Comfort 200-1000 µL single channel pipette	Kinesis GmbH (Langenfeld, Germany)
Discovery Comfort 20-200 µL single channel pipette	Kinesis GmbH (Langenfeld, Germany)
DNA LoBind® tubes PCR clean 0.5 mL	Eppendorf AG (Hamburg, Germany)
DNA LoBind® tubes PCR clean 1.5 mL	Eppendorf AG (Hamburg, Germany)
DNA LoBind® tubes PCR clean 2.0 mL	Eppendorf AG (Hamburg, Germany)
DNA LoBind® tubes PCR clean 5.0 mL	Eppendorf AG (Hamburg, Germany)
DTS1070 folded capillary zeta cells	Malvern Panalytical (Kassel, Germany)
Falcon™ Express™ Cordless Pipet-Aid	Corning Inc. (Corning, NY, USA)

Injekt® Solo 20 mL syringes	B. Braun Melsungen AG (Melsungen, Germany)
Multipette® M4	Eppendorf AG (Hamburg, Germany)
PC Membranes 0.2 µm (Avanti Mini Extruder membranes)	Merck KGaA (Darmstadt, Germany)
Pierce™ Protein Concentrator PES, 100K MWCO, 5-20 mL	Thermo Fisher Scientific GmbH (Dreieich, Germany)
QS cuvettes 1.0 mm thickness	Hellma GmbH & Co. KG (Müllheim, Germany)
QS cuvettes 2.0 mm thickness	Hellma GmbH & Co. KG (Müllheim, Germany)
Quartz-glass capillaries, ends cut, 100 mm, 1.0 mm, 0.1 mm wall thickness	Hilgenberg GmbH (Malsfeld, Germany)
SafeSeal SurPhob pipette tips, 10 µL, sterile	Biozym Scientific GmbH (Hessisch Oldendorf, Germany)
SafeSeal SurPhob pipette tips, 1000 µL, sterile	Biozym Scientific GmbH (Hessisch Oldendorf, Germany)
SafeSeal SurPhob pipette tips, 20 µL, sterile	Biozym Scientific GmbH (Hessisch Oldendorf, Germany)
SafeSeal SurPhob pipette tips, 200 µL XL, sterile	Biozym Scientific GmbH (Hessisch Oldendorf, Germany)
SafeSeal SurPhob pipette tips, 200 µL, sterile	Biozym Scientific GmbH (Hessisch Oldendorf, Germany)
Serological pipettes ROTILABO®, 10 ml	Carl Roth GmbH + Co. KG (Karlsruhe, Germany)
Serological pipettes ROTILABO®, 50 ml	Carl Roth GmbH + Co. KG (Karlsruhe, Germany)
SiLibeads ZY 0.8-1.0 mm	Sigmund Lindner GmbH (Warmensteinach, Germany)
Single-channel microlitre pipette ROTILABO® 0.5-10 µL	Carl Roth GmbH + Co. KG (Karlsruhe, Germany)
Single-channel microlitre pipette ROTILABO® 100-1000 µL	Carl Roth GmbH + Co. KG (Karlsruhe, Germany)
Single-channel microlitre pipette ROTILABO® 20-200 µL	Carl Roth GmbH + Co. KG (Karlsruhe, Germany)
Single-channel microlitre pipette ROTILABO® 2-20 µL	Carl Roth GmbH + Co. KG (Karlsruhe, Germany)
Single-use cuvettes UV Micro (z = 15 mm) 0.07-0.55 mL	BRAND GmbH + Co. KG (Wertheim, Germany)
Soft-Ject® 1 mL syringes	Henke-Sass, Wolf GmbH (Tuttlingen, Germany)
Sterican® single use hypodermic needles, G 27	B. Braun Melsungen AG (Melsungen, Germany)
Syringe filters ROTILABO® PVDF 0.22 µm	Carl Roth GmbH + Co. KG (Karlsruhe, Germany)
Syringe filters ROTILABO® PVDF 0.45 µm	Carl Roth GmbH + Co. KG (Karlsruhe, Germany)
TwistTop Vials 0.65 mL skirted	Sorenson™ BioScience Inc. (Salt Lake City, UT, USA)
TwistTop Vials 2.0 mL skirted	Sorenson™ BioScience Inc. (Salt Lake City, UT, USA)
Xplorer® 1-100 µL 8-channel pipette	Eppendorf AG (Hamburg, Germany)

2.1.3 Instruments

Not included in this list are the technical compositions of the SANS and SAXS beamlines, which are listed in their respective methods paragraph.

Name	Supplied by
Avanti Mini Extruder Set with Holder/Heating Block	Merck KGaA (Darmstadt, Germany)
Axioscope 5 Microscope with Axiocam 208 color Camera and N-Achroplan 100x/1.25x Oil Lens	Carl Zeiss Microscopy Deutschland GmbH (Oberkochen, Germany)
BD FACSCanto II cell analyzer	BD Biosciences (San Jose, CA, USA)
Binder Drying Cabinet	Binder GmbH (Tuttlingen, Germany)
Centrifuge 5804 R	Eppendorf AG (Hamburg, Germany)
DMA 4100 M Density Meter	Anton Paar GmbH (Graz, Austria)
Easy R40 refractometer	Mettler Toledo GmbH (Gießen, Germany)
EasyPhor Medi horizontal gel electrophoresis chamber	Biozym Scientific GmbH (Hessisch Oldendorf, Germany)
Holten LaminAir Model 1.2 Laminar Air Bench	Heto-Holten GmbH (Wettenberg, Germany)
Infinite 200Pro plate reader	Tecan Group AG (Männedorf, Switzerland)
Infinite F200 plate reader	Tecan Group AG (Männedorf, Switzerland)
LA-30 syringe pump	Landgraf Laborsysteme HLL GmbH (Langenhagen, Germany)
LE225D-OCE semi-micro lab balance	Sartorious AG (Göttingen, Germany)

Magnetic stirrer RSM-10 B	Phoenix Instruments (Garbsen, Germany)
Milli-Q® Advantage A10 Water Purification System with Q-Pod® remote dispenser	Merck KGaA (Darmstadt, Germany)
NanoDrop™ 2000 microvolume spectrophotometer	Thermo Fisher Scientific Inc. (Wlatham, MA, USA)
NanoVel custom DLS	Nanovel Ltd. & Co. KG (Langenlonsheim, Germany)
Rotavapor R-3 with V-700 vacuum pump and V-850 controller	BÜCHI Labortechnik GmbH (Essen, Germany)
RS-VA 10 test tube shaker (vortexer)	Phoenix Instruments (Garbsen, Germany)
Savant Refrigerated Condensation Trap RT400	Thermo Fisher Scientific Inc. (Wlatham, MA, USA)
SAVANT Speed Vac SVC 200	Thermo Fisher Scientific Inc. (Wlatham, MA, USA)
SKANAIR VertikalFlow VFC-120 Laminar Air Bench	Skan AG (Basel, Switzerland)
Speedmixer™ DAC 150.1 CM 41	Hauschild & Co. KG (Hamm, Germany)
Tecnai G2 12 BioTwin transmission electron microscope with MegaVIew III Soft Imaging System	FEI Company (Hillsboro, OR, USA) and EMSIS GmbH (Münster, Germany)
Typhoon trio+	Amersham Biosciences (UK)
Ultrasonic Cleaner USC-THD	VWR International GmbH (Darmstadt, Germany)
Vapro® Vapor Pressure Osmometer	Wescor Inc. (Logan, UT, USA)
ViCELL XR cell viability analyzer	Beckman Coulter GmbH (Krefeld, Germany)
WTW pH 538 pH-meter with InLab Micro pH electrode	LaboTec GmbH & Co. KG (Dillenburg-Manderbach, Germany) and Mettler-Toledo GmbH (Gießen, Germany)
Zetasizer Nano ZS	Malvern Panalytical (Kassel, Germany)

2.1.4 Software

Name	Developer	Purpose
Adobe Illustrator CC	Adobe Inc. (Mountain View, CA, USA)	Illustration
Adobe Photoshop CC	Adobe Inc. (Mountain View, CA, USA)	Illustration
ALV Correlator 7	ALV-Laser Vertriebsgesellschaft.m.b.H. (Langen, Germany)	Data Analysis
ATSAS package	EMBL Hamburg (Germany)	Data Analysis
BD FACSDiva™	BD Biosciences (San Jose, CA, USA)	Data Analysis
blender	Blender Foundation (Amsterdam, Netherlands)	Illustration
Citavi 6	Swiss Academic Software GmbH (Germany)	Bibliography
FlowJo™ V10.7.1	Treestar inc. (Ashland, Oregon, USA)	Data Analysis
ImageJ 1.5q	Wayne Rasband / National Institutes of Health NIH (USA)	Data Analysis
Microsoft Excel	Microsoft (Redmond, WA, USA)	Data Analysis
QtiPlot 1.0.0	IONDEV SRL (Romania)	Data Analysis
Rstudio 1.4.453	RStudio PBC (Boston, MA, USA)	Data Analysis
SasView 5.0.4	SasView Project[88]	Data Analysis
Typhoon Scanner Control	Amersham Biosciences (UK)	Data Analysis
Zen Core 3.1	Carl Zeiss Microscopy Deutschland GmbH (Oberkochen, Germany)	Data Analysis
Zetasizer software	Malvern Panalytical (Kassel, Germany)	Data Analysis

2.2 Methods

The following methods and work practices were applied during the experimental portion of this thesis:

2.2.1 Nuclease-free Working Conditions

To ensure that no mRNA degradation due to nucleases would occur, only certified RNase-free disposable labware and chemicals were used whenever possible. Where this was not possible, other appropriate measures, such as treatment of surfaces with the nuclease-degrading agent RNaseZap™, dry-heat sterilization at temperatures ≥ 250°C for at least 6 hours, or ultra-filtration of MilliQ-water, were set in place.

2.2.2 Buffers and Media

If not stated otherwise, a 10 mM solution of glycylglycine (GG) in water for injections (WFI, Ampuwa) or MilliQ-water was used for the preparation of most formulations. Glycylglycine buffer has been established for a long time, shown low toxicity, and can easily be prepared.[89] The short dipeptide allows for steric and electrostatic stabilization of charged particles and the low molarity ensures no interference with characterization methods (such as zeta potential measurements) and miscibility with pH-buffers. Routinely performed pH-measurements of this buffer resulted in a reproducible pH of 5.7±0.1, making it ideal for the preparation of pH-dependent systems as well.

When determining pH-dependent properties of the delivery systems, phosphate buffers based on those proposed by Sörensen were used at different molarities, such as 66.7 or 150 mM.[90] These were prepared by mixing different ratios of KH_2PO_4 and Na_2HPO_4 (e.g., 81.8 mL Na_2HPO_4 solution and 18.2 mL KH_2PO_4 solution for pH 7.4 – for an extensive list see chapter 7.4.1 in the supplement) and subsequent adjustment of the pH with 0.1 M NaOH or HCl, until it was within ±0.05 of the target pH. For quantitative analysis of experiments where the buffer was mixed with other media (such as 10 mM GG), the resulting pH of the mixing ratio was measured and used for further calculations.

Additionally, for permanently charged systems which were characterized by SANS, two trehalose buffers were prepared. These consisted of 10% (m/V) or 60% (m/V) trehalose in either H_2O or D_2O (deuterated water), which were then mixed to gain different H_2O/D_2O ratios (for a detailed explanation, see 2.2.4.7.2 Small Angle Neutron Scattering Parameters).

2.2.3 Lipoplex and Lipid Nanoparticle Preparation

2.2.3.1 Nomenclature

While all systems described within this thesis represent lipid-based mRNA delivery systems, two different terms are used throughout the text: lipoplex (LPX) and lipid nanoparticle (LNP). No standardized definition as to what kind of system should be called which name could be found in the literature, but in general the term lipoplex seems to be historically used for liposome-like systems based on (often permanently charged) cationic lipids and nucleic acids (and, of course, helper lipids). The term LNP on the other hand seems to have recently evolved describing mainly particles that utilize pH-responsive lipids, contain additional components such as cholesterol, and are often prepared via modified ethanol injection methods which seem to result in more solid particle-like structures without an aqueous core. However, both terms are often interchanged.[13,49,53,57,91,92] Therefore, for the purpose of this thesis, the following definition is given:
Systems comprising only helper lipid, cationic lipid (both permanently charged or pH-responsive), and mRNA are called “lipoplexes (LPXs)”, while systems that also include cholesterol and functionalized lipids are called “lipid nanoparticles (LNPs)”. Systems that are basically lipoplexes with the addition of

only functionalized lipids, but no cholesterol, are called "intermediates (IMs)". This nomenclature is used irrespective of the particle preparation method.

2.2.3.2 mRNA Concentration and Quantification

In order to prepare highly concentrated lipoplexes and LNPs for scattering experiments, the mRNA had to previously be concentrated to a higher concentration. For this, mRNA at a concentration of 0.5 mg/mL was filled into a Pierce Protein Concentrator, whose membrane had a molecular weight cut-off of 100,000 Da, and then centrifuged at 2500 RPM and at 4 °C in 5-minute intervals until an appropriate concentration could be visually observed (remaining volume about 1/20 of the starting volume, proportional to an approximate concentration of 10 mg/mL). The resulting mRNA concentration was then quantified after dilution using UV spectrophotometry on a NanoDrop™ 2000.

2.2.3.3 Sample Composition and Calculation

Due to the variety of systems, compositions, and preparation methods used in this thesis, only a general overview over the sample composition and their calculation is given here. For specific sample compositions, see the respective tables in the results chapter (Chapter 3). All samples presented within this thesis are composed of (A) a helper lipid, such as DOPE or DOPC, (B) a permanently charged or pH-responsive cationic lipid, such as DOTMA or DODMA, and (C) mRNA. As previously mentioned, some systems also comprise a functionalized lipid (D) and/or cholesterol (E). In addition, every system can be characterized by several key parameters: Their total lipid concentration, their molar composition, their relative mass composition, their N/P ratio, and their mRNA concentration. The total lipid concentration is the total combined concentration (m/V) of all their components except mRNA (A+B+D+E). The molar composition states the percent-wise (mol%) distribution of all lipid molecules, with ∑mol% (A,B,D,E) = 100%, whereas the relative mass composition states the same but in mass percentages (wt%). The molar composition and the relative mass composition differ due to different molecular weights of different lipids. The N/P ratio states the ratio of nitrogen atoms in cationic lipid headgroup amines (N) and phosphate groups in the nucleic acid (P), and therefore represents the positive to negative charge ratio within the particle. For the calculation of this, a mean nucleotide molecular weight of 330 Da is assumed, as is common practice.[92] Therefore, particles with differing molar content of cationic lipid can still have the same N/P-ratio, as long as the mRNA ratio is changed appropriately as well. Depending on the type of assay utilized, either constant lipid concentrations or constant mRNA concentrations between different samples can be important (e.g., pK_a-determination or cell-culture experiments, respectively). Therefore, both calculation methods were applied when preparing the samples and the used concentration is stated with the results. Two sample compositions, one prepared with an even total lipid concentration, and one with an even mRNA concentration, are shown in Table 3. As can be seen, both samples display the same N/P-ratio, even though their compositions differ. An exemplary step-by-step calculation for the formulation #1 (LNP-04 from chapter 3.2.1.2) utilizing both approaches can be found in the supplement (see chapter 7.4.2).

#	Total lipid	(A) DOPE	(B) DODMA	(D) pSar (MC12-50)	(E) cholesterol	(C) mRNA	N/P
1	1.00 mg/mL 1.73 mM	10.0 mol% 12.9 wt% 0.129 mg/mL	40.0 mol% 42.9 wt% 0.429 mg/mL	2.0 mol% 12.2 wt% 0.122 mg/mL	48.0 mol% 32.1 wt% 0.321 mg/mL	8.0 mol% 4.6 wt% 0.046 mg/mL	5
2	1.82 mg/mL 3.03 mM	10.0 mol% 12.4 wt% 0.225 mg/mL	50.0 mol% 51.5 wt% 0.939 mg/mL	2.0 mol% 11.7 wt% 0.214 mg/mL	38.0 mol% 24.4 wt% 0.445 mg/mL	10.0 mol% 5.5 wt% 0.100 mg/mL	5

Table 3. Example compositions of differently calculated LNP systems with matching N/P-ratios. Note, that the sum of both the mol% and wt% of all components except mRNA always adds up to 100% and that the quotient of mol%(B) and mol%(C) is defined as the N/P ratio. Example #1 is normalized to an even total lipid concentration (1.00 mg/mL), while #2 is normalized to an even mRNA concentration (0.100 mg/mL).

2.2.3.4 Thin Lipid Film Method

Samples prepared via the thin lipid film method were manufactured using the following protocol: First, stock solutions of each lipid were prepared by dissolving the appropriate amount in chloroform, resulting in concentrations of either 25 mg/mL (DOTAP), 50 mg/mL (DODMA, DOTMA) or 100 mg/mL (DOPC). These stock solutions were pipetted into a glass vial in the required ratios, mixed, and the solvent was then evaporated using stepwise rotary evaporation (Büchi Rotavapor) at room temperature. The resulting thin lipid films were then frozen at approximately -25 °C and stored at that temperature for at least 12 h. The previously concentrated mRNA was then diluted to the desired concentration in 10 mM GG, 10 mM HEPES/EDTA buffer, or trehalose buffer and subsequently added to the lipid films. The samples were immediately vortexed for about 5 seconds and then left for hydration at room temperature for another 12 h (or overnight). The fully hydrated samples were then vortexed again, until no residual film could be seen anymore, and finally collected for further characterization. If stated, samples were additionally extruded through polycarbonate (PC) membranes with 450 nm or 200 nm pore size at room temperature for size control.

2.2.3.5 Dual Asymmetric Centrifugation

The dual asymmetric centrifuge (DAC) represents a special kind of mixer which rotates around two axes (see Figure 5), allowing the sample within the inserted vials to be thoroughly mixed by the previously added small ceramic or glass beads. The method can generally be seen as an alteration of the thin lipid film method described above, but is more suitable for small sample volumes. This is beneficial for systems comprising costly materials, such as the specialized lipids and mRNA in lipoplexes. Additionally, both mRNA complexation and vesicle size control happen in the same step, allowing for less polydisperse systems without the need of additional size-control steps such as extrusion.[93]

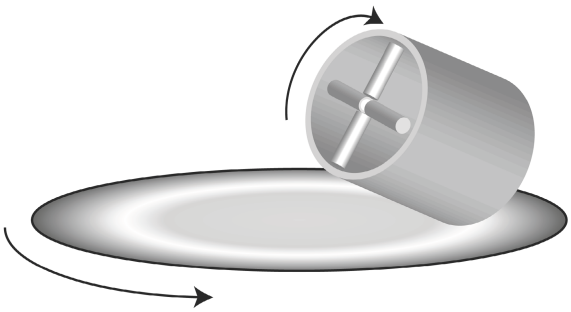

Figure 5. Schematic representation of the mixing process in a dual asymmetric centrifuge (DAC).

Again, lipid stock solutions were prepared in chloroform, which were then pipetted into TwistTop vials, which in turn were placed inside a Speed Vac centrifuge. A vacuum was applied during centrifugation, resulting in a mixed lipid film after evaporation of the solvent. Then, a small amount (enough to cover the bottom of the vial) of 0.8-1.0 mm ceramic beads (SiLiBeads) was placed inside the vial and an appropriate amount of concentrated mRNA solution was added. The vials were placed into a dual asymmetric centrifuge (Speedmixer™), which was run for 10 minutes at 3000 RPM. After the addition of buffer to reach the desired sample concentration, the samples were mixed for another 10 minutes at 3000 RPM, before being transferred into sample tubes for further characterization.

2.2.3.6 Ethanol Injection Method

The ethanol injection method for the preparation of liposomes was first described over 40 years ago and has since been used in various forms.[94] To be exact, there is no single ethanol injection method – instead, different variations can be used – and have been used – throughout the years, from classical

ethanol injection, or manual protocols thereof, to automated microfluidic mixing processes, which have the benefit of being scalable to higher industrial production volumes. [25,95–97] While the technical details differ, all of these methods utilize the same principle: Lipids are dissolved in ethanol (or sometimes isopropyl alcohol) and premixed in the desired proportions. This ethanolic stock solution is then diluted with an aqueous solution, which can also already contain the mRNA, to lower the lipid solubility and force the formulation of liposomes, lipoplexes, or LNPs.[95] Additional steps are also possible, such as in-line dilution or dialysis for buffer exchange.[60]

For the systems used in this thesis, two protocols were used: A "classic" protocol, where the ethanolic lipid solution was injected into the aqueous phase on a magnetic stirrer with a syringe, and a "manual protocol" (MP) where the aqueous phase was pipetted onto the ethanolic solution, immediately followed by vortex mixing (see Figure 6 for an illustration). For both protocols, lipid stock solutions at concentrations of either 15 mg/mL (cholesterol), 25 mg/mL (DOPE, C16-PEG2000-Ceramide), 50 mg/mL (most cationic or ionizable lipids), or 100 mg/mL (DOPC) were prepared in absolute ethanol, while the mRNA was diluted to the desired final concentration with 10 mM glycylglycine solution. Then, for the classic injection method, the mRNA was pipetted into a small round-bottom glass flask and placed onto a magnetic stirrer which was set to 500 RPM. The lipid stock solutions were mixed appropriately before the mix was then taken up into a syringe and injected into the aqueous mRNA solution through a 27G needle under constant stirring. The resulting vesicles were transferred into a test tube and kept at 4-8 °C until further characterization. For the manual protocol, the lipid stock solutions were mixed in a test tube and the aqueous mRNA solution was then pipetted on top, followed by immediate thorough mixing on a test tube shaker (vortexer). Again, the resulting samples were stored at 4-8 °C until further characterization.

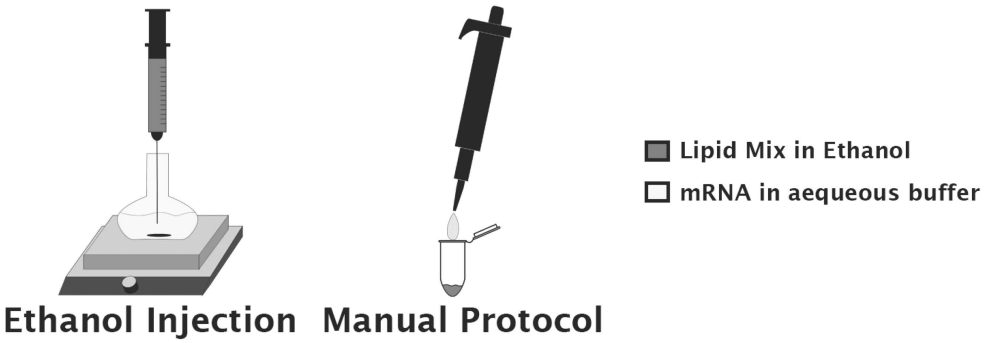

Figure 6. Schematic representation of the two variations of the ethanol injection method utilized in this thesis: the "classic" injection protocol (left) and the "manual protocol" (right).

While the classic ethanol injection method is only suitable for sample volumes of 500 µL or higher, small sample volumes from 100 µL up to 1.5 mL can easily be handled by the manual protocol. Additionally, the manual protocol can be performed using only disposable, single-use, certified nuclease-free materials, while both the glass vials and magnetic stirrers utilized in the classic method have to be previously treated to guarantee nuclease-free conditions. It must be said however, that these methods can result in slightly differing structures, depending on the system. For more information on this, see chapter 3.2.1.2 (Structural Differences Between Lipoplexes and LNPs).

2.2.4 Physiochemical Characterization

2.2.4.1 Dynamic Light Scattering

Dynamic Light Scattering (DLS), also known as Photon Correlation Spectroscopy (PCS), was used for the determination of the hydrodynamic radius of the prepared delivery systems, for which it is considered

a standard method.[39,98] For DLS, particles in solution are placed in a laser beam and the intensity fluctuation of the light scattered by the particles, which is caused by constructive and destructive interferences due to the constantly moving particles, is measured. This fluctuation is then correlated against short decay intervals and displayed as the so-called autocorrelation function. The correlation function itself is dependent on both the translational diffusion coefficient D_t and the scattering vector q, with the latter itself being dependent on multiple factors, as can be seen here: [99]

$$|q| = \frac{4 \cdot \pi \cdot \eta_0}{\lambda_0 \cdot sin\frac{\theta}{2}} \quad (1)$$

The diffusion coefficient for spherical particles can be derived from the Stokes-Einstein equation:[100]

$$D_t = \frac{R \cdot T}{N} \cdot \frac{1}{6 \cdot \pi \cdot \eta \cdot R_H} \quad (2)$$

Taking both equations into account, the autocorrelation function is dependent on the refractive index (η_0), the temperature (T), and the absolute viscosity (η) of the dispersion medium, as well as on the hydrodynamic radius (R_H) of the particles and several device constants, such as the laser wavelength (λ_0) or the scattering angle (θ). Therefore, the hydrodynamic radius can be calculated when all other variables of the medium are known.

Two devices were used for particle size determination in this thesis: If not stated otherwise, a Malvern Zetasizer Nano ZS was used. The samples were diluted to an approximate total lipid concentration of 1 mg/mL and measured within their respective medium at 25 °C (after a 30 s equilibration time) and at a backscattering angle of 173°. No variation was applied to the standard measurement parameters for water, as measurements of the refractive index of 10 mM glycylglycine showed no significant differences to that of water, and literature values for the absolute viscosity of low molarity glycylglycine solutions also reported no differences.[101] One measurement consisted of approximately 11-15 ten second runs (automatically determined by the device). All calculations mentioned in the previous paragraph were performed automatically by the device software and the data was then exported for further use. Additionally, a Nanovel custom DLS, equipped with a 5 mW HeNe laser operating at a wavelength of 638 nm and measuring at a backscattering angle of 170°, was used where stated explicitly. Samples were measured for 30 s or 100 s and a regularized fit was applied to the decay function via the ALV Correlator software. The resulting size distribution curves were then exported for further examination.

Particle sizes given in this thesis are given as the Z-Average (Z-Ave), which represents the intensity based harmonic mean of the particle diameter.[102] The distribution of the particle size is expressed via the polydispersity index (PDI), which ranges from 0 (monodisperse) to 1 (very polydisperse).[99] Additionally, intensity- or number-distributions are shown, where beneficial.

2.2.4.2 Zeta Potential

Another important parameter for nanosized formulations is the so-called Zeta potential (ζ potential), which is defined as the potential difference between the electric double layer (EDL) around the electrophoretically mobile particle and the dispersant layer around it.[99] The EDL itself consists of an inner layer – the so-called Stern layer – of ions charged oppositely to the particle surface and an outer layer of mixed charge molecules that extends to the slipping plane. This the hypothetical plane that divides those ions moving with the particle during electrophoresis and those staying in place in the surrounding dispersant (for a schematic representation see **Figure 7**). As the surface potential of the particle itself (also known as the Nernst potential) cannot be measured directly, zeta potential

measurements are used to get a grasp of the particle charge instead. While zeta potentials close to 0 mV can lead to aggregation, zeta potentials from ± 30 mV upwards are usually considered stable, with the threshold to prevent aggregation being considered to be ± 15 mV in most cases.[39]

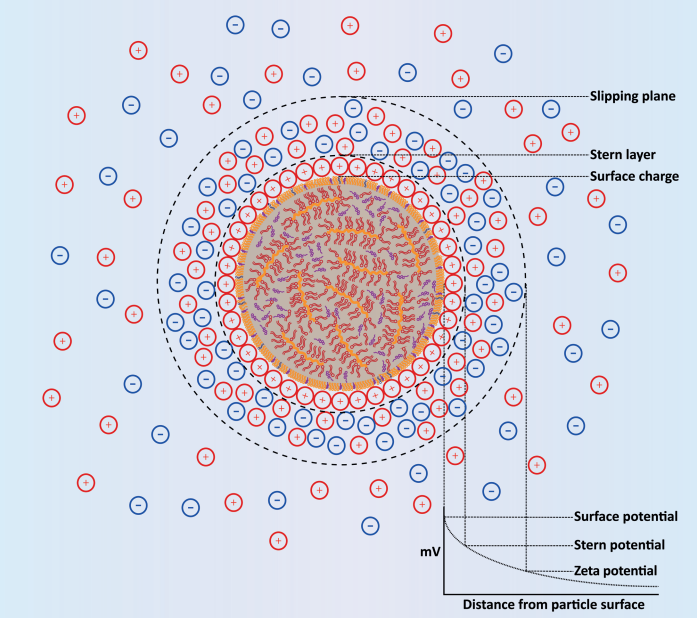

Figure 7. Schematic representation of the different layers around a lipid nanoparticle and their respective potentials (adapted from [103]).

When measuring the zeta potential of nano-sized delivery vehicles, an electric field is applied to the sample dispersion in a special measuring cell and the particle movement is measured by laser doppler velocimetry (LDV). Similarly to the previously described DLS measurements, the zeta potential can then be calculated as long as key characteristics of the dispersant medium are known. In this case the Henry equation is applied, with U_e being the electrophoretic mobility, ε the dielectric constant of the medium, η the absolute viscosity, and f(κα) the Henry function, which depends on the ratio of the particle radius to the Debye length: [104]

(3) $$U_e = \frac{2 \cdot \varepsilon \cdot z \cdot f(\kappa\alpha)}{3 \cdot \eta}$$

Zeta potential measurements in this thesis were performed on a Malvern Zetasizer Nano ZS using the appropriate zeta cells (DTS1070). The samples were measured in their respective medium (as stated with the results) at 25 °C after a 30 s equilibration time, and with a minimum of 10 and a maximum of 100 runs. The exact number of runs as well as the attenuation setting was automatically determined by the device itself. Water was defined as the dispersant and the Smoluchowski model integrated in the software was used for f(κα). Zeta potentials presented in this thesis are presented as the mean of at least three independent preparations ± SD, unless stated otherwise.

2.2.4.3 mRNA Loading and Accessibility

Since dosing of mRNA based nanomedicines is based on the dose of mRNA applied to the patient, reliable and reproducible loading of the (intact) mRNA inside or onto the lipoplexes and LNPs is a prerequisite for reliable therapeutics. Therefore, two different methods were applied to determine consistent loading of the mRNA without degradation. While the fluorescence-based Ribogreen assay was used to quantify the amount of accessible mRNA (both in solution and bound to the particle, but

still accessible to the fluorescent dye), agarose gel electrophoresis was used to determine the amount of free mRNA and check for mRNA degradation.

2.2.4.3.1 Ribogreen Assay

The amount of accessible mRNA was measured with the commercially available Quant-iT™ RiboGreen® assay, as it is commonly used for exactly this purpose.[57,105,106] It utilizes an RNA-binding fluorescent dye so that the amount of mRNA accessible to the dye can be measured using fluorescence measurements on a 96-well plate reader. The amount of mRNA can be quantified by preparing calibration curves of different mRNA concentrations, which can then be compared with the amount of mRNA used during the particle preparation step. Another way of calculating the amount of accessible mRNA is possible by the addition of Triton X-100 – a surfactant which will disrupt the nanoparticle structure and release all mRNA from the delivery system, facilitating the quantification of all mRNA present in the samples.[57] The amount of accessible mRNA can then be calculated from the fluorescence intensity without addition of Triton X-100 (F_0) and the fluorescence intensity after its addition (F_t) as follows:

$$mRNA\ incorporation\ [\%] = \left(1 - \frac{F_0}{F_t}\right) \cdot 100 \quad (4)$$

Quantification of the accessible mRNA or mRNA incorporation rate in this thesis was performed on a Tecan Infinite F200 plate reader as top-down measurements at an excitation wavelength of 465 nm and an emission wavelength of 535 nm in black 96-well plates (no cover). Samples were measured in their respective buffer (e.g., 10 mM GG), as stated with the results. Each well contained 200 µL of 0.5x Ribogreen RNA reagent (1:400 dilution of the commercially available 200x DMSO stock solution) in the desired buffer, 1 µL of sample at an mRNA concentration of 0.05 - 0.2 mg/mL, and – if applicable – 5 µL of 1:100 Triton X-100 (in water) or buffer, with this ratio of sample to Triton X-100 having been tested via DLS to be sufficient for particle disruption.

2.2.4.3.2 Agarose Gel Electrophoresis

Agarose gel electrophoresis is a commonly used tool when working with RNA, offering multiple possibilities such as quantification, strand size / integrity determination, and more. Within this thesis, agarose gel electrophoresis was used to differentiate between accessible mRNA (as determined by the much more sensitive Ribogreen assay) and free mRNA that is not bound to the delivery system in any way and can freely diffuse through the pores of an agarose gel when a current is applied. RNAs move through the gel towards the positive electrode due to their negative charge, with small RNAs moving quicker than their larger counterparts. Therefore, a separation by size can be performed and possible RNA fragments can be detected further towards the front (or bottom) than the intact, larger RNA they were a part of, while particle-bound mRNA is retained within the loading pocket. The agarose concentration can be varied depending on the application, as higher concentrations result in stronger retention (and therefore separation) while lower concentrations facilitate the analysis of larger ranges of RNA size, but with compromises in the separation of similar RNA strand lengths.

Gels used within this thesis were prepared at non-denaturing conditions at an agarose concentration of 1%. Agarose was dispersed in 1x TRIS-borate EDTA (TBE) buffer (1:10 dilution of the 10x TBE buffer stated in the materials table) containing 1x Gel-Red staining agent (final concentration after dilution of the commercially available 3x stock solution in the TBE buffer). The dispersion was heated until the agarose had dissolved completely and was then cooled down to approximately 60 °C before being cast into a gel tray. The cooled down gel was placed into an electrophoresis chamber containing 1x TBE. All samples (at mRNA concentrations of 0.03-0.05 mg/mL) were mixed with a 40% solution of glycerol at a ratio of 1:1 before adding 5 vol% of bromophenol blue to the samples as a loading- and moving front-marker. Then, the samples were loaded into the lane pockets. Additionally, free mRNA from the same

batch was prepared in the same way, as was an RNA size ladder (RiboRuler High Range RNA Ladder, 200-6000 nucleotides). Both were loaded onto the gel as markers. Then, the electrophoresis was performed at about 114 V for approximately 60 minutes. The detection of the mRNA was then carried out on a Typhoon trio+ gel scanner, using the green laser at a wavelength of 532 nm, a pixel size of 200 microns, and a photomultiplier tube (PMT) setting of 450. The gel was pressed during the measurement and the focal plane was set to + 3 mm. The scanned gel's contrast was optimized while taking care not to cause signal clipping and the image was exported.

2.2.4.4 TNS Assay (pK_a Determination)

This fluorescence-based assay is a common tool in the characterization of ionizable lipids and is often used for the determination of pK_a values of ionizable lipids or formulations comprising these.[95,107] It utilizes the fluorescent dye 6-(p-toluidino)-2-naphthalenesulfonic acid (TNS), which is negatively charged and therefore binds to the cationic charges of the protonated ionizable lipid, resulting in higher lipophilicity and therefore the loss of associated water molecules that would otherwise quench the fluorescence.[107] Therefore, a high amount of charged ionizable lipid leads to a high amount of measured fluorescence, while no fluorescence can be measured for uncharged lipids.

For this thesis, the following method was applied: All measurements were performed as separate measurements of three different preparations, each individually measured as triplicates in black 96-well plates. Each well contained 90 µL of buffer (pH buffer, as described under 2.2.2 Buffers and Media), 10 µL of sample at a concentration of 0.1 mg/mL total lipid, and 2 µL of TNS in DMSO (300 µM). A pH-variation was performed from pH 4.5 to approx. pH 8-9 in steps of 0.5, with the resulting pH of the 9:1 pH buffer to sample buffer mixture having been measured and being used for all consequent calculations. The fluorescence was measured as a top-down measurement using a TECAN infinite 200Pro plate reader at 325 nm excitation and 435 nm emission wavelength after incubation for 15 minutes. The mean fluorescence intensity at pH 4.5 was normalized to 1 for each triplicate and a sigmoidal (Boltzmann) fit was applied (see 2.2.6 Data Treatment and Analysis) to determine the formulation pK_a. All pK_a values reported in this thesis represent the mean of at least three independently prepared formulations.

2.2.4.5 Polarizing Light Microscopy

For the microscopic images shown in this thesis, an Axioscope 5 microscope with an Axiocam 208 color camera and N-Achroplan 100x/1.25x oil lens was used. Samples were prepared at or diluted to a concentration of 1 mg/mL unless stated otherwise and approximately 40 µL were pipetted onto a slide. A droplet of immersion oil was placed on the cover slip and the sample was placed under the 100x lens immersed in the oil. A polarizing and an analyzing filter were used. All images and size measurements were performed with Zen Core software.

2.2.4.6 Transmission Electron Microscopy

Transmission electron microscopy (TEM) utilizes a focused electron beam (instead of light) in a vacuum passing the sample before hitting a detector which in turn translates the registered electrons into an image. As electrons behave in wave-like manner, they can interact with the sample and thereby be scattered elastically by the atomic core or inelastically by the electrons of the sample atoms. By using apertures that hinder strongly scattered electrons from reaching the detector, a contrast can be created between electron dense regions, which scatter strongly, and electron scarce regions of the sample, which cause little inelastic scattering. Therefore, regions with high electron density appear dark in the final image.[108] While the resolutions reached by electron microscopy are vastly superior to that of light microscopy, facilitating the imaging of size scales in the nanometer region instead of the micrometers reached by light microscopy, this also comes with the downside of allowing only very restricted analysis of small sample subsets. The possibility (and restriction) of looking at single particles

at once therefore functions as almost the total opposite of averaging methods such as small angle scattering (see chapter 2.2.4.7 below), which analyze all particles within a sample at the same time. Therefore, these methods should be seen as complementary to each other. Another downside to standard TEM is the necessity of drying samples beforehand, which can of course destroy systems with an aqueous core, such as liposomes. This can be circumvented by utilizing cryo-EM, which is a much more complex and costly method and was not used within this thesis.

The TEM-images shown in this thesis were collected on a Tecnai G2 12 BioTwin transmission electron microscope equipped with a MegaView III Soft Imaging System. The samples were prepared at a total lipid concentration of 1 mg/mL and dried on a copper electron microscopy grid with a grid size of 300 µm, before being transferred into the electron microscope. The image contrast was optimized for print using the software Adobe Photoshop.

2.2.4.7 Small Angle Scattering

Small angle scattering (SAS) methods, such as small angle X-ray scattering (SAXS) or small angle neutron scattering (SANS) are advanced methods capable of generating structural insights into a variety of biological and non-biological materials and structures. For example, typical uses include the structural characterization of biological macromolecules such as proteins, nucleic acids, or structures assembled from these, of biological membranes, and of inorganic nanoparticles.[109] While the general principle is the same as that of microscopic methods – a focused beam (be it visible light, electrons, X-rays, or neutrons) interacts with the sample and afterwards gets detected – the insights gained from SAS differ vastly to those gained from microscopic methods. As previously mentioned, microscopical methods are non-averaging and used for characterizing single specimen (particles, cells, etc.) at a time. Therefore, insights gained from these methods can be affected by a selection bias as to which area of a sample is displayed and analyzed. Small angle scattering on the other hand lacks the possibility of analyzing one specimen at a time, but instead always gives an average structure for all particles inside the illuminated sample volume.

Since SAXS and SANS are very similar methods, both will be explained here together. For details on the experimental setups used in this thesis however, please refer to their respective sub-chapters below (2.2.4.7.1 and 2.2.4.7.2). All small angle scattering instruments are built up by the same basic parts, which are illustrated in Figure 8. They consist of an X-ray or neutron source, a collimation system for creating a focused beam, a sample holder, a beam stop, and a detector.[109] While the basic parts are the same, their size can differ vastly, especially for SAXS instruments. The X-ray source for example can be a sealed X-ray tube less than 10 cm in size or a synchrotron light source such as the Petra III synchrotron at DESY in Hamburg (Germany), which measures 2.3 km in circumference, resulting in vastly different X-ray flux and costliness of measurements.[110] A synchrotron is a pulsed X-ray source generating X-rays as Bremsstrahlung from charged particles in a particle accelerator moving along a circular path at relativistic speeds (close to the speed of light). The continuous wavelength spectrum of the X-rays generated there is then focused and passed through a monochromator at a so-called beamline, where the actual experiment is set up.[111] In all instruments, the monochromatized beam is then focused onto a sample using a collimation system, which can either be a point collimation or a line collimation, before illuminating the sample in the sample holder (often in a vacuum) and interacting with it. In line with the incident beam and located between the sample and the detector is a beam stop, which protects the detector from the very strong beam intensity of the non-scattered beam contributions. The lowest angle detection limit is therefore limited by the size of the focused beam, the size of the beam stop, and the sample-detector distance. Increasing the latter facilitates the measurement of lower scattering angles, but at the cost of scattering intensity and wider-angle signal. Therefore, different sample-detector distances can be utilized for the same sample, depending on the scattering angle range of interest, and the resulting scattering profiles can then be combined. As the

scattering of particles in solution, which are of course oriented randomly, is isotropic, the resulting 2D scattering patterns are centrally symmetric in concentric circles around the incident beam and are therefore radially averaged to be displayed as a 1D-scattering profile.[109,112]

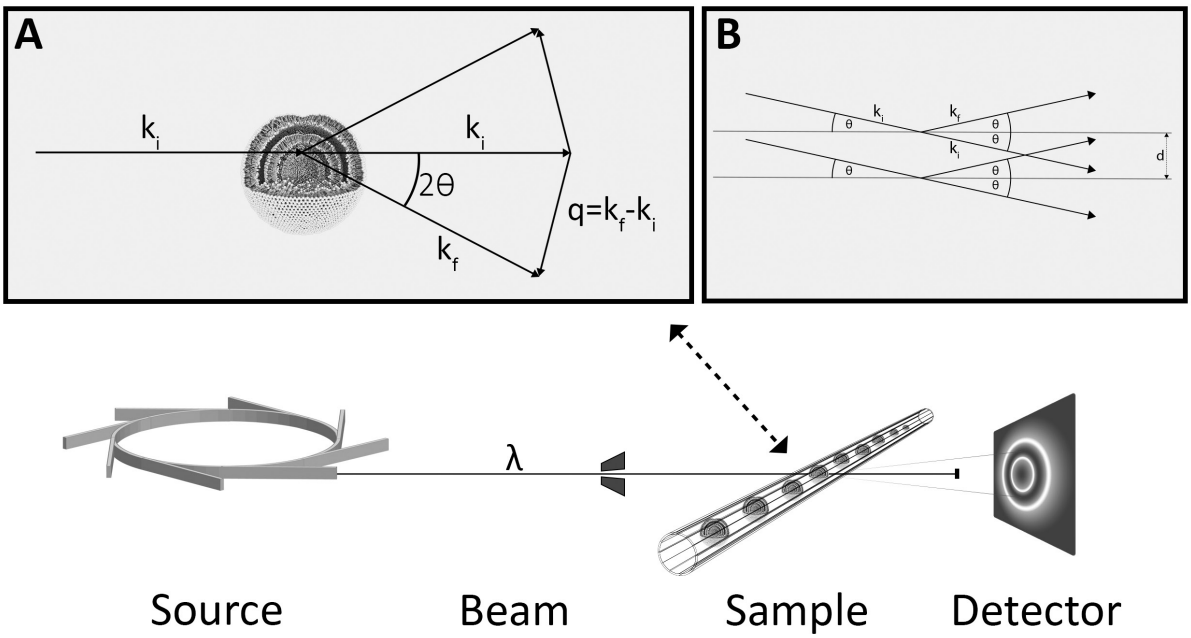

Figure 8. Illustration of an SAS-instrument, consisting of a source (depicted here by a synchrotron), the beamline, the sample holder, and the detector.
Inserts A and B: Relationship between the incident wave vector k_i, the scattered wave vector k_f, the scattering angle 2θ, the scattering vector q, and the lattice spacing d (adapted from [111]).

Both X-rays and neutrons can be characterized by wave-like and particle-like properties. In the case of X-rays the wavelength is < 10 nm and the particles are called photons, while for neutrons their de Broglie wavelength depends on their velocity.[113,114] Both X-rays and neutrons interact with atoms in the sample – for X-rays this interaction is caused by charged subparticles (mainly the electron shell), while for neutrons, which themselves represent uncharged subparticles, these interactions mainly take place within the atomic nuclei.[114,115] Therefore, the intensity of the scattered signal (or contrast) increases with the atomic number of the sample molecules for X-rays, while for neutrons this is not the case and a more complex relationship between molecules and their scattering contrast is given (for details see further below).[114] Three types of interaction are known for the interaction of X-rays with matter: X-rays can be either absorbed by the atom, they can be scattered elastically, or they can be scattered inelastically.[109] While absorption is an important factor and can be utilized in specialized techniques such as anomalous small angle X-ray scattering (ASAXS), its benefit for the techniques applied in this thesis is negligible and therefore it is preferred to be kept small. Inelastic or incoherent scattering (also called Compton scattering) involves energy transfer to a sample atom, resulting in a longer wavelength of the scattered radiation compared to the wavelength of the incident beam radiation.[116] It does not contribute to any interference phenomena and is therefore not useful for structural analysis as it just contributes to the scattering background. Elastic or coherent scattering (also called Thomson scattering) on the other hand takes place without a transfer of energy. Here, the electrons (in the case of X-rays) start oscillating at the same frequency as the incoming beam radiation.[117] The hereby emitted dipole radiation hence has the same wavelength as the X-ray beam from the source and can be the basis for constructive and destructive interference patterns, as the electron oscillation and therefore also the emitted radiation is synchronous between neighboring atoms. The angle between the wave vector of the incoming beam k_i and the scattered beam k_f, who are both of the magnitude $2\pi/\lambda$, is defined as the scattering angle 2θ. The difference between the wave

vectors (k_f-k_i) measured at the sample-to-detector distance L is defined as the scattering vector q (see also **Figure 8 inserts**). It has the dimension of inverse length units (e.g., nm^{-1}), its magnitude is given as

$$q = |\vec{q}| = \frac{4 \cdot \pi \cdot sin\theta}{\lambda} \tag{5}$$

and it is often also called the momentum transfer or wave vector transfer in a mechanical analogy.[117,118] The definition given in **equation (5)** has the advantage of being normalized by the applied (X-ray or neutron) wavelength and is therefore universal and independent of the source used in the experiment, which is not the case for the modulus of the scattering vector.[119] As explained above, coherent scattering is the cause of the recorded 2D interference patterns, as the scattered waves can be either completely in phase (pathlengths between the wavefronts shifted only by integer multiples of the wavelength), leading to constructive interference, or completely out of phase (shifted by half of the wavelength), leading to destructive interference, or somewhere in between.[119,120]

Generally speaking, two main pieces of information are contained in a SAS curve – the form factor P(q) and the structure factor S(q) – with the observed scattering curve being a product of both factors and a variety of experimental setup variables, such as the incident intensity I_0, the sample-to-detector distance L, the beam size A, or the transmission T, which are of course either independent of the measured particle or can be recorded during the experiment:[118]

$$I(q) = I_0 \cdot \frac{r_0^2}{L^2} \cdot T \cdot A \cdot d \cdot n \cdot P(q) \cdot S(q) \tag{6}$$

The form factor represents the interference patterns of all the beams scattered by all the atoms across the particle and is therefore a function of the size and the shape of the studied particle species. It can be divided into three sections: At low q lies the so-called Guinier-region, which can be used to raise information on the particle size, the central part contains characteristic oscillations dependent on the particle shape, and at higher q one can use the so-called Porod-region to gain insights on the particle surface.[109]
As interference depends on the pathlengths between the different waves, and these pathlengths in turn depend on the distance between the atoms, the sum of all interferences caused by the particle is therefore a measure of all distances between all atom pairs within a particle. Therefore, the form factor can be used to calculate the so-called (radial) pair-distance distribution function p(r) from the Fourier-transfer of the form factor, which shows the distribution of all inter-atom distances given within a particle. It is derived from the oscillating part of the form factor and different characteristic distributions arise from different particle shapes, such as globular, core-shell, cylindrical, or lamellar particles (see **Figure 9**). Form factors for a variety of geometric shapes have been calculated and comprehensive lists can be found in the literature.[121]
As mentioned, the lowest-angle part of the scattering curve is called the Guinier region. The Guinier region is characterized by a linear decay of the ln(I) vs q^2 curve and fitting a linear function in this region can be used for the calculation of the particle size, also called the radius of gyration R_g, with the slope of the linear decay fit being $-(R_g^2/3)$.[122] This calculation is however only valid for q-ranges where $q \cdot R_g$ is smaller than the square-root of three and therefore limited by the instrument itself, with the smallest and largest detectable particle sizes being defined by the smallest and largest recordable scattering vectors (dependent on detector size and sample-detector distance) as follows:[123]

$$r_{min} = \frac{\pi}{q_{max}};\ r_{max} = \frac{\pi}{q_{min}} \tag{7}$$

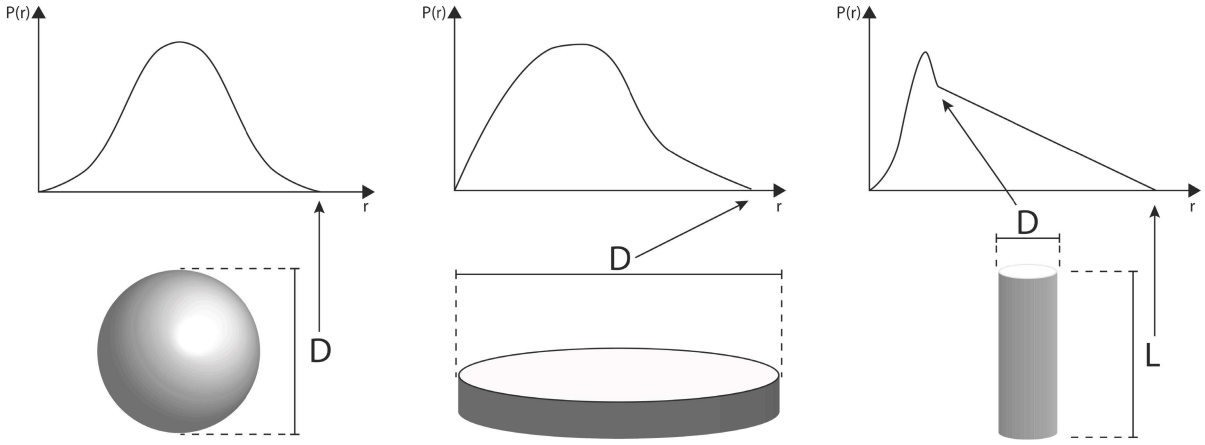

Figure 9. Characteristic shapes of the pair-distribution function for globular, cylindrical, and lamellar particle shapes (adapted from [109]).

The third region of the form factor – the Porod- or power-law region – can be characterized by an exponential decay in the form of q^{-n}, with steep Porod-slopes (n=4) being indicational of a smooth particle surface, Porod-slopes in the range of 2-3 indicating surface fractals (rough surfaces), and those below caused by other structures, such as mass fractals, collapsed polymer coils, or Gaussian chains.[109,118]

The observed scattering pattern however only adheres to the form factor, if the sample is monodisperse and diluted. Polydisperse samples lead to different form factor functions and therefore less concise minima in the scattering curve, while dilute samples are needed to keep the inter-particle distance very large compared to the beam wavelength. [109]

While the form factor is a result of dilute particle solutions, ignoring their interactions, the structure factor is the result of interactions between concentrated and ordered scatterers. It is generally known, that scattering from ordered, repeating structures results in strongly constructive interference patterns, which are known as Bragg peaks (see Figure 10). In crystalline and liquid crystalline structures, the relationship between the scattering angle θ, at which these peaks are found, and the lattice spacing d causing them, is given by Bragg's law (see also Figure 8 insert B):[124]

(8) $$n\lambda = 2 \cdot d \cdot sin\theta$$

Taking into account equation (5), this can be simplified and expressed wavelength independent as:

(9) $$q = n \cdot \frac{2\pi}{d}$$

These Bragg-peaks contain several important pieces of structural information.[119] The first was already mentioned above and can easily be seen in equation (9). By determining the peak position, the lattice spacing d (also called d-spacing) can be calculated, with n being the order of the observed peak. Secondly, the width of the peak is characteristic for the so-called correlation length or crystallite size. This parameter describes the length scale over which the ordered correlation between the particle molecules persists (see Figure 11 for an illustration) and can be calculated using the Scherrer equation:[119,120]

(10) $$L = \frac{k \cdot \lambda}{\beta_s \cdot cos(\theta_{max})}$$

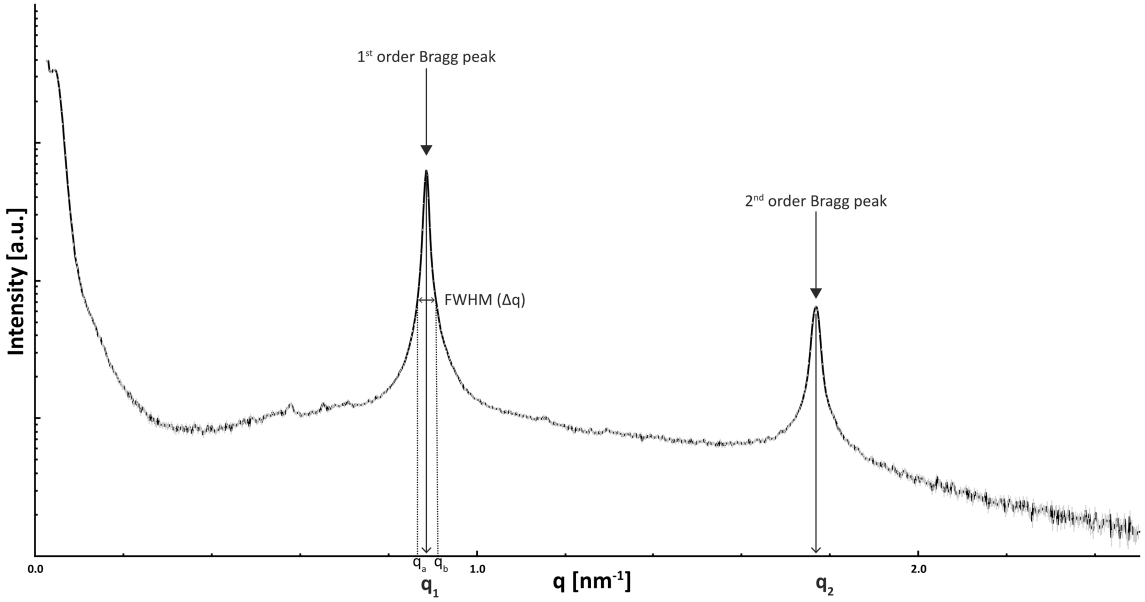

Figure 10. An exemplary SAXS curve with clearly visible 1st and 2nd order Bragg peaks and their peak positions q_1 and q_2, respectively. FWHM (or Δq) is the full width of the peak at half its maximum intensity ($\Delta q = q_b - q_a$).

Here, L represents the average correlation length, β_s is the peak width (full width at half maximum FWHM, see also Figure 10) in 2θ, and θ_{max} is the peak position or Bragg angle. K is a constant, which is usually taken as close to unity. In liquid crystalline samples, a more simplified approximation is often used, which takes into account exponentially decaying correlations (see further below) and defines the correlation length ξ as follows (with Δq being the FWHM in nm^{-1}):[111]

$$\xi = \frac{2}{\Delta q} \tag{11}$$

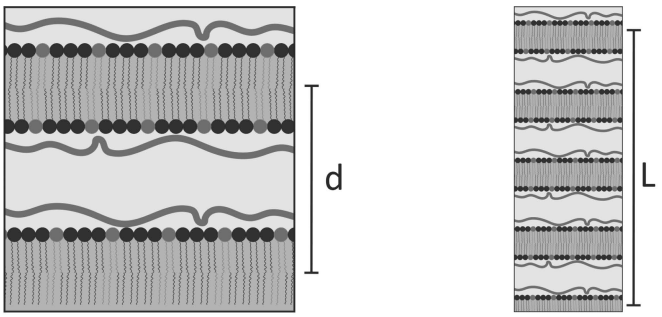

Figure 11. Illustration of the difference between the lattice spacing d and the correlation length L in multilamellar lipoplex systems.

Additional information of the structural order of the probed systems can be gained from the higher order Bragg peaks. Crystalline or liquid crystalline systems can exist in lots of different symmetries, each resulting in characteristic repeat patterns of their resulting Bragg peaks (see Table 4).[54,82,109] Therefore, if at least two orders of reflections are visible, a conclusion on the type of lipid phase present in the system can be drawn. While crystalline structures are known to form a multitude of different symmetries (thermotropic phases), this is not the case for liquid crystalline structures.[111] The lyotropic phases which have been shown to exist under excess water conditions are the lamellar fluid phase L_α, the bicontinuous cubic phases, the inverse hexagonal H_{II} phase, and one micellar cubic phase.[54]

Lyotropic phase	Peak repeat ratio
Lamellar liquid crystal (L_α)	1, 2, 3, 4, 5, …
Cubic (Pn3m)	1, √2, √3, √4, √5, …
Inverse Hexagonal (H_{II})	1, √3, √4, √7, √9, …

Table 4. Repeat patterns of the most relevant crystalline symmetries / lipid mesophases as multiples of q_1. While the higher order peaks of lamellar systems only occur at integer multiples of q_1 (as seen in Figure 10), the repeating patterns of other biologically relevant phases are more complex.

Additionally, if even more orders of reflection are visible, an electron density map (in the case of SAXS; scattering length density profile in the case of SANS) can be calculated from the scattering profile, depicting the probed structure in real space as opposed to the reciprocal space seen in a scattering profile (see Figure 12). Explaining this procedure in detail would go beyond the scope of this section, but in general this can be described as follows:[119] After fitting all of the peaks with Lorentzian line shapes (see chapter 2.2.6.1), the scattering intensities (peak areas) are adjusted with a so-called Lorentz-correction, which corrects for several parameters such as the instrumental setup. From these corrected intensities, the amplitudes of the probed electron density contrasts are calculated by taking their square-root. The electron density map $\tilde{\rho}(z)$ is then calculated as the sum of the Fourier transform of the scattering profile for each individual electron density contrast as follows (with h being the Miller indices (peak order), α_h the phase of their amplitude (can be ±1), F_h the corrected amplitudes, s_h the momentum transfer ($s=q/2\pi$), and z the distance in real space):

$$\tilde{\rho}(z) = \sum_{h=1}^{h\,max} \alpha_h \cdot F_h \cdot cos(2\pi \cdot s_h \cdot z) \tag{12}$$

It has to be noted, that as the phase information of the scattered beam is lost in SAXS, the detector can only measure its intensity (also called the phase-problem).[114] Hence, information on the correct phase of the different diffraction orders have to be taken from the literature.[119,125] The resulting electron density profile can then, for example, be used to calculate the headgroup-headgroup distance (d_{HH}), as the highest electron density in phospholipid bilayers is given by their headgroups, which contain atoms with a higher atomic number than those of the lipid tails. This in turn can then be used to calculate the thickness of the water layer (d_w) between lipid bilayers in a multilamellar bilayer system (L_α phase) by subtracting d_{HH} from the already calculated d-spacing.

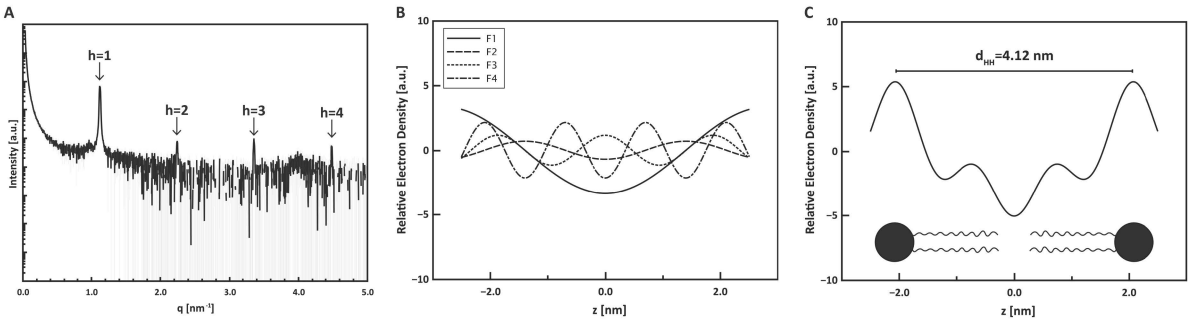

Figure 12. Calculation of an electron density profile from a SAXS curve. (A) SAXS curve of a multilamellar liposome with four observable Bragg peaks in reciprocal space. (B) The individual electron density contrasts F1-F4 with the frequency d, d/2, d/3, and d/4, respectively. (C) The sum of the individual electron density contrasts yields the electron density profile in real space. The highest electron density is given by the phospholipid headgroups, enabling the calculation of the headgroup-headgroup distance d_{HH}.

Unfortunately, the higher order reflections cannot always be seen in the scattering profile. In an ideal system, the repeating structures are equally separated from each other and in the case of bilayer

membranes also absolutely flat. This would lead to a very high long-range order and to diffraction peaks that would neither decay nor change their width with higher orders. However, when dealing with liquid crystalline systems, several types of disorder are introduced, which can be caused by thermal fluctuation, stacking disorder, and bilayer bending.[54,119,126] These deviations from the ideal case lead to an exponential decrease in peak intensity for higher order peaks, making them sometimes difficult to discern from the increasing noise caused by incoherent scattering at higher q.[126] Therefore, lipid phase identification and electron density profile calculations can only be performed for samples that are either highly concentrated or show very high long-range order, such as multilamellar lipoplexes.

Combining all the insights from analyzing the form factors and structure factors explained above can therefore enable users of small angle scattering methods to make precise statements about a given system. For example, the following parameters can be extracted for a sufficiently small and strongly ordered multilamellar liposome: Its size can be calculated using the Guinier approximation, its surface smoothness can be probed by Porod-analysis, its multilamellar structure can be confirmed by the peak repeat ratio, the bilayer spacing and the thickness of the water layer in between can be calculated using Bragg's law and electron density profile calculation, and the average number of stacked bilayers can be calculated by dividing the correlation length by the d-spacing.

While small angle X-ray scattering is more commonly used due to the possibility of faster measurements enabled by the much higher photon flux at synchrotrons compared to the neutron flux of most SANS instruments, small angle neutron scattering holds one advantage over SAXS, especially when it comes to the analysis of multi-component systems. As stated above, the contrast in SAXS experiments is dependent on the atomic number of the sample particle and its matrix material – the higher the difference in electron density between these two, the higher the contrast, as the matrix material just contributes to the incoherent background scattering. Adjusting the contrast in SAXS measurements is complicated and often involves the incorporation of heavy metal atoms into the particles, which may come with changes to the particle structure, or the utilization of the more complicated anomalous SAXS (ASAXS) method.[109,115] Contrast variation in SANS however, can be much more easily achieved. As already mentioned, the interaction of neutrons with atomic nuclei is complex and there is no general trend throughout the periodic table, as there is for SAXS. Interestingly, even different isotopes of the same element can show differing interaction with neutrons and therefore different contrasts.[114] This phenomenon is particularly distinct for ^{1}H and ^{2}H, resulting in very different so-called scattering length densities for H_2O and D_2O, and can be explained – and utilized – as follows:[115]

In general, the scattering cross-section describes the number of scattered neutrons or photons during a given time period and in neutron scattering this is dependent on the scattering length b of the atomic nucleus, which in turn is a measure of the scattering ability of an atomic nucleus. If the atomic nucleus has a non-zero spin, it can interact with the neutron spin and can therefore give cause to both coherent and incoherent scattering. Therefore, each isotope is characterized by a coherent and an incoherent scattering length b. Most biological materials, such as phospholipids, proteins, and nucleic acids are made up from mostly carbon, oxygen, nitrogen, phosphorous and hydrogen. While most of these atoms mainly cause coherent scattering, this is not the case for hydrogen (^{1}H), which is characterized by a negative scattering length. Deuterium (^{2}H) however, has a strongly positive scattering length.[114] This can be utilized in a technique which is called contrast matching. Due to the effects mentioned above, the scattering length densities of most biological (macro-)molecules can be matched by mixtures of H_2O, which has a lower scattering length density than all of them, and D_2O, which has a higher scattering length density than the rest (see **Figure 13**). If a component is contrast matched like this, the scattering from it becomes indiscernible from the background scattering, rendering its

contribution to the scattering curve invisible. Therefore, the scattering signal from one material in a mixed system (e.g., mRNA in a lipoplex) can be evaluated in isolation, if the other material is contrast matched. Subsequently, the structure/organization or its location (by calculating the scattering length density profile) of this single component can be obtained. This technique can be further optimized by utilizing deuterated versions of the components in order to vary their scattering length density (e.g., deuterated lipid chains).[109,114,127]

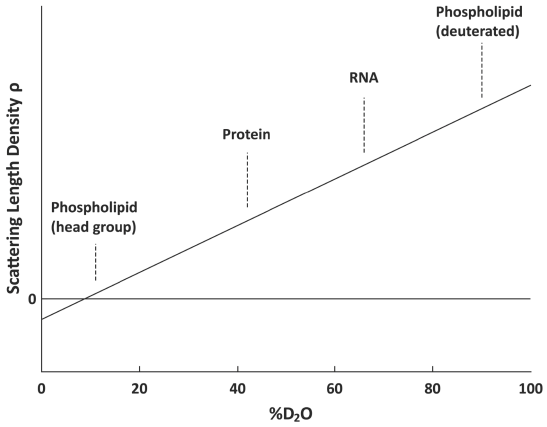

Figure 13. Schematic representation of the resulting scattering length densities of 0-100% D_2O in H_2O mixtures and the respective matching points for different biologically relevant molecules (after [114]).

2.2.4.7.1 Small Angle X-Ray Scattering Parameters

The SAXS data presented within this thesis was generated at different institutions / beam lines and at different experimental setups, which were as follows:

	Setup 1	Setup 2	Setup 3	Setup 4	Setup 5
Institution	EMBL / DESY Hamburg	EMBL / DESY Hamburg	LNLS Campinas	EMBL / DESY Hamburg	EMBL / DESY Hamburg
Beamline	P12 [112]	P12 [112]	SAXS1 [128]	P12 [112]	P12 [112]
Sample holder	In-air capillary	In-vacuum sample changer and in-air capillary	In-vacuum capillary	In-air capillary	In-vacuum sample changer
Sample thickness	0.8 mm	0.9 mm 0.8 mm	*not recorded*	0.8 mm	0.9 mm
X-ray wavelength / energy	0.124 nm 10 keV	0.124 nm 10 keV	0.155 nm 8 keV	0.124 nm 10 keV	0.124 nm 10 keV
Energy resolution ΔE/E	*not recorded*	*not recorded*	0.1	*not recorded*	*not recorded*
Flux	5 x 10^{12} ph/s	1 x10^{13} ph/s	1x10^{12} ph/s	1 x10^{13} ph/s	1 x10^{13} ph/s
Beam size	0.15 x 0.25 mm	*not recorded*	1.5 mm²	*not recorded*	*not recorded*
Detector	Pilatus 2M	Pilatus 6M	Pilatus 300K	Pilatus 6M	Pilatus 6M
Sample-detector distance	3.0 m	3.0 m	1.0 m 1.5 m	3.0 m	3.0 m
q-range	0.03-5.0 nm^{-1}	0.03-7.3 nm^{-1}	0.13-5.0 nm^{-1} 0.08-2.9 nm^{-1}	0.03-7.3 nm^{-1}	0.03-7.3 nm^{-1}
Exposure time	0.095 s	0.045 s	100-150 s	0.0495 s	0.095 s
Sample concentration	12.5 mg/mL	12.5 mg/mL	2 mg/mL	5 mg/mL	2-5 mg/mL

Table 5. Experimental Setups for SAXS measurements. The stated sample concentrations are the resulting sample concentrations after mixing of the sample with its respective buffer, where applicable.

2.2.4.7.2 Small Angle Neutron Scattering Parameters

The SANS data presented within this thesis was generated at the KWS2 instrument at the FRM-II neutron source at the JCNS outstation at the Heinz Maier-Leibnitz Zentrum (MLZ) in Garching (Germany).[129] All samples were prepared with the film method and hydrated with an mRNA in H_2O solution containing 10% (100 mg/mL) trehalose, resulting in a total lipid concentration of 100 mg/mL. These samples were then diluted with different H_2O/D_2O mixtures (0-99% D_2O) containing either 10% or 65% trehalose, resulting in D_2O concentrations of 0/11.11/22.22/33.33/55.56/ 66.67/88.89% (vol%), 10% or 60% trehalose, and a total lipid concentration of 10 mg/mL. The measurements were performed at a neutron wavelength of 6 Å and sample-detector distances of 2 m, 8 m, and 20 m and the measurements were later combined, resulting in a total q-range from 0.03 $Å^{-1}$ to 0.5 $Å^{-1}$. 1 mm path length QS quartz cuvettes were used for D_2O contrasts below 33%, while 2 mm cuvettes were used for higher D_2O concentrations. The reached measurement times ranged from 300 s to 1400 s, depending on the sample to detector distance. Empty cell correction and merging of the different q-ranges was performed by the beamline staff and the buffer subtraction was performed after scaling the buffer intensities by comparing their high q ranges in the Porod plot ($I \cdot q^4$ vs q) with those of the samples.

2.2.5 Biological Methods

2.2.5.1 *In vitro* Transfection

All cell culture experiments were performed by Isabell Keil at TRON Mainz. Samples were prepared with mRNA coding for the enzyme Luciferase, the murine CD90.1 (Thy1.1) protein, or a mixture of both, as stated with the results. The experiments were either performed in JURKAT cells, isolated peripheral blood mononuclear cells (PBMCs), or in EDTA-coated human whole blood, with PBMCs being isolated via density gradient centrifugation. The transfection assays were performed in the presence of pooled human serum. The total cell number was determined using an automated cell counting device (ViCELL XR) and the formulation dosing was calculated as ng mRNA per $2.5 \cdot 10^6$ cells. The cells were co-incubated with the formulations at 37 °C and 5% CO_2 for 2 h, then washed with hDC medium (human dendritic cell medium; RPMI medium1640 (1x) + GlutaMAX-I containing 5% pooled-human-serum, 1% Sodium Pyruvate 100 mM (100x) and 1% MEM NEAA (100x)), resuspended, and then incubated for another 4 h, accounting for a total incubation time of 6 h.[130] Luciferase expression was detected via the commercially available Bright-Glo™ luciferase assay, while Thy1.1 expression was determined via anti-CD90.1 antibody staining and subsequent flow cytometry analysis.

2.2.5.2 Fluorescence Activated Cell Sorting

Fluorescence activated cell sorting (FACS) was utilized to gather information on cell-type specific transfection efficacies in PBMCs and whole blood. This technique utilizes flow cytometry and fluorescence-staining (via dyes or antibodies) to differentiate between different cell types, which can then be sorted for additional analysis.[131] Additionally, it provides a readout for a successful transfection with murine CD90.1, as this surface protein can also be stained with a fluorescent antibody, which can be measured simultaneously due to multiple lasers and readouts at different wavelengths.[132]

All flow cytometry was performed by Isabell Keil at TRON Mainz. While the monoclonal antibody CD90.1-BB515 was used for the staining of Thy1.1 transfected PBMCs, a variety of mononuclear antibodies was used for the extracellular staining of different PBMCs: Anti-CD14 antibody was used for the staining of monocytes, anti-CD19 antibody for the staining of B-cells, anti-CD56 antibody for that of NK cells, and anti-CD4 and anti-CD8 antibodies for that of CD4+ and CD8+ T cells, respectively. The cell viability was determined using fixable viability dye. Transfected cells were stained with their respective markers in flow buffer and then washed, centrifuged, and resuspended in stabilizing fixative

for flow cytometry. Flow cytometric measurements were then performed on a BD FACSCanto II flow cytometer and analyzed with the FlowJo V10.7.1 software.

2.2.6 Data Treatment and Analysis

A variety of software was used to process raw data from the experiments performed in this thesis, often using proprietary protocols embedded in the software. Standard methods utilized commonly (such as the calculation of a mean value) will not be explained here, as this would go beyond the scope of this thesis. Therefore, the following paragraphs will be used to give an overview and allow for understanding of non-standard or less commonly used data analysis, such as the processing and analysis of scattering curves or statistical analysis using R.

2.2.6.1 Scattering Data

Scattering data from SAXS and SANS measurements is provided as a 1D-scattering curve of scattering vectors q and their respective scattering intensity, sometimes including an experimental error value for the intensity. The first step in processing this data is the subtraction of the scattering intensity measured for a blank sample, or buffer, which can easily be done utilizing software such as the ATSAS package or QtiPlot. In some cases, it might be necessary to include a scaling of the measured intensities beforehand. This is the case when the scattering intensity of the sample is in fact lower than that of its respective blank, resulting in so-called over subtraction, which for example could be caused by small air bubbles in the capillary or minor differences in the buffer composition. For this, the scaling factor can be determined by confining the analyzed intensities to the high q ranges (which contains only incoherent scattering) and using the "scale"-functionality in the ATSAS package, which tries to equalize the scattering intensities of two curves over the analyzed range. The factor gained from this step is then used when subtracting the buffer signal from the sample signal, limiting over subtraction to a reasonable amount. The error of the subtracted intensity $\delta I_{subtracted}$ follows the propagation laws of the addition of uncertainties and multiplication with a constant and can therefore be calculated as follows:[133]

$$\delta I_{subtracted} = \sqrt{\left(\delta I_{Sample}\right)^2 + \left(\delta I_{Buffer} \cdot scaling\ factor\right)^2} \tag{13}$$

The resulting subtracted scattering curves can then be analyzed using a variety of different methods. The most common one is the fitting of a (multi-peak) Lorentzian function to the scattering data to determine the properties of observed Bragg peaks (for more details on Bragg peaks see **Small Angle Scattering**).[56,92,119] For this, the multi-peak Lorentzian fit function in QtiPlot was used with the scaled Levenberg-Marquardt algorithm, which uses the following equation:

$$y = y_0 + \sum_{i=1}^{n}\left[\frac{2 \cdot A_i}{\pi} \cdot \frac{w_i}{4 \cdot \left(x - x_{c,i}\right)^2 + w_i^2}\right] \tag{14}$$

Here, y represents the scattering intensity, with y_0 being the peak baseline, and x represents the scattering vector q, with x_c being the peak center / peak position. Additional parameters are the peak area A and the peak width w (full width at half maximum). As already explained, these parameters can be used for calculating the d-spacing via the Bragg equation (see **equation (9)**) and the correlation length via the Scherrer equation (see **equation (10)**). Reasonable starting points for the peak position were given to the software by inspecting the curve for maxima visually and, if available, the experimental intensity errors included in the data were used for weighting in the fitting process.

As these fit parameters come with an error value as well, their errors have to be propagated for all parameters calculated from the fitted values. The calculation of the particle d-spacing only involves the inverse of q and the multiplication of a constant factor (2π). Therefore, the error propagation is relatively straightforward. The uncertainty in a power function $y=x^n$ can be given as:[133]

$$\frac{\delta y}{y} = |n| \cdot \frac{\delta x}{x} \tag{15}$$

Therefore, the error for an inverse (n = -1) can be given as:

$$\frac{\delta y}{y} = |n| \cdot \frac{\delta x}{x} = 1 \cdot \frac{\delta x}{x} \tag{16}$$

This means the relative error of d is the same as that of q and can be calculated as follows:

$$\delta d = \frac{\delta q}{q} \cdot d \tag{17}$$

The calculation of the correlation length via the Scherrer equation (see **equation (10)**) on the other hand involves the cosine function of the scattering angle θ and therefore the uncertainties provide a bit more difficult to propagate. In general, the absolute error δf of a function f(x) is given as

$$\delta f = \delta x \cdot |f'(x)| \tag{18}$$

with δx being the absolute error of x.[133] The scattering angle θ can be calculated from the peak position q as follows:[111]

$$\begin{aligned} q &= \frac{4\pi}{\lambda} \cdot sin\left(\frac{2\theta}{2}\right) \\ \Leftrightarrow\ sin\,\theta &= \frac{q \cdot \lambda}{4 \cdot \pi} \\ \Leftrightarrow\ \theta &= arcsin\left(\frac{q \cdot \lambda}{4 \cdot \pi}\right) \end{aligned} \tag{19}$$

Therefore, if sinθ is defined as x and f(x) therefore is arcsin(sinθ)=θ, the error for θ is given by:

$$\begin{aligned} \delta\theta &= \delta x \cdot |f'(x)| \\ \Leftrightarrow\ \delta\theta &= \delta x \cdot \left|f'\left(arcsin(x)\right)\right| \\ \Leftrightarrow \delta\theta &= \delta x \cdot \left|\frac{1}{\sqrt{1-x^2}}\right| \\ \Leftrightarrow\ \delta\theta &= \frac{\delta q \cdot \lambda}{4 \cdot \pi} \cdot \left|\frac{1}{\sqrt{1-\left(\frac{q \cdot \lambda}{4 \cdot \pi}\right)^2}}\right| \end{aligned} \tag{20}$$

The Scherrer equation (see **equation (10)**) to calculate the correlation length utilizes the peak position (in 2θ) as well as the peak width β. Therefore, both errors need to be taken into account. Here, the propagation rules for an inverse (see **equation (16)**), a function **(see equation (18)**), and for multiplication must be used, with the latter being (for z=x·y):[133]

(21) $$\frac{\delta z}{z} = \sqrt{\left(\frac{\delta x}{x}\right)^2 + \left(\frac{\delta y}{y}\right)^2}$$

Therefore, the uncertainty of the correlation length L can be calculated as:

(22)
$$\delta(L)_{absolute} = \delta(L)_{relative} \cdot L$$
$$\Leftrightarrow \delta(L)_{absolute} = \sqrt{\left(\frac{\delta(\beta_s)}{\beta_s}\right)^2 + \left(\frac{\delta(cos(\theta))}{\cos(\theta)}\right)^2} \cdot L$$
$$\Leftrightarrow \delta(L)_{absolute} = \sqrt{\left(\frac{\delta(\beta_s)}{\beta_s}\right)^2 + \left(\frac{\delta\theta \cdot f'(cos(\theta))}{\cos(\theta)}\right)^2} \cdot L$$
$$\Leftrightarrow \delta(L)_{absolute} = \sqrt{\left(\frac{\delta(\beta_s)}{\beta_s}\right)^2 + \left(\frac{\delta\theta \cdot [-\sin(\theta)]}{\cos(\theta)}\right)^2} \cdot L$$

Another aspect of analyzing small angle scattering curves is the fitting of the Porod-slope. For this, an exponential fit-function of the following type was applied, with n being the parameter to be fitted, and the q-range to be fitted reaching rom 0.03 nm^{-1} to 0.2 nm^{-1}:

(23) $$I = I_0 \cdot q^{-n}$$

As for the Lorentzian peak fitting, the instrumental error was used for weighting and the Levenberg-Marquardt algorithm was used for the fitting process.

2.2.6.2 Statistical Analysis

For determining statistically significant differences in *in vitro* expression levels between different formulations, an adapted script in the programming language R, based on one previously published online, was used (for the script see **chapter 7.4.3** in the appendix).[134] This script performs a one-way ANOVA analysis with the Bonferroni method for multiple comparison in order to differentiate between the different formulations, detect significant differences, and evaluate the significance levels.[135]

All other statistical analysis, such as the calculation of means, standard deviations, or standard errors were performed with the "Descriptive Statistics" function in QtiPlot, while the paired t-tests were performed with the "Hypothesis Testing" tool within the same software.

2.2.6.3 Sigmoidal Fits of pH-Responsive Data Points

Experimental values showing pH-dependent sigmoidal behavior were fitted using the Boltzmann fit option in QtiPlot. This option fits the following function to the data:

(24) $$A_2 = \frac{A_1 - A_2}{1 + e^{\frac{(x - x_0)}{dx}}}$$

A_1 represents the plateau before and A_2 that after the inflection point, while x_0 marks the deflection point and dx is the time constant. The inflection point x_0 is the value around which the sigmoidal shift

takes place and is therefore interpreted as the formulation pK_a, for example. If needed, restraints were given to the fitting values to prevent nonsensical fit results.

3 | Results

3.1 Permanently Charged Systems

As mentioned previously, mRNA delivery systems based on permanently charged cationic lipids have been well known and used as transfection reagents for many years.[136] However, many questions concerning the structure and mechanism of action still remain unanswered. Previous studies within this working group have elucidated many features of these systems and led to the development of a structural model for permanently charged cationic lipoplexes.[92,137,138] However, some questions, e.g. regarding the influence of different preparation techniques or the exact location of the mRNA within the lipoplex, still remained unanswered and were therefore investigated within the scope of this thesis.

3.1.1 General Structural Investigations

To confirm the previously established model of a multilamellar bilayer-ordered system for permanently charged mRNA lipoplexes, additional physicochemical characterization of these systems was performed.

3.1.1.1 Small Angle Neutron Scattering

Small angle neutron scattering with deuterium contrast variation was utilized to differentiate between scattering contributions from the lipid and the mRNA fraction within permanently charged lipoplexes. For this, six different sample compositions based on the helper lipid DOPC and the cationic lipid DOTAP were prepared with the thin lipid film method in both 10% and 60% trehalose buffer and measured at up to five different deuterium contrasts (for details see chapter 2.2.4.7.2). The 60% trehalose buffer was chosen to minimize sample sedimentation, which had been a problem in previous SANS experiments. Interestingly, these previous experiments had also indicated a swelling effect which might be caused by the changes in osmotic pressure from the high trehalose content.[137] Therefore, this effect was to be monitored as well. The sample compositions and their measurement conditions can be seen in Table 6.

Sample		SANS-1	SANS-2	SANS-3	SANS-4	SANS-5	SANS-6
Description		no DOTAP	N/P 1:2	N/P 1:1	N/P 2:1	pure mRNA	no mRNA
Preparation concentration		100 mg/mL total lipid	100 mg/mL total lipid	100 mg/mL total lipid	100 mg/mL total lipid	4.2 mg/mL mRNA	100 mg/mL total lipid
Measurement concentration		10 mg/mL total lipid	10 mg/mL total lipid	10 mg/mL total lipid	10 mg/mL total lipid	0.42 mg/mL mRNA	10 mg/mL total lipid
DOPC mol%		100	95	90	80	0	90
DOTAP mol%		0	5	10	20	0	10
mRNA mol%		10	10	10	10	"10"	0
10% trehalose	D00	-	-	✓	-	✓	-
	D11	-	-	✓	-	-	-
	D33	-	-	-	-	-	-
	D66	-	-	-	-	-	-
	D88	-	-	✓	-	-	-
60% trehalose	D00	✓	✓	✓	✓	✓	✓
	D11	✓	✓	✓	✓	-	✓
	D33	-	✓	✓	✓	✓	-
	D66	-	-	✓	-	-	✓
	D88	✓	✓	✓	✓	✓	✓

Table 6. Sample composition and measurement parameters for the performed SANS experiments. Note that 4.2 mg/mL mRNA is the equivalent of 10 mol% at 100 mg/mL total lipid. The stated D_2O contrasts (D00-D88) are labels only, for more information please refer to the text and Table 7. "✓" represents a measured combination of sample and contrast, while combinations marked with "-" were not measured.

Since the buffers were prepared as mass/volume (calculated as free trehalose but prepared with trehalose dihydrate) and mixed as volumes, the resulting real concentrations (m/m) for the different

mixtures had to be calculated. The densities of the 10% and 65% trehalose solutions in H_2O and D_2O as well as those of the mixed deuterium contrasts were measured with an Anton Paar DMA 4100M density meter at 20±0.1°C and the resulting concentrations of the different mixtures were then calculated. Using these parameters, the scattering length densities (SLD) of the deuterium contrast buffers were calculated using an SLD calculator tool in the software SasView.[88] The results can be seen in Table 7.

	D_2O Contrast	D00	D11	D33	D66	D88	D100
10% trehalose	**Trehalose (pure)**	8.9	8.8	8.7	8.4	8.2	8.2
	H_2O (incl. dihydrate from trehalose)	91.1	80.2	59.2	29.1	10.1	0.9
	D_2O	0.0	10.9	32.2	62.5	81.6	90.9
	Density [g/cm³]	1.0355	-	1.0689	1.1021	-	1.1352
	SLD coherent [·10⁻¹⁴ cm·Å⁻³]	0.49	-	1.30	2.13	-	2.95
	SLD incoherent [·10⁻¹⁹ cm·Å⁻³]	4.72	-	4.11	3.48	-	2.86
60% trehalose	**Trehalose (pure)**	35.4	35.1	34.6	33.9	33.4	35.7
	H_2O (incl. dihydrate from trehalose)	64.6	57.7	44.1	24.5	11.8	3.8
	D_2O	0.0	7.2	21.2	41.6	54.7	60.5
	Density [g/cm³]	1.1567	1.1651	1.1819	1.2070	1.2239	1.2348
	SLD coherent [·10⁻¹⁴ cm·Å⁻³]	0.95	0.93	1.09	1.35	1.54	1.59
	SLD incoherent [·10⁻¹⁹ cm·Å⁻³]	4.64	4.19	4.26	4.35	4.40	4.40

Table 7. Actual content (mass%) of trehalose, H_2O, and D_2O of the different deuterium contrast mixtures and the resulting coherent and incoherent scattering length densities of the buffers (calculated with SasView).

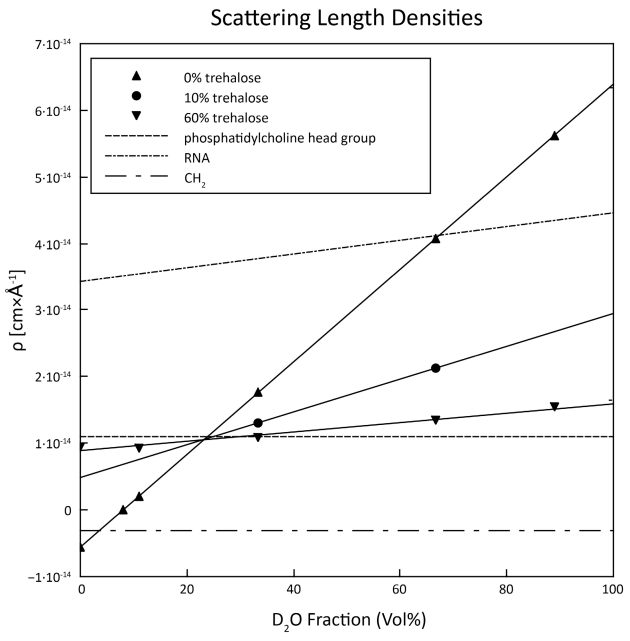

Figure 14. Calculated coherent scattering length densities of H_2O/D_2O mixtures containing 0%, 10%, or 60% trehalose (with linear fits), as well as those of a phospholipid head group (dashed line), RNA (dashed-dotted line), and a CH_2 group (long dashed-dotted line).

Figure 14 shows the calculated coherent scattering length densities of the different trehalose-containing deuterium contrasts alongside scattering length densities of H_2O/D_2O mixtures containing no trehalose and the scattering length densities of a phospholipid headgroup, its alkyl chain, and RNA (values taken from literature).[114] In it, one can clearly see that adding trehalose to the buffer strongly

changes its scattering length density, making it impossible to reach the matching point for mRNA or the CH_2 groups of the lipid tails. Additionally, for the buffers containing 60% trehalose, the scattering length density changes much less when increasing the D_2O fraction, resulting in the fact that lipid headgroup contributions can probably only be seen strongly at very high D_2O fractions.

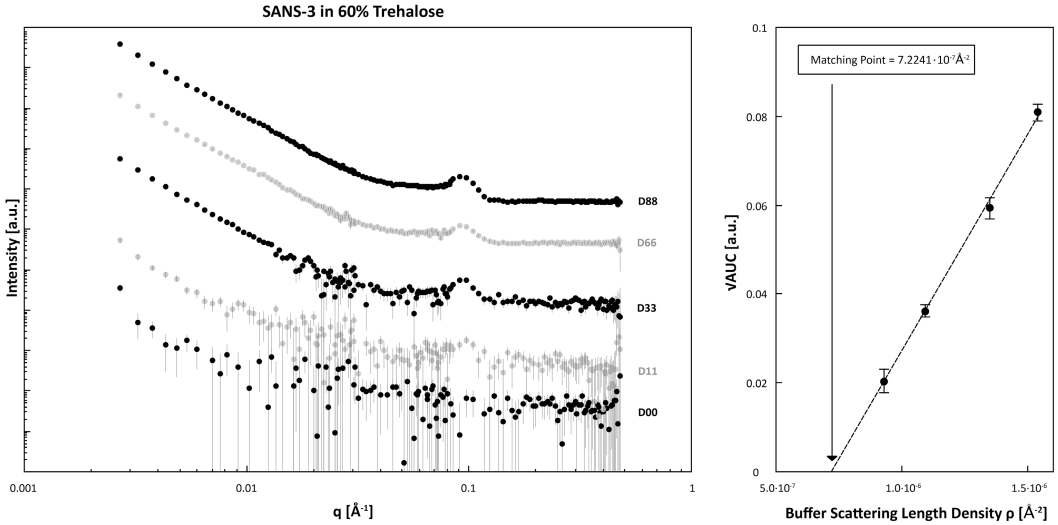

Figure 15. Left: SANS curves of a DOPC/DOTAP lipoplex with an N/P of 1:1 at different deuterium contrasts. Right: Linear fit approach to determine the scattering length density of the component causing the main Bragg peak at ~0.09 Å^{-1}.

Figure 15 (left) shows the performed contrast variation of the sample SANS-3 (N/P 1:1) in 60% trehalose as an example, a full collection of all measured scattering curves can be found in the supplementary data (see Suppl. Fig. 1 in chapter 7.4.4). SANS-1, SANS-2, and SANS-3 (negative charge excess to neutral charge) showed a strong Bragg peak at around 0.1 Å^{-1} that appeared more strongly at higher deuterium contrasts (e.g., see D33-D88 in Figure 15), while SANS-4 and SANS-6 (positive charge excess) showed a less clear double peak and SANS-5 (pure mRNA) showed no peak at all at higher deuterium contrasts. Two examples of this can be seen in Figure 16. These peaks were fitted with a multi-peak Lorentzian fit as explained in the methods section (see chapter 2.2.6.1), however, this only worked well for the strong single Bragg peaks at ~0.09 Å^{-1}. Therefore, a qualitative description of the results can be seen in Table 8.

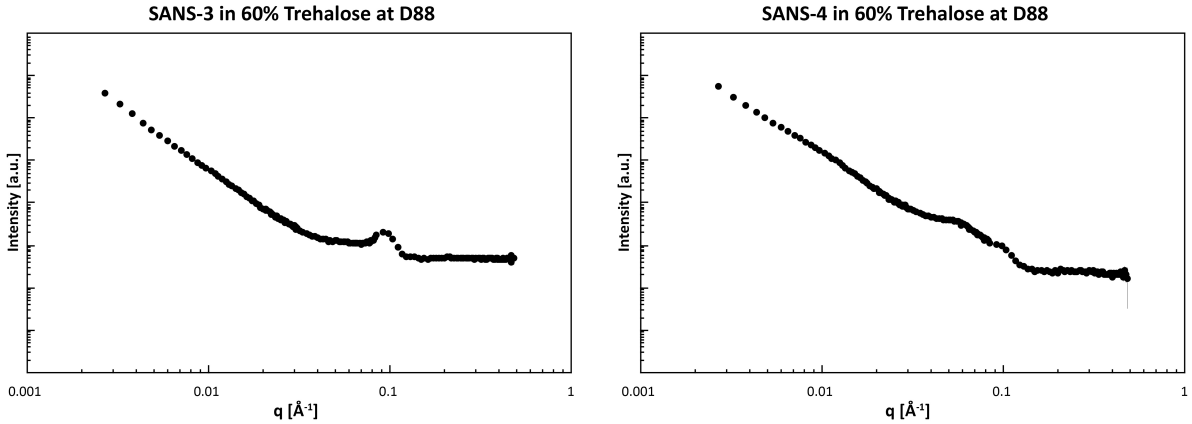

Figure 16. Examples of the SANS curves showing a strongly visible single Bragg peak (left) or a less clear double peak (right).

D_2O Contrast	SANS-5 (mRNA)	SANS-1 (no DOTAP)	SANS-2 (N/P 1:2)	SANS-3 (N/P 1:1)	SANS-4 (N/P 2:1)	SANS-6 (no mRNA)
D00	noisy peak at ~0.019 Å^{-1}		no clear characteristic feature			
D11-D33	n.a.	small peak at ~ 0.014-0.020 Å^{-1}				-
	too noisy	n.a.	both peaks, but weaker (0.014 & 0.09 Å^{-1})		both peaks, but weaker (<0.02 Å^{-1} & double peak)	n.a.
D66-D88	flat curve	strong single Bragg peak at ~ 0.09 Å^{-1}			broad double peak at ~ 0.05 Å^{-1} & 0.09 Å^{-1}	

Table 8. Qualitative description of the main SANS curve characteristics.

Several observations can be made: Firstly, the increasing intensity (area under the peak, AUC) of the Bragg peaks in the q-range of 0.05-0.1 Å^{-1} with increasing scattering length density of the buffer indicates that this signal is caused by the lipid component of the lipoplex systems. This is supported by the fact that pure mRNA (SANS-5) does not display this characteristic feature in the scattering curves. Secondly, the smaller peak that can be seen at approximately 0.019 Å^{-1} appears mainly at low deuterium contrasts and therefore close to the matching point of the lipid components. Contrary to the main Bragg peak, it is also visible for pure mRNA and not visible in liposomes which do not contain mRNA (SANS-6). Therefore, the assumption can be made that this scattering contribution is caused by ordered mRNA domains within the systems. However, other than determining the peak position manually, a concise quantitation of this peak via Lorentz fitting was not possible due to the high amount of incoherent scattering causing noise at low deuterium contrasts. Lastly, the broad double peak at high deuterium contrasts appears only for systems which are expected to feature DOTAP which is not electrostatically bound to mRNA (N/P > 1 or no mRNA at all). The double peak can be seen as a combination of the single peak seen for most other systems at ~0.09 Å^{-1} and a second peak at slightly lower q (~0.58 Å^{-1}).

The fitted position of the main Bragg peak in SANS-3 across six deuterium contrasts did not change substantially and was 0.093±0.001 Å^{-1}, which gives a calculated d-spacing of 67.4±0.8 Å. This is in line with previously performed SAXS experiments, which measured a d-spacing of 68.4 Å for this system.[92] When plotting the square-root of the peak AUC against the scattering length density of the buffer (**Figure 15, right**), a linear relationship becomes apparent. A linear fit was therefore used to calculate the matching point (zero intensity) of the scatterer. The calculated scattering length density for this amounts to ~0.72 ·10^{-14} cm·Å^{-3} and is therefore below that of a phosphatidylcholine headgroup (1.10 ·10^{-14} cm·Å^{-3}), but very close to that reported for the trimethylamine-headgroup of DOTAP (0.76 ·10^{-14} cm·Å^{-3}).[139,140] Therefore it can be concluded, that the observed Bragg peak is caused by ordered arrays of DOTAP headgroups and its corresponding d-spacing does in fact relate to the bilayer-bilayer spacing within these multilamellar lipoplexes.

The appearance of a second peak at slightly lower q (higher d-spacing) for systems with excess DOTAP (compared to mRNA), causing a broad double peak, also fits previous SAXS results from our group. Here, it is thought that the unscreened cationic charge of the DOTAP molecules leads to a second particle species with strongly increased d-spacing (in this case approximately 100-125 Å for SANS-4), as the bilayers are electrostatically repelled with no anionic mRNA charge to screen these interactions.

As two last points it should firstly be noted that no “osmotic swelling” effect due to differing amounts of trehalose could be noted in terms of d-spacing, as this parameter only changed by up to one angstrom between matching sample pairs. Also, no radius of gyration R_g could be calculated for the measured systems due to the particles being much larger (as measured by DLS, data not shown) than the maximum detectable particle size of the experimental setup (r_{max}=116 nm).

3.1.1.2 Transmission Electron Microscopy

Transmission electron microscopy was performed to further confirm the previously proposed multilamellar model for these permanently charged cationic lipoplex systems. A selection of the recorded images can be seen in Figure 17.

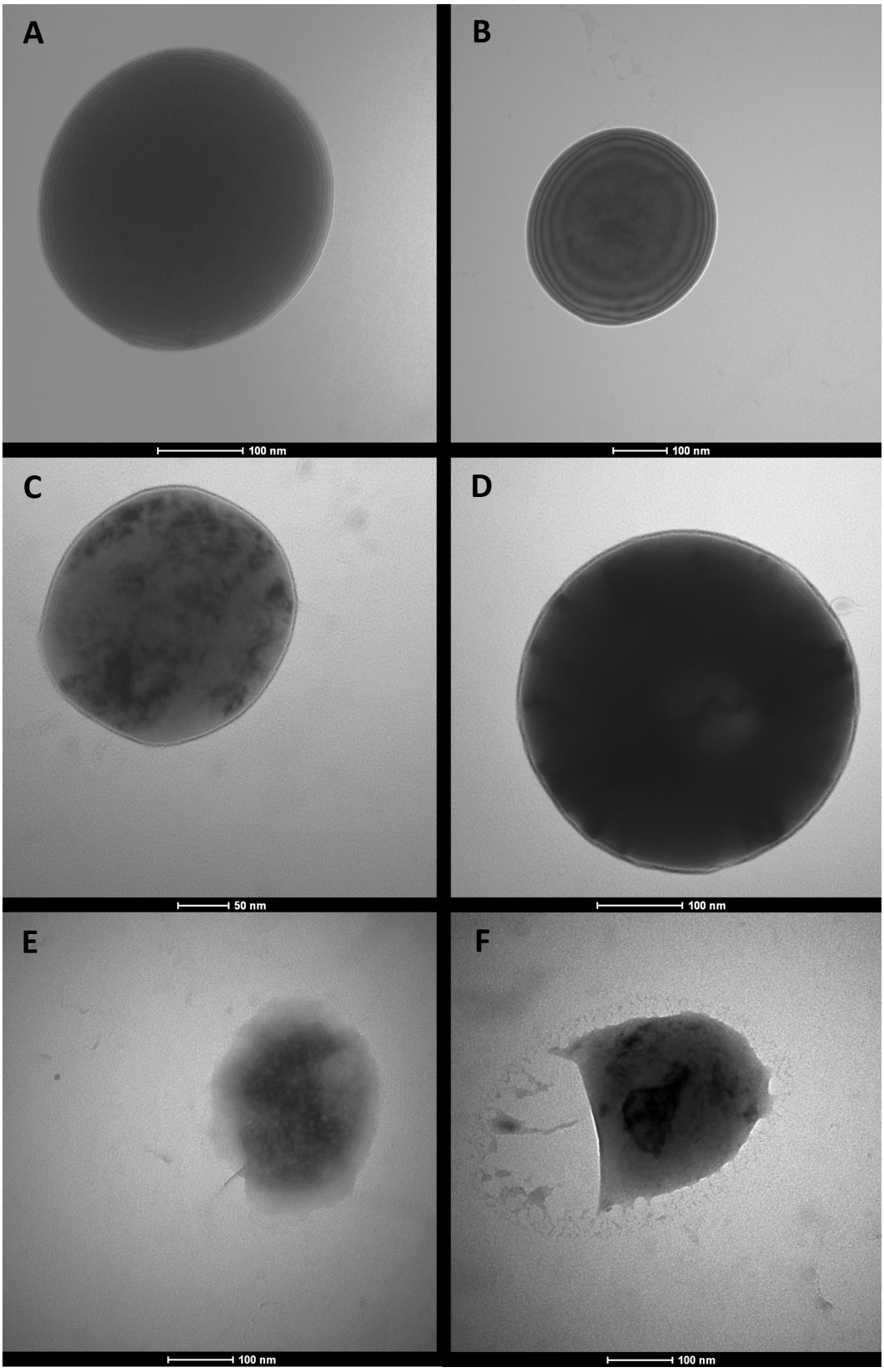

Figure 17. TEM images of DOPC/DOTMA/mRNA lipoplexes (50:50:10 mol%, prepared via ethanol injection).

Panels A and B show representative particles that clearly comply with the multi-bilayer structural model, but on the other hand some other structures could be seen as well. Panel C and D show particles that seem to have been formed more of a core-shell structure, with a clearly visible outer shell and an electron-rich condensed core. However, it has to be questioned if these structures would also appear in solution, as panel E and F clearly show the disruptive effect that the drying process utilized in normal (non-cryo) EM has on the examined particle systems. In general, it was not easy to find intact particle systems (such as panels A-D) in the analyzed samples at all. Therefore, Cryo-EM should be the method of choice for further evaluation, as it conserves the particles as they were in solution through the rapid freezing process during sample preparation.

3.1.2 Influence of the Preparation Method

While the thin lipid film method is a widely established and relatively straightforward protocol, it has some disadvantages as well, namely missing size control and limited scalability. Lipoplexes prepared via this method are relatively large (up to over 1 µm) and polydisperse if no additional size control step, such as membrane extrusion, is added after the hydration step. This makes a process, that already involves a lot of effort and time, even more complex, especially if nuclease free conditions are needed. Secondly, this preparation method is only scalable in terms of a laboratory scale (larger evaporation flasks), not in industrial scales, and the number of different samples that can be prepared in a short time is highly limited by the number of rotary evaporators at one's disposal, making it unsuited for screening experiments. Therefore, a part of this dissertation was dedicated to evaluating the transferability of the previously established structural models to more sophisticated preparation methods. The dual asymmetric centrifugation (DAC) method, which represents a higher throughput version of the film method, and the ethanol-injection method, which is the basic principle behind most modern industrial preparation methods, were chosen for this purpose.

3.1.2.1 Particle Size

Firstly, it was tested how switching to a different buffer system might affect particle stability. Previously, lipoplexes in this group had been prepared and stored in either HEPES/EDTA or trehalose solutions. However, aggregation over time had been a problem with these systems. Therefore, the dipeptide glycylglycine was considered as a new buffering agent, as its short dipeptide structure with polar end-groups might be able to provide steric and electrostatic stabilization to the particles. A 10 mM glycylglycine (GG) aqueous solution was found to be beneficial already in terms of lower polydispersity during the hydration step and was able to stabilize the small size and low polydispersity of extruded lipoplexes over several days (data not shown). In addition, the pH level of a 10 mM glycylglycine solution in water for injections was found to be suitable for the preparation of ionizable delivery systems (see chapter 2.2.2) and, as the buffer had previously been shown to be non-toxic, it was chosen as the preparation buffer for all forthcoming experiments.[89]

The next step was evaluating the three different preparation methods already stated above. For this, permanently charged lipoplexes comprising DOPC as a helper lipid and DOTAP or DOTMA as the cationic lipid were prepared at various N/P ratios and their sizes were measured via DLS. While particle diameters for non-extruded lipoplexes prepared with the thin lipid film method often exceeded 1000 nm and the particles were very polydisperse (PDI close to 1), the diameters of particles prepared by dual asymmetric centrifugation were consistently in the range of 500-1000 nm and their PDIs were lower (mostly 0.4-0.8). Preparation via the ethanol injection method however proved to be the most successful method, with particle sizes in the range of 150-400 nm and very low polydispersity (PDI mostly < 0.3). Figure 18 shows representative lipoplexes of the same composition (DOPC/DOTAP/mRNA 80:20:10 mol%) prepared with the three different preparation methods and measured both with DLS and viewed through a light microscope. For the film method (A), one can

clearly see very large particles (up to 10 µm, which is not detectable anymore by the used DLS system) dominating the picture, with fewer medium-sized and small lipoplexes also visible. Moving to the preparation in the DAC (**B**), one can already see a more homogenous picture of particles in the nanometer size range, however the sizes still show some variety and a small number of larger particles remains visible both through the microscope and in the DLS data. Particles prepared by ethanol injection method on the other hand (**C**) show a very homogenous picture with lots of evenly sized and very small particles (< 500 nm) and almost no larger particles visible, which is confirmed by the DLS data.

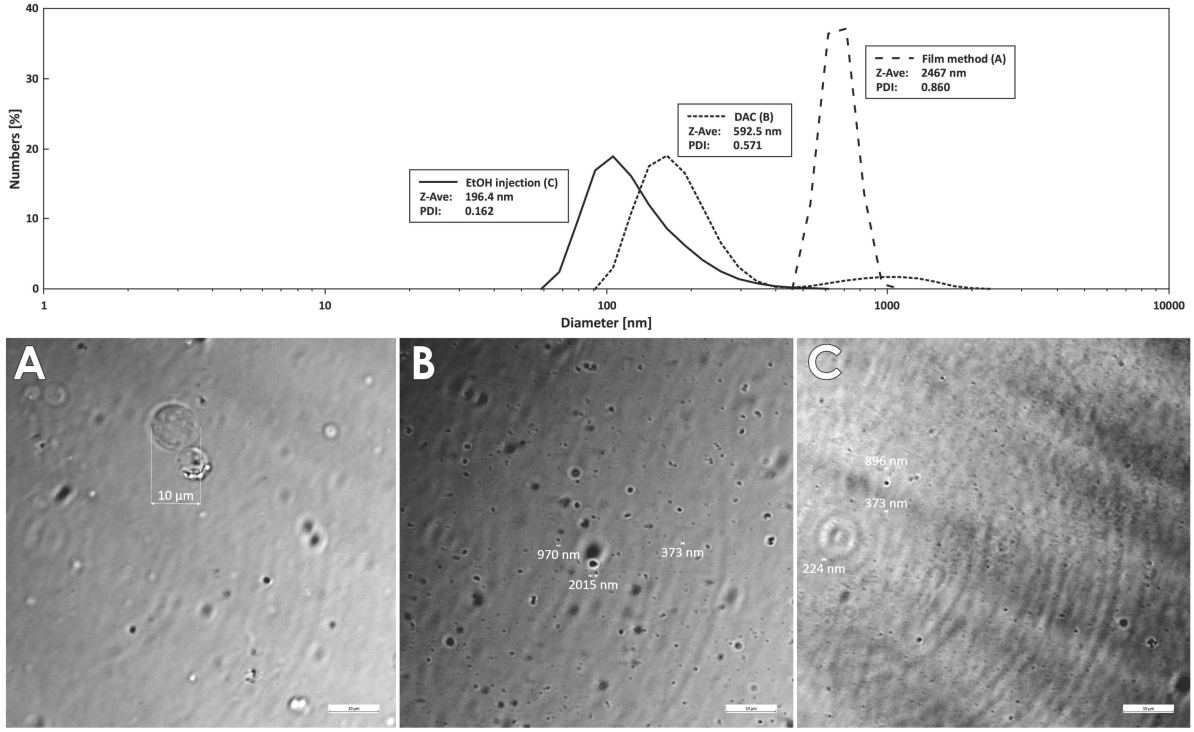

Figure 18. Number distributions of the particle diameter (top) and the same samples viewed through a light microscope (bottom) of DOPC/DOTMA/mRNA lipoplexes (N:P 2:1) prepared via the film method (A), dual asymmetric centrifugation (B), or ethanol injection (C).

3.1.2.2 Small Angle X-Ray Scattering

Next, it was examined if the different preparation techniques made a difference in terms of the resulting internal particle structure, or if they only resulted in different particle sizes, but with the same morphology. For this, SAXS measurements were performed on particles prepared with all three preparation methods, at different N/P ratios, and comprising one of two different cationic lipids. The full list of samples can be seen in Table 9. The experiments were performed with the SAXS parameters stated under "Setup 2" in the methods section (see chapter 2.2.4.7.1). The full set of recorded scattering curves can be found in the supplementary data (see Suppl. Fig. 2 in chapter 7.4.5).

Sample	Helper lipid	Helper lipid mol%	Cationic lipid	Cationic lipid mol%	mRNA mol%	N/P ratio	Preparation concentration	Comment
DAC-00	DOPC	80	DOTAP	20	0	-	12.5 mg/mL	No mRNA
DAC-01	DOPC	95	DOTAP	5	10	0.5	12.5 mg/mL	
DAC-02	DOPC	90	DOTAP	10	10	1	12.5 mg/mL	
DAC-03	DOPC	80	DOTAP	20	10	2	12.5 mg/mL	
DAC-04	DOPC	50	DOTAP	50	10	5	12.5 mg/mL	
DAC-05	DOPC	95	DOTMA	5	10	0.5	12.5 mg/mL	
DAC-06	DOPC	90	DOTMA	10	10	1	12.5 mg/mL	
DAC-07	DOPC	80	DOTMA	20	10	2	12.5 mg/mL	
DAC-08	DOPC	50	DOTMA	50	10	5	12.5 mg/mL	
EtOH-00	DOPC	80	DOTAP	20	0	-	12.5 mg/mL	No mRNA
EtOH-01	DOPC	95	DOTAP	5	10	0.5	12.5 mg/mL	
EtOH-02	DOPC	90	DOTAP	10	10	1	12.5 mg/mL	
EtOH-03	DOPC	80	DOTAP	20	10	2	12.5 mg/mL	
EtOH-04	DOPC	50	DOTAP	50	10	5	12.5 mg/mL	
EtOH-05	DOPC	95	DOTMA	5	10	0.5	12.5 mg/mL	
EtOH-07	DOPC	80	DOTMA	20	10	2	12.5 mg/mL	
EtOH-08	DOPC	50	DOTMA	50	10	5	12.5 mg/mL	
EtOH-09	DOPC	80	DOTAP	20	10	2	1 mg/mL	Reference
EtOH-10	DOPC	80	DOTAP	20	10	2	1 mg/mL	Extruded 200 nm
EtOH-11	DOPC	80	DOTAP	20	10	2	1 mg/mL	No 10mM GG
Film-00	DOPC	80	DOTAP	20	0	-	50 mg/mL	No mRNA
Film-01	DOPC	80	DOTAP	20	10	2	50 mg/mL	

Table 9. Compositions of samples used in the SAXS measurements investigating the preparation method influence.

A comparison of the scattering curves for lipoplexes comprising the cationic lipid DOTAP can be seen in Figure 19. For systems comprising only DOPC and DOTAP, but no mRNA (top curves), the broad signal from the uncorrelated bilayer scattering previously reported for these systems can clearly be seen again.[92] Here, the missing mRNA leads to unscreened cationic charge and strong repulsion between the bilayers, resulting in a very low order incapable of causing clear Bragg peaks. For all systems containing mRNA, these charges are screened by the mRNA and well-ordered bilayers lead to the strong 1st and 2nd order Bragg peaks visible in the scattering curves. When comparing the scattering curves of the different preparation methods at each N/P ratio, no clear difference can be made out visually. This becomes especially clear when looking at the inlay in Figure 19, which shows the scattering curves of all three preparation methods at an N/P ratio of 2:1 in the q-range containing the 1st and 2nd order Bragg peaks, which were scaled to the same intensity of the 1st order Bragg peak and then overlayed. These scattering curves match so well that one cannot really distinguish between them. In addition to the similarity between the preparation methods, some trends can be made out both for preparations prepared via DAC as well as for those prepared via ethanol injection. While N/P ratios below and up to 1:1 result in very sharp Bragg peaks, indicative of a high long-range particle order, N/P ratios above 1 result in broader 1st order and less visible 2nd order Bragg peaks, indicating a loss of this high range order at higher N/P ratios. Also, rather interestingly, some smaller peak shoulders can be seen for the 1st order Bragg peak for several formulations (marked with arrows). While these appear on the right side (higher q) for N/P ratios ≤ 1, they move to the left of the peak (lower q) for N/P ratios above 1. Generally speaking, these peak shoulders can be indicative of additional particle species or domains within the particles with a slightly different repeat ratio.

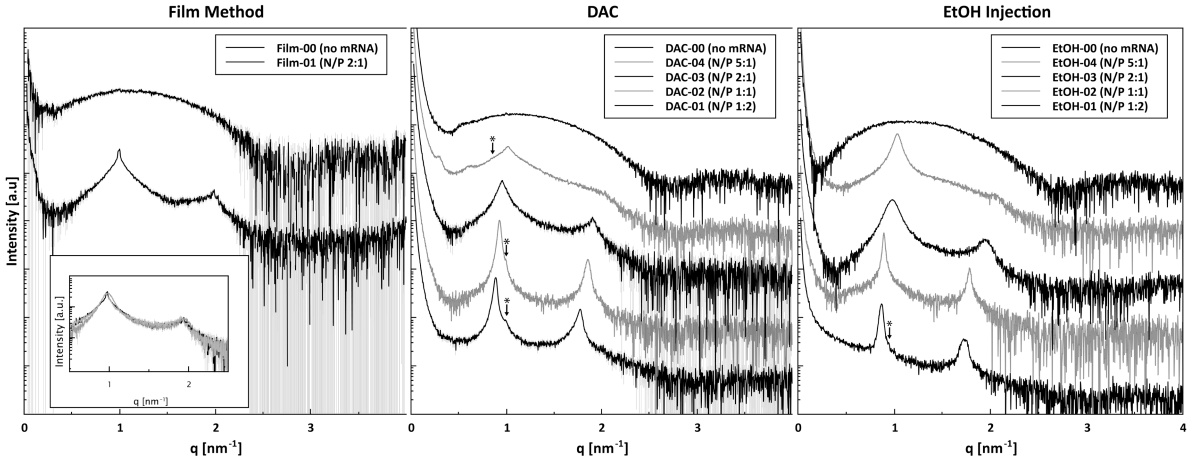

Figure 19. SAXS curves of DOPC/DOTAP lipoplexes at different N/P ratios and prepared with three different preparation methods. The scattering curve intensities were shifted vertically for illustration purposes and for the sake of better depiction of the Bragg peaks the q-range from 4-8 nm^{-1} is not displayed, as it contains only incoherent background scattering. Clearly visible peak shoulders are marked with arrows (*). The inlay shows the Bragg peak region of all three preparation methods at an N/P of 2:1, scaled to the same intensity for the 1st order Bragg peak.

While one can see that the scattering curves of the same compositions already look qualitatively very similar, a quantitative comparison is obviously much more meaningful. For this purpose, the Bragg peaks were fitted with Lorentz fits and the results were compared between the different preparation methods. The results can be seen in Table 10.

Sample	Peak 1 position [nm^{-1}]	Peak 2 position [nm^{-1}]	Repeat ratio	d-spacing [nm]	Correlation length [nm]
DAC-00	-	-	-	-	139.5±1.3
DAC-01	0.8670±0.0001	1.7248±0.0007	1.99	7.247±0.001	143.6±1.2
DAC-02	0.9285±0.0001	1.8549±0.0003	2.00	6.767±0.001	56.4±1.3
DAC-03	0.9560±0.0005	1.9014±0.0019	1.99	6.572±0.004	33.2±0.8
DAC-04	1.0140±0.0009	1.8297±0.0124	1.80	6.196±0.006	118.2±1.6
DAC-05	0.8674±0.0002	1.7317±0.0005	2.00	7.244±0.002	125.9±1.2
DAC-06	0.9361±0.0002	1.8701±0.0005	2.00	6.712±0.001	68.5±0.7
DAC-07	0.9539±0.0003	1.8969±0.0009	1.99	6.587±0.002	18.5±0.4
DAC-08	1.0114±0.0019	1.8448±0.0117	1.82	6.213±0.011	139.5±1.3
EtOH-00	-	-	-	-	-
EtOH-01	0.8672±0.0003	1.7255±0.0011	1.99	7.245±0.003	142.2±3.2
EtOH-02	0.8939±0.0003	1.7819±0.0009	1.99	7.029±0.002	160.6±6.7
EtOH-03	0.9811±0.0003	1.9378±0.0014	1.98	6.404±0.002	38.0±0.3
EtOH-04	1.0316±0.0003	1.9571±0.0095	1.90	6.091±0.002	54.8±0.5
EtOH-05	0.8465±0.0005	1.6833±0.0020	1.99	7.423±0.005	147.0±5.7
EtOH-07	0.9801±0.0005	1.9443±0.0040	1.98	6.411±0.003	39.1±0.4
EtOH-08	1.0399±0.0003	1.8061±0.0181	1.74	6.042±0.002	53.6±0.5
EtOH-09	0.9693±0.0012	1.9028±0.0076	1.96	6.482±0.008	37.3±1.0
EtOH-10	0.9665±0.0018	1.9100±0.0090	1.98	6.501±0.012	51.4±2.5
EtOH-11	1.0043±0.0020	-	-	6.256±0.013	34.8±1.4
Film-00	-	-	-	-	-
Film-01	0.9935±0.0012	-	1.99	6.324±0.008	34.8±0.8

Table 10. Bragg peak parameters of samples used in the SAXS measurements investigating the preparation method influence.

First, it should be mentioned that fitting of the 2nd order Bragg peaks at the N/P ratio of 5:1 proved unreliable due the absence of a clearly defined peak. Therefore, these results should be interpreted with caution. For example, while all other N/P ratios showed the repeat ratio of the 1st and 2nd order Bragg peak to be almost exactly 2, proving the lamellar bilayer structure of these systems, this was not

the case for N/P 5:1. However, in this case this is probably more due to the less meaningful 2nd order Lorentz fit, and not likely to be indicative of a non-lamellar structure.

Figure 20 shows the calculated d-spacing and correlation lengths for all formulations. A clear trend towards lower d-spacings with higher N/P ratios (higher cationic lipid content) can be seen for all formulations. While overall negatively charged lipoplexes have an approximate repeat spacing of 7.3±0.1 nm, this is steadily reduced to 6.1±0.1 nm at an N/P ratio of 5:1. When looking at the correlation lengths, the effect of the N/P ratio revealed itself in a more abrupt manner. As already suspected from the visual interpretation of the scattering curves, systems with an N/P ratio of up to 1 showed high correlation lengths (118-161 nm), while the correlation lengths for N/P ratios above 1 were calculated to be in the range of 18-55 nm, confirming the loss of long-range order. Combining the proven lamellar structure and the calculated d-spacings and correlation lengths of the systems, an estimation of the number of stacked bilayers can be made.[141] For the highly correlated systems (N/P ≤ 1), this was in the range of an average of 16-23 stacked bilayers per lipoplex. For the systems displaying lower order (N/P > 1), this number dropped to about 3-10.

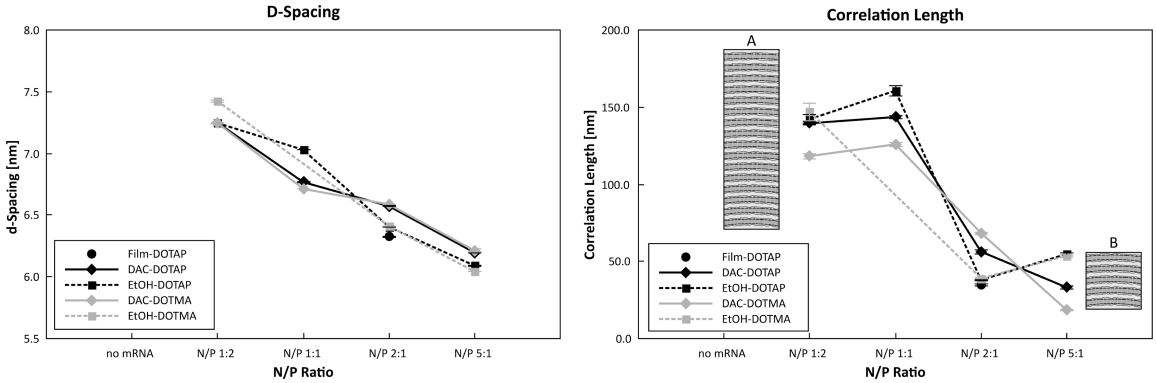

Figure 20. Comparison of d-spacing (left) and correlation lengths (right) of samples used in the SAXS measurements investigating the preparation method influence at the different N/P ratios tested. Inlays A and B illustrate the interpretation of the drop in correlation length as a drop in the number of stacked bilayers within the individual systems.

In addition, a pairwise two-sample t-test was performed to determine if there were any significant differences between the samples prepared via dual asymmetric centrifugation or ethanol injection. For this, pairs comprising the same cationic lipid and N/P ratio while comparing the two preparation methods were formed, resulting in a total set of seven pairs. At the p=0.05 level, no significant difference between the two populations could be found – neither in terms of d-spacing nor in terms of correlation length. This further solidifies the conclusion from the qualitative curve analysis that there is no structural difference between systems prepared with either method. Another paired t-test was performed to compare between the two cationic lipids used (DOTAP and DOTMA). Pairs were assembled from systems prepared with the same preparation method and at the same N/P ratio, again resulting in a total set of seven pairs. As was the case for the preparation methods, no significant difference in d-spacing or correlation length between the cationic lipids could be determined at the p=0.05 level.

The mentioned peak shoulders (marked with arrows in Figure 19) at N/P ratios ≤ 1 correspond to a slightly lower d-spacing of 6.3-6.4 nm and could be caused by an additional species of liposomes comprising only the helper lipid DOPC, but no DOTAP or mRNA. There, the lack of electrostatic repulsion between bilayers caused by DOTAP or DOTMA leads to lower overall bilayer spacings and similar values of d-spacing have been previously reported for liposomes comprising only DOPC.[137] At N/P ratios above 1, the peak shoulders move to the left side of the main Bragg peak, as mentioned above. Here, the excess of cationic lipid leads to unscreened cationic charges, resulting in particle

species or subdomains with increased d-spacing due to electrostatic repulsion. For example, the peak shoulder for DAC-08 corresponds to a d-spacing of 9.9 nm – much higher than that of the main 1st order Bragg peak (6.2 nm) – and at even lower q an additional peak corresponding to a d-spacing of approximately 22 nm is visible.

An additional set of samples (EtOH-09/10/11), comprising DOTAP as the cationic lipid and prepared via ethanol injection at an N/P ratio of 2:1, was measured to check if the results gained from the highly concentrated samples are also valid for samples prepared at lower concentrations (which are closer to realistic therapeutic mRNA concentrations), whether extrusion has an effect on already size-controlled particles in terms of structure, and whether the buffer used (10 mM glycylglycine) has any structural influence. Their scattering curves can be seen in Suppl. Fig. 2 (bottom row). All of these particles showed a bilayer structure, but with a less visible 2nd order Bragg peak, which was probably due to the overall lower scattering intensity at lower sample concentrations. The d-spacing and correlation length of these three samples were close to those of the corresponding highly concentrated, non-extruded sample EtOH-03, with only the d-spacing of EtOH-10 (no 10 mM GG) being slightly lower. Therefore, there seems to be no meaningful internal structural difference between particles prepared at high or low sample concentrations and extrusion does not affect the internal structure of these lipoplex systems. The slightly lower d-spacing of particles prepared in the absence of 10 mM GG might be indicative of an osmotic effect but could also be a statistical error due to the noisier scattering curve making the Bragg peak fitting process harder.

3.1.3 Influence of Different Helper Lipids

In addition to the preparation process, the utilized helper lipid is also often assumed to be influential on the lipoplex structure. Therefore, an additional set of lipoplexes prepared via the film method was investigated concerning their structural properties. The sample list, which can be seen in Table 11, involved both variation of the lipid acyl chains in terms of length and saturation, as well as variation of the phospholipid headgroup.

3.1.3.1 Particle Size

No influences on the particle size by the helper lipid could be seen. As all particles were prepared with the film method without additional size control, their diameters were in the range of > 1000 nm, as expected from chapter 3.1.2.1 (data not shown).

3.1.3.2 Small Angle X-Ray Scattering

The samples shown in Table 11 were again measured with the SAXS conditions stated as "Setup 2" in the methods section (see chapter 2.2.4.7.1).

Sample	Helper lipid	Helper lipid mol%	Cationic lipid	Cationic lipid mol%	mRNA mol%	N/P ratio	Preparation concentration	Comment
F-DOPC-00	DOPC (18:1-PC)	80	DOTAP	20	0	-	50 mg/mL	= "Film-00"
F-DSPC-00	DSPC (18:0-PC)	80	DOTAP	20	0	-	50 mg/mL	
F-DOPG-00	DOPG (18:1-PG)	80	DOTAP	20	0	-	50 mg/mL	
F-DOPE-00	DOPE (18:1-PE)	80	DOTAP	20	0	-	50 mg/mL	
F-DPPE-00	DPPE (16:0-PE)	80	DOTAP	20	0	-	50 mg/mL	
F-DOPC-01	DOPC (18:1-PC)	80	DOTAP	20	10	2	50 mg/mL	= "Film-01"
F-DSPC-01	DSPC (18:0-PC)	80	DOTAP	20	10	2	50 mg/mL	
F-DOPG-01	DOPG (18:1-PG)	80	DOTAP	20	10	2	50 mg/mL	
F-DOPE-01	DOPE (18:1-PE)	80	DOTAP	20	10	2	50 mg/mL	
F-DPPE-01	DPPE (16:0-PE)	80	DOTAP	20	10	2	50 mg/mL	

Table 11. Sample compositions of samples used in the SAXS measurements investigating the structural influence of the utilized helper lipid. Note that F-DOPC-00 and F-DOPC-01 are the same samples as Film-00 and Film-01 from the previous chapter.

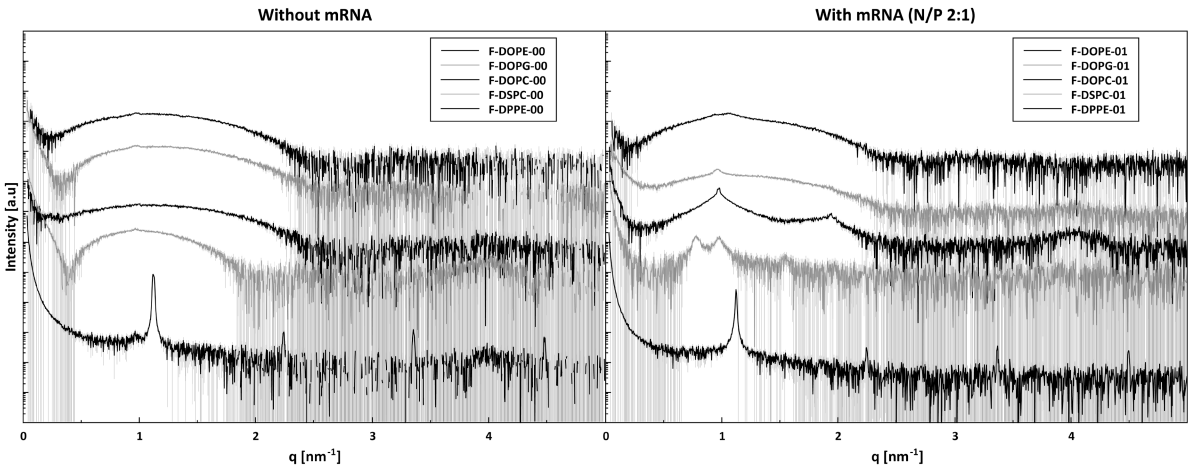

Figure 21. SAXS curves of lipoplexes comprising different helper lipids with (right) and without (left) mRNA prepared via the film method. The scattering curve intensities were shifted vertically for illustration purposes and for the sake of better depiction of the Bragg peaks the q-range from 5-8 nm^{-1} is not displayed, as it contains only incoherent background scattering.

Figure 21 shows the resulting scattering curves in the relevant q-ranges, with major differences already visible at a first glance. Almost all samples without mRNA present to screen cationic charges (with the exception being F-DPPE-00) show the expected broad signal from the uncorrelated bilayers as a result of the unscreened DOTAP charges. F-DPPE-00 however shows strong, sharp Bragg peaks visible up to the 4th order. The scattering curves of lipoplexes containing mRNA differ much more from each other. F-DOPE-01 shows only a glimpse of a double Bragg peak at around 1 nm^{-1}, while one of these Bragg peaks becomes more apparent for F-DOPG-01 and even more for F-DOPC-01. F-DPSC-01 shows a strong double peak (at q=1 nm^{-1} and lower), with higher order peak also visible, albeit noisy, and F-DPPE-01 shows the same strong Bragg peaks up to the 4th order already visible without mRNA.

Lorentz fitting of the visible Bragg peaks revealed a d-spacing of 6.5 nm for F-DOPG-01, 6.3 nm for F-DOPC-01, and 5.6 nm for F-DPPE-01. The 2nd, 3rd, and 4th order Bragg peaks of F-DPPE-01 appeared at integer multiples of the 1st order Bragg peak, proving a clear lamellar order. The double Bragg peak of F-DSPC-01 was calculated to represent d-spacings of 6.4 and 8.0 nm. 2nd order Bragg peaks for both of these peaks were present at double q-values of the 1st order peaks, indicating the presence of two separate lamellar systems. The small double peak of F-DOPE-01 relates to d-spacings of 5.9 and 6.7 nm. Since no higher order peaks were visible, clear conclusions on the lipid phase cannot be made for this system.

The presence of Bragg peaks up to the 4th order for the samples comprising DPPE made it possible to calculate an electron density map and Figure 12 in the methods section shows this process for F-DPPE-00 (see page 32). The calculation for F-DPPE-01 resulted in the same calculated bilayer thickness (d_{HH}) of 4.12 nm. Combining this with the d-spacing of 5.6 nm for both systems, a water-layer thickness (d_w) of 1.48 nm can be concluded.

While these results are interesting, no systematic conclusions or even a model can be derived from it. The experiment was at the time limited by available materials and no systematic headgroup and acyl-chain variation comprising more data points could be performed to generate a systematic layout. Therefore, these effects should be further examined in a way that systematically varies lipid chains (e.g., C14:0-C18:0 / C14:1-C18:1 / C14:2-C18:2) and phospholipid headgroups (PC, PE, PG, …) to further elucidate these effects and derive trends for the structural particle parameters that can be connected to the varied lipid properties. However, while no systematic conclusion can be drawn yet, these results show the importance of choosing the correct helper lipid depending on the desired particle properties.

Utilizing different lipid chain lengths and saturation levels can clearly have strong effects on the intraparticle order, as can be seen with the dramatically higher ordered lipoplex structures resulting from the use of DPPE when compared to those using DOPE. The effect of utilizing different helper lipid head groups such as phosphatidylcholine (PC) or phosphorylethanolamine (PE) could also be seen and the choice of helper lipid head group has previously been discussed to play a major role in the fusogenic properties of lipid particle systems with biological membranes.[48] The structural implications hereof are explored further in the context of pH-responsive systems in chapter 3.2.1.3, while the influence on biological activity is investigated in chapter 3.2.2.2.

3.2 pH-Responsive Systems

While permanently charged cationic lipids have been used as transfection reagents for many years, recent developments have mainly used so-called ionizable lipids, whose headgroup charge is pH-dependent, e.g. by implementing a tertiary amine instead of a quaternary amine (see Figure 22 for an example of a homologue pair of a permanently charged and an ionizable lipid).[136,142] The main portion of the research presented in this dissertation was focused on elucidating the structural and functional properties of systems utilizing these pH-responsive lipids in order to further expand the models for permanently charged lipoplexes previously established in this group. For this, both simple model lipoplex systems comprising only one helper lipid, one ionizable lipid, and mRNA, as well as more complex so-called lipid nanoparticle (LNP) systems, comprising additional components such as cholesterol, were prepared and studied in terms of their physicochemical properties, such as pH-responsiveness and structure, as well as in terms of their biological efficacy *in vitro*.

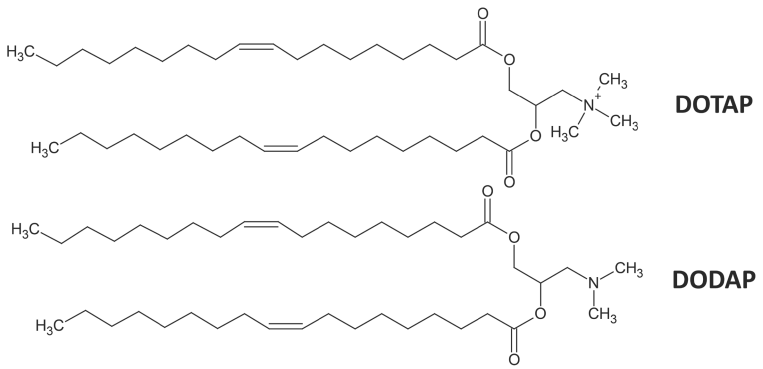

Figure 22. The permanently charged lipid DOTAP (top) and its ionizable homologue DODAP (bottom). While the quaternary amine group of DOTAP always carries a cationic charge, the tertiary amine group of DODAP can be protonated or unprotonated depending on the environmental pH.

3.2.1 Physicochemical Characterization

First, several aspects of pH-responsive mRNA delivery systems were characterized using physicochemical methods such as SAXS and fluorescence assays. These aspects included the structural difference between the previously used model lipoplex systems and modern LNPs, the influence of the preparation method on the resulting lipoplex or LNP structure, the influence of different lipid components, and the structural changes occurring in response to changes in environmental pH.

3.2.1.1 pH-Responsive Structural Changes of Lipoplexes

The results presented in this chapter have been previously published as a journal article in *Langmuir* (see Disclaimer).[143] The systems that were prepared via the film method for characterization by SAXS were prepared by Antje Ziller. Their SAXS data was also shown in a previous dissertation but is included here for reference and further analysis.[137]

Model lipoplex systems, based on the permanently charged lipoplexes previously studied in our group, were prepared by using the homologue ionizable lipids to the previously used permanently charged lipids (e.g. DODMA for DOTMA, DODAP for DOTAP) or DLin-MC3-DMA, which is the ionizable lipid used in the first commercially available RNA drug Onpattro®.[81] For ease of understanding, the samples were named systematically using the naming scheme shown in Figure 23, which gives information on the preparation method used, the utilized cationic or ionizable lipid, and the N/P ratio. The samples were prepared either via the film method (F) or ethanol injection (E) and DOPC was used as the helper lipid for all samples described in this chapter.

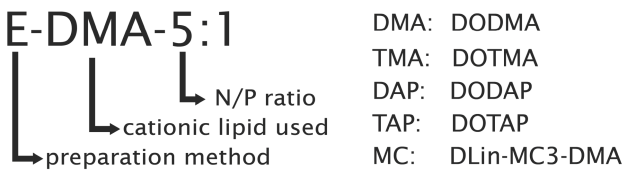

Figure 23. Nomenclature system of the samples used for investigating the pH-responsive structural changes of lipoplexes. The preparation method is marked with either an E or an F for the ethanol injection or the lipid film method, respectively.

3.2.1.1.1 Particle Size

First, the prepared formulations were characterized in terms of size reproducibility. Each composition was prepared at least three times and measured independently in order to show the reproducibility of the preparation method. As expected, particles prepared via the film method were rather large in size and prone to be polydisperse, while particles prepared with the ethanol injection method were reproducibly smaller in size and more monodisperse (see Figure 24). Therefore, all preparations from then on out (apart from the already mentioned film systems prepared by Antje Ziller) were prepared with the ethanol injection method in order to minimize errors caused by polydispersity.

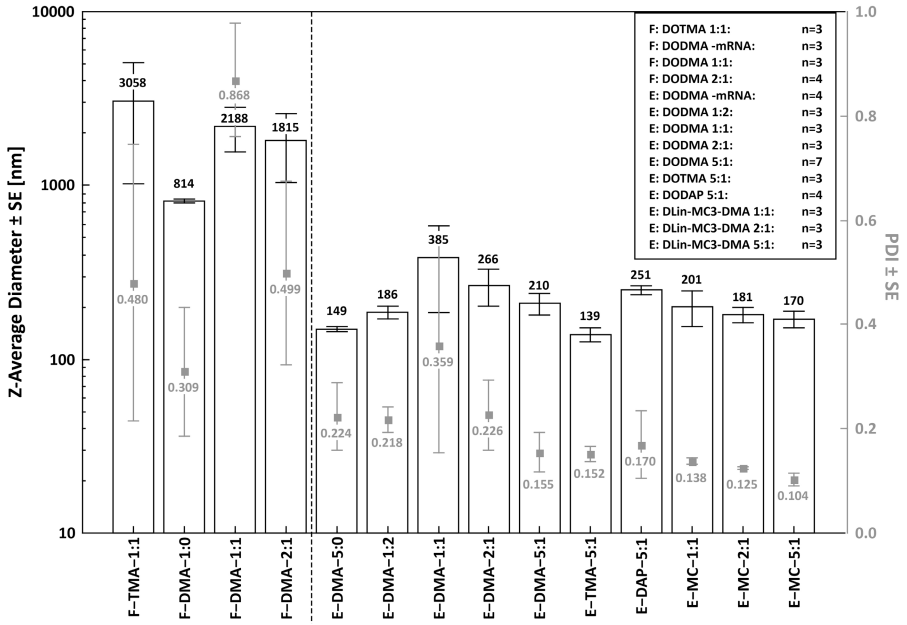

Figure 24. Diameter (Z-Average, black vertical bars, left y-axis) and polydispersity index (PDI, grey scatter plot, right y-axis) of pH-responsive lipoplexes and some permanently charged counterparts. The number (n) of independently prepared systems measured is stated in the legend. The standard error of the mean (SE) is displayed as error bars, since it is commonly used for the comparison of population mean values (due to it visualizing the uncertainty of the mean rather than the precision of the measurement).[144]

3.2.1.1.2 mRNA Loading, mRNA Accessibility, and Zeta Potential

To investigate the insertion of mRNA into the lipoplex systems under different conditions, the formulations were characterized using the Ribogreen® assay and agarose gel electrophoresis. The particles were formulated in 10 mM glycylglycine and the mRNA was quantified either directly or after mixing with DPBS to simulate the injection into a physiological milieu. Additionally, a set of lipoplexes was prepared in DPBS instead of 10 mM GG to compare the difference in mRNA loading at pH 7.4 to that at pH 5.6. The results of three independently prepared formulations each, with the fluorescence measured as triplicates for each independent formulation, can be seen in Figure 25.

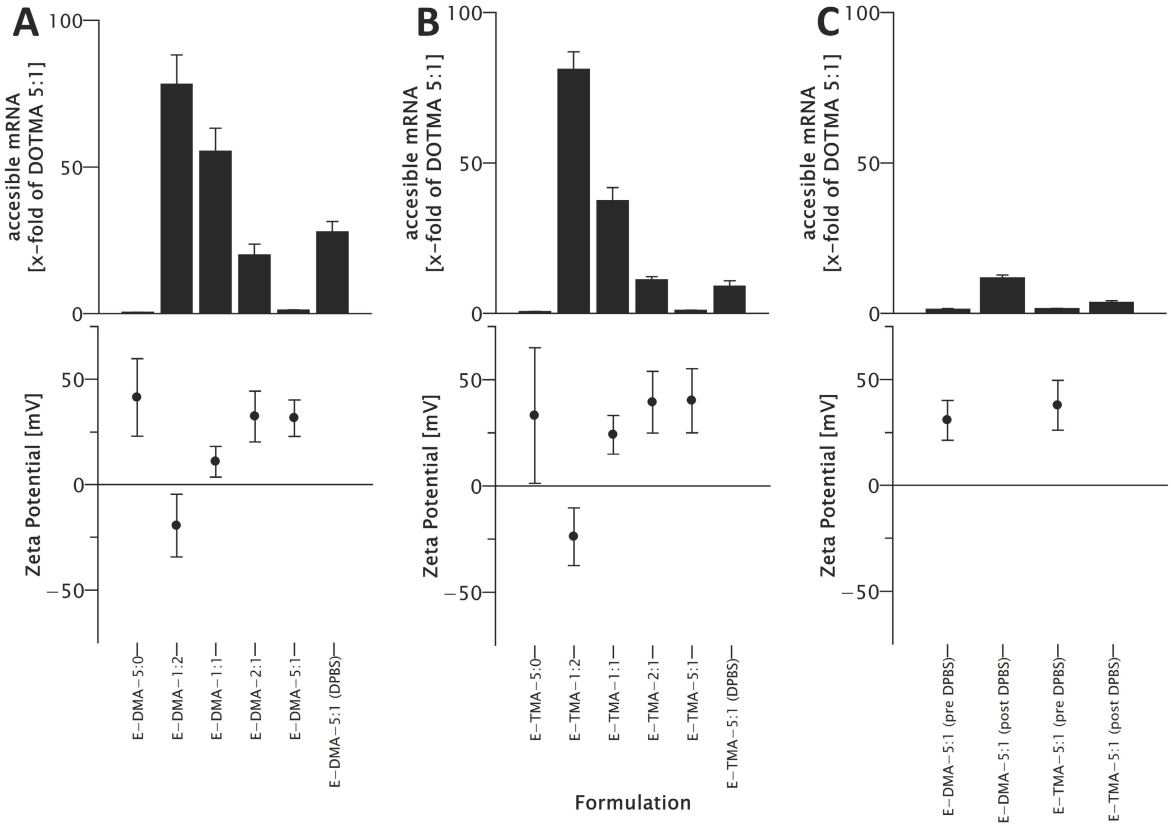

Figure 25. Ribogreen® accessible mRNA (top) and zeta potential (bottom) as a function of the N/P ratio for different formulations. (A) DODMA-based formulations and (B) DOTMA-based formulations prepared in 10 mM GG or DPBS (where stated). (C) DODMA- and DOTMA-based formulations were prepared in 10 mM GG and measured before (pre DPBS) and after (post DPBS) being mixed 1:1 with DPBS.
Ribogreen® data is shown as mean ± SD of triplicate measurements of three separate preparations each; zeta potentials are shown as zeta potential ± SD of single measurements of three separate preparations each; no zeta potential is shown for samples in DPBS, as zeta potential measurements in DPBS are not possible due to the high ionic strength compressing the electric double layer (EDL).[99]

An N/P-ratio dependent mRNA incorporation was found both for samples comprising the ionizable lipid DODMA (A) and for those comprising the permanently charged DOTMA (B), with higher N/P ratios leading to higher mRNA incorporation. However, higher mRNA loading at N/P ratios below 5:1 was achieved for permanently charged lipoplexes. For example, when comparing E-DMA-2:1 to E-TMA-2:1, the amount of freely accessible mRNA at the N/P ratio of 2:1 was 1.8 times as high for the ionizable samples as for the permanently charged ones, while at an N/P ratio of 1:1 the ionizable formulations showed about 1.5 times as much accessible mRNA. A switch from negative to positive zeta potentials could be made out when going from mRNA excess (N/P 1:2) to cationic lipid excess (N/P 2:1), which was expected. When prepared in DPBS instead of 10 mM GG, the incorporation rate was lower for both ionizable and permanently charged systems, however, the effect was much stronger for the pH-

responsive formulation (E-DMA-5:1 DPBS), where the amount of accessible mRNA was about 23 times higher when prepared in DPBS. Samples comprising DODMA that were prepared in 10 mM GG and then incubated mixed with DPBS showed a small pH-dependent increase (release) of accessible mRNA (9-fold, C). However, the amount of released mRNA was much lower than when the samples were prepared directly in DPBS, indicating that most of the mRNA is in fact stably kept within the delivery system after the preparation, which is crucial for potential clinical applications. Only a much smaller effect could be seen for the permanently charged systems, possibly due to osmotic effects.

To confirm these results, and to differentiate between accessible and free mRNA, non-denaturing agarose gel electrophoresis was performed. A representative gel (from at least three gels per shown lane) is shown in Figure 26.

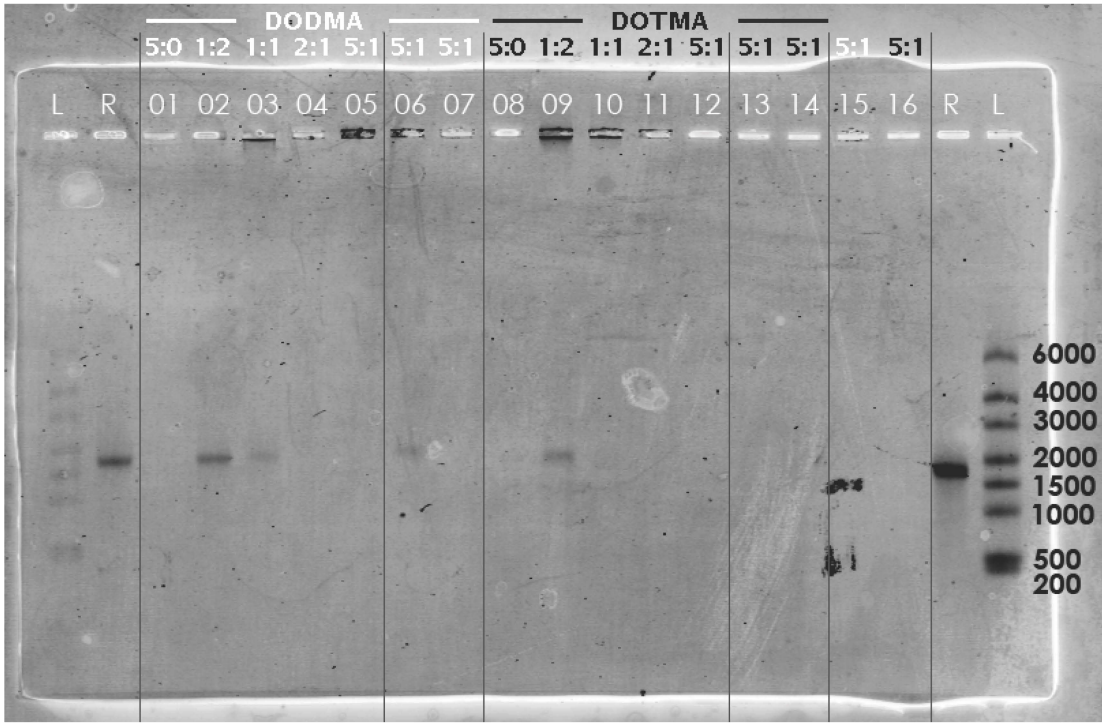

Figure 26. Determination of free mRNA in lipoplex samples by agarose gel electrophoresis. Lanes marked as "L" and "R" represent the RNA ladder and pure mRNA (as used for the sample preparation), respectively. Lanes 01-05 represent samples E-DMA-5:0, E-DMA-1:2, E-DMA-1:1, E-DMA-2:1, and E-DMA-5:1, prepared in 10 mM GG. Lanes 06 and 07 show E-DMA-5:1 prepared in DPBS and 10 mM Sörensen buffer pH 7.4, respectively. Lanes 08-10 represent samples E-TMA-5:0, E-TMA-1:2, E-TMA-1:1, E-TMA-2:1, and E-TMA-5:1, prepared in 10 mM GG, while lanes 13 and 14 show E-TMA-5:1 prepared in DPBS and 10 mM Sörensen buffer pH 7.4, respectively. Lanes 15 and 16 show E-DMA-5:1 and E-TMA-5:1 prepared in 10 mM glycylglycine and subsequently incubated 1:1 with DPBS.

The free mRNA eluated in between the 1500 nucleotide (nt) and 2000 nt fractions of the used RNA ladder and no smaller fragments are visible, confirming that neither the buffer nor the assay lead to mRNA disintegration. For lipoplexes comprising the ionizable lipid DOTMA (lane 08-12), free mRNA could only be detected at an N/P ratio of 1:2, which shows that the excess of mRNA used during the preparation step cannot be completely bound to the lipoplex. As soon as all of the mRNA charge was complexed by the cationic lipid (N/P ≥ 1), it was completely bound to the lipoplex and, while still partly accessible to the Ribogreen® dye (see above), no free mRNA could be found in the solution anymore. For lipoplexes utilizing the ionizable lipid DODMA (lane 01-05), free mRNA could be detected both at an N/P ratio of 1:2 and at 1:1. This can likely be explained by the fact that not all DODMA molecules might be protonated at the preparation pH, resulting in a lack of cationic charge to bind all of the mRNA. At N/P ratios of 2:1 and higher, the vast excess of ionizable lipid molecules outweighs this fact,

and all of the input mRNA was bound to the lipoplexes. Again, a small amount of free mRNA was detectable when preparing the pH-responsive lipoplex systems in DPBS instead of 10 mM GG (lane 06) – this effect was not visible for DOTMA (lane 13), as its cationic charge is not pH-dependent. No free mRNA was also detected after incubation of lipoplexes prepared in 10 mM GG with DPBS (lane 15 and 16), again showing that this effect is much smaller than that of the preparation medium, as already shown by the Ribogreen® assay.

3.2.1.1.3 pK_a-Determination (TNS-Assay)

The fluorescence-based TNS assay was performed to determine factors affecting the overall formulation pK_a, such as the ionizable lipid used or the N/P ratio of the lipoplex. Figure 27 shows the normalized fluorescence intensities and the applied sigmoidal (Boltzmann) fits.

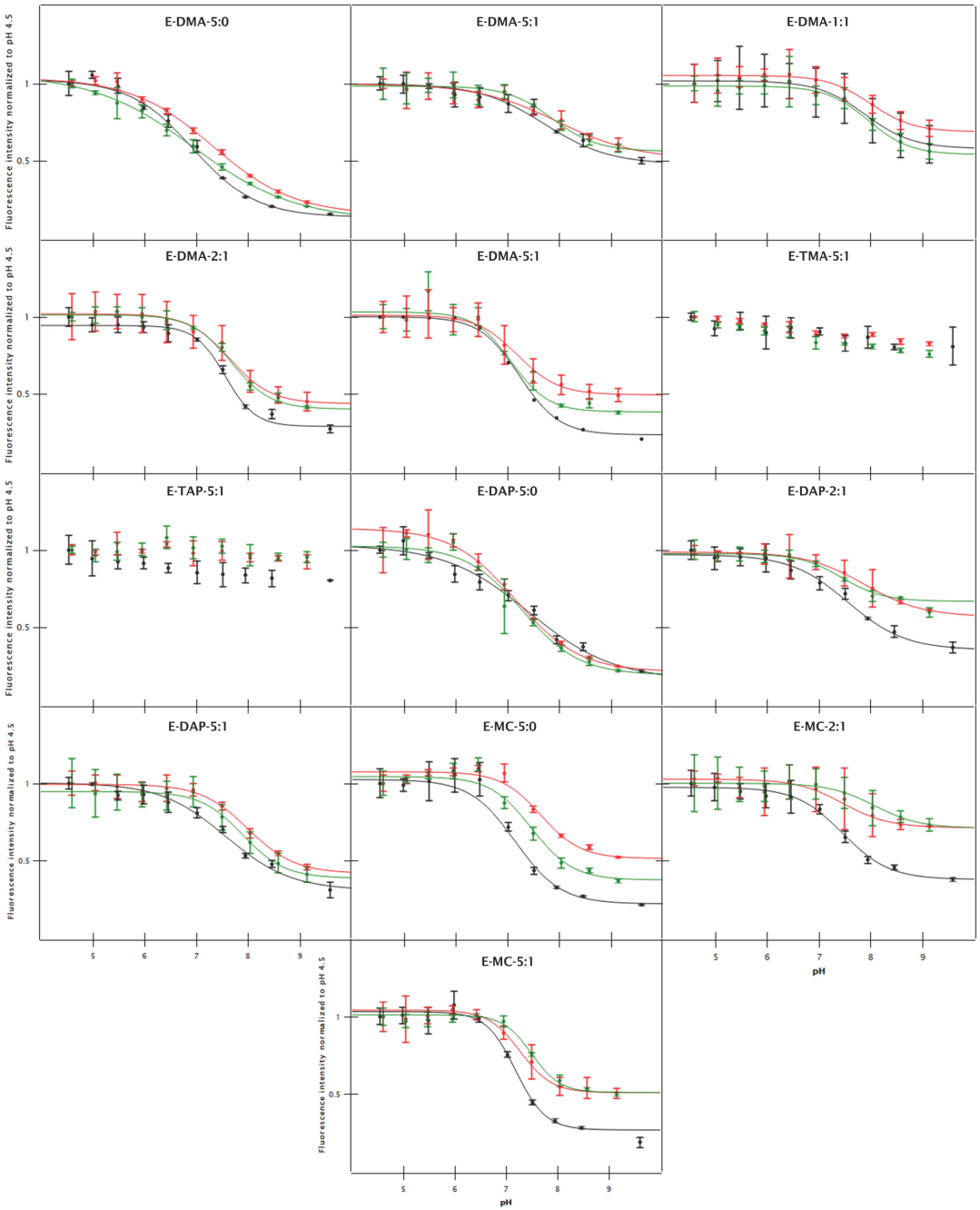

Figure 27. Results of the TNS-based formulation pK_a assay. The data is shown as fluorescence intensity (±SD) normalized to the intensity at pH 4.5 for triplicate measurements of three independently prepared formulations (green, red, black) each. The curves depict sigmoidal (Boltzmann) fits of the experimental data.

Looking at the results, one can see that lipoplexes comprising the permanently charged cationic lipids DOTMA or DOTAP (E-TMA-5:1, E-TAP-5:1) showed no pH-dependency in the fluorescence signal – as expected since there should be no change in cationic charge. All systems utilizing ionizable lipids (DODMA, DODAP, DLin-MC3-DMA) showed a clear drop in fluorescence intensity at higher pH levels that got stronger with higher N/P ratios, was highest for systems containing no mRNA, and was well described by the applied Boltzmann fit. The inflection points of these fits were collected and defined as the apparent formulation pK_a. They can be seen in Table 12. The increased change in fluorescence for higher N/P ratios and for the absence of mRNA can be explained by the mechanism of action behind the assay. Since TNS can only show fluorescence if it is bound to cationic charges, higher fractions of ionizable lipids result in higher fluorescence intensities for constant TNS concentrations – as long as there is an excess of TNS. As the mRNA competes for electrostatic binding sites with TNS, its absence leads to higher concentrations of lipid-bound TNS and therefore higher maximum intensities. The same overall trends could be seen for the apparent formulation pK_a as well, with those formulations containing the highest fraction of ionizable lipid and no mRNA displaying the lowest apparent pK_a.

N/P ratio	DOTMA pK_a	DODMA pK_a	DOTAP pK_a	DODAP pK_a	DLin-MC3-DMA pK_a
no mRNA	-	7.1 ± 0.2	-	7.3 ± 0.1	7.4 ± 0.2
1:2	-	7.9 ± 0.1	-	-	-
1:1	-	8.0 ± 0.0	-	-	-
2:1	-	7.6 ± 0.0	-	7.5 ± 0.1	7.7 ± 0.3
5:1	n.c.	7.2 ± 0.1	n.c.	7.8 ± 0.2	7.3 ± 0.1

Table 12. Apparent formulation pK_a of lipoplexes determined with the TNS assay. The reported pK_a values are stated as mean±SD for three independently prepared formulations measured in triplicates each. Formulations not measured are marked with "–" and measurements where no meaningful Boltzmann fit could be applied are marked as "n.c." (not calculated).

3.2.1.1.4 Small Angle X-Ray Scattering

Small angle X-ray scattering was performed in combination with pH-variation to elucidate the internal structural reorientation occurring within pH-responsive lipoplexes when exposed to different environments pH-wise. Two sets of lipoplexes comprising the helper lipid DOPC and different ionizable lipids or their non-ionizable counterparts were prepared at various N/P ratios. The detailed compositions can be seen in Table 13. The samples were prepared either via the film or the ethanol injection method in their respective buffers, mixed with the pH buffers described in the methods section (see chapter 2.2.2) in a pH-range of 4.5-8.0, and measured directly after mixing. The relevant q-ranges of the resulting scattering curves can be seen in Figure 28. As described in the previous chapters, characteristic features of the scattering patterns were fitted with the appropriate fit function (Lorentz fit for Bragg peaks) and parameters such as the lipid phase, the d-spacing, and the correlation length were calculated. These results can be seen in detail in the supplementary data (see chapter 7.4.6).

As expected, lipoplexes comprising DOPC and the permanently charged lipid DOTMA (Figure 28, top row, center panel) together with mRNA resulted in pronounced Bragg peaks in the q-range of 0.8-1.0 nm^{-1} with second order Bragg peaks at approximately double q-values (marked as red and blue arrows, respectively). As previously mentioned, these scattering patterns are the result of the lipoplex multilayer stacks, consisting of repeating lipid bilayers where the mRNA is inserted into the hydrophilic slabs in between the lipid headgroups. Looking at the pH-variation of this lipoplex system, no obvious change in the scattering patterns could be made out with changing pH. The calculated d-spacing was approximately 72 Å, with only minor changes below 1 Å over the whole pH-range. Detailed analysis of the peak repeat ratio (see Figure 29) revealed only integer multiples as repeat ratios and therefore confirmed the lamellar lipid phase. Additionally, a second set of weak Bragg peaks at lower q was visible

at pH levels ≥ 5.0, indicating a possible second and smaller population of lamellar structures with higher d-spacing.

Sample	Preparation concentration [total lipid mg/mL]	DOPC [wt%] [mol%]	Cationic lipid	Cationic lipid [wt%] [mol%]	mRNA	mRNA [wt%] [mol%]	Medium	pH-buffer-molarity	SAXS-setup
F-TMA-1:1	100	90.0 88.5	DOTMA	10.0 11.5	R18	5.0 11.7	H/E	66.7 mM	Setup 1
F-DMA-1:0	100	90.0 87.7	DODMA	10.0 12.3	-	0.0 0.0	H/E	66.7 mM	Setup 1
F-DMA-1:1	100	90.0 87.7	DODMA	10.0 12.3	R18	5.0 11.6	H/E	66.7 mM	Setup 1
F-DMA-2:1	100	80.0 75.9	DODMA	20.0 24.1	R18	5.0 11.3	H/E	66.7 mM	Setup 1
E-DMA-5:1	10	55.9 50.0	DODMA	44.1 50.0	R159	4.7 10.0	GG	150 mM	Setup 3 0.13-5.0 nm^{-1}
E-TAP-5:1	10	54.2 50.0	DOTAP	45.8 50.0	R159	4.6 10.0	GG	150 mM	Setup 3 0.08-2.9 nm^{-1}
E-DAP-5:1	10	54.8 50.0	DODAP	45.2 50.0	R159	4.6 10.0	GG	150 mM	Setup 3 0.13-5.0 nm^{-1}
E-MC-2:1	10	83.1 80.0	DLin-MC3-DMA	16.9 20.0	R159	4.4 10.0	GG	150 mM	Setup 3 0.08-2.9 nm^{-1}
E-MC-5:1	10	55.1 50.0	DLin-MC3-DMA	44.9 50.0	R159	4.6 10.0	GG	150 mM	Setup 3 0.13-5.0 nm^{-1}

Table 13. Sample composition and measurement conditions for the SAXS analysis of pH-responsive lipoplexes and their nonresponsive homologues (quaternary ammonium cationic lipids). Samples are named with the nomenclature system shown in Figure 23. Total lipid is the combined lipid concentration (helper lipid and cationic lipid) at which samples were prepared, which was defined as 100 wt%. The N/P ratio stated in the sample names is the approximate molar ratio of the cationic charge to the anionic charge within the samples in integer numbers. mol% refers to the total lipid molarity within the sample (mol% (helper lipid) + mol% (cationic lipid) = 100%). The mRNA used was noncoding and either ~1900 nt (R18) or ~1670 nt (R159) long. The preparation medium was either 10 mM HEPES and 0.1 mM EDTA buffer (H/E) or 10 mM glycylglycine solution (GG). As mentioned in the text, samples prepared via the film method were prepared by Antje Ziller.

In contrast, the scattering curves of lipoplexes comprising DOTMA's ionizable homologue DODMA and mRNA showed a clear shift of the main Bragg peak position towards lower q with increasing pH levels (Figure 28, middle row). This translates to an increase in d-spacing and therefore less densely packed bilayers, even though the charge density of the ionizable lipid decreases. Intuitively, one might therefore expect a decrease in d-spacing due to less electrostatic repulsion between the bilayers, and this was in fact the case for F-DMA-1:0, which did not contain mRNA to screen the high cationic charge density at low pH levels. There, low pH-levels showed higher d-spacing and even an almost complete loss of ordered structure, visible as the strong broadening and eventual almost disappearance of the characteristic Bragg peak (Figure 28, top right panel). However, when mRNA is added to the formulation, it acts as a "glue", screening the cationic charge and strongly binding the sandwiched mRNA from neighboring bilayers, which leads to the tighter bilayer packing visible for positively charged DODMA (at low pH). By increasing the environmental pH levels, this effect becomes less pronounced and the anionic charge from the mRNA eventually even leads to electrostatic repulsion and an increase in d-spacing. It can therefore also be indirectly concluded that the mRNA remains immobilized in between the lipid bilayers even at higher pH levels.

Additionally, small peak shoulders to the right of the 1st order Bragg peak could be seen for these samples at pH-levels of 6 and higher, again indicating the presence of lateral phase separation into regions of higher and lower mRNA content due to also present uncharged DODMA, which is not able to bind mRNA and acts more like the formally uncharged helper lipid DOPC. The lack of charge in these regions would therefore lead to the lower d-spacing visible for these additional peak shoulders.

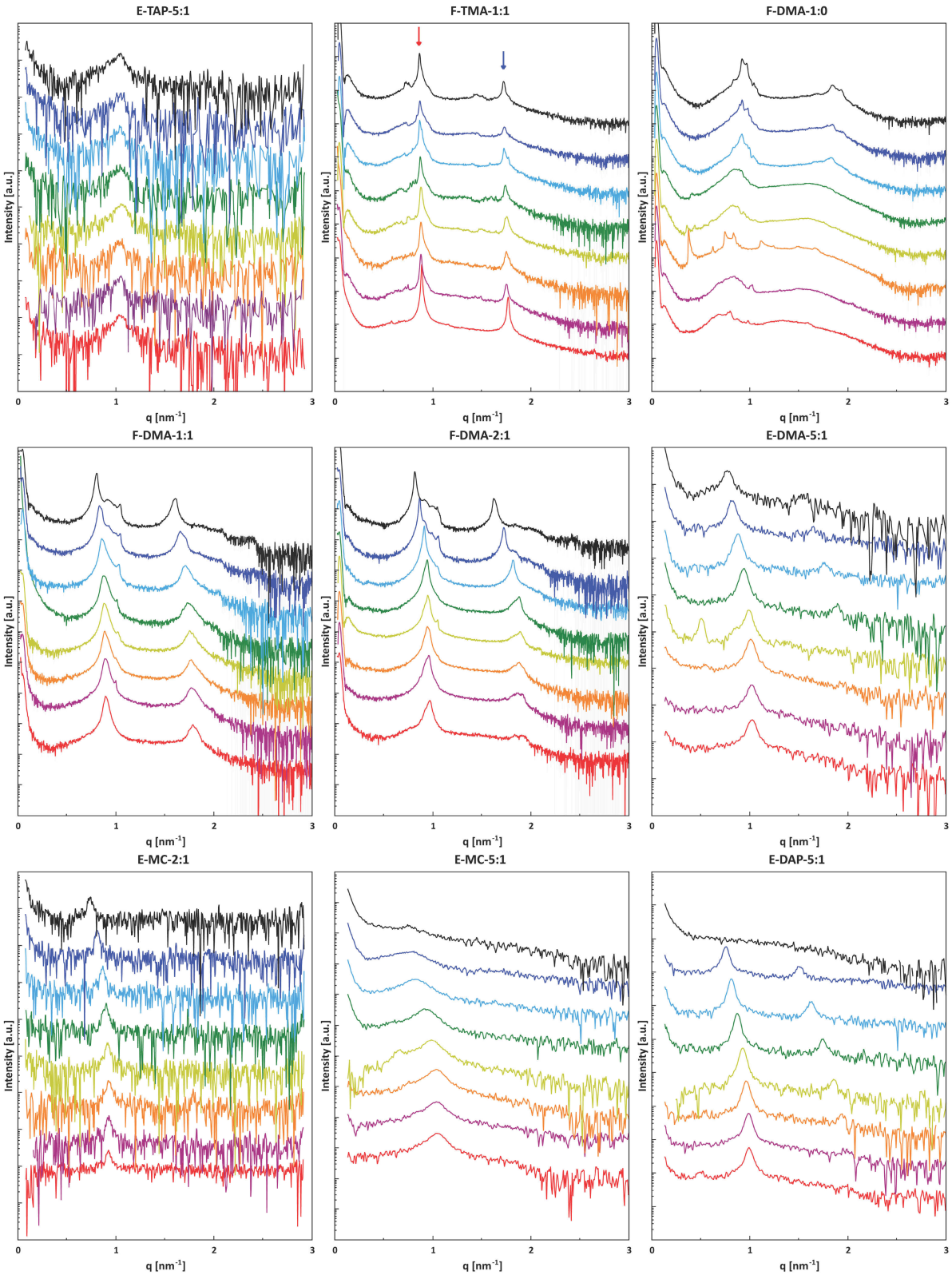

Figure 28. SAXS curves of ionizable lipoplexes and their permanently charged homologues over a pH range of 4.5 (red curves, bottom) to 8.0 (black curves, top) in ΔpH = 0.5 steps. The N/P ratio of 1:0 indicates an mRNA-free sample. The intensities recorded at different pH values are displaced along the logarithmic axis for visualization. In the scattering curves of F-TMA-1:1 (top, center), the first and second orders of the main Bragg peaks are marked as red and blue arrows, respectively, representative of all scattering curves. The difference in noise level is due to different experimental setups (beamlines and sample–detector distance) and does not indicate a difference in sample quality. For the compositions of each sample see Table 13.

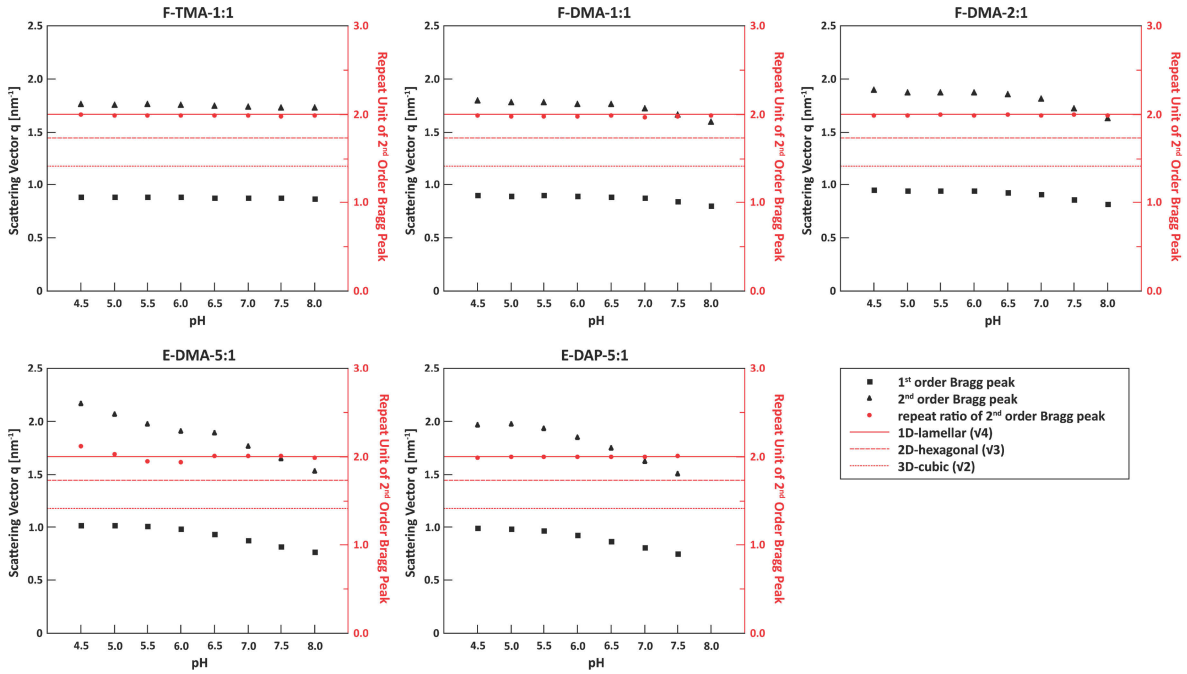

Figure 29. Peak positions of the 1st and 2nd order Bragg peak (black, left axis) and their calculated repeat ratio (right, red axis) for all systems where a well-defined 2nd order Bragg peak was visible. The 2nd order repeat ratios describing lamellar (√4), hexagonal (√3), and cubic (√2) lipid mesophases are marked as horizontal lines.

Quantitative analysis of the change in d-spacing showed a shift from around 77-78 Å to 70 Å and 65 Å for F-DMA-1:1 and F-DMA-2:1, respectively, indicating that the pH-responsive structural changes increase with higher fractions of ionizable lipid or the N/P ratio (see Figure 30). Even though the peak position for these samples changed over the observed pH-range, their repeat ratio stayed constant at almost exactly 2 (√4), again proving the lamellar bilayer structure of the studied systems (see Figure 29).

As the pH-responsive effects seemed to correlate with the ionizable lipid fraction, the second set of formulations was prepared at higher ionizable lipid fractions, while keeping the amount of mRNA constant (leading to higher N/P ratios), in order to better elucidate and quantify the observed structural changes.

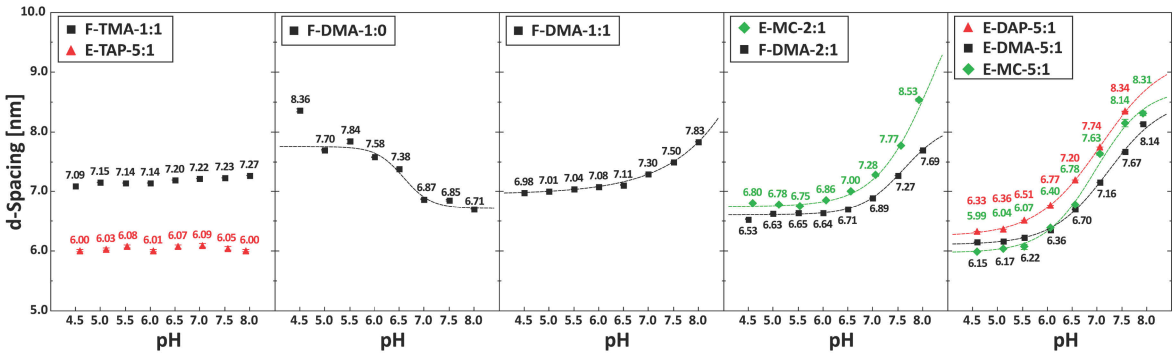

Figure 30. D-spacing calculated from the peak position of the first maximum for all formulations measured via SAXS. Sigmoidal (Boltzmann) fits (dashed lines) were calculated using QtiPlot, where applicable. Error bars represent the (propagated) errors from the peak fitting process. The increasing change in d-spacing with increasing ionizable lipid fraction (center panel to right panel) can be very well discerned.

As expected, lipoplexes comprising DODMA at an N/P ratio of 5:1 (E-DMA-5:1) showed decreasing d-spacing with decreasing pH and an even stronger overall shift (Δd~19 Å). A monotonously increasing relationship between the molar fraction of DODMA and the maximum pH-dependent d-spacing could be made out (see **Figure 31**), confirming the aforementioned dependency.

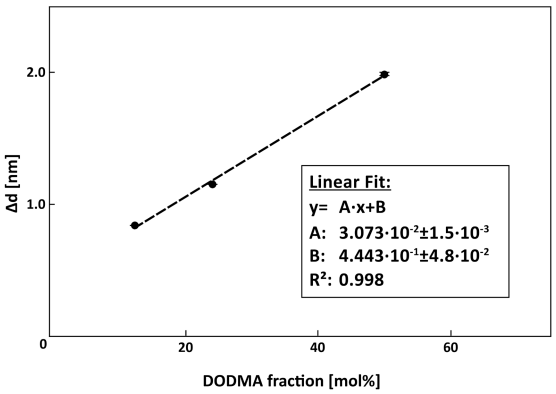

Figure 31. Monotonously increasing relationship between the molar fraction of DODMA and the maximum pH-dependent shift in d-spacing (Δd). The dashed line represents a linear fit of the experimental data.

Systems comprising either the ionizable lipid DODAP or its permanently charged homologue DOTAP showed the same characteristics as those containing DODMA or DOTMA, with the permanently charged system (E-TAP-5:1, **top left in Figure 28**) still showing no pH-responsive structural changes over the observed pH-range at this higher N/P ratio, and the DODAP containing system (E-DAP-5:1**, bottom right**) showing a strong sigmoidal shift in d-spacing from 63 Å at pH 4.5 to 83 Å at pH 7.5 (Δd~20 Å). Quite interestingly, E-DAP-5:1 also showed a complete absence of Bragg peaks and therefore an abrupt loss of correlated structure at pH 8.0, which had not been observed for the lipoplex system comprising DODMA. Again, the analysis of the repeat ratio confirmed the lamellar structure for E-DAP-5:1. For E-TAP-5:1, the experimental setup did not allow for the visibility of 2nd order Bragg peaks and therefore this analysis could not be performed.

When looking at those lipoplex systems that contained the commercially successful ionizable lipid DLin-MC3-DMA, two kinds of observations can be made. Firstly, systems containing 20 mol% of the ionizable lipid (E-MC-2:1) showed the same kind of structural changes previously observed for the other ionizable systems – a sigmoidal shift of d-spacing with increasing pH levels, with the shift in d-spacing amounting to approximately 17 Å. While the experimental setup did not allow for complete analysis of the 2nd order Bragg peak, the lamellar order could be confirmed for those pH-values where it was visible (e.g., pH 5.5). Samples comprising 50 mol% (E-MC-5:1) also showed the pH-dependent shift in d-spacing (Δd~21 Å), but in addition to this a transition in the shape of the main Bragg peak was visible (see **Figure 28, bottom center panel**). While a clear and relatively narrow Bragg peak could be made out at pH 4.5, this shifted towards a broader, more asymmetrical peak, until finally, at pH 8.0, barely any sign of this Bragg peak was visible at all. In contrast to the aforementioned abrupt loss of positional order for E-DAP-5:1, this effect was much more gradual and happened across the whole pH-range.

As already mentioned, and as is very well visible in **Figure 30**, the changes in d-spacing followed the sigmoidal behavior which is typical for pH-dependent processes. Therefore, sigmoidal (Boltzmann) fits were applied and the inflection points of these fits were defined as the conformational pH values. These conformational pH values were thought as similar to a pK_a value, but this time describing the pH around which the structural changes of these lipoplex systems occur. For E-MC-2:1, the measured peak position for pH 8.0 was not included in the fitting range, as including it in the fitting process produced nonsensical results. The resulting fits can be seen as dashed lines in **Figure 30** and the quantitative results are shown in **Table 14**.

N/P ratio	DOTMA	DODMA	DOTAP	DODAP	DLin-MC3-DMA
no mRNA	n.c.	6.6±0.2	-	-	-
1:2	-	-	-	-	-
1:1	-	7.7±0.1	-	-	-
2:1	-	7.5±0.1	-	-	7.4±0.5
5:1	n.c.	7.0±0.1	n.c.	6.8±0.1	6.8±0.1

Table 14. Conformational pH of lipoplexes (pH around which the structural changes of these lipoplex systems occur) calculated from sigmoidal fits of the scattering vector q of the first order Bragg peak over a pH-range of 4.5-8.0. Formulations not studied due to limitations in beam time are marked with "–" and measurements where no meaningful Boltzmann fit could be applied are marked as "n.c." (not calculated).

A trend towards lower conformational pH values with increasing N/P-ratios can clearly be made out both for samples comprising DODMA as well as for those comprising DLin-MC3-DMA. This shows, that increased acidification is needed to change the lipoplex structure when more ionizable lipid is included in the formulations. This is in strong contrast to just measuring the pk_a value of an ionizable lipid, which would be independent of the amount of lipid used. Therefore, the choice of ionizable lipid is not the only variable to be taken into consideration when designing an ionizable formulation for a specific target. This is discussed in chapter 4.2.2.

In addition to the d-spacing, the pH-dependency of the Bragg peak width, which corresponds to the correlation length, was also examined to gain further insight into the observed changes in peak shape. As already suspected from the qualitative peak description, F-DMA-1:0 and E-MC-5:1 showed the strongest changes concerning peak width, as can be seen in Figure 32 (panels A and B). As increasing peak width comes from the loss of long-range order, the effect of the repulsive interactions from positively charged DODMA molecules at low pH, with no mRNA to screen these charges, can be very well discerned. While the correlation length at pH 8.0 was around 80 nm (representing approximately 12 bilayers at a d-spacing of 67 Å) and was therefore in the range of that displayed by DODMA-based lipoplexes comprising mRNA, the correlation length decreased to around 20 nm at pH 4.5, confirming the loss of long-range order perpendicular to the bilayer plane (panels C and E). Samples comprising 50 mol% of DLin-MC3-DMA showed the opposite trend, displaying a constant decrease in correlation length with increasing pH. This decrease went from approximately 35 nm correlation length at pH 4.5 down to the range of the determined d-spacing at pH 8.0, implying that these lipoplexes were in average only made up of one bilayer structure that complexed the mRNA at high pH (panels D and E). Interestingly, all other studied systems showed higher average bilayer numbers in the range of 7-30 bilayers, with no obvious pH-dependent trends, making it possible that this effect might contribute to the very strong transfection efficacy of systems comprising high contents of DLin-MC3-DMA previously shown in certain settings, such as hepatic targeting.[85,145]

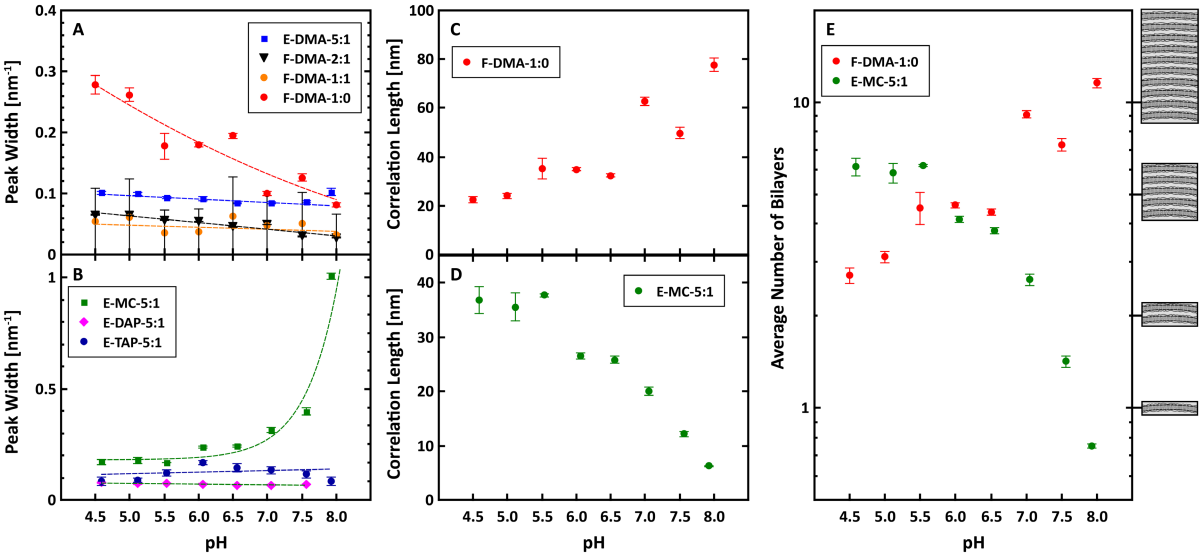

Figure 32. (A, B) Peak width vs pH for the first order Bragg peak of lipoplexes measured by SAXS, as determined from the Lorentz fit analysis. Error bars represent the propagated errors from the peak fitting process. Dashed lines are meant as a guide to the eye and do not represent the fitting of a physical model. (A) Samples comprising DODMA. (B) Other samples with an N/P of 5:1. (C, D) Correlation length vs pH calculated from the peak width for F-DMA-1:0 and E-MC-5:1. (E) Average number of bilayers per lipoplex vs pH calculated from the correlation length and the d-spacing for F-DMA-1:0 and E-MC-5:1 (correlation length divided by d-spacing).

The long-range particle order (measured as correlation length) decreases at lower pH for the sample comprising no mRNA (F-DMA-1:0, panel C) due to repulsive interactions between unscreened positive DODMA charges. The formulation comprising 50 mol% DLin-MC3-DMA (E-MC-5:1, panel D) at an N/P ratio of 5:1 shows a trend in the opposite direction, while formulations containing other ionizable lipids at the same N/P ratio do not show any major changes at all. This responsivity in particle structure to changes in environmental pH levels might be a reason why systems comprising high contents of DLin-MC3-DMA have previously shown very strong transfection efficacy in hepatic targeting.

3.2.1.2 Structural Differences Between Lipoplexes and LNPs

While the lipoplex systems discussed in the previous chapters are well suited for structural model generation due to their simple composition consisting only of helper lipid, cationic or ionizable lipid, and mRNA, recent clinical advancements have mainly been made with so-called lipid nanoparticles (LNPs), which typically also contain cholesterol or cholesterol-derivates and stealth-functionalized lipids, such as PEG-lipids (lipids with covalently bound polyethylene glycol (PEG)) in addition to the aforementioned lipids and the mRNA. To gather insights on the structural changes occurring within the particle systems when incorporating these new components, lipoplex (LPX), LNP, and intermediate (IM) formulations were prepared, with the latter including one of the extra components (cholesterol or stealth-lipid), but not both. DOPC and DODMA were chosen as the helper and ionizable lipid, respectively, and the N/P ratio was kept at 5:1 to maintain comparability to the lipoplex systems analyzed in the previous chapters. Samples were prepared both with the manual protocol and the classic ethanol injection and utilizing two different stealth-functionalized lipids – one based on PEG and one utilizing polysarcosine (pSar) as the hydrophilic chain. For the latter, MC12-50 was chosen since its hydrophilic chain length contains 44 sarcosine monomers (as determined by NMR), which makes it comparable to the 45 ethylene glycol monomers of the commonly used PEG-lipid C16-PEG2000-Ceramide. mRNA with a length of approximately 1900 nucleotides (R159) was used for all physicochemical characterization. The detailed sample compositions and the respective preparation method used are shown in Table 15.

Sample	Helper Lipid	[mol%]	Ionizable Lipid	[mol%]	Cholesterol [mol%]	Stealth Lipid	[mol%]	mRNA [mol%]	N/P	Prep.
LPX-01	DOPC	50	DODMA	50	0	-	0	10	5	MP
LPX-02										Inj.
LNP-03	DOPE	10	DODMA	40	48	PEG	2	8		MP
LNP-04						pSar				MP
LNP-05	DOPC					PEG				MP
LNP-06						pSar				MP
LNP-07	DOPE		DLin-MC3-DMA			PEG				MP
LNP-08						pSar				MP
LNP-09	DOPC					PEG				MP
LNP-10						pSar				MP
LNP-11	DOPE	10	DODMA	40	48	pSar	2	8		Inj.
IM-13	DOPE	48	DODMA	50	0	PEG	2	10		MP
IM-14						pSar				MP
IM-15		10			40	-	0	10		MP

Table 15. Formulation compositions of the lipoplexes and LNPs used for investigating structural influences and differences. LPX=lipoplex; LNP=lipid nanoparticle; IM=intermediate particle; PEG=C16-PEG2000-Ceramide; pSar=BA12-50; Prep.=preparation method; MP=manual protocol; Inj.=Injection method.

3.2.1.2.1 Particle Size and Zeta Potential

Particle diameters of LNPs prepared with the manual protocol were reproducibly in the range of 200 to 400 nm, with their polydispersity indices mostly under 0.3 (with the exception of LNP-05, see Figure 33). All formulations showed positive zeta potentials above 25 mV due to the strong excess of ionizable lipid compared to the mRNA (N/P 5:1). Intermediate formulations prepared without stealth lipids but including cholesterol (IM-15) did not result in defined particles but in visually agglomerated lipid clumps (not measurable in DLS). Intermediate formulations without cholesterol but comprising stealth-lipids, however, produced defined, positively charged particles without problems, albeit being a bit less reproducible for those containing the PEG-lipid C16-PEG2000-Ceramide (IM-13). Compared to the lipoplexes discussed in the previous chapter, one can see that the particle diameters were in a similar size range and that the PDIs of the LNPs were slightly higher but still below the aforementioned value of 0.3, which is widely accepted as the acceptable limit for pharmaceutical applications.[47]

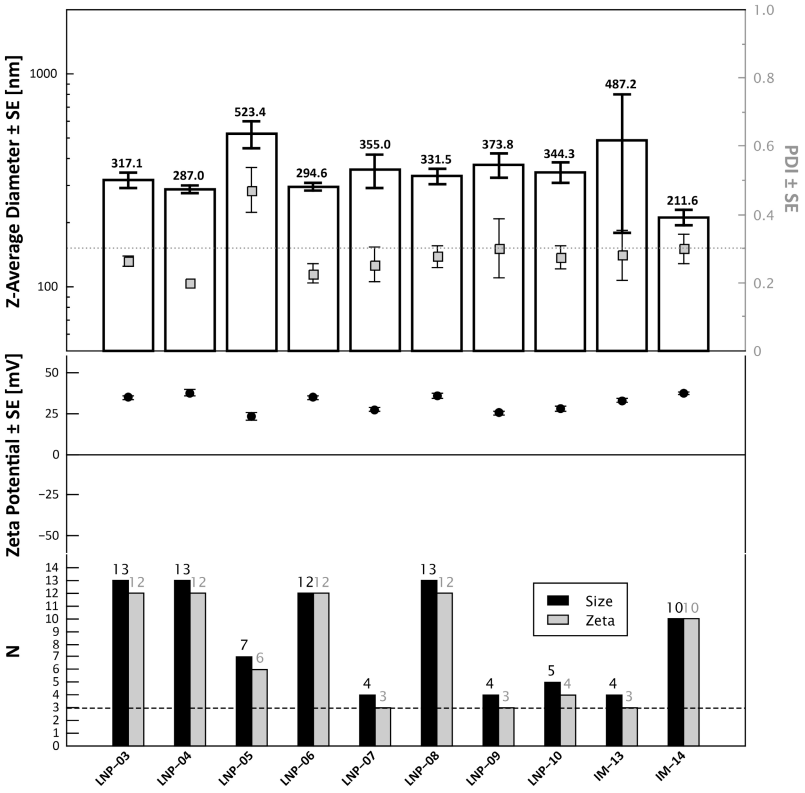

Figure 33. Size (top, bar chart, left y-axis), PDI (top, scatter plot, right y-axis), zeta potential (middle), and number of measurements (N, bottom) for a selection of investigated LNPs and intermediate formulations.

3.2.1.2.2 Small Angle X-Ray Scattering

All samples discussed in this subchapter were prepared at 10 mg/mL total lipid except where explicitly stated otherwise and measured with the instrumental parameters described as "Setup 4" in the methods section (see chapter 2.2.4.7.1). The measurement concentration of 5 mg/mL was achieved by mixing 1:1 with 10 mM GG.

Before the investigation of their structural differences described below, it was also tested whether using the classic ethanol injection or the manual protocol made a difference on the resulting particle properties and structures of both lipoplexes and LNPs. Therefore, two pairs of formulations comprising the ionizable lipid DODMA were prepared with each method, while keeping their molecular composition constant (LPX-01 / LPX-02 and LNP-04 / LNP-11). Figure 34 shows their scattering curves, as well as the d-spacing and correlation length calculated from Lorentz fitting of the main Bragg peaks at around 1 nm^{-1}. Lipoplexes prepared via the ethanol injection method (LPX-02, orange) showed a sharper peak and a second order Bragg peak was visible much more clearly, indicating a higher order and verifying the presence of a lamellar internal structure due to their integer repeat ratio. The higher order was also confirmed by their much higher correlation length (~150 nm) in comparison to the same lipoplex formulation prepared with the manual protocol (LPX-01, navy blue, ~80 nm). Lipoplex formulations prepared via the ethanol injection method were also more easily reproducible and showed more monodisperse and controlled particle sizes (DLS data not shown). Interestingly, while there was an obvious influence on the long-range order of the particles (in terms of correlation length), the inter-bilayer spacing (d-spacing) stayed approximately the same (64-65 Å) between the two manufacturing methods and therefore does not seem to be influenced by the choice of preparation method, but only by other parameters such as the N/P ratio or the pH. For the LNP formulation, no effect of the preparation method was found. Visually, the scattering curves looked the same and

analysis of the peak data showed that there was no difference in d-spacing or correlation length for LNPs prepared via the ethanol injection method (LNP-11, purple) or the manual protocol (LNP-04, red). Size characteristics were also very similar, indicating that the formation process of the LNPs is purely determined by electrostatic interactions and other molecular processes, but independent of the preparation protocol. Therefore, it was decided to continue the experiments with LNPs prepared with the manual protocol, as it has several advantages over the classic injection method, such as the elimination of glass ware (only single use, nuclease-free material can be used) and the ability to handle smaller sample volumes.

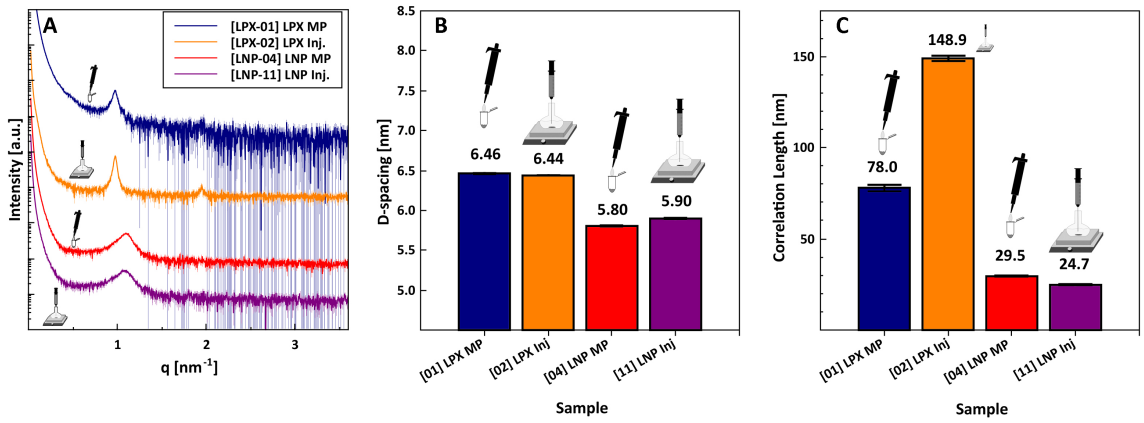

Figure 34. SAXS Scattering curves (A), d-spacing (B), and correlation length (C) of lipoplexes and LNPs prepared with either the ethanol injection method (orange, purple) or the manual protocol (navy blue, red). The intensities of the scattering curves are shifted vertically for visual clarity and only shown in the relevant q-ranges.

Next, the structural transition from a classic lipoplex formulation to a modern LNP formulation was investigated. For this, the already mentioned DOPC/DODMA based lipoplex formulation prepared via the manual protocol (LPX-01) was compared to very similar "intermediate" particles containing the additional stealth moiety C16-PEG2000-Ceramide (IM-13) or the polysarcosine (pSar) lipid BA12-50 (IM-14) and to LNPs comprising DOPC, DODMA, C16-PEG2000-Ceramide or BA12-50, and cholesterol (LNP-05 and LNP-06, respectively). As mentioned above, a comparison to intermediates containing helper lipid, ionizable lipid, and cholesterol was not possible due to their extreme aggregation. Figure 35 shows the results from the scattering experiments.

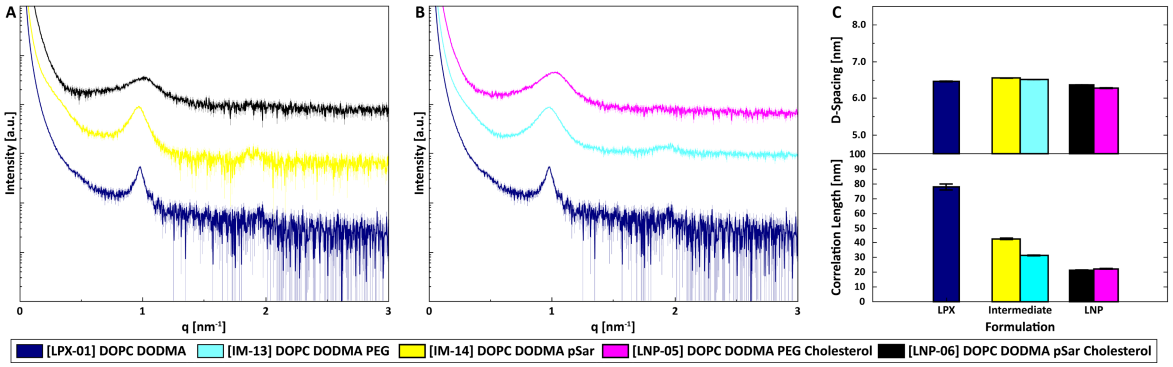

Figure 35. Transition from lipoplexes to LNPs. The intensities of the scattering curves are shifted vertically for clarity. (A) Transition of formulations utilizing pSar from lipoplexes prepared via the manual protocol (LPX-01, navy blue) over intermediate systems (IM-14, yellow) to LNPs (LNP-06, black). (B) Transition of formulations utilizing PEG from lipoplexes prepared via the manual protocol (LPX-01, navy blue) over intermediate systems (IM-13, cyan) to LNPs (LNP-05, magenta). (C) Calculated d-spacing and correlation lengths. While the d-spacing stayed the same for all formulations, a clear loss of order can be seen in the scattering curves and from the calculated correlation length.

As already discussed above, the study of the lipoplex formulation (blue scattering curve) revealed a highly ordered lamellar structure with a d-spacing of approximately 65 Å. Addition of the stealth component (pSar- or PEG-lipid) led to a broader main Bragg peak with a still visible, but weaker, 2nd order peak (yellow and cyan scattering curves). While this did not influence the inter-bilayer spacing, it indicates a loss of long-range order which could be seen as a clear decrease in correlation length. Addition of cholesterol (leading to a much lower fraction of DOPC and a small decrease in DODMA) continued this trend. The main Bragg peak became even broader and a 2nd order peak was barely visible in the scattering curves. Only a very small change in d-spacing could be determined ($\Delta d \sim 2$ Å), but the correlation length decreased again, resulting in approximately half of that of the lipoplex formulation (Figure 35, C).

In summary, LNPs are characterized by a strong decrease in internal order while displaying the same values of d-spacing as comparable (same N/P) lipoplex systems. This decrease seems to be induced both by the addition of stealth-lipids and by the incorporation of cholesterol, and the latter is not possible without the former. In contrast to lipoplex systems, the low order is independent of the preparation method used, when comparing classic ethanol injection and the manual protocol.

3.2.1.3 Lipid-Variation and pH-Responsive Structural Changes of LNPs

After establishing the structural changes occurring during the transition from lipoplexes to LNPs, the structural influences caused by varying the LNPs' components and exposure to changes in the environmental pH levels were investigated. In a first set of experiments, LNPs were prepared via the manual protocol and a "standard" formulation comprising DOPE, DODMA, cholesterol, and the pSar lipid BC12-50 (LNP-04) was defined. Then, all components were systematically exchanged – the helper lipid (DOPE vs DOPC), the ionizable lipid (DODMA vs DLin-MC3-DMA), and the stealth moiety (pSar- vs PEG-lipid) – and the resulting LNPs were analyzed in the preparation buffer (10 mM GG) as well as after mixing with varying pH buffers in terms of particle size, mRNA incorporation, apparent formulation pK_a, and internal structural changes. The full sample compositions can be seen in Table 15. Those formulations, which differed from the standard formulation LNP-04 only by the exchange of one component each (LNP-03, LNP-06, LNP-08, and IM-14), are referred to throughout this chapter as the "main" formulations.

3.2.1.3.1 Reproducibility (Size, Zeta Potential, and mRNA Incorporation)

Figure 33 shows the particle size, PDI, and zeta potential reproducibility for at least three independent preparations each. As mentioned, all particle sizes (with the exception of LNP-05) were reproducibly in the range of 200-400 nm, with PDIs below 0.3, and positive zeta potentials. No systematic difference in size could be discerned when switching between the different lipid components.

Additionally, it was tested whether the hydrophilic chain length of the polysarcosine lipid has an influence on the particle size, as it is thought to stabilize the particle. PEG-lipids with hydrophilic chain lengths of approximately 45 ethylene glycol units (such as C16-PEG2000-Ceramide) are commonly used for the preparation of LNPs. Polysarcosine lipids with chain lengths of 26, 44, 61, and 77 sarcosine monomers on average (MC12-25, MC12-50, MC12-75, and MC12-100, respectively) were used for the formulation of three independent preparations each of LNPs comprising DOPE, DODMA, cholesterol, mRNA, and the pSar-lipid (10:50:38:10:2 mol%) and their particle diameter and polydispersity index was measured (see Figure 36, left panel). The results show that the incorporation of MC12-25 did not lead to LNPs in the desired size range, while MC12-50, MC12-75, and MC12-100 all led to reproducible particle sizes between 200 and 300 nm, with PDIs below 0.3, and a small, but insignificant, trend to smaller particle sizes with longer chain lengths. Therefore, it was decided that the use of MC12-50 as a comparable alternative to C16-PEG2000-Ceramide was justified.

Another important quality parameter is the incorporation of the mRNA cargo. To determine the amount of incorporated mRNA, Ribogreen® assays and agarose gel electrophoresis were performed before and after incubation of the LNP formulations with Triton X-100. Figure 36 (right panel) shows the incorporation rates of three independent preparations of the main LNP formulations each (batches used for the *in vitro* PBMC assay in chapter 3.2.2.2) and Figure 37 shows an agarose gel of these formulations.

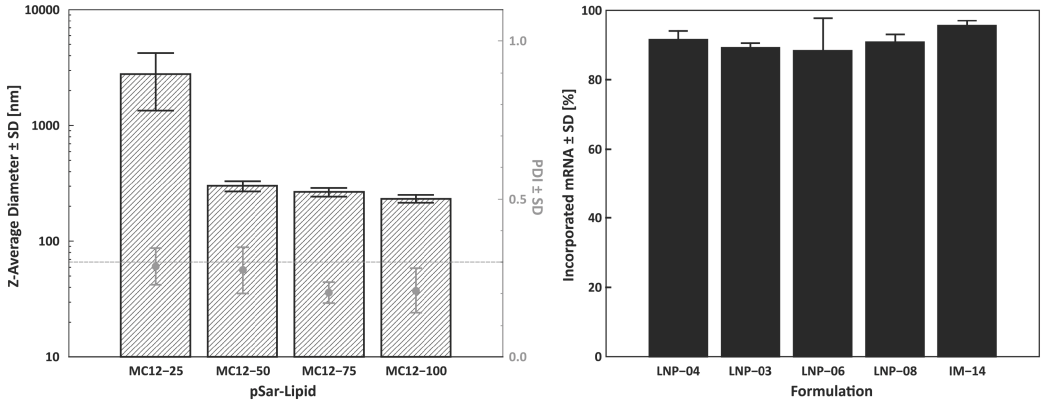

Figure 36. Left panel: Particle diameter (bars, left y-axis) and PDI (scatter plot, right y-axis) of variations of LNPs comprising DOPE, DODMA, cholesterol, mRNA, and pSar-lipids with chain lengths from 25 to 100 sarcosine monomers (10:50:38:10:2 mol%, N=3). Right panel: Incorporated mRNA determined by Ribogreen® assay for the main LNP preparations used in the *in vitro* experiments (N=3).

As can be seen from the Ribogreen® assay, mRNA incorporation rates of approximately 90% or higher were reproducibly reached for all of the main formulations. The agarose gel image confirms the incorporation of the intact mRNA without degradation (no free mRNA without Triton-X and mRNA of the correct length after incubation with Triton-X), making these formulations suitable for further characterization of both physicochemical and biological nature.

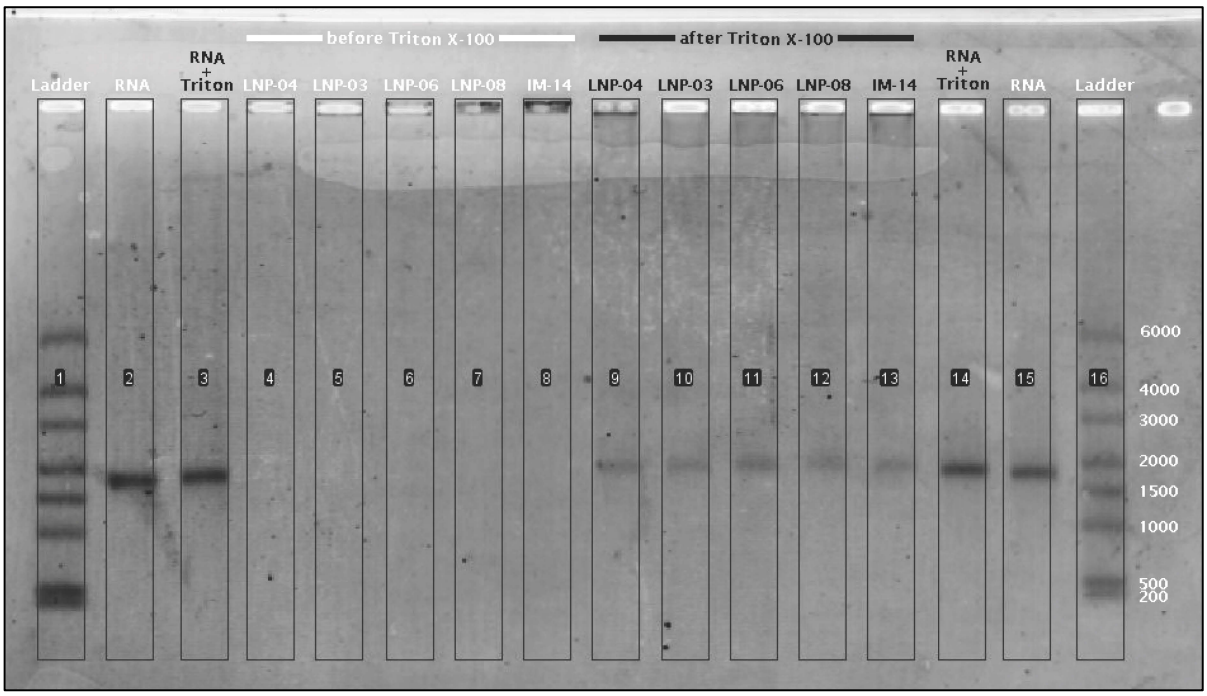

Figure 37. Agarose gel of the main LNP formulations before (lane 4-8) and after (lane 9-13) incubation with Triton X-100. Lanes 1&16, 2&15, and 3&14 were loaded with the RNA ladder, pure mRNA, and pure mRNA incubated with Triton X-100, respectively.

3.2.1.3.2 pK_a-Determination (TNS-Assay)

Again, the TNS assay was performed to determine the apparent formulation pK_a. All formulations were examined as at least three independent preparations, measured in triplicates each. For three formulations (LNP-04, LNP-10, IM-14), one of the first three preparations showed a differing pK_a calculated from the Boltzmann fit, therefore a fourth run was performed for these formulations to gain more statistical safety and rule out the possibility of an outlier. The results from the assay are shown in Figure 38.

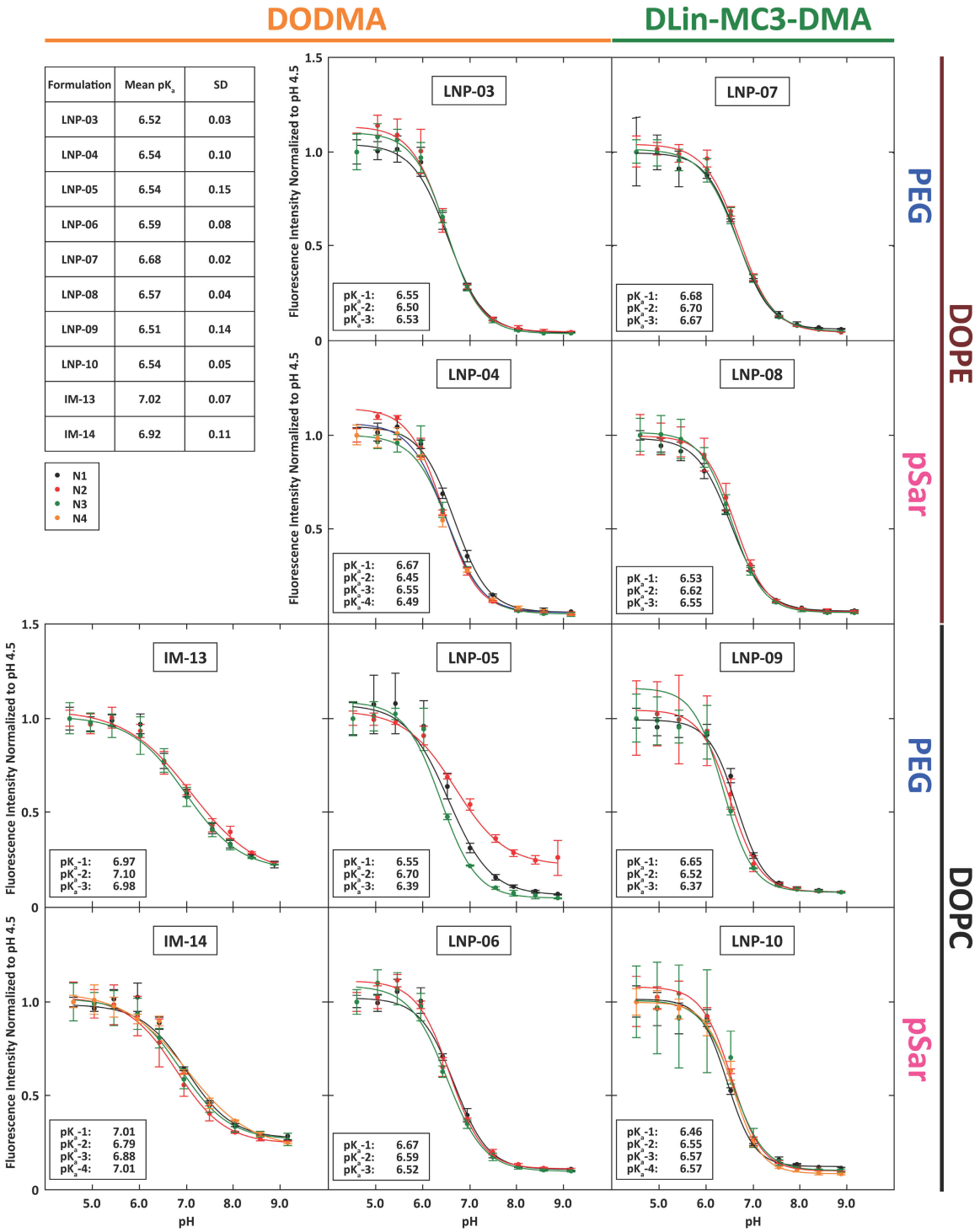

Formulation	Mean pK_a	SD
LNP-03	6.52	0.03
LNP-04	6.54	0.10
LNP-05	6.54	0.15
LNP-06	6.59	0.08
LNP-07	6.68	0.02
LNP-08	6.57	0.04
LNP-09	6.51	0.14
LNP-10	6.54	0.05
IM-13	7.02	0.07
IM-14	6.92	0.11

Figure 38. TNS assay of LNPs and intermediate formulations at an N/P ratio of 5:1. The data is shown as fluorescence intensity (±SD) normalized to the intensity at pH 4.5 for triplicate measurements of three or four independently prepared formulations (black, red, green, orange) each. The curves depict sigmoidal (Boltzmann) fits of the experimental data.

A statistical analysis using a paired t-test was performed. Each pair was formed by two formulations that had the same overall composition apart from the tested variation (e.g., DOPC vs DOPE), resulting in four pairs each (five pairs for PEG vs pSar due to the IM-formulations). Quite interestingly, no significant differences in formulation pK_a could be discerned. All LNP formulations showed almost the same apparent pK_a of approximately 6.6±0.1. Intermediate formulations showed slightly higher apparent pK_a values at 6.9 and 7.0, despite them comprising a higher molar fraction of ionizable lipids. Also, their decrease in fluorescence with increasing pH was lower than that of all LNP formulations, seemingly showing them as less responsive to the TNS assay.

3.2.1.3.3 Small Angle X-Ray Scattering

Small angle X-ray scattering was performed on the samples stated in Table 15 with the experimental conditions stated under "Setup 4" in the methods section (see chapter 2.2.4.7.1). Samples were prepared at a concentration of 10 mg/mL total lipid and then mixed with either 10 mM GG or pH buffers to achieve a measurement concentration of 5 mg/mL. In addition, a second set of samples was prepared at 1 mg/mL and measured directly, to rule out any concentration dependent structural effects. The full set of scattering curves can be seen in the supplementary data (see Suppl. Fig. 3 & 4 in chapter 7.4.7).

As expected from the results in chapter 3.2.1.2.2, all LNP formulations showed a single Bragg peak at around 1.0 nm^{-1}, which was broader than that previously observed for lipoplexes. Lorentz fitting of these Bragg peaks was performed, as for all other samples before. The results can be seen in Table 16.

pH	LNP-03 d-spacing [nm]	LNP-03 CorrL [nm]	LNP-04 d-spacing [nm]	LNP-04 CorrL [nm]	LNP-05 d-spacing [nm]	LNP-05 CorrL [nm]	LNP-06 d-spacing [nm]	LNP-06 CorrL [nm]	IM-13 d-spacing [nm]	IM-13 CorrL [nm]
GG	5.77±0.00	30.02±0.20	5.80±0.00	29.46±0.34	6.28±0.00	22.21±0.18	6.37±0.01	21.38±0.39	6.51±0.00	31.47±0.18
4.76	5.55±0.00	31.54±0.19	5.61±0.00	25.31±0.19	5.97±0.00	23.42±0.24	5.96±0.00	24.56±0.41	6.09±0.00	21.83±0.14
5.57	5.67±0.00	26.64±0.23	5.67±0.00	23.84±0.20	-	-	6.16±0.01	21.21±0.45	-	-
6.53	5.84±0.00	31.79±0.21	5.88±0.00	29.29±0.23	-	-	6.58±0.01	19.77±0.29	-	-
7.56	7.30±0.04	2.42±0.62	7.85±0.03	7.23±0.16	-	-	7.25±0.15	11.62±1.53	-	-
8.04	6.13±0.01	16.32±0.41	6.57±0.03	10.86±0.31	/	/	/	/	/	/
pH	LNP-07 d-spacing [nm]	LNP-07 CorrL [nm]	LNP-08 d-spacing [nm]	LNP-08 CorrL [nm]	LNP-09 d-spacing [nm]	LNP-09 CorrL [nm]	LNP-10 d-spacing [nm]	LNP-10 CorrL [nm]	IM-14 d-spacing [nm]	IM-14 CorrL [nm]
GG	5.55±0.00	28.85±0.23	5.56±0.00	30.91±0.57	5.83±0.00	24.70±0.19	5.81±0.00	26.49±0.37	6.56±0.00	42.59±0.54
4.76	5.14±0.00	26.20±0.28	5.15±0.00	30.03±0.31	5.46±0.00	33.79±0.25	5.47±0.00	35.60±0.24	6.11±0.00	28.27±0.49
5.57	-	-	5.22±0.00	40.20±0.34	-	-	5.49±0.00	38.06±0.32	6.18±0.00	32.50±0.68
6.53	-	-	5.55±0.00	30.85±0.31	-	-	5.93±0.01	30.88±0.77	6.61±0.00	38.90±0.71
7.56	-	-	6.33±0.03	11.93±0.50	-	-	/	/	8.16±0.01	17.61±0.35
8.04	5.75±0.01	18.46±0.51	6.10±0.02	30.91±0.57	6.29±0.05	14.41±1.07	7.64±0.13	7.69±0.46	/	/

Table 16. SAXS peak fit data of LNPs in different media.; CorrL = correlation length; GG = 10 mM glycyl-glycine (pH 5.8); "-" = not measured; "/" = no peak suitable for Lorentz-fitting.

Several observations were made from the experimental data. All samples showed a clear responsiveness to changes in environmental pH, with the d-spacing increasing with increasing pH across all formulations. Additionally, a strong decrease of the long-range order for all samples was observed upon changing the pH from 6.5 to pH 7.6. Quantitatively, the change in d-spacing between pH 4.8 and pH 7.6 ranged from approximately 12 Å (LNP-08) to about 21 Å (LNP-04).

No difference in d-spacing or correlation length was observed between samples comprising the pSar-lipid MC12-50 (LNP-04/06/08/10) and samples comprising the PEG-lipid C16-PEG2000-ceramide (LNP-03/05/07/09). Samples comprising the ionizable lipid DLin-MC3-DMA (LNP-07/08/09/10) consistently showed lower d-spacing than their DODMA-based counterparts (LNP-03/04/05/06), with the former having a 5-10% lower d-spacing on average. Samples comprising DODMA, however, showed lower correlation lengths than samples based on DLin-MC3-DMA. Comparing the helper lipid DOPE (LNP-03/04/07/08) to DOPC (LNP-05/06/09/10), one can clearly see that formulations comprising

DOPC had a higher d-spacing than those comprising DOPE, with the difference in d-spacing ranging from 2.7 Å to 5.2 Å in 10 mM glycylglycine and even larger differences when subjected to pH-changes. Again, the samples with the higher d-spacing (DOPC-based) showed lower correlation lengths. Additionally, the scattering curves of DOPC-based samples displayed more asymmetric Bragg peak shapes than their counterparts.

To further delve into these systematic differences, a statistical analysis using a paired t-test was performed (see Figure 39). Each pair was formed by two samples that had the same overall composition apart from the tested variation (e.g., DOPC vs DOPE) and were measured at the same pH, resulting in 14 pairs (15 pairs for PEG vs pSar). This statistical analysis confirmed the differences in d-spacing described above, showing high significances ($p<0.01$) or, in the case of the d-spacings of LNPs comprising DODMA vs those comprising DLin-MC3-DMA, even very high significances ($p<0.0001$) for the compared sample variations across all pH levels. The latter comparison also confirmed highly significant differences between the correlation lengths of LNPs comprising DODMA and those comprising DLin-MC3-DMA. No significant difference could be shown for both d-spacing and correlation length when comparing samples comprising the PEG-lipid to those comprising the pSar-lipid, however.

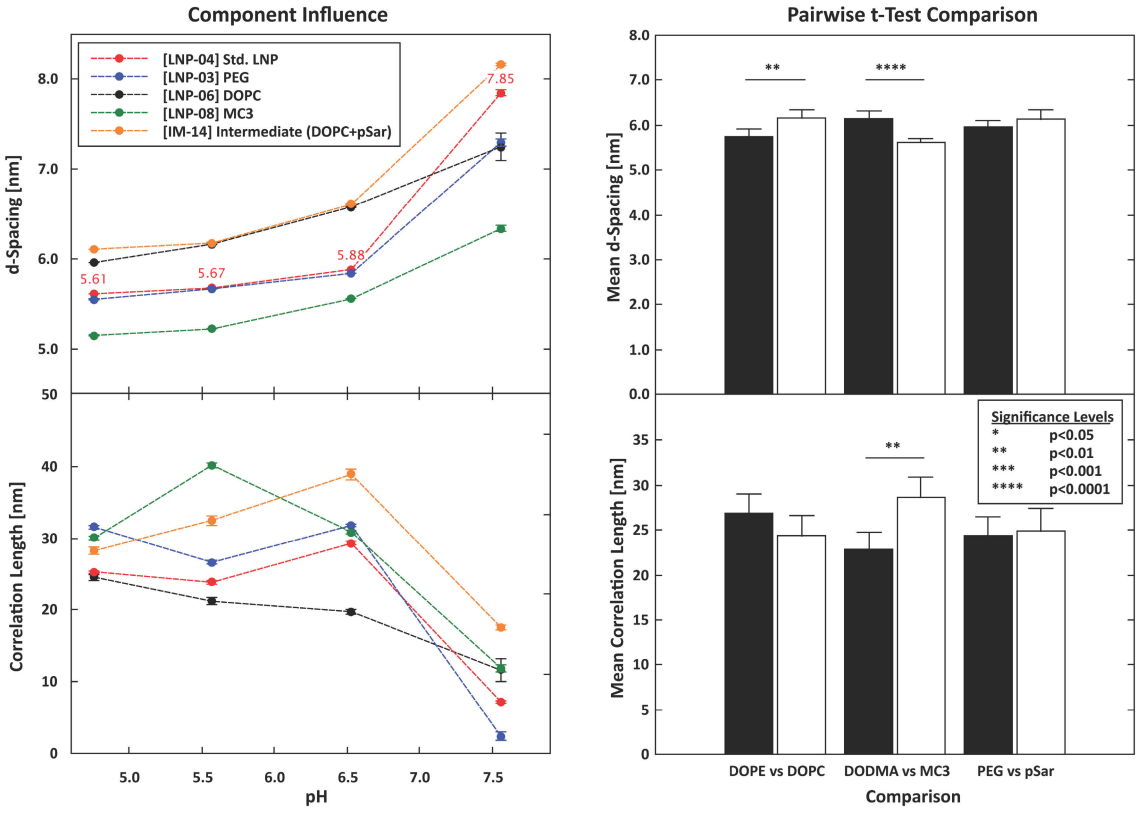

Figure 39. Bragg peak analysis of the main LNP samples. Left panels: Starting from the standard formulation (LNP-04, red), either the helper lipid (LNP-06, black), ionizable lipid (LNP-08, green), or the stealth moiety (LNP-03, blue) was exchanged. The DOPC-based intermediate formulation (IM-14, yellow) is also shown for comparison. Peaks at pH 8.0 are not included due to problematic peak fitting caused by flattening of the peaks. Right panels: Paired t-test analysis of the components' influence on d-spacing and correlation length across all samples at all pH-values where a pair could be formed from the performed measurements. Pairs were formed from samples that differed in the stated component, but were identical in their remaining composition (e.g., DOPE/DODMA/pSar at pH 5.5 vs DOPC/DODMA/pSar at pH 5.5). The data is presented as mean±SE and N=14 (15 for PEG vs pSar).

In addition to analyzing the Bragg peak characteristics for these samples, an exponential decay function was fitted to all scattering curves in the q-range of 0.03-0.175 nm^{-1} to determine the Porod-slope, as described in chapter 2.2.6.1. The results are stated in Table 17.

pH	LNP-03 slope	LNP-04 slope	LNP-05 slope	LNP-06 slope	IM-13 slope
GG	4.03±0.02	3.90±0.02	4.01±0.01	3.89±0.02	3.44±0.02
4.76	3.83±0.03	3.55±0.01	3.85±0.02	3.46±0.02	3.69±0.03
5.57	4.10±0.01	4.13±0.01	-	4.23±0.02	-
6.53	4.05±0.01	4.06±0.01	-	4.05±0.01	-
7.56	3.81±0.01	3.91±0.01	-	4.03±0.01	-
8.04	3.78±0.01	3.98±0.01	3.91±0.01	4.08±0.01	3.55±0.01
pH	LNP-07 slope	LNP-08 slope	LNP-09 slope	LNP-10 slope	IM-14 slope
GG	3.78±0.01	3.59±0.01	3.83±0.01	3.53±0.01	3.24±0.03
4.76	3.64±0.02	3.22±0.02	3.66±0.02	3.72±0.03	3.24±0.02
5.57	-	3.31±0.02	-	3.67±0.02	3.43±0.01
6.53	-	3.81±0.01	-	3.68±0.02	3.46±0.01
7.56	-	3.67±0.01	-	3.73±0.03	3.48±0.02
8.04	3.68±0.01	3.74±0.01	3.89±0.01	3.74±0.03	3.43±0.01

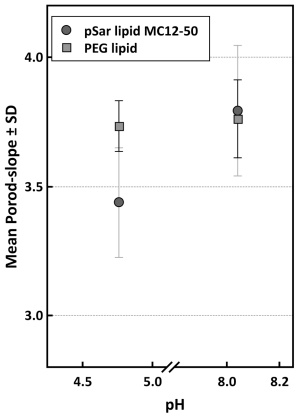

Table 17 and Figure 40. Porod-slopes determined by fitting an exponential decay function in the q-range of 0.03-0.175 to the scattering curves of LNPs. The figure illustrates the difference in pH-responsiveness between samples comprising the pSar lipid MC12-50 (LNP-04/06/08/10 and IM-14) and those comprising the PEG lipid C16-PEG2000-Ceramide (LNP-03/05/07/09 and IM-13) by comparing their mean Porod-slopes at pH 4.76 and pH 8.04. Only formulations comprising the pSar-lipid display a trend towards higher surface roughness (lower Porod-slopes) at acidic pH.

As explained in the methods section, Porod-slopes around 4 are indicative of a smooth particle surface, while a slope of 3 indicates a rough particle surface. Taking this into account, several observations can be made: Firstly, formulations comprising the pSar-lipid MC12-50 (LNP-04/06/08/10 and IM-14) displayed a trend towards higher Porod-slopes – and therefore smoother particle surfaces – with increasing pH, while those comprising PEG (LNP-03/05/07/09 and IM-13) did not seem to react to pH changes in this regard (as illustrated in Figure 40). Additionally, pairwise two-sample t-tests of the Porod-slopes in 10 mM GG showed significantly ($p<0.05$) less smooth surfaces for pSar- and MC3-comprising formulations compared to those comprising PEG and DODMA, respectively (N=5, N=4), while no significant impact seems to come from the selection of the helper lipid (N=4, Figure 41, A-C). When comparing pairs at all buffer conditions however (N=18), no significant changes between PEG and pSar could be detected anymore (Figure 41, D). This could be due to the first observation made above, as it leads to pSar particles showing higher surface smoothness at high pH and lower surface smoothness at low pH when compared to the PEG-containing samples. For the comparison of the ionizable lipids, the increase in sample size meant an increase in significance ($p<0.001$) for the already observed higher particle smoothness of DODMA-comprising LNPs, while still no difference between the helper lipids could be detected (N=18, Figure 41, F and E, respectively).

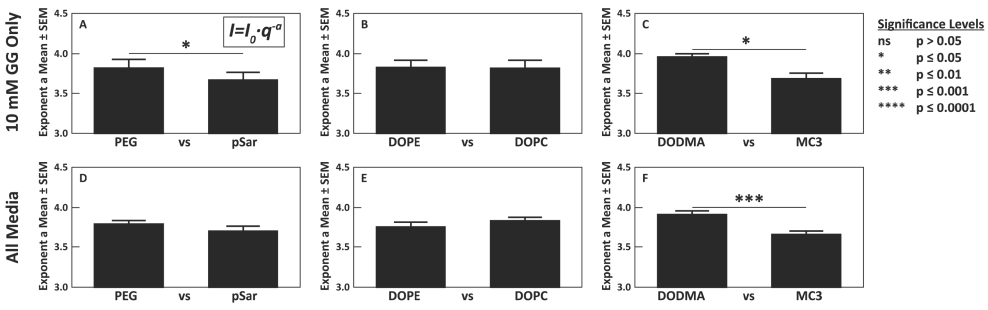

Figure 41. Pairwise two-sample t-test comparison of the Porod-slopes in the preparation buffer (A-C) and in all measured media (D-F). The Porod-slope is the value of the exponent "a" from the equation shown in the insert of panel (A).

Comparing all samples in 10 mM GG to their lower concentrated versions (see Suppl. Fig. 4 in chapter 7.4.7) showed stronger Bragg peak signals for the higher concentrated samples, as expected. However, other than some buffer over-subtraction issues at low q, no real difference could be seen, showing that these structural discoveries should apply both to formulations prepared at high concentrations needed for SAXS and those prepared at lower concentrations suitable for therapeutic applications.

3.2.1.4 Influence of the Helper Lipid / Cholesterol- and the N/P-Ratio on the LNP structure

While the first set of experiments on LNPs studied formulations with constant molar proportions, the second set of experiments was designed to elucidate the influence of varying the molar ratio of the helper lipid (DOPE) to cholesterol at different N/P ratios. All samples were prepared with the manual protocol and comprised DOPE as the helper lipid, cholesterol, and the polysarcosine lipid pSar-23 as the stealth moiety. Three different ionizable lipids – DPL-14, DLin-MC3-DMA, and DODMA – were used, N/P ratios of 0.65, 5, and 8 were prepared, and the cholesterol fraction was changed from 0-50% in 10% steps for each N/P ratio. Additionally, one set of samples comprising DPL-14 was mixed on-site (directly before measuring) with a range of pH buffers from pH 4.5 to pH 7.4 (0.5 steps), while another set of samples was premixed with both pH-extremes – pH 4.5 and pH 7.4 – before shipping for the mail-in experiment, resulting in their measurements being performed 4 days after mixing. The mRNA R159 (~1900 nucleotides) was used for the preparation of all samples. The full sample compositions can be seen in Table 18 (pH-variation) and Table 19 (cholesterol- and N/P-variation).

Purpose	Sample ID	Ionizable lipid	Ionizable lipid fraction	Cholesterol fraction	DOPE fraction	pSar-23 fraction	mRNA fraction	N/P ratio	Comment
pH-variation on-site	071	DPL-14	25	50	20	5	5	5	mixed on-site with pH 4.5
	072								mixed on-site with pH 5.0
	073								mixed on-site with pH 5.5
	074								mixed on-site with pH 6.0
	075								mixed on-site with pH 6.5
	076								mixed on-site with pH 7.0
	077								mixed on-site with pH 7.4
	081		3.25	50	41.75			0.65	mixed on-site with pH 4.5
	082								mixed on-site with pH 5.0
	083								mixed on-site with pH 5.5
	084								mixed on-site with pH 6.0
	085								mixed on-site with pH 6.5
	086								mixed on-site with pH 7.0
	087								mixed on-site with pH 7.4
premixed pH 4.5 & 7.4	101	DPL-14	3.25	10	81.75			0.65	premixed pH 4.5
	102								premixed pH 7.4
	103			50	41.75				premixed pH 4.5
	104								premixed pH 7.4
	105		25	10	60			5	premixed pH 4.5
	106								premixed pH 7.4
	107			50	20				premixed pH 4.5
	108								premixed pH 7.4
	109		40	10	45			8	premixed pH 4.5
	110								premixed pH 7.4
	111			50	5				premixed pH 4.5
	112								premixed pH 7.4

Table 18. Sample composition of LNPs for the investigation into pH-responsiveness via SAXS. All fractions are given in mol%. The lipid fractions sum up to 100 mol%. The N/P ratio is calculated by dividing the ionizable lipid fraction by the mRNA fraction.

Purpose	Sample ID	Ionizable lipid	Ionizable lipid fraction	Cholesterol fraction	DOPE fraction	pSar-23 fraction	mRNA fraction	N/P ratio	Comment
N/P variation + cholesterol variation	001	DPL-14	3.25	0	91.75	5	5	0.65	
	002			10	81.75				
	003			20	71.75				
	004			30	61.75				
	005			40	51.75				
	006			50	41.75				
	007		25	0	70			5	N/P 5 with 25 mol% DPL-14
	008			10	60				
	009			20	50				
	010			30	40				
	011			40	30				
	012			50	20				
	013		40	0	55			8	N/P 8 with 40 mol% DPL-14
	014			10	45				
	015			20	35				
	016			30	25				
	017			40	15				
	018			50	5				
	019		40	0	55		8	5	N/P 5 with 40 mol% DPL-14
	020			10	45				
	021			20	35				
	022			30	25				
	023			40	15				
	024			50	5				
	025	DLin-MC3-DMA	3.25	0	91.75		5	0.65	
	026			10	81.75				
	027			20	71.75				
	028			30	61.75				
	029			40	51.75				
	030			50	41.75				
	031		25	0	70			5	
	032			10	60				
	033			20	50				
	034			30	40				
	035			40	30				
	036			50	20				
	037		40	0	55			8	
	038			10	45				
	039			20	35				
	040			30	25				
	041			40	15				
	042			50	5				
	043	DODMA	3.25	0	91.75			0.65	
	044			10	81.75				
	045			20	71.75				
	046			30	61.75				
	047			40	51.75				
	048			50	41.75				
	049		25	0	70			5	
	050			10	60				
	051			20	50				
	052			30	40				
	053			40	30				
	054			50	20				
	055		40	0	55			8	
	056			10	45				
	057			20	35				
	058			30	25				
	059			40	15				
	060			50	5				

Table 19. Sample composition of LNPs for the investigation into cholesterol- and N/P-variation via SAXS. All fractions are given in mol%. The lipid fractions sum up to 100 mol%. The N/P ratio is calculated by dividing the ionizable lipid fraction by the mRNA fraction.

3.2.1.4.1 Particle Size

Due to limitations in the amount of supplied lipid material, all samples were only prepared once and their size was measured via DLS. The results can be seen in Figure 42. Quite interestingly, an effect of the N/P ratio on the particle size can be seen. While almost all LNPs with positive charge ratios (N/P ratio > 1) showed particle diameters from 200-300 nm and low polydispersity, this was not the case for LNPs with the negative charge ratio (N/P = 0.65). These particles showed Z-averages of the particle diameter up to the 1 µm range and also displayed much higher polydispersity. When looking at the number distributions (not shown), this was explained by the presence of a small number of larger particles or aggregates, with the majority of the LNPs still in the 100-300 nm range.

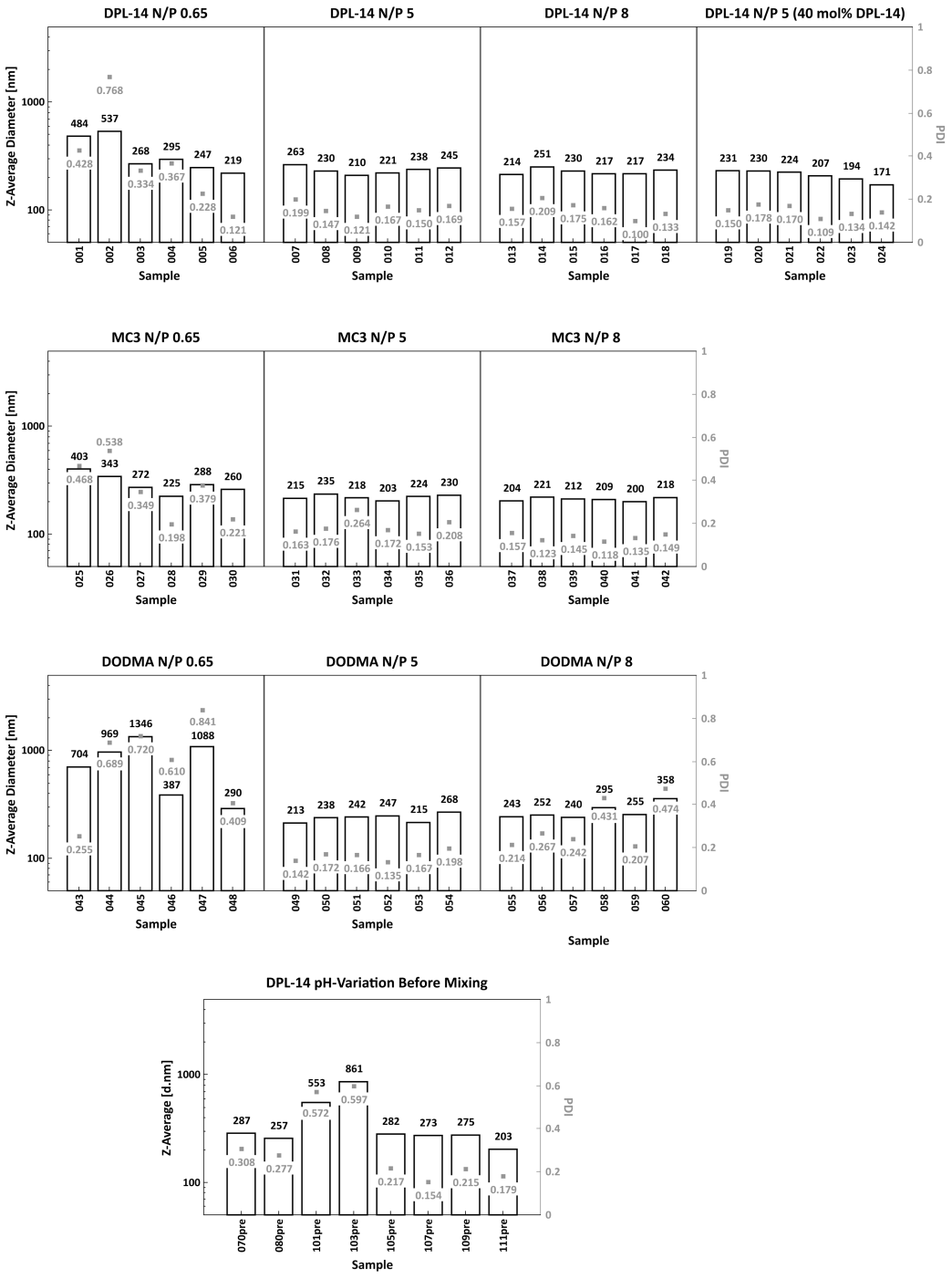

Figure 42. Particle diameter (Z-average, left y-axes) and polydispersity indices (PDI, right y-axes) for LNPs used in chapter 3.2.1.4.2. Samples named "-pre" were measured before mixing with their respective pH-buffer.

3.2.1.4.2 Small Angle X-Ray Scattering

Small angle X-ray scattering was performed on the samples stated in **Table 18** and **Table 19** with the experimental conditions stated under "Setup 5" in the methods section (see **chapter 2.2.4.7.1**). Samples were prepared at either 0.2 mg/mL mRNA (pH-variation) or 0.1 mg/mL mRNA (cholesterol- & N/P-variation) – equating to approximately 7-10 mg/mL or 2-5 mg/mL total lipid concentration, respectively – and either measured directly (cholesterol- & N/P-variation) or after mixing 1:1 with 150 mM pH buffer. The quantitative results from the curve fitting process can be found in the supplement (see **chapter 7.4.8**).
Figure 43 shows the resulting scattering curves from the cholesterol- & N/P-variation as well as the fit functions and parameters resulting from single- and multi-peak Lorentzian fitting. A more detailed view can be found in the supplement (**Suppl. Fig. 8 -Suppl. Fig. 10**). Just from looking at the scattering curves, one can already see that strong structural reorganizations took place within these systems, both from varying the N/P-ratio as well as from varying the cholesterol to DOPE ratio. Therefore, the peak analysis needs to be performed carefully and consistently across all systematic sample variations, in order to understand the trends visible here.

To ease the transition from previously studied systems, **LNPs with an N/P ratio of 5:1 were studied first**. One iteration of cholesterol variation from 0-50 mol% was performed for each ionizable lipid (DPL-14, DLin-MC3-DMA, and DODMA; **middle row or Suppl. Fig. 9**) comprising 25 mol% ionizable lipid each. One additional set, which contained 40 mol% ionizable lipid (and 8 mol% mRNA; samples 019-024; see **Figure 45**), was performed for DPL-14, as this was the molar fraction of ionizable lipid used in the previous chapters. A visualization of the DOPE content for all samples can be seen in **Figure 44**.
As with the LNPs studied previously, all systems with an N/P of 5:1 displayed a **main Bragg peak at around 1.05 nm^{-1} (blue fit)** – corresponding to a d-spacing of approximately 6 nm – at all cholesterol concentrations. For samples comprising DODMA or DLin-MC3-DMA, this peak's area decreased with increasing cholesterol fractions (decreasing DOPE fractions), suggesting its origin to be DOPE-dependent. For samples comprising 25 mol% DPL-14, this decrease in main Bragg peak area was visible from 10 to 40 mol% cholesterol, while the trend was visible over the whole cholesterol range for those containing 40 mol% DPL-14.
Additionally, **a peak shoulder (orange fit) to the right of the main Bragg peak** appeared with increasing cholesterol fractions for all ionizable lipids, but was not visible at 40 mol% DPL-14. This peak appeared at around 1.4 nm^{-1} and moved towards higher q (~1.7 nm^{-1}) with increasing cholesterol fractions. For samples comprising DODMA, this peak then disappeared at 40 and 50 mol% cholesterol, however, this might also be due to the signal being too weak to be detected over the noise at higher q. Notably, this peak already appeared at 0 mol% cholesterol for DODMA comprising samples, while it only started to appear at 10 and 20 mol% for DLin-MC3-DMA and DPL-14, respectively. The change in peak position translates to an approximate decrease in d-spacing of about 1 nm (from 4.8 to 3.8 nm) with increasing amounts of cholesterol.
A very interesting observation was made at 0-10% cholesterol (70-60% DOPE) for samples comprising the ionizable lipid DLin-MC3-DMA. Here, **two small peaks (cyan fit) in the q-range of 1.8-2.1 nm^{-1}** are visible (**marked with blue arrows**). Lorentz fitting revealed their position to be at $\sqrt{3}\cdot$ and $\sqrt{4}\cdot$ the position of the **main Bragg peak**, making them possible 2nd and 3rd order Bragg peaks indicative of an inverse hexagonal H_{II} phase. The fact that these higher order peaks were only visible at high DOPE fractions, combined with the observation that the area of the 1st order peak decreased with decreasing DOPE content, indicates a DOPE-dependent inverse hexagonal phase for these particles. As the fusogenic capabilities of DOPE are known to be a result of DOPE facilitating a transition to the inverse hexagonal phase, this conclusion is very likely.[107] A similar, but very weak, 2nd order peak was also visible for the DPL-14 system comprising 0% cholesterol. However, the signal intensity here was too weak to confidently draw the same conclusion as before.

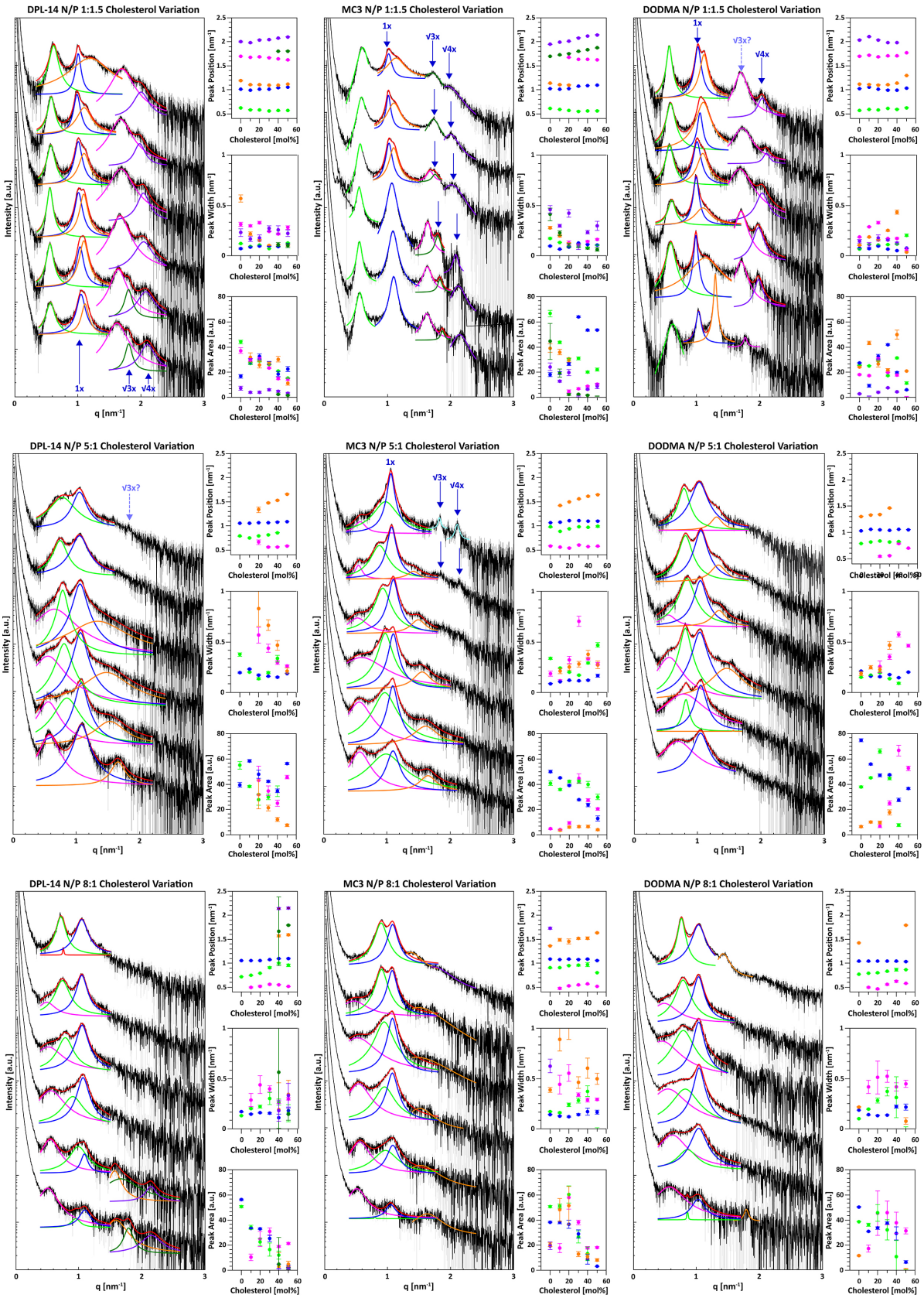

Figure 43. SAXS curves from the cholesterol- and N/P-variation experiments and their Bragg peak fits. SAXS curves are shifted vertically for clarity (0% cholesterol at the top, 50% cholesterol at the bottom). Bragg peaks were either fitted as multi-peak Lorentzian (red curve = full function, other colors = single peaks) or single peaks, depending on their characteristics. The respective peak data (position, width, area) is shown in the adjacent panels in the peaks' colors. Error bars represent the error from the peak fitting process.

Another characteristic for samples at an N/P ratio of 5:1 was the existence of a peak shoulder to the left of the main peak (green fit) as well as the appearance of a broad peak at even lower q (0.5-0.7 nm^{-1}, magenta fit) with increasing cholesterol fractions. The former did not show any trends with increasing cholesterol fraction and translates to a d-spacing of approximately 8 nm. The latter was much more visible at high cholesterol concentrations and translates to a very high d-spacing of approximately 10-12 nm. Previous publications have accredited such high d-spacings to be related to the distance between separate ordered phases of the same kind over a larger distance.[82] Therefore, an overlaying higher order of the separate highly ordered lipid-mRNA complexes, facilitated by high cholesterol concentrations, seems plausible.

Next, **formulations with an excess of mRNA charge (N/P 0.65)** were analyzed. Their scattering curves (**top row in Figure 43, Suppl. Fig. 8**) displayed a more complex array of Bragg peak contributions than previously studied systems. **Again, the Bragg peak visible for all formulations at around 1 nm^{-1} (blue fit) was defined as the main Bragg peak.** Additionally, **all systems displayed one peak to the left of the main Bragg peak at around 0.5-0.6 nm^{-1} (green fit)**, as well as **up to three peaks at higher q (magenta, purple, and 2nd green fit)** and a **peak shoulder to the immediate right of the main peak (orange fit)**.
The **main Bragg peak** did not show any major trends over the course of the cholesterol/DOPE titration for all three ionizable lipids, staying at 1.0-1.1 nm^{-1}, and therefore being representative of a d-spacing of approximately 6.0±0.2 nm. A slight increase in the scattering vector of ~0.1 nm^{-1} with increasing cholesterol fractions could however be observed. This increase in q was also visible more clearly for the two Bragg peaks at higher q (**2nd green** and **purple** fit) for samples comprising DPL-14 or DLin-MC3-DMA. Analysis of the peak repeat ratio across all cholesterol/DOPE ratios which showed these peaks revealed their positions to always be at √3· and √4· of the position of the **main Bragg peak** (displayed as blue arrows), therefore proving the presence of an inverted hexagonal H_{II} phase. This was the case at all cholesterol to DOPE ratios for samples comprising DLin-MC3-DMA and for DPL-14 based samples comprising 20% or 30% DOPE. For higher DOPE concentrations of the DPL-14 comprising samples, the √4·-repeat was still visible, however, the √3·-position moved into the range of the **magenta-fitted Bragg peak** at around 1.7 nm^{-1}. Therefore, despite not being visible, it might just have been overshadowed by this much stronger contribution, as suggested by the remaining presence of the **√4·-repeat ratio peak**. While these clearly inverse hexagonal H_{II} repeat ratios could only confidently be seen for samples comprising DPL-14 or DLin-MC3-DMA, samples comprising the ionizable lipid DODMA also displayed a moving √4·-repeat ratio (**purple fit**) and a strong, but stationary, **peak at around 1.7 nm^{-1}**. Therefore, the possibility of an overshadowed 2nd order √3·-repeat ratio is also given here.
In contrast to the previously discussed N/P 5:1 formulations, the **low-q Bragg peak (green fit)** visible here did not only appear at high cholesterol fractions, but was in fact visible across all samples and actually decreased in area with increasing cholesterol. For samples comprising DODMA, it moved toward slightly higher q (from 0.57 nm^{-1} to 0.63 nm^{-1}), translating to a change in d-spacing from 11 nm to 10 nm. For the two other ionizable lipids, this trend was exactly opposite, as the peak moved from 0.62 nm^{-1} and 0.61 nm^{-1} to 0.57 nm^{-1} and 0.56 nm^{-1}. Again, the very high d-spacings could indicate that these peaks are the result of the repeat distance between separate mesophases, but this time the decrease in intensity was in line with the decrease in DOPE content, suggesting an array of separate inverse hexagonal H_{II} phases. The overall stronger intensity of this signal in these samples compared to the LNPs with a positive charge excess discussed above also leads to the conclusion that this large-scale order is in fact caused by the electrostatic repulsion between different mRNA molecules.
This leaves **the right shoulder of the main Bragg peak (orange fit)**. This peak moved from higher (~1.2 nm^{-1}) to lower q with increasing cholesterol fractions until it merged with the **main peak**. For DLin-MC3-DMA-comprising samples, no distinction between the two peaks was possible from 30 mol% cholesterol onward. For samples comprising the other two ionizable lipids, two separate peak contributions could still be made out from the shape of the merged peak, and for DODMA-containing

samples the peaks actually separated again at the maximum cholesterol concentration. Due to the main peak slightly moving towards higher q and the peak shoulder moving towards lower q, it is in fact possible that these two peaks swapped their position at high cholesterol content. However, since this cannot be said for sure, their fits are still colored in their order of appearance in the scattering curves. The interpretation of this peak is not clear. Its position in relation to the other peaks does not indicate it being a lower or higher order of one of the other Bragg peaks and therefore, a separate ordered structure with a d-spacing of approximately 5-6 nm is assumed. However, no conclusion can be drawn as to what lipid mesophase is adopted due to the missing presence of higher order peaks.

Formulations with an N/P ratio of 8:1 (bottom row in Figure 43, Suppl. Fig. 10) showed more resemblance in their scattering curves to those with an N/P ratio of 5:1 than to those with a negative charge ratio (N/P ratio < 1). Again, a main Bragg peak was visible for all samples at around 1 nm^{-1} (blue fit), which stayed at the same position for all cholesterol levels and decreased in intensity and area with decreasing DOPE content. Samples comprising DLin-MC3-DMA also displayed a peak to the right of the main peak (1.4-1.6 nm^{-1}, orange fit) which shifted towards higher q with increasing cholesterol content across all cholesterol levels, as was the case for the N/P 5:1 samples. For the other two ionizable lipids, this peak was only well visible / fitable at some cholesterol levels.
Two more peaks at lower q, that had also previously been observed for the N/P 5:1 samples, were visible as well. The peak directly to the left of the main Bragg peak (green fit) was well defined at low cholesterol levels and shifted towards higher q with increasing cholesterol fractions, decreasing in intensity and merging with the main Bragg peak. The peak at lowest q (~0.5 nm^{-1}, magenta fit) appeared at 10 mol% cholesterol for all ionizable lipids and increased in intensity with increasing cholesterol content.
In addition, the scattering curves of DPL-14-comprising samples at 40 mol% and 50 mol% cholesterol also displayed peaks in the q-range of 1.5-2.2 nm^{-1} (2nd green and purple fit). While the peak position of the purple fit did fit a 2· repeat ratio, possibly indicative of being the 2nd order of the main Bragg peak in a lamellar phase, it is unclear why this would not be visible at lower cholesterol concentrations, where the main Bragg peak appeared much more prominently. However, a 2· (= √4·) repeat ratio could also be a 3rd or 4th order reflection of a hexagonal or cubic phase, respectively. In that case, peaks at √3· or √2· and √3· the scattering vector of the main Bragg peak position should be visible. The already mentioned peak to the right of the main Bragg peak (orange fit) does fit a √2· repeat ratio of the main Bragg peak, indicating a possible cubic phase. However, no clear peak at √3· the main peak position was seen. Therefore, this possibility cannot be confirmed.

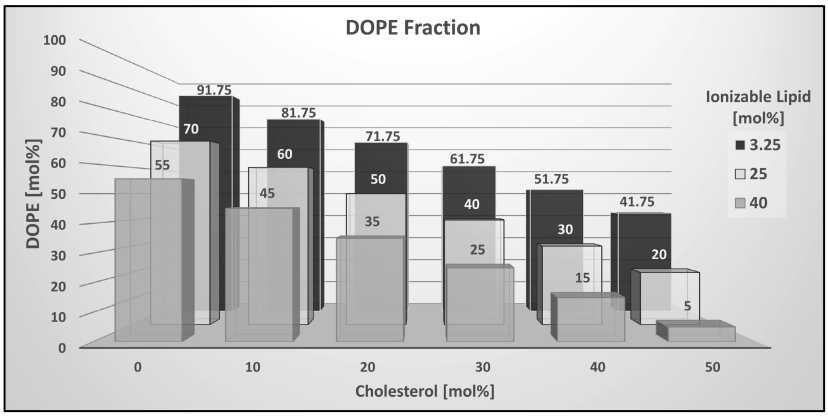

Figure 44. DOPE content of the different cholesterol and ionizable lipid concentrations in mol%. 40 mol% ionizable lipid represents both the N/P 8:1 samples as well as the additional N/P 5:1 sample set for DPL-14.

Figure 44 visualizes the particle composition in regards of DOPE content across all samples. From it, it becomes clear that just characterizing these samples by their N/P ratio and their cholesterol content

only tells half the story. Samples with very different cholesterol and ionizable lipid content can for example be characterized by almost the same amount of DOPE content, while samples with the same cholesterol content can have very differing DOPE fractions, depending on the amount of ionizable lipid used. In addition, as the additional DPL-14 N/P 5:1 set of samples (019-024) and the DPL-14 N/P 8:1 set both comprised 40 mol% ionizable lipid, but with differing amounts of mRNA resulting in different N/P ratios, their molar compositions in terms of lipid fractions were exactly the same. Therefore, trends concerning the observed structural parameters need to be analyzed in dependency of several factors, not just concerning the cholesterol ratio.

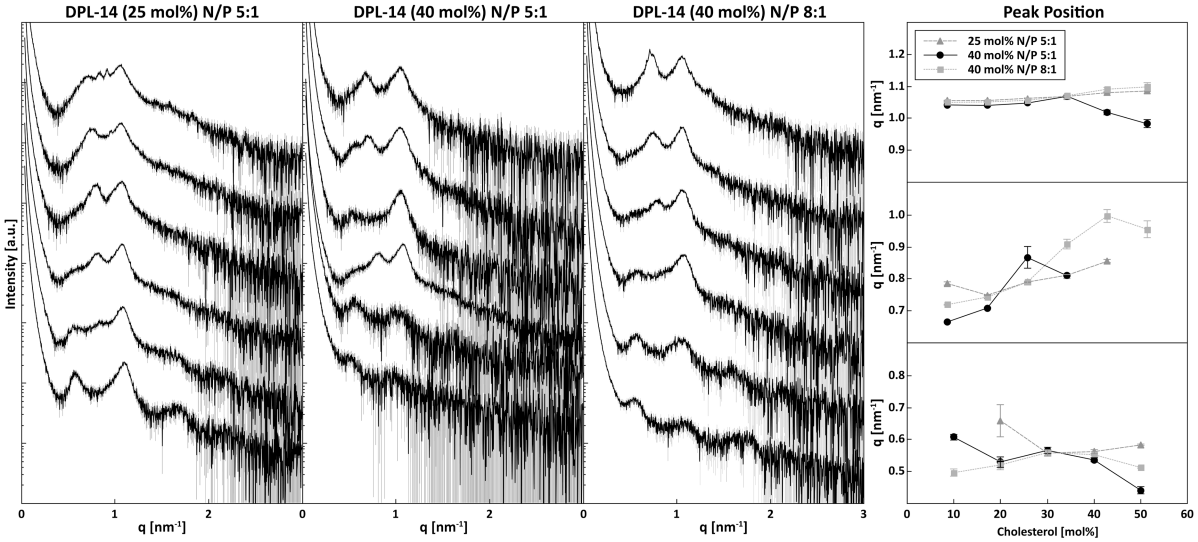

Figure 45. Scattering curves of formulations comprising DPL-14 at 25 mol% (left) and 40 mol% from 0% (top) to 50% (bottom) cholesterol. The panels on the right show the position of the main Bragg peak (top), the peak to the left of it (middle), and the lowest q peak (bottom) against the cholesterol content for all three sets. Error bars represent the error from the peak fitting process.

As mentioned above, the additional DPL-14 N/P 5:1 set of samples (019-024) and the DPL-14 N/P 8:1 set both comprised 40 mol% ionizable lipid. Figure 45 shows a side-by-side comparison of the three DPL-14 sample sets with a positive charge ratio. It is clear that even though samples 007-012 (N/P 5:1, 25 mol% DPL-14, **left**) and samples 019-024 (N/P 5:1, 40 mol% DPL-14, **center**) share the same N/P ratio, their scattering curves differ even from a qualitative analysis. This becomes especially clear at 0% cholesterol (topmost scattering curves), where the sample comprising 40 mol% DPL-14 showed a clear peak separation, and at 50% cholesterol (bottommost scattering curves), where barely any ordered peaks were visible for the 40 mol% sample. Comparing these cholesterol ratios (but also the ones in between), samples 013-018 (N/P 8:1, **right**) displayed much more similar scattering curves to those of samples 019-024, due to them having the same molar ratios in terms of lipid composition. Therefore, the amount of incorporated mRNA does seem to have a lesser impact in terms of particle structure than the lipid composition.

The three major take-aways so far can be summarized as follows:

- The main Bragg peak can be seen at all N/P ratios, its intensity is DOPE-dependent (especially at positive charge ratios), and it is probably related to an inverse hexagonal H_{II}-phase (mainly visible at N/P 0.65) with a d-spacing of ~6 nm, indicated by the presence of √3· and √4· repeat ratios.
- A cholesterol-dependent structure with a very high d-spacing (10-12 nm) can be seen at positive charge ratios. An overlaying higher order of the separate highly ordered lipid-mRNA complexes, facilitated by high cholesterol concentrations, seems to be a plausible explanation for this. At

negative charge ratios however, the structural contribution with high d-spacing is DOPE-dependent and much more prominently visible.

- The lipid composition has a higher impact on particle structure than the N/P ratio.

For further identification and analysis of the different structure factor contributions, a pH variation was performed using LNPs comprising DPL-14 as the ionizable lipid at an N/P of 0.65 (samples 081-087) and at an N/P of 5 (samples 071-077). The samples contained 50 mol% cholesterol and were prepared in 10 mM GG before being mixed in equal volumes with 150 mM pH buffer in a range from pH 4.5 to pH 7.4. The resulting pH values after mixing of the buffers were measured separately. The resulting scattering curves can be seen in Figure 46.

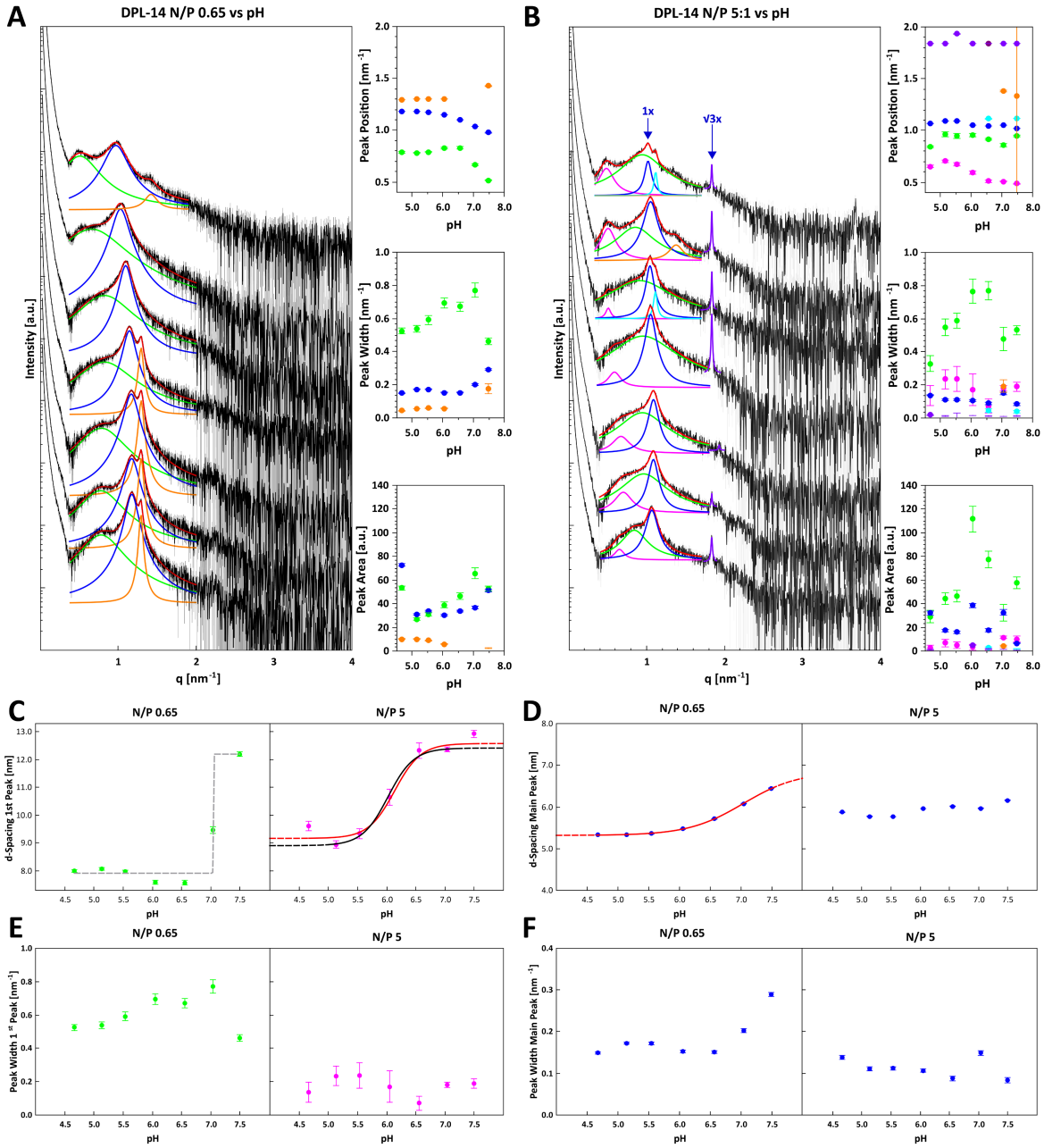

Figure 46. pH variation of DPL-14 comprising LNPs. Top row (A, B): Scattering curves with Lorentz fits from pH 4.5 (bottom) to pH 7.4 (top) and the resulting fit parameters (panels next to scattering curves). Middle row: d-spacings vs pH for the 1st (C) and the main (D) Bragg peak with sigmoidal (Boltzmann) fits (red, grey, or black curves). Bottom row: Peak widths vs pH for the 1st (E) and main (F) Bragg peak.

Both sample sets showed clear pH-responsive structural changes, which manifested themselves slightly differently. For the sample set with a negative charge ratio (N/P ratio <1, A), several trends were observed with increasing pH: The scattering vector q of both the early (green fit) and the main (blue fit) Bragg peak shifted towards lower q (higher d-spacing) over the course of the pH-variation and their peak width increased (except for the early peak at pH 7.4), as observed in the previous chapters for other pH-responsive systems. As these structure factor contributions are therefore the result of pH-responsive components of the LNP, it is quite safe to assume that they are caused by the DPL-14-mRNA-complex. Interestingly, the right peak shoulder (orange fit) of the main Bragg peak stayed at a constant position from pH 4.5 to pH 6.0 and then disappeared, before reappearing with a much lower intensity at pH 7.4. Even though the position for the fit at pH 7.4 was higher, this is probably more a result of the less clear peak contribution. The abrupt loss of structural signal cannot be assigned as easily as the pH-responsiveness of the other two peaks. However, the cholesterol variation experiment suggested a cholesterol/DOPE-dependent structure that was independent from the other recorded peaks causing this scattering contribution. The results seen here suggest that this structure only exists at pH ≤ 6.0. The buffer used during the cholesterol variation experiment – 10 mM GG – had a pH of ~5.8, therefore the contribution could also be detected there. Sigmoidal fitting of the main Bragg peak's d-spacing (D) suggested a conformational pH of 7.03±0.02 (R^2=0.9996), while fitting of the early peak's d-spacing resulted in nonsensical fits (see grey curve in Figure 46, C, left panel). However, a conformational pH also in the pH 7.0 range seems plausible from the data.

The LNP formulation with an N/P of 5:1 (B) also displayed the main Bragg peak at around 1 nm^{-1} (blue fit) across the whole pH-range, however, only a slight change in peak position, if any, could be detected. A very well-defined 2nd order reflection of this peak was visible at all pH values at $\sqrt{3}\cdot q$ of the main Bragg peak (purple fit, marked by blue arrows), suggesting an inverse hexagonal H_{II} lipid phase that was not pH-responsive in terms of d-spacing. Interestingly, a peak shoulder to the right of the main Bragg peak (cyan fit), that could not be detected at low pH or in 10 mM GG, was visible at pH 6.5 and 7.4. This peak-feathering at high pH had previously also been observed for pH-responsive lipoplexes (see chapter 3.2.1.1.4), where it was explained by the presence of local domains or additional systems comprising uncharged and not mRNA-complexed ionizable lipid. This explanation is suitable here as well. The peak shoulder marked with an orange fit, that had previously been visible in the cholesterol variation experiment, was also visible here. However, it was only well visible at pH 7.0 and 7.4, voiding the possibility of any assertions of pH-responsiveness. While no pH-responsiveness was visible for these three structure factor contributions, this was not the case for the two early peaks (fitted magenta and green). The early peak (magenta) showed a clear and strong pH-responsiveness in terms of peak position, translating to a difference in d-spacing from approximately 9 nm to 12 nm. While the peak was clearly visible at high pH, the move towards higher q with decreasing pH also resulted in a stronger overlap with the 2nd peak (green fit), making it hard to discern between the two peaks at low pH. Therefore, peak positions at low pH have to be considered with reservations. While it may look like the magenta peak actually disappeared at low pH, a multi-peak Lorentzian fit with only 2 peak contributions (green and blue fit) instead of three did not result in good fitting of the scattering curve, supporting the claim that the contribution is still there and just strongly overlapped with the second early contribution (green fit). Sigmoidal fitting of the early peak's d-spacing (C) resulted in a suggested conformational pH of 6.14±0.08 (R^2=0.9745, red curve). A better fit was attained by excluding the d-spacing values at pH 4.5 and 7.4, resulting in a conformational pH of 6.02±0.08 (R^2=0.9986, black curve). The 2nd peak (green fit) showed a slight decrease in peak position (increase in d-spacing) from pH 5.0 to pH 7.0 and a clear increase in peak width from pH 4.5 to pH 6.5. The sudden drop in peak width at the two highest pH levels was probably due to the inclusion of a fourth peak contribution into the Lorentz fit model, withdrawing the necessity for the green peak contribution to cover the whole widening of the signal. Therefore, the increase in peak width at pH levels ≤ 6.5 could both be due to a pH-responsive decrease in correlation length (as observed earlier for other systems) or due to the

increasing contribution of the other structure factor which could only be fitted as a separate (orange) peak at pH levels above pH 6.5.

Measurements of the pre-mixed formulations (sample 101-112) showed similar trends of pH-responsiveness, with the samples at pH 7.4 displaying a loss of correlation (see **Suppl. Fig. 6 in chapter 7.4.9**). However, when comparing their scattering curves to those of the pH-variations performed on-site, a much stronger loss of order in terms of peak intensity and peak feathering could be observed, indicating long-term instability of these particles in the buffer system used here (see **Suppl. Fig. 7 in chapter 7.4.9**). Therefore, these scattering curves were not analyzed in more detail.

Therefore, the two major take-aways from the pH-variation are:

- **Systems with an N/P ratio < 1** showed a pH-dependency in terms of d-spacing and peak width of both the DOPE-dependent main Bragg peak representing the ionizable lipid-mRNA complex and the cholesterol-dependent early contribution. The conformational pH of this dependency seems to be around pH 7.0.
- **Systems with an N/P ratio >1** did not show pH-dependency of the main Bragg peak. However, the cholesterol-dependent early contribution previously interpreted to be linked to a higher order of separate ionizable lipid-mRNA complexes showed a strong pH-dependency with its conformational pH being approximately 6.0.

As mentioned above, observations across all of the measurement and formulation parameters have to be taken into account in order to identify and explain the different structural contributions. **Suppl. Fig. 5** (see **chapter 7.4.8**) represents a visualization of the scattering curves that differs from the one in **Figure 43**, designed to better compare the recorded scattering curves across the whole experimental range. Several observations can be made here. As described above, the scattering curves of formulations with a positive N/P ratio (N/P ratios of 5:1 and 8:1, red and green curves in **Suppl. Fig. 5**, respectively) share similar characteristics. Keeping in mind the DOPE content as visualized in **Figure 44** (e.g., the 40 mol% DOPE content of the 30 mol% cholesterol samples at N/P 5:1 being in between the DOPE content of the 10 mol% and 20 mol% cholesterol samples at N/P 8:1), the continuation of structural trends with increasing or decreasing DOPE content across both sample sets can be made out for all three ionizable lipids. For example, the ratio of the peak intensities of the main Bragg peak (blue fit in previous paragraphs) compared to the early peak (magenta fit) decreases with decreasing cholesterol fractions. The early peak cannot be seen at 0% cholesterol for positively charged samples and only appears at higher cholesterol content, while the main Bragg peak, which is prominently visible at 70% DOPE (0% cholesterol, N/P 5:1), already decreases in intensity at 30-35% DOPE (40% cholesterol, N/P 5:1; 20% cholesterol, N/P 8:1), and almost completely disappears at 5% DOPE (50% cholesterol, N/P 8:1). Therefore, this structural contribution should clearly be regarded as DOPE-dependent.

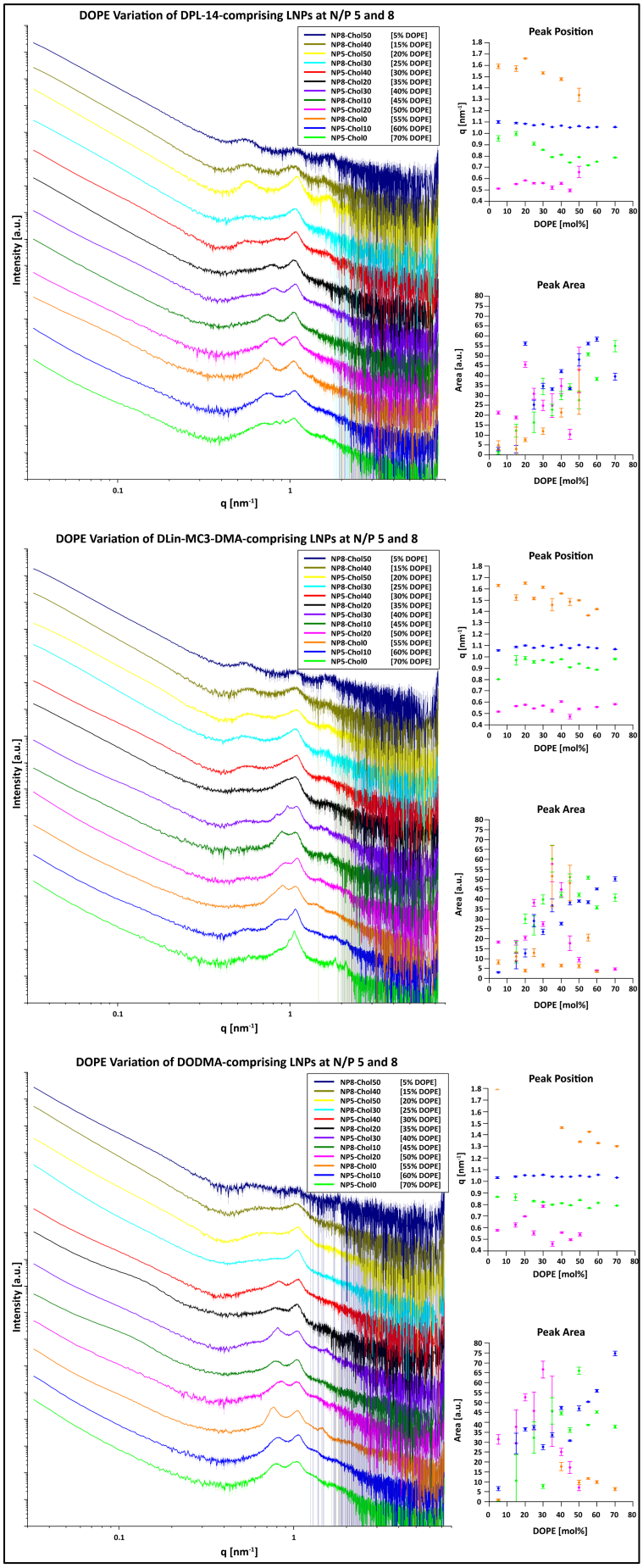

Figure 47. Visualization of the DOPE-dependent changes in the SAXS curves of positively charged LNPs.

Figure 47 was therefore created to visualize the DOPE-dependent changes, by combining the scattering curves from LNPs with an N/P of 5 and 8 and arranging them by increasing DOPE content (5% DOPE at the top, 70% DOPE at the bottom), and with their respective Lorentz fit parameters in the panels to the right of the scattering curves. This facilitated several observations: Firstly, looking only at the peak positions, the main Bragg peak (blue) and the early Bragg peak at ~0.5 nm^{-1} (magenta) did not show any trends in respect to the DOPE content of the formulation. The same can be said for the Bragg peak contribution in between (green fit) for samples comprising DLin-MC3-DMA and DODMA, but not for the sample set comprising DPL-14 as the ionizable lipid. Instead, a clear DOPE-dependent shift towards lower q could be observed for the latter. The previously orange-fitted peak (~1.3-1.8 nm^{-1}) showed a shift towards lower q with increasing DOPE across all samples where it was detectable. When analyzing their associated areas, both the main Bragg peaks (blue) and their left shoulders (green) showed a clear increase of scattering signal with increasing DOPE content, reinforcing the theory that these are signals caused by DOPE-comprising domains. No clear trend in signal intensity could be seen for the late (orange) peak on the other hand, with samples comprising DLin-MC3-DMA and DODMA, but not those comprising DPL-14, showed a transient increase in intensity around 30 mol% DOPE. However, this signal decreased again at molar ratios > 40%. Therefore, this contribution could be indicative of a phase-transition or the presence of a transition structure that only exists at certain cholesterol/DOPE ratios. This transition structure could also be responsible for the decrease of the Porod slope (q-range for fitting = 0.035-0.08 nm^{-1}) that could be seen in the DOPE content range from 30% to 55%, as depicted in Figure 48. While this decrease was only slightly visible for samples comprising DLin-MC3-DMA; it was very clear for both DPL-14- and DODMA-comprising samples. As mentioned previously, a high Porod-slope (~4) is indicative for a smooth particle surface, while Porod slopes closer to 3 indicate surface roughness. Therefore, this structural transition seemed to be accompanied by a transient increase in surface roughness, while formulations with lower or higher DOPE content had a smoother particle surface, especially if they comprised the ionizable lipid DODMA.

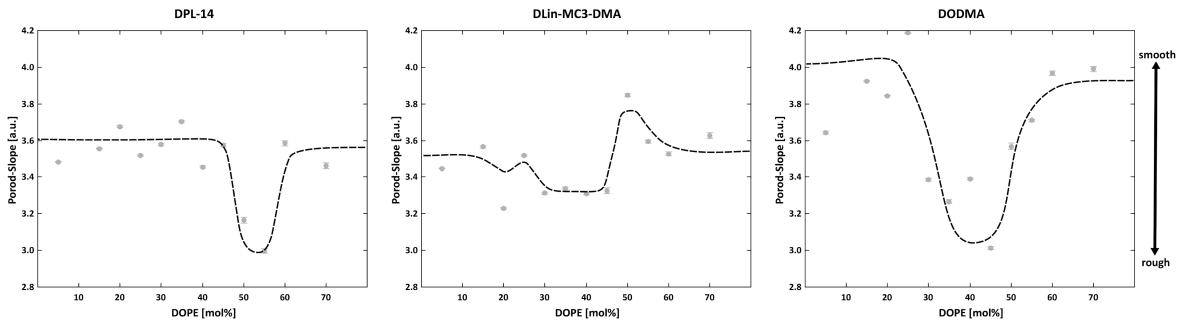

Figure 48. Porod-slopes vs DOPE-content for all three ionizable lipids. The dashed lines represent only a visual "guide to the eye" and not the fit of a mathematical function. A high Porod-slope (~4) is indicative for a smooth particle surface, while Porod slopes closer to 3 indicate surface roughness.

Therefore, the major take-aways from this DOPE-dependent analysis approach are:

- The main and early Bragg peak contributions are clearly induced by domains comprising DOPE, as their scattering intensity is dependent on the DOPE-content.
- The peak to the right of the main Bragg peak (orange shoulder) showed a DOPE-dependency in terms of d-spacing.
- A possible phase transition or transition structure could be seen in the range of 30-55 mol% DOPE, accompanied by a transient increase in surface roughness.

3.2.2 Biological Characterization

In addition to their physicochemical characterization, selected formulations were also tested for their biological transfection efficacy *in vitro*.

3.2.2.1 Transfection Efficacy of Lipoplexes

Lipoplexes comprising DOPC and either permanently charged lipids (DOTAP, DOTMA) or ionizable lipids (DODAP, DODMA, DLin-MC3-DMA) at an N/P-ratio of 2:1 and 5:1 (as characterized physiochemically in chapter 3.2.1.1) were prepared with a 1:1 mix of two mRNAs and at a total mRNA concentration of 0.2 mg/mL (4.2-4.6 mg/mL total lipid). The two mRNAs coded for either the luciferase enzyme or the cell surface protein CD90.1 (also known as Thy1.1), allowing for two separate transfection readouts. The transfection was tested in the Jurkat cell line (immortalized T-lymphocytes) as well as in human peripheral blood mononuclear cells (PBMCs), which are composed of Monocytes, B-Cells, NK cells, $CD4^+$ T cells, and $CD8^+$ T cells. In addition to the functional readout, the cell viability was also tested as a marker for the lipoplex toxicity.

All tested systems showed only low to no transfection efficacy in Jurkat cells at the tested dosage strengths (250/500/1000/2500 ng of each mRNA per $1{\cdot}10^5$ cells). In general, systems with an N/P of 5:1 showed slightly higher transfection than their N/P 2:1 counterparts, but no more than approximately 1.5-2.0 % Thy1.1 positive cells were detected. The maximum luminescence signal was in the range of 10^0-10^3 (arbitrary relative units), which was significantly lower than that of a polyplex formulation used as a positive control (10^4-10^6). Increasing the Jurkat cell concentrations to $2{\cdot}10^5$ cells did not increase the luminescence signal or the Thy1.1 transfection rates. Transfection rates and luminescence signal in $2{\cdot}10^5$ PBMCs were in the same range, with a maximum of ~4% Thy1.1 positive cells and a maximum luminescence signal of ~10^2. Again, the positive control showed much higher transfection, with >20% Thy1.1 positive cells and a maximum luminescence signal of 10^4.

In terms of viability, almost no negative effects were seen, with most formulation and dosage strengths showing 80-100% viable cells. The only exceptions were permanently charged lipoplexes based on the permanently charged cationic lipids DOTMA and DOTAP, which showed a dose-dependent toxicity and strongly decreased viability at the 1000 and 2000 ng dosage levels. This effect was strongest in N/P 5:1 DOTAP formulations in Jurkat cells, where only about 10% viable cells could be detected at the 2000 ng dosage strength.

Therefore, it can be concluded that, while no difference in transfection could be detected between the permanently charged lipids and their ionizable homologues, the ionizable lipids proved their lower toxicity at physiological pH levels due to the absence of excess cationic charge. However, the transfection levels of these systems were much too low for a potential clinical application.

3.2.2.2 Transfection Efficacy of LNPs

LNPs with the same composition as the "main" samples from chapter 3.2.1.3 (LNP-03, LNP-06, LNP-08, and IM-14) were prepared with mRNA coding for Thy1.1 at an mRNA concentration of 0.1 mg/mL and their transfection efficacy was tested both in human PBMCs and in whole blood. For the PBMC assay, both batch variability (N=3 independently prepared formulation batches tested in PBMCs from one donor) and donor variability (PBMCs from N=2 donors transfected with the same formulation batch) were tested, while the whole blood assay was only performed as N=1.

Figure 49 shows the batch and donor variability of the PBMC assay for the different formulations and at the tested dosage strengths (100/250/500/1000/2000 ng mRNA per $2{\cdot}10^5$ cells) in terms of transfection of monocytes (left) and cell viability (right), while Figure 50 shows the transfection efficacy across all cell populations at the highest tested dosage strength. All five formulations showed no loss

of viability within the tested dosage range of 100-2000 ng / 20 µL mRNA per $2.5 \cdot 10^6$ / mL PBMCs, indicating non-toxic particles. Only small variations could be determined for the batch variability and the donor variability.

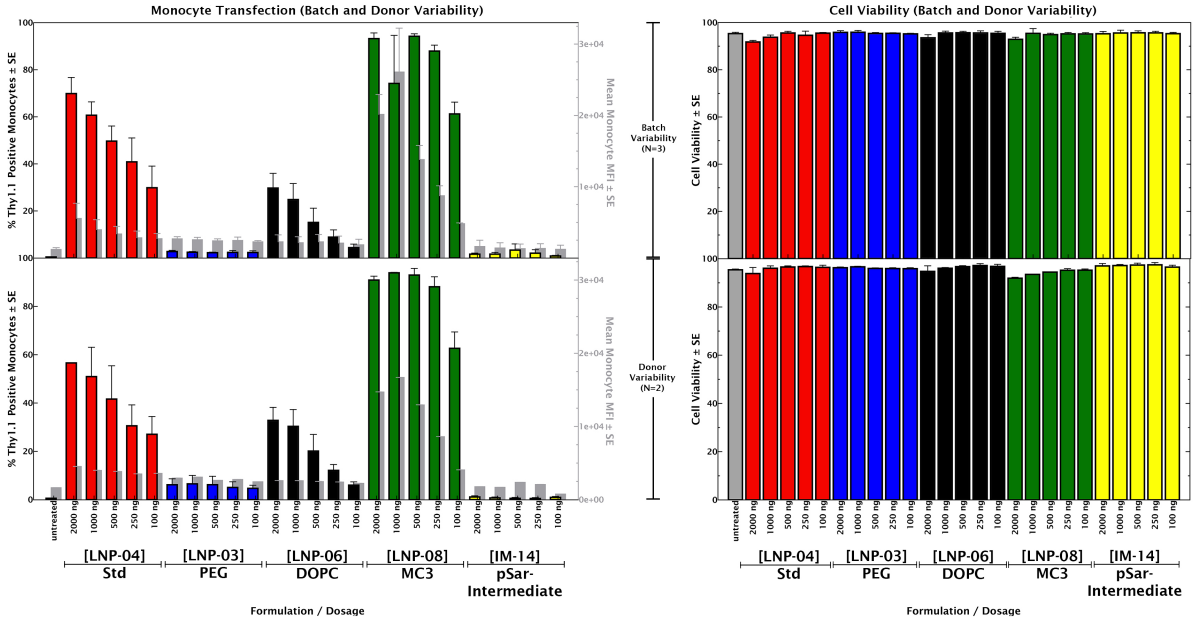

Figure 49. Transfection results in monocytes from the PBMC assay. Transfection efficacy (left panels) is displayed as the combination of the percentage of Thy1.1 transfected cells (left y-axis, coloured bars) and their mean fluorescence intensity (MFI, right y-axis, grey bars). Toxicity is inversely measured by showing the percentage of live cells (right panels). Data is shown as the mean value ± SE from batch (top, N=3) and donor (bottom, N=2) variability experiments.
While measuring Thy1.1 positive cells is a binary readout (transfected vs. not transfected), MFI includes the average expression level per cell by measuring the fluorescence intensity.
Batch variability relates to separately produced batches of the same formulation tested in the same blood donor's cells, whereas donor variability results come from testing one batch in separate blood donors' cells.

In general, the highest transfection rates could be observed in monocytes. However, both the intermediate particle IM-14 and the PEG-containing lipid nanoparticle LNP-03 showed no or only very low transfection in this cell type. Even at the highest tested dose no significant difference to untreated cells could be observed. LNPs comprising DOPC instead of DOPE (LNP-06) showed medium and dose-dependent transfection of up to 30% Thy1.1 expression, while both the standard LNP formulation (LNP-04) and its DLin-MC3-DMA homologue (LNP-08) showed high transfection efficacies of up to 70% and 93% Thy1.1 positive monocytes, respectively (see Figure 49, left panels, and Figure 51, panel B). Interestingly, while LNP-04 showed clear dose-dependency of its transfection efficacy, no difference could be discerned between the highest four dosage strengths of LNP-08, with all of them reaching at least 75% of Thy1.1 positive monocytes. This indicates a higher potency of this system, as lower doses were needed to reach saturated levels of Thy1.1 positive monocytes. When comparing the mean fluorescence intensity (MFI) of the monocytes however, the expression levels continued to rise at higher doses, suggesting that while a saturation of Thy1.1 positive cells is already reached at low doses, higher doses still result in higher surface protein expression levels (see Figure 51, panel C). One-way ANOVA testing was performed using the post-hoc Bonferroni multiple comparison method to compare the transfection efficacy of the different formulations to each other, confirming the aforementioned differences as significant (see Figure 51, panel A). The transfection levels in B cells were overall much lower, with almost no differences between the different formulations (see Figure 50). Only the DLin-MC3-DMA containing formulation LNP-08 stood out from the rest and reached significantly higher transfection levels than untreated cells, reaching up to 7% Thy1.1 positive

B cells. All formulations showed low (NK cells) to no ($CD4^+$ T cells, $CD8^+$ T cells) transfection in the other observed cell populations.

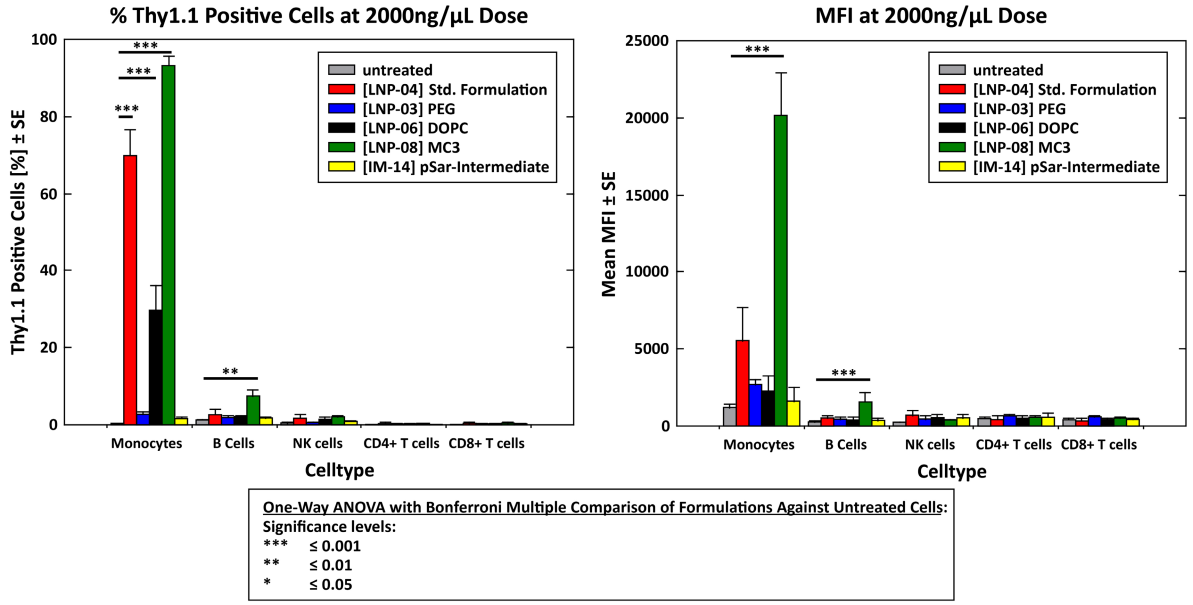

Figure 50. Transfection efficacy of different PBMC subtypes for the main sample variations at the highest tested dose (shown as mean percentage of Thy1.1 positive cells, left panel) and mean MFI (mean fluorescence intensity, right panel) from the batch variation experiment (N=3). One-Way ANOVA testing with the post-hoc Bonferroni simultaneous multiple comparison method of treatment pairs was performed to compare the formulations against untreated cells.[146] While three formulations showed significant differences to untreated cells in terms of % Thy1.1 positive monocytes ($p<0.001$), only the DLin-MC3-DMA-containing formulation LNP-08 showed significant transfection in B-cells ($p<0.01$ and $p<0.001$). No formulations showed significant transfection of NK, $CD4^+$, or $CD8^+$ cells.

When looking at the transfection efficacies in whole blood, the overall trends concerning cell viability and transfection remained the same and the formulation comprising DLin-MC3-DMA still showed the highest efficacy of the original formulations, together with a now added formulation comprising the ionizable lipid DPL-14, which showed similar efficacy (see Figure 52, panel B). However, the overall transfection rates were much lower compared to those observed in isolated PBMCs, indicating that additional factors introduced by the more complex *in vitro* test environment, such as the presence of plasma proteins facilitating the possible formation of a protein corona, could also lower the transfection efficacy of these systems *in vivo*. Interestingly, dose-dependency was not observed for the percentage of transfected monocytes, with the two highest transfecting formulations actually showing an inverse dose-dependency (panel C). However, dose-dependency was conserved when looking at the mean fluorescence intensity (panel D). Considering that these measurements were only performed as N=1 (concerning both batch and donor variability), no confident conclusion should be drawn from these measurements. However, the whole blood assay shows that the experimental design should try to aim as close to the target biological system as possible when evaluating biological efficacies, to include all possible disturbing factors.

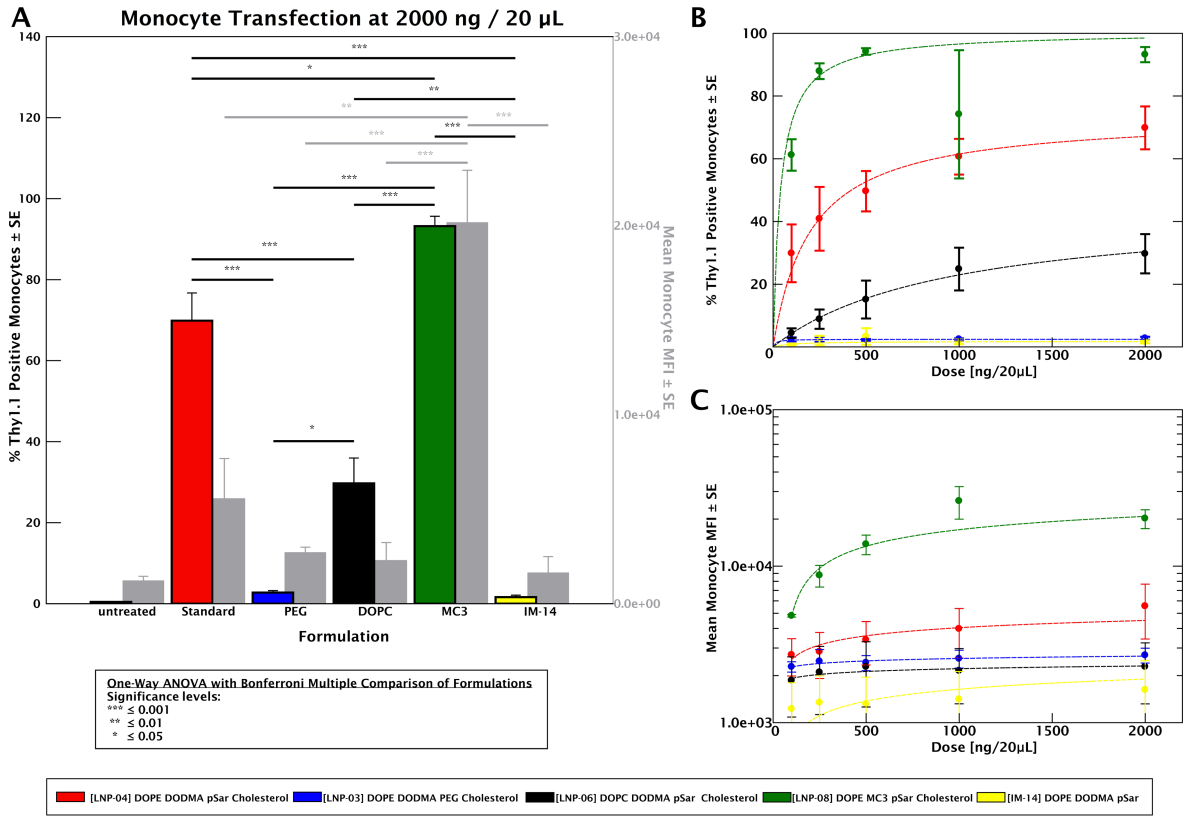

Figure 51. Transfection in monocytes. A. Monocyte transfection shown as % Thy1.1 positive cells (coloured bars, left y-axis) and mean MFI (mean fluorescence intensity, grey bars, right y-axis). Significant differences in transfection levels between the main formulations could be determined via One-Way ANOVA testing with the post-hoc Bonferroni simultaneous multiple comparison of treatment pairs.[146] B. Monocyte transfection shown as % Thy1.1 positive cells is dose-dependent and follows a saturation fit model (dashed lines). C. Monocyte transfection shown as mean MFI is dose-dependent and can be described by a logarithmic fit model (dashed lines).

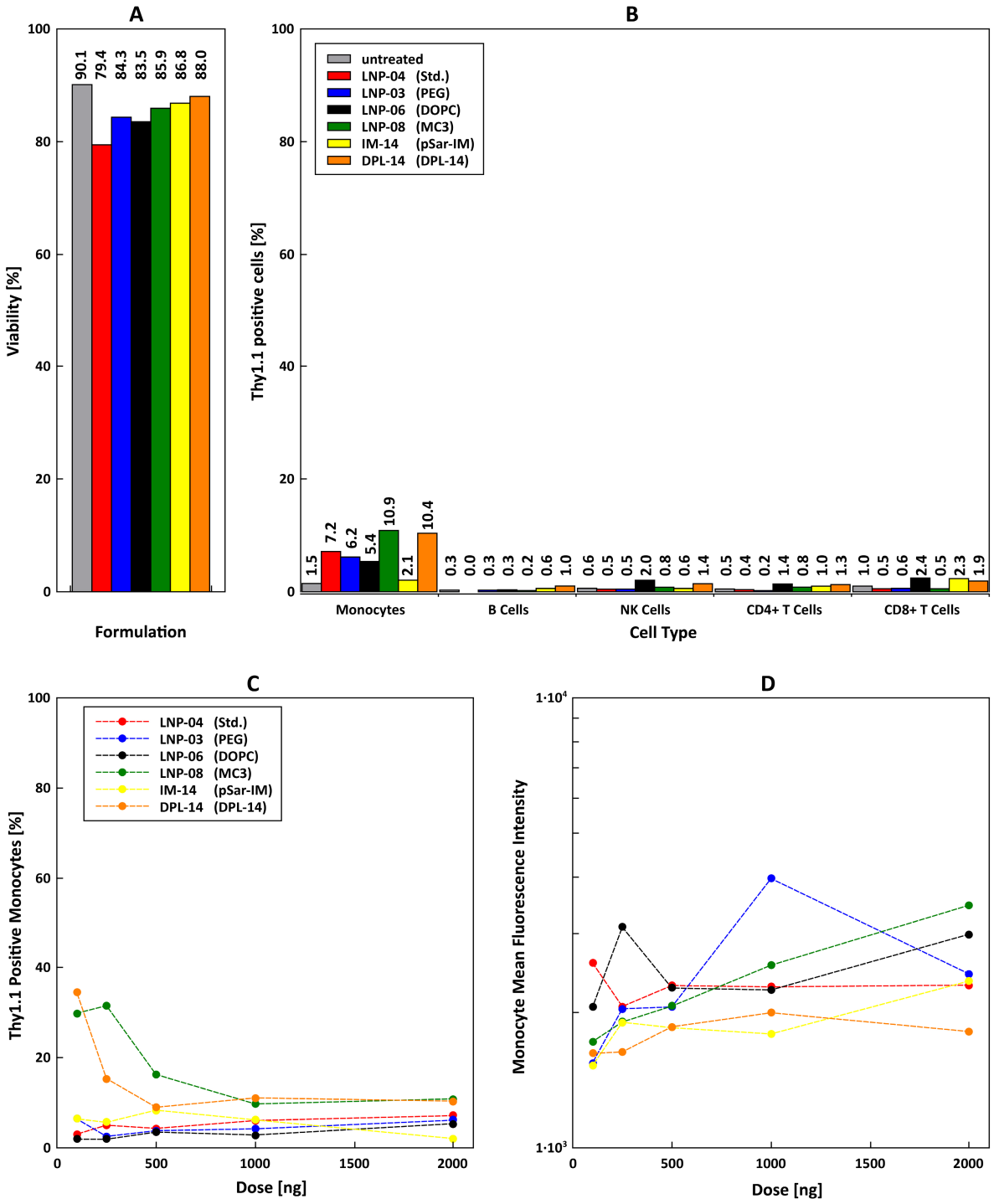

Figure 52. Transfection efficacy in whole blood (N=1). (A). Cell viability at the highest dosage strength (2000 ng) in percent. (B). Transfection of the different formulations at the highest dosage strength (2000 ng) shown as the percentage of Thy1.1 positive cells. (C). Monocyte transfection shown as % Thy1.1 positive cells vs mRNA dose. (D). Monocyte transfection shown as MFI vs mRNA dose (logarithmic scale).

4 | Discussion

4.1 Permanently Charged Systems

4.1.1 Previous Research in This Group

Previous research in this group had mainly focused on the structural elucidation of model lipoplex systems comprising different phosphatidylcholines and permanently charged cationic lipids, such as DOPC and DOTAP. This had led to the development of a structural model, describing these model systems as multilayered systems made up of lipid bilayers, with the mRNA located in the hydrophilic water slab in between those bilayers and electrostatically bound to local cationic lipid clusters (see Figure 53).[92,137] However, since this structural model was based only on X-ray scattering experiments and other physicochemical characterization methods, no differentiation could be made concerning the contribution of the different lipoplex components on the scattering signal seen in SAXS. In addition, these model systems were prepared using the classic lipid film method due to it enabling high sample concentrations well suitable for scattering experiments. However, as mentioned before, this preparation method is not very well reproducible in terms of lipoplex size control or suited for upscaling. Therefore, one additional task of this current work was to establish more reproducible formulation preparation protocols and to determine if the structural model derived in the previous work was also valid for formulations prepared with these more sophisticated preparation methods, such as DAC or ethanol injection.

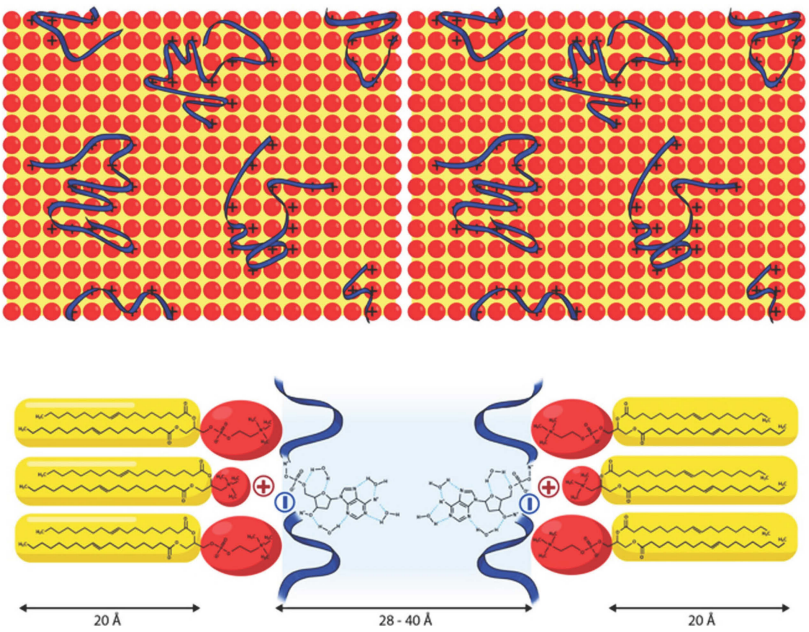

Figure 53. Structural model of permanently charged lipoplexes previously developed in this group. (Reprinted with permission from Ziller et al (2018).[92] Copyright 2018 American Chemical Society.)

4.1.2 Confirmation of the mRNA / Lipid Bilayer Model via TEM and SANS

As mentioned above, previous SAXS experiments did not allow for the differentiation between individual structural signal contributions. Therefore, in theory, it would also be possible for the mRNA, and not the lipid components, to have taken up an ordered lamellar structure causing the strong Bragg peaks in the SAXS signal. To confirm the previously derived structural model, the SANS and TEM experiments described in chapter 3.1.1 were performed. The TEM images showed multilayered systems, confirming this part of the structural model. SANS experiments also showed the strong Bragg peak contribution (translating to a d-spacing of approximately 6.8±0.1 nm) which had previously been observed in the SAXS experiments (see also Figure 54). Deuterium contrast variation revealed the

strong Bragg peak contribution to be caused by ordered lipid structures – namely the DOTAP headgroups – again confirming the previously established model.

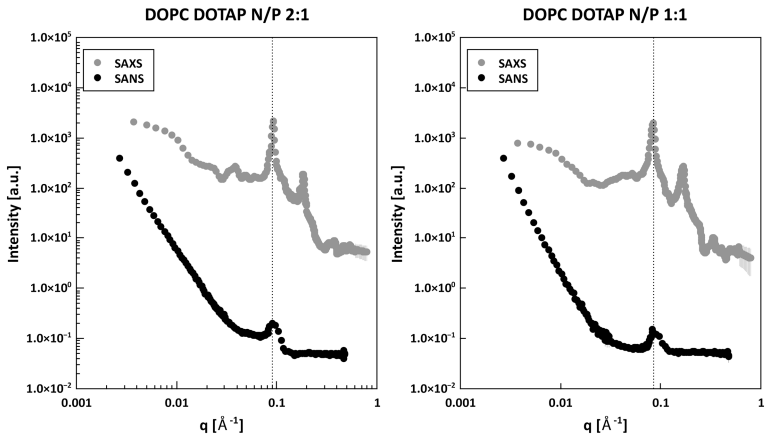

Figure 54. Comparison of SAXS curves from previous work and SANS curves from this thesis for the same systems. The SAXS curves were recorded by Antje Ziller, the SANS curves are SANS-3 and SANS-2 (left and right, respectively) from chapter 3.1.1.1 at 60% trehalose and the D88 contrast.

Additionally, the presence of ordered mRNA structures was also revealed. However, no quantification or detailed structural analysis of these structures was possible due to poor signal quality. Therefore, a further examination of these mRNA structures should be performed in the future, possibly using fully deuterated lipid components to enhance the contrast of the mRNA fraction. Structural investigations utilizing deuterium contrast variation in lipid-based mRNA delivery systems comprising deuterated components have previously been shown to enable better differentiation of scattering contributions in multicomponent systems and therefore have the possibility to elucidate structural reorganizations of single components.[61] Therefore, it should be possible to enhance the mRNA signal even at high deuterium contrasts by matching the deuterated lipid scattering length densities and in the process reducing the noise from incoherent background scattering. In addition, these experiments should be performed without the addition of excipients causing strong incoherent scattering, such as the previously used trehalose. The use of trehalose buffers in this work had been for experimental continuity from previous work, but proved to be hindering in terms of contrast matching due to the trehalose molecule's high hydrogen content. A salt-based, physiologically tolerated buffer – such as 10 mM glycylglycine or DPBS – without the addition of polyalcohols should therefore be used for future experiments which aim at performing deuterium contrast variation.

4.1.3 Optimization of the Preparation Methods

Chapters 3.1.2 and 3.1.3 deal with the influence of different preparation parameters, such as the utilized helper lipids or the preparation method, on the resulting physicochemical and structural properties of permanently charged lipoplexes.

Switching the preparation method – away from the classically used thin lipid film method – resulted in smaller and more reproducible systems, which is important for clinical applications.[39] While the parameters of the DAC method still offered opportunities for optimization, the ethanol injection method immediately produced systems of a favorable size with low polydispersity. This, combined with the scalability of the method (which is not easily given for either the lipid film or the DAC method), shows that it is well suitable for industrial production of lipid-based mRNA delivery systems. Structural analysis using SAXS showed barely distinguishable scattering curves and the same N/P-dependent trends in terms of d-spacing and correlation lengths, with no statistically significant differences between the thin lipid film method, the DAC method, and the ethanol injection method. No meaningful

difference between different preparation concentrations could be discerned either. In addition, the buffer used in the formulation process was exchanged. While previous work in this group had used either trehalose or HEPES/EDTA buffers, a switch towards 10 mM glycylglycine was performed, which resulted in improved colloidal stability. The pH level of this buffer is slightly acidic. While this has no direct influence on the preparation of lipoplexes comprising permanently charged systems, it is favorable in terms of preparing lipid systems comprising pH-responsive lipids, where an acidic pH is needed to ensure the presence of cationic charges to complex the anionic mRNA during the preparation step. However, while not directly essential for the formulation of permanently charged lipids, the pH of 5.8 also falls into the range at which the phosphodiester-bond of the mRNA is the most stable.[147,148] Therefore, storage of the aqueous mRNA solution in this medium prior to the formulation process should cause no problems.

In recent years, several advancements have been made in the field of scalability, leading to the availability of devices with GMP conformity that can produce liposomes or lipid nanoparticles in industrial batch sizes.[25,96,97,149–151] Recently approved RNA LNP systems are produced using so-called microfluidic chip techniques, where the aqueous mRNA phase and the alcoholic lipid phase are mixed under reproducible conditions (such as the flow rates and flow rate ratios) in very small channels with defined geometry and surface parameters.[81,150–152] The manufactures of these devices claim to enable easy upscaling by using the same microfluidic channel geometry in lab-scale, preclinical scale, and GMP-scale devices. If the structural insights gained in this thesis are in fact also valid for formulations prepared with these techniques remains to be investigated. However, since the formation process of lipoplexes and LNPs seems to be mainly driven by their composition, it is likely that the structural insights gained here are also valid for systems prepared by microfluidics, especially since LNPs prepared with this technique have shown similar characteristics in SAXS to those described in this work (see chapter 3.2.1.2).[60]

Variation of the utilized helper lipid resulted in structurally distinct systems, displaying structures such as weakly correlated bilayers, highly ordered bilayers, or the simultaneous presence of two well-defined individual bilayer systems with differing dimensions. However, considering the limitations in experimental design due to the limited material supply mentioned in chapter 3.1.3, no systematic conclusions could be drawn as to what caused these distinct structural changes. In classical bilayer-based lipoplex systems, the addition of a formally uncharged lipid such as DOPC, DSPC, or DOPE is thought to help form stable bilayer structures – hence the name helper lipids – but previous research has suggested another role of the helper lipid: The ability of the lipid bilayers to undergo the transition to the inverse hexagonal H_{II} phase has been shown to play an important role during both the uptake process of the lipid vesicle into the cell and during the endosomal escape step.[48,55,66,83] In addition, pH-responsiveness (as discussed in chapter 4.2) could also be introduced via the helper lipid instead of the cationic lipid, expanding the possibilities of tailoring the delivery system properties to its intended site of action. Therefore, further experiments utilizing systematic variation of helper lipid parameters, such as the head group structure, the lipid chain length, and the lipid chain saturation, are suggested in order to develop a component-structure correlation, which could be used for the fine-tuning of future delivery systems depending on their clinical purpose.

4.2 pH-Responsive Systems

While first developments of lipoplex systems were made using permanently charged cationic lipids, the development over the years has led to the almost exclusive use of ionizable lipids, due to their improved transfection efficacy and lower toxicity. [48,53,85,136,153] While some key parameters relating to the formulation efficacy, such as the lipid pK_a or the lipid chain saturation level, have been identified, mechanistical explanations concerning the pH-responsive structural changes in lipid-based delivery

systems is still lacking.[85,107,154,155] Therefore, the largest portion of this work was dedicated to the structural elucidation of pH-responsiveness in lipid-based mRNA delivery systems. For this, model systems, represented through classical three-component lipoplex systems, and more modern five-component LNP systems were used, and their composition was systematically varied to try and derive component-structure-function relationships.

4.2.1 Preparation Method Selection and Structural Differences Between Lipoplexes and LNPs

Chapter 4.1.3 already discusses the advantages of the ethanol injection method with 10 mM GG used for the aqueous phase and why it was chosen as the preferred preparation method. However, there is no single one ethanol injection method, but rather a number of variations all using the same principle of rapid solvent mixing under (semi-)controlled conditions.[94,97,150,156,157] Chapter 3.2.1.2 explores the driving forces behind the lipoplex and lipid nanoparticle formation process and determines the process to be mainly driven by the electrostatic interaction between the positively charged ionizable lipid and the negatively charged phosphate backbone of the mRNA. Interestingly, variation of the initial mixing conditions (injection through a thin needle under constant stirring vs pipetting together) only showed an effect on the highly ordered multilamellar lipoplex structures. Here, using slower mixing conditions (manual protocol) resulted in a lower amount of membrane stacks. LNPs on the other hand seem to have a much lower ordered structure to begin with. They are often considered to have a condensed core consisting of ionizable lipid, mRNA, and cholesterol, with an outer mono- or bilayer of helper lipid and stealth-lipid, as illustrated in Figure 55.[57,61,86] This lower order, which is characterized by broad Bragg peaks, was also visible in the SAXS experiments performed in this work, as shown in chapter 3.2.1.2.2. However, due to this inherent lower order, the LNP structure seems to be less sensitive to the initial mixing speed, showing no difference in d-spacing, correlation length, or other structural characteristics between the two preparation methods. Therefore, pH-responsive lipoplexes were prepared with the "classical" ethanol injection method throughout the course of this work, while LNPs were prepared using the more flexible and less labor-intensive manual protocol, allowing for lower material costs and faster screening processes, while also omitting the need for non-single-use labware, such as glass vials or magnetic stirring bars.

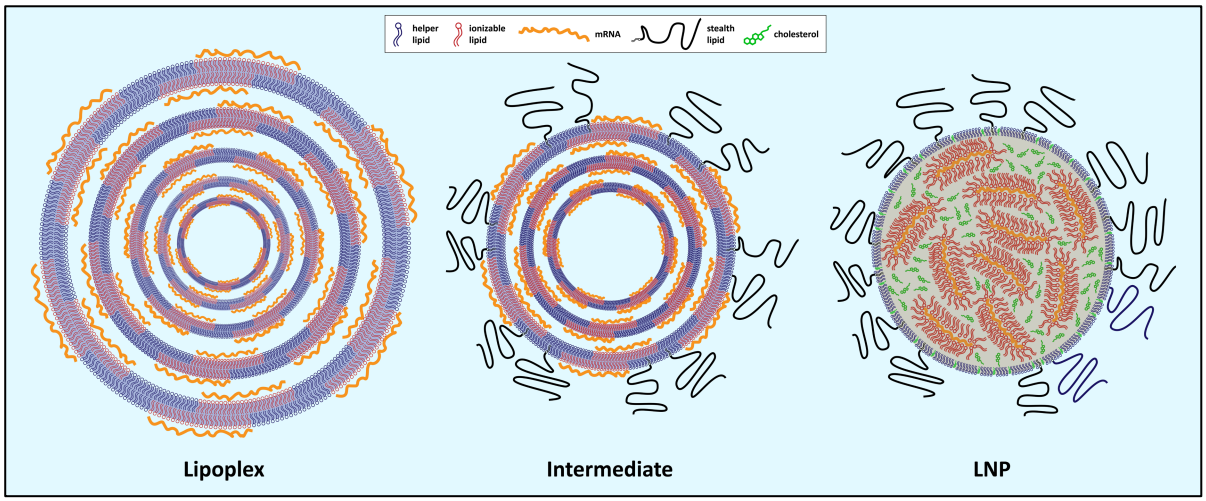

Figure 55. Illustration of the transition from highly ordered lipoplexes (left) to lower ordered LNPs (right) with a core-shell structure. The mRNA is illustrated in orange, ionizable lipid in red, helper lipid in blue, cholesterol in green, and stealth lipid in black.

4.2.2 pH-Responsive Structural Changes of Lipoplexes

As mentioned above, the lipid pK_a has been identified and is widely accepted as one of the key parameters determining the transfection efficacy of RNA lipoplexes. The responsiveness to changes in the environmental pH is considered an important aspect in terms of facilitating the endosomal escape and delivering the mRNA to the cytosol for translation. Several mechanisms, such as phase transitions towards the inverse hexagonal H_{II} phase, a lipid flip-flop effect, or the proton sponge effect have been credited with facilitating the endosomal escape and being pH-dependent. [48,66,83,86] So far however, only theories or indirect measurements concerning the pH-dependent structural changes of lipoplex systems have been published, while direct *in situ* measurements had not been performed.[143] Utilizing small angle X-ray scattering, the present work gave the possibility to accurately measure structural reorganizations in lamellar model lipoplex systems as a function of pH. A clear pH-dependency of the repeat distances inside the multilamellar vesicles was visible, which enabled the calculation of the conformational transition points (conformational pH) in chapter 3.2.1.1.4. In addition, some formulations showed strong changes in correlation length. The latter was particularly the case for the formulation containing a high amount of the ionizable lipid DLin-MC3-DMA, which is a component of the first approved siRNA drug product *Onpattro*® (patisiran).[81] This formulation also displayed lower order in terms of average bilayer numbers than all other samples, making it possible that this effect might contribute to the very strong transfection efficacy of systems comprising high contents of DLin-MC3-DMA previously shown in certain settings, such as hepatic targeting.[85,145] The increase in d-spacing with increasing pH for all ionizable systems containing mRNA can be well explained by the different protonation levels of the ionizable lipid. Due to a decrease in protonation upon increasing pH levels, the attractive forces between the localized ionizable lipid clusters in the lipid membrane and the mRNA decrease, leading to elevated distances between the bilayers and lower long-range correlation between the lipid stacks. This protonation effect was additionally verified by the observations of the mRNA-free systems. For these, the pH variation had the opposite effect, with a decrease in pH leading to an increase in d-spacing and a decrease in long-range order. Here, the unscreened cationic charge led to repulsion between the lipid bilayers. Notably, although the SAXS measurements showed less dense packing for systems comprising mRNA at high pH, the majority of the mRNA was not released from the multilayer stacks as shown by both gel electrophoresis and the RiboGreen Assay (see chapter 3.2.1.1.2), indicating that the integral stability in circulation should be maintained.

Cationic lipid	N/P ratio	Conformational transition point (from SAXS)	Apparent formulation pK_a (from TNS-assay)
DOTMA	1:1	n.c.	-
	5:1	n.c.	n.c.
DODMA	no mRNA	6.6 ± 0.2	7.1 ± 0.2
	1:2	-	7.9 ± 0.1
	1:1	7.7 ± 0.1	8.0 ± 0.0
	2:1	7.5 ± 0.1	7.6 ± 0.0
	5:1	7.0 ± 0.1	7.2 ± 0.1
DOTAP	5:1	n.c.	n.c.
DODAP	no mRNA	-	7.3 ± 0.1
	2:1	-	7.5 ± 0.1
	5:1	6.8 ± 0.1	7.8 ± 0.2
DLin-MC3-DMA	no mRNA	-	7.4 ± 0.2
	2:1	7.4 ± 0.5	7.7 ± 0.3
	5:1	6.8 ± 0.1	7.3 ± 0.1

Table 20. Comparison of the formulations' conformational transition point (conformational pH) and lipid pK_a for samples comprising different ionizable or cationic lipids as determined by SAXS and TNS, respectively. Formulations not measured with the respective method are marked with "–", and measurements where no meaningful Boltzmann fit could be applied are marked with "n.c." (not calculated).

As the ionizable lipid protonation had already been suspected as the main driving factor for pH-dependent structural changes, previous publications have used the fluorescence based TNS assay to easily determine the lipid pK_a and try to predict the pH-responsiveness of different formulations.[95,107,158] However, the present work shows that while the pK_a results from the TNS assay and the conformational pH calculated from the SAXS data do correlate, a systematic shift between the two values can be observed (see Table 20 and Figure 56). This discrepancy amounted to values as high as about 1.2 for the formulation comprising DLin-MC3-DMA at an N/P ratio of 2:1. It appears plausible that the structural changes observed in lipoplexes depend not only on the protonation level of the ionizable lipid and that the overall lipid composition – the lipoplex as a whole – has to be taken into account. This becomes even more evident when seeing that the conformational transition also depends on the N/P ratio of the lipoplex, which does not change the lipid molecule pK_a. Thus, the conformational transition pH seems to be dependent on three factors: the ionizable lipid, its molar fraction within the particles, and the ratio of the ionizable lipid to the mRNA (known as the N/P ratio).

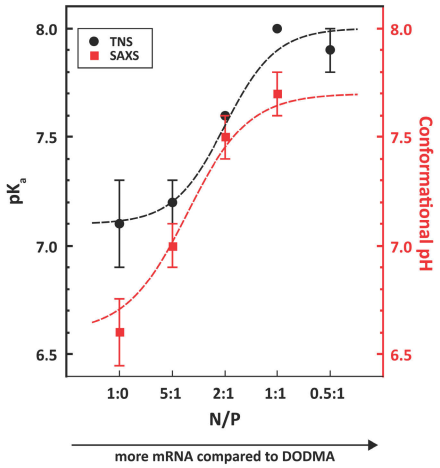

Figure 56. Comparison of the formulations' conformational transition point (conformational pH) and lipid pK_a for samples comprising the ionizable lipid DODMA as determined by SAXS (red) and TNS (black), respectively. Dashed lines are meant as a guide to the eye and do not represent the fitting of a mathematical or physical model.

4.2.3 pH-Responsive Structural Changes of LNPs

The previous chapter discussed pH-responsive changes of classical lipoplexes. However, the pH-dependent changes observed mainly concerned the bilayer structure of these model systems while modern LNP systems are in fact not multi-bilayer-organized systems, as discussed in chapter 4.2.1. Therefore, the effect of changes in environmental pH on these condensed systems was investigated in chapters 3.2.1.3 and 3.2.1.4.2, again using SAXS and the well-established TNS-assay.

The TNS-assay in chapter 3.2.1.3 proved the pH-responsiveness of the investigated formulations in terms of cationic charge, but no systematic differences between the exchanged helper, ionizable, and stealth lipids could be discerned. It must be noted though, that only one N/P ratio was tested here, and that the two tested ionizable lipids – DODMA and DLin-MC3-DMA – only showed minor differences when tested in lipoplexes as well (see Table 20 in the previous chapter). Therefore, the lack of a detectable difference could be due to the structural differences between LNPs and lipoplexes. As previously explained, the ionizable lipid in LNPs is confined within the particle core and consequently less accessible to the fluorescent dye. Hence, this could negate those minor differences between the ionizable lipids that had still been visible in lipoplexes, resulting in very similar or non-distinguishable TNS-assay results.

Small angle X-ray scattering showed mainly two pH-dependent characteristics. The first one – increase of d-spacing with increasing pH – matched the results previously observed for the model lipoplex systems. The second one was a strong decrease of long-range order between pH 6.5 and 7.6, which was observed for all tested samples. The increase of d-spacing with increasing pH proves the presence of lipid nanoparticles with mRNA bound to the ionizable lipid, as described for lipoplexes, since non-mRNA-bound ionizable lipid would show higher d-spacing at low pH, due to non-neutralized charges leading to strong electrostatic repulsion (see mRNA-free systems in chapter 3.2.1.1.4). As mentioned in chapter 4.2.1, such models, describing mRNA lipid nanoparticles as systems with internalized mRNA bound to the ionizable lipid molecules have been previously suggested.[57,86] The observed broad Bragg peaks therefore correspond to the ordered ionizable lipid - mRNA complexes and their distinctive repeat pattern. In classical lipoplexes, these complexes are integrated in the strongly ordered helper lipid bilayers, resulting in the observed high correlation length manifested as sharp Bragg peaks. In LNPs however, this long-range order is not maintained to the same extent, due to their abovementioned condensed structure. This results in lower correlation lengths for LNPs, as discussed in chapter 4.2.1. The d-spacing however does not change drastically between the different systems, as it is an indicator for the compactness of the ionizable lipid - mRNA complex, which seems to be the same for lipoplexes, intermediate systems, and LNPs. The additional drop in correlation length at high pH confirms this structural model of LNPs. When the environmental pH exceeds the pK_a of the utilized ionizable lipid it starts to lose its cationic charge and can therefore not form electrostatic complexes with the mRNA. This leads to a particle core comprising both charged and uncharged ionizable lipid molecules. The anionic charge of the mRNA is not neutralized anymore and therefore the repulsive forces are screened less efficiently. This leads to higher d-spacing and a lower particle order, with the latter resulting from the fact that only charged ionizable lipid molecules can contribute to the ordered lipid - mRNA complexes (see illustration in Figure 57).

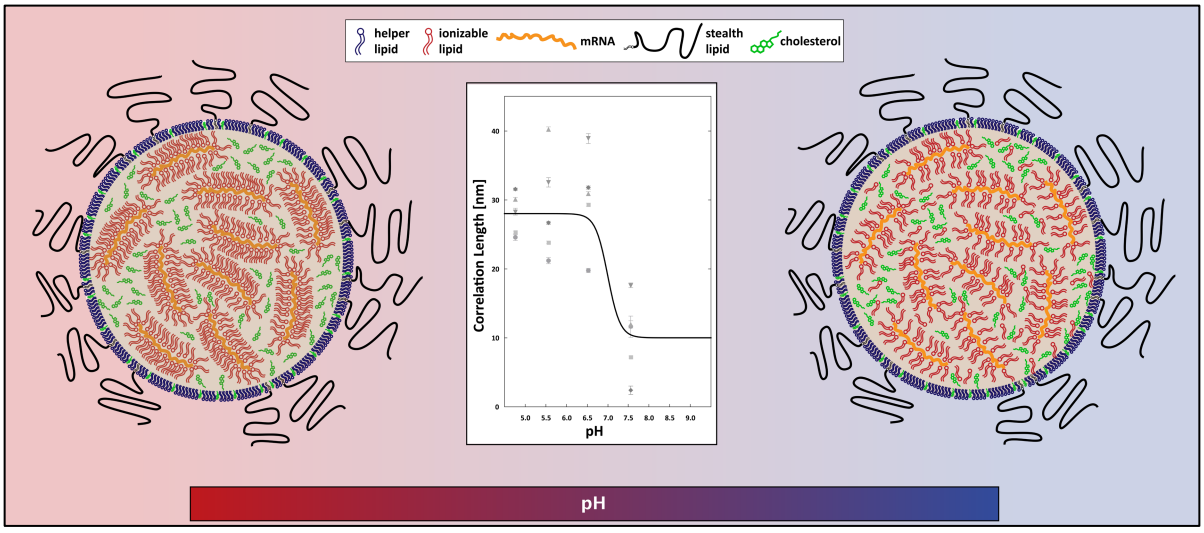

Figure 57. Illustration of the change in particle order due to uncharged ionizable lipid at higher pH levels. The mRNA is illustrated in orange, ionizable lipid in red, helper lipid in blue, cholesterol in green, and stealth lipid in black. The inlayed graphic shows the resulting general trend towards lower correlation length as a function of pH for the main formulations (as determined by SAXS in chapter 3.2.1.3.3).
As the pH level rises and the ionizable lipid is protonated to a lesser degree, the higher amount of unscreened negative charge of the mRNA leads to repulsive interactions and therefore less efficient packing, which results in a lower particle order.

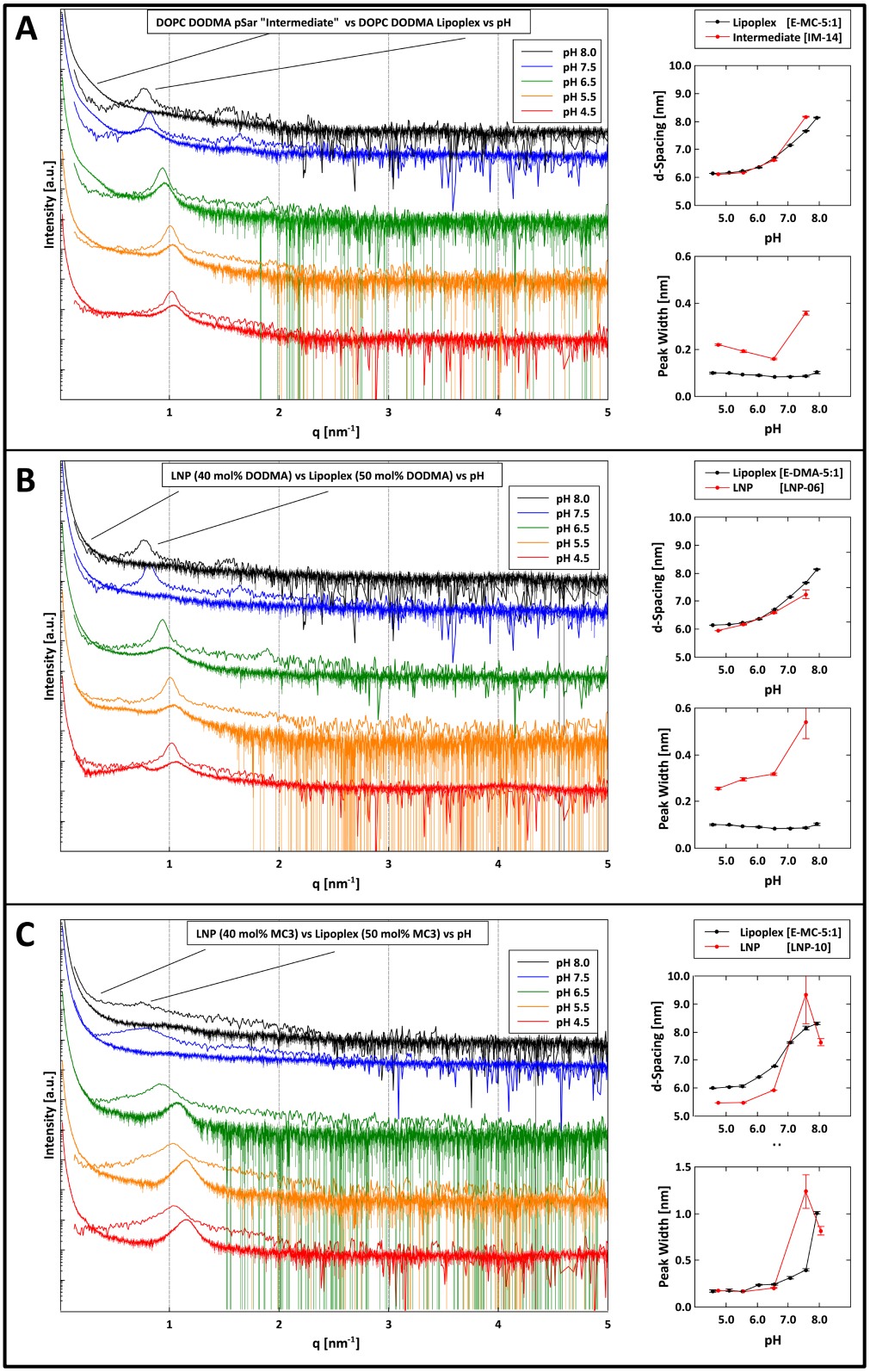

Figure 58. Comparison of "Intermediate" or LNP formulations (from chapter 3.2.1.3) to lipoplex systems of similar composition (as discussed in chapter 3.2.1.1) at different pH-levels. The graphs to the right show the quantitative peak data (calculated d-spacing and fitted peak width).
A. Comparison of a polysarcosine-based intermediate formulation (IM-14) and a lipoplex formulation lacking the stealth lipid (E-DMA-5:1). B. Comparison of a DODMA-comprising LNP (LNP-06) and a DODMA-comprising lipoplex (E-DMA-5:1). While both formulations were prepared at an N/P-ratio of 5:1, the LNP contains 40 mol% DODMA, while the lipoplex contains 50 mol%. C. Comparison of a DLin-MC3-DMA comprising LNP (LNP-10) and a DLin-MC3-DMA comprising lipoplex (E-MC3-5:1). Again, the LNP contains 40 mol% of the ionizable lipid, while the lipoplex contains 50 mol%.

Figure 58 reinforces these observations by comparing the pH-responsiveness observed in intermediate particles and LNPs with those observed in lipoplexes of very similar composition. As one can see, both show the same trends concerning pH-responsiveness in terms of d-spacing and peak width (and therefore long-range order), with LNP systems displaying a lower overall order (higher peak width), matching the results from before. Quite remarkably, d-spacing observed in DODMA-comprising systems did not differ from one another over the whole tested pH-range (see d-spacing graphs in **panel A and B**) and only minor differences could be observed for the DLin-MC3-DMA-comprising systems (**panel C**), confirming that this value describes the compactness of the ionizable lipid - mRNA complex without major influences of the surrounding particle system.

The experiments shown in **chapter 3.2.1.4** enabled further extension of the model derived above (and illustrated in **Figure 57**) by utilizing in-vacuum measurements (facilitating a better signal to noise ratio) and extensive sample variation. A systematic approach utilizing three different ionizable lipids, three N/P ratios, six different cholesterol percentages, and pH-variation was used here. The analysis was performed both in terms of cholesterol and DOPE content, as well as in terms of pH-dependency and N/P ratio. Combining the analysis from all these different angles it becomes clear that a straightforward statement about the structural implications of the utilized formulation parameters cannot easily be made. However, several statements describing the observed structural features and their dependencies are possible:

Firstly, a clear differentiation has to be made between LNPs with a negative N/P ratio (in this case 0.65) and those with a positive one (in this case 5 and 8). The latter are mainly characterized by a DOPE-dependent inverse hexagonal H_{II} phase with a d-spacing of approximately 6 nm causing the Bragg peak at around 1 nm^{-1} as well as its higher orders. This structural contribution does not show any strong pH-dependent changes and was visible for all three ionizable lipids used. At very low DOPE to cholesterol ratios (<20% DOPE), the possibility of a transition to a cubic phase also exists, which has also been reported as a possibility for the core of lipid-based DNA-delivery systems before.[82] The transition itself is accompanied by a change in surface-roughness. An additional DOPE-dependent phase with a variable d-spacing of approximately 6-8 nm is also well defined at high DOPE-concentrations, with lower DOPE-concentrations resulting in higher repeat spacings. Additionally, a pH-dependent ordered structure, likely facilitated by cholesterol, is also visible and displays very high repeat spacings of approximately 9-12 nm, with more acidic pH levels leading to higher compactness.

The d-spacing of approximately 6 nm mentioned for the DOPE-dependent phase was previously postulated to represent the mRNA-ionizable lipid complex (see above). An inverse hexagonal H_{II} array of the ionizable lipid around the mRNA molecules facilitated by the fusogenic helper lipid DOPE seems plausible. While bilayer-ordered lipid-mRNA complexes showed a pH-dependency of the inter-bilayer spacing due to attractive and repulsive electrostatic forces, this does not seem to be the case for the immediate inverse hexagonal H_{II} organization. The hydrophilic headgroups of the ionizable lipids should favor close proximity to the hydrophilic mRNA within the solid lipid nanoparticles independent of the electrostatic attraction caused by ionization, just due to polarity effects caused by the absence of a water layer. However, these inverse hexagonal lipid-mRNA complexes themselves also seem to be ordered in a secondary order facilitated by cholesterol. Here the pH-dependency becomes prominent, as different individual mRNA-molecules do not have their negative charge screened anymore by the surrounding ionizable lipid headgroups at high pH levels, resulting in repulsive electrostatic interactions between the individual – overall negatively charged – mRNA-lipid complexes and a higher spacing of this secondary order, as displayed by the change in d-spacing from approximately 9 nm to 12 nm. An illustration of this model was attempted in **Figure 59**.

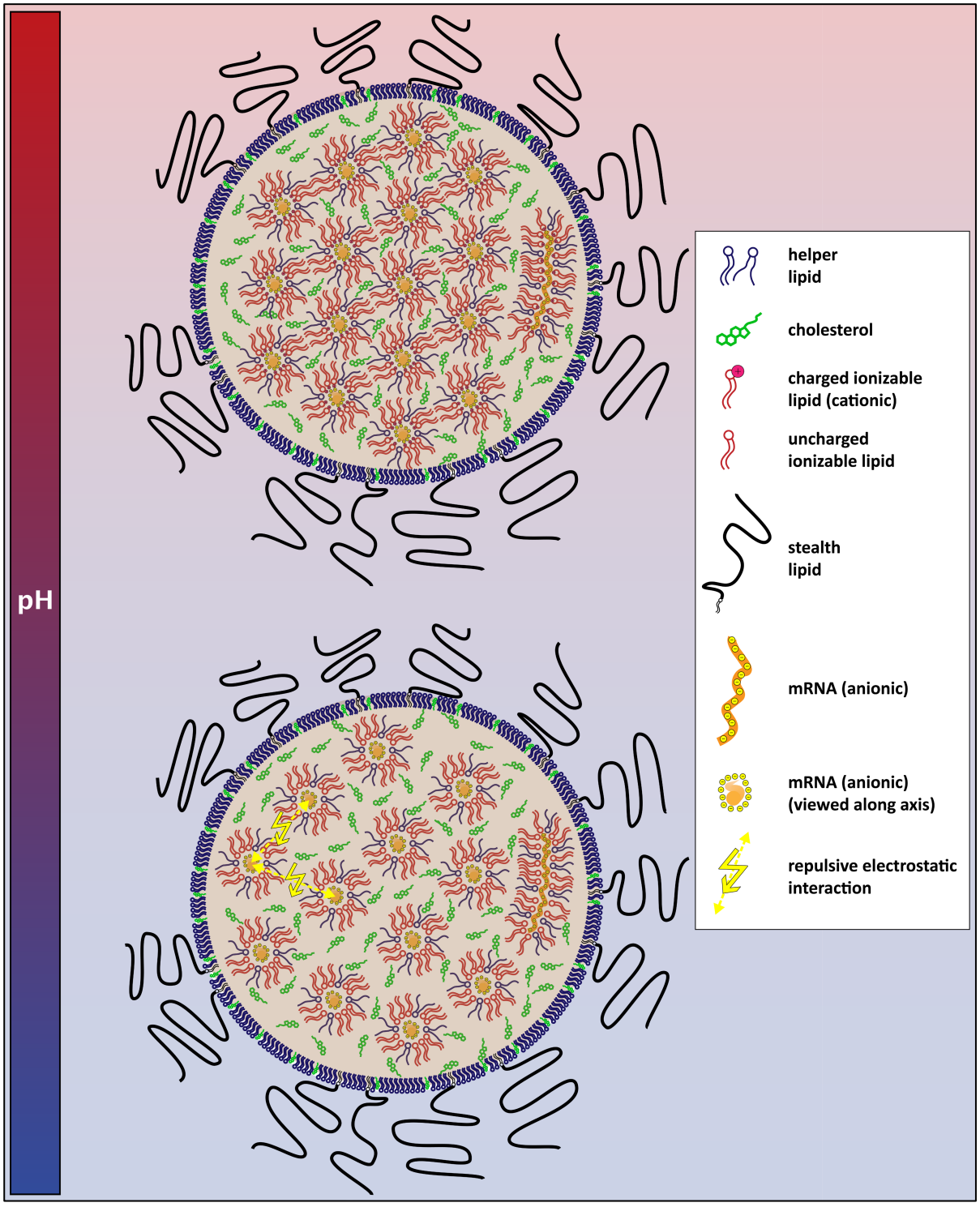

Figure 59. Illustration of the DOPE-dependent inverse hexagonal mRNA ionizable lipid complex inside LNPs and the pH-responsiveness of the secondary long scale structure. The mRNA is illustrated in orange, ionizable lipid in red, helper lipid in blue, cholesterol in purple, and stealth lipid in black. Cationic and anionic charges are represented in pink and yellow, respectively, and exemplary repulsive charges are displayed as yellow arrows. For the sake of illustration, all but one complex in each LNP are shown as a view along the axis of the inverse hexagonal phase, while one complex per particle is shown perpendicular to that axis (right side in both particles).
At low pH (top), the charged ionizable lipid is tightly complexed with the mRNA in an inverse hexagonal structure, which itself is arranged in a secondary order facilitated by cholesterol. At high pH (bottom), the anionic mRNA is screened less efficiently due to the lack of cationic charges, resulting in repulsive electrostatic interactions and therefore a higher spacing of the secondary order between the individual inverse hexagonal mRNA-lipid complexes.

LNPs with an excess negative charge showed slightly different structural features. Again, the DOPE-dependent inverse hexagonal phase could be detected very prominently, however, this time it showed pH-dependent changes in d-spacing. The pH-dependent secondary structure also discussed above was even stronger than for positive N/P ratios and displayed a change in d-spacing from approximately 8 nm to about 12 nm with increasing pH, similar to before. The significance behind the additional and strongly visible structure (orange peak), which displayed a cholesterol-dependent intensity and d-spacing and which was not visible at pH 6.5 – 7.0, could however not be determined. It could be theorized that this contribution is caused by an array of excess mRNA and helper lipid, formed by hydrophilic helper lipid headgroups interacting with the mRNA to stabilize the polar nucleic acid within the lipophilic core, and that the packing order and density of this array is facilitated by cholesterol insertion. However, this is only an attempt at an explanation and cannot be directly derived from the data.

4.2.4 Structure-Function Correlation of LNPs

Comparing the physicochemical results with their corresponding biological efficacies, several interesting observations can be made. The differences in structure between systems comprising different lipid components can also be seen in their transfection efficacy. The intermediate system IM-14, which was lacking cholesterol compared to the LNP-06 formulation, showed low to no transfection in monocytes, while LNP-06 showed dose-dependent Thy1.1 expression in up to 30% of cells, indicating the importance of including this component. Previous studies have also looked at the structural and functional implications of different cholesterol analogues, coming to the same conclusion and attributing this to enhanced membrane fusion capabilities.[86] Interestingly, combining the parameters gained from the SAXS experiments (shown in chapter 3.2.1.3.3) with the transfection data (shown in chapter 3.2.2.2) suggests that lower overall d-spacing (MC3 < DODMA; DOPE < DOPC) seems to correlate with formulation efficacy (LNP-06 < LNP-04 < LNP-08). This could mean that more "compact" particles in terms of internal structure lead to better transfection results. On the other hand, not all biological behavior seems to be influenced by the LNP systems' internal structure, as can be seen by comparing LNP-03 and LNP-04. While no difference in d-spacing, size, or mRNA incorporation could be made out from the SAXS experiments and further physicochemical characterization, the pSar-based system LNP-04 showed significantly higher transfection efficacies than its PEG-based counterpart. However, LNPs comprising pSar-lipids showed higher surface roughness at low pH levels, as determined by Porod-slope analysis. Irregular particle surfaces have only recently been hypothesized to facilitate endosomal escape, which could explain the higher transfection efficacy seen here, as well as those of DLin-MC3-DMA containing formulations compared to those comprising DODMA.[61] In general, the higher transfection efficacy of pSar-functionalized LNPs is in line with previous results in the literature and shows the importance of different surface modifications when comparing LNP formulations.[60] PEG-lipids have previously been discussed to be the cause of several adverse reaction phenomena, a concern that has re-emerged recently after the observation of anaphylactic reactions to the newly approved mRNA-based Covid-19 vaccines.[159,160] Several different mechanistic explanations have been proposed, such as a complement-activation-related pseudoallergy (CARPA), IgE mediated anaphylactic reactions, or anti-PEG antibodies, with the latter also facilitating an accelerated blood clearance (ABC) phenomenon for nanosized delivery systems comprising PEG.[39,161–164] However, Polysarcosine-lipid use in LNPs has been shown not to succumb to these problems.[59,60] Combining the superiority in efficacy of polysarcosine-lipids over PEG-lipids with their other advantages over the previous standard, such as the decreased risk for hypersensitivity reactions, it is clear that pSar-based systems are a major advance in the development of intravenously applicable LNPs for mRNA delivery.

5 | Conclusion and Outlook

Currently, mRNA- and other nucleic acid-based drug products are being clinically tested for a vast variety of potential applications, such as vaccinations against infectious diseases (e.g., seasonal influenza, rabies, hepatitis B, cytomegaloviruses, or the Zika virus), immunotherapies addressing various forms of cancer where current therapies lack encouraging prospects (e.g., melanoma, prostate cancer, and triple negative breast cancer), or protein replacement therapies against rare diseases like methylmalonic acidemia.[165–168] In addition, even more potential therapies are being investigated in the laboratory or preclinical stages, including possible mRNA-based vaccinations against autoimmune diseases such as multiple sclerosis or the aforementioned possibility of *in vivo* gene-editing using LNP-delivered CRISPR-Cas9 technology.[38,169] This shows that the recently approved lipid-based RNA drug products, such as the Covid-19 vaccines, will only have been the start to a new era of pharmaceutical drug products with entirely different characteristics and critical quality attributes to consider, compared to more traditional small molecule API-based drugs.

As mentioned in the introduction, strong efforts in recent years have been spent on efficacy studies and optimization of the transfection efficacy of these nucleic acid drug candidates. However, without the much-needed thorough understanding of the underlying structural properties of the delivery systems, these optimization steps were often based on high-throughput screenings on a trial-and-error basis, rather than on an intelligent design approach. The results in this thesis give accurate *in situ* insights into the structural organization of lipid-based mRNA delivery systems – be it lipoplexes or LNPs – by utilizing potent and seldom applied characterization methods in the shape of small angle scattering techniques. This enabled the confirmation and optimization of previously described models to describe the internal structures and changes thereof more accurately in terms of both formulation and environmental parameters. New models were developed describing the pH-responsiveness of both lipoplexes and lipid nanoparticles, as well as the differences between these kinds of RNA delivery systems. Additionally, a first attempt to draw conclusions about a structure-function relationship was made.

Overall, the results described within this thesis should therefore provide better understanding of the functional and structural coherencies inside lipid-based mRNA delivery systems, which will help in the intelligent design and fine-tuning of the next generation of delivery systems in this just beginning new era of nucleic acid drug products.

6 | References

(1) Helmstädter, A.; Staiger, C. Traditional use of medicinal agents: a valid source of evidence. *Drug discovery today* 2014, *19* (1), 4–7. DOI: 10.1016/j.drudis.2013.07.016. Published Online: Aug. 6, 2013.

(2) Schirrmacher, V. From chemotherapy to biological therapy: A review of novel concepts to reduce the side effects of systemic cancer treatment (Review). *International journal of oncology* 2019, *54* (2), 407–419. DOI: 10.3892/ijo.2018.4661. Published Online: Dec. 10, 2018.

(3) Couzin-Frankel, J. Cancer Immunotherapy. *Science (New York, N.Y.)* 2013, *342* (6165), 1432–1433. DOI: 10.1126/science.342.6165.1432.

(4) Mattiuzzi, C.; Lippi, G. Current Cancer Epidemiology. *Journal of epidemiology and global health* 2019, *9* (4), 217–222. DOI: 10.2991/jegh.k.191008.001.

(5) Beatty, G. L.; Gladney, W. L. Immune escape mechanisms as a guide for cancer immunotherapy. *Clinical cancer research : an official journal of the American Association for Cancer Research* 2015, *21* (4), 687–692. DOI: 10.1158/1078-0432.CCR-14-1860. Published Online: Dec. 12, 2014.

(6) Waldman, A. D.; Fritz, J. M.; Lenardo, M. J. A guide to cancer immunotherapy: from T cell basic science to clinical practice. *Nature reviews. Immunology* 2020, *20* (11), 651–668. DOI: 10.1038/s41577-020-0306-5. Published Online: May. 20, 2020.

(7) Mellman, I.; Coukos, G.; Dranoff, G. Cancer immunotherapy comes of age. *Nature* 2011, *480* (7378), 480–489. DOI: 10.1038/nature10673. Published Online: Dec. 21, 2011.

(8) Yip, A.; Webster, R. M. The market for chimeric antigen receptor T cell therapies. *Nature reviews. Drug discovery* 2018, *17* (3), 161–162. DOI: 10.1038/nrd.2017.266. Published Online: Jan. 29, 2018.

(9) Sahin, U.; Kariko, K.; Tureci, O. mRNA-based therapeutics—developing a new class of drugs. *Nature reviews. Drug discovery* 2014, *13* (10), 759–780. DOI: 10.1038/nrd4278.

(10) Conry, R. M.; LoBuglio, A. F.; Wright, M.; Sumerel, L.; Pike, M. J.; Benjamin, R.; Lu, D.; Curiel, D. T. Characterization of a Messenger RNA Polynucleotide Vaccine Vector. *Cancer Research* 1995, *55* (7), 1397–1400.

(11) Sahin, U.; Derhovanessian, E.; Miller, M.; Kloke, B.-P.; Simon, P.; Löwer, M.; Bukur, V.; Tadmor, A. D.; Luxemburger, U.; Schrörs, B.; Omokoko, T.; Vormehr, M.; Albrecht, C.; Paruzynski, A.; Kuhn, A. N.; Buck, J.; Heesch, S.; Schreeb, K. H.; Müller, F.; Ortseifer, I.; Vogler, I.; Godehardt, E.; Attig, S.; Rae, R.; Breitkreuz, A.; Tolliver, C.; Suchan, M.; Martic, G.; Hohberger, A.; Sorn, P.; Diekmann, J.; Ciesla, J.; Waksmann, O.; Brück, A.-K.; Witt, M.; Zillgen, M.; Rothermel, A.; Kasemann, B.; Langer, D.; Bolte, S.; Diken, M.; Kreiter, S.; Nemecek, R.; Gebhardt, C.; Grabbe, S.; Höller, C.; Utikal, J.; Huber, C.; Loquai, C.; Türeci, Ö. Personalized RNA mutanome vaccines mobilize poly-specific therapeutic immunity against cancer. *Nature* 2017, *547* (7662), 222–226. DOI: 10.1038/nature23003.

(12) Sahin, U.; Türeci, Ö. Personalized vaccines for cancer immunotherapy. *Science (New York, N.Y.)* 2018, *359* (6382), 1355–1360. DOI: 10.1126/science.aar7112.

(13) Kranz, L. M.; Diken, M.; Haas, H.; Kreiter, S.; Loquai, C.; Reuter, K. C.; Meng, M.; Fritz, D.; Vascotto, F.; Hefesha, H.; Grunwitz, C.; Vormehr, M.; Husemann, Y.; Selmi, A.; Kuhn, A. N.; Buck, J.; Derhovanessian, E.; Rae, R.; Attig, S.; Diekmann, J.; Jabulowsky, R. A.; Heesch, S.; Hassel, J.; Langguth, P.; Grabbe, S.; Huber, C.; Tureci, O.; Sahin, U. Systemic RNA delivery to dendritic cells exploits antiviral defence for cancer immunotherapy. *Nature* 2016, *534* (7607), 396–401. DOI: 10.1038/nature18300.

(14) Grabbe, S.; Haas, H.; Diken, M.; Kranz, L. M.; Langguth, P.; Sahin, U. Translating nanoparticulate-personalized cancer vaccines into clinical applications: case study with RNA-lipoplexes for the treatment of melanoma. *Nanomedicine (London, England)* 2016, *11* (20), 2723–2734. DOI: 10.2217/nnm-2016-0275.

(15) European Medicines Agency. *EU Clinical Trials Register. EudraCT Number: 2020-002195-12:An open-label, randomized Phase II trial with BNT111 and cemiplimab in combination or as single agents in patients with anti-PD1-refractory/relapsed, unresectable Stage III or IV melanoma*. https://www.clinicaltrialsregister.eu/ (accessed 2021-07-12).

(16) NIH U.S. National Library of Medicine. *ClinicalTrials.gov Identifier: NCT03897881:An Efficacy Study of Adjuvant Treatment With the Personalized Cancer Vaccine mRNA-4157 and Pembrolizumab in Participants With High-Risk Melanoma (KEYNOTE-942)*. https://clinicaltrials.gov/ (accessed 2021-07-12).

(17) Sadoff, J.; Gray, G.; Vandebosch, A.; Cárdenas, V.; Shukarev, G.; Grinsztejn, B.; Goepfert, P. A.; Truyers, C.; Fennema, H.; Spiessens, B.; Offergeld, K.; Scheper, G.; Taylor, K. L.; Robb, M. L.; Treanor, J.; Barouch, D. H.; Stoddard, J.; Ryser, M. F.; Marovich, M. A.; Neuzil, K. M.; Corey, L.; Cauwenberghs, N.; Tanner, T.; Hardt, K.; Ruiz-Guiñazú, J.; Le Gars, M.; Schuitemaker, H.; van Hoof, J.; Struyf, F.; Douoguih, M. Safety and Efficacy of Single-Dose Ad26.COV2.S Vaccine against Covid-19. *The New England journal of medicine* 2021, *384* (23), 2187–2201. DOI: 10.1056/NEJMoa2101544. Published Online: Apr. 21, 2021.

(18) Voysey, M.; Clemens, S. A. C.; Madhi, S. A.; Weckx, L. Y.; Folegatti, P. M.; Aley, P. K.; Angus, B.; Baillie, V. L.; Barnabas, S. L.; Bhorat, Q. E.; Bibi, S.; Briner, C.; Cicconi, P.; Collins, A. M.; Colin-Jones, R.; Cutland, C. L.; Darton, T. C.; Dheda, K.; Duncan, C. J. A.; Emary, K. R. W.; Ewer, K. J.; Fairlie, L.; Faust, S. N.; Feng, S.; Ferreira, D. M.; Finn, A.; Goodman, A. L.; Green, C. M.; Green, C. A.; Heath, P. T.; Hill, C.; Hill, H.; Hirsch, I.; Hodgson, S. H. C.; Izu, A.; Jackson, S.; Jenkin, D.; Joe, C. C. D.; Kerridge, S.; Koen, A.; Kwatra, G.; Lazarus, R.; Lawrie, A. M.; Lelliott, A.; Libri, V.; Lillie, P. J.; Mallory, R.; Mendes, A. V. A.; Milan, E. P.; Minassian, A. M.; McGregor, A.; Morrison, H.; Mujadidi, Y. F.; Nana, A.; O'Reilly, P. J.; Padayachee, S. D.; Pittella, A.; Plested, E.; Pollock, K. M.; Ramasamy, M. N.; Rhead, S.; Schwarzbold, A. V.; Singh, N.; Smith, A.; Song, R.; Snape, M. D.; Sprinz, E.; Sutherland, R. K.; Tarrant, R.; Thomson, E. C.; Török, M. E.; Toshner, M.; Turner, D. P. J.; Vekemans, J.; Villafana, T. L.; Watson, M. E. E.; Williams, C. J.; Douglas, A. D.; Hill, A. V. S.; Lambe, T.; Gilbert, S. C.; Pollard, A. J.; on behalf of theOxford COVID Vaccine Trial Group. Safety and efficacy of the ChAdOx1 nCoV-19 vaccine (AZD1222) against SARS-CoV-2: an interim analysis of four

randomised controlled trials in Brazil, South Africa, and the UK. *The Lancet* 2021, *397* (10269), 99–111. DOI: 10.1016/S0140-6736(20)32661-1.

(19) Tatsis, N.; Ertl, H. C. J. Adenoviruses as vaccine vectors. *Molecular therapy : the journal of the American Society of Gene Therapy* 2004, *10* (4), 616–629. DOI: 10.1016/j.ymthe.2004.07.013.

(20) Lowe, D. *Brazil Rejects the Gamaleya Vaccine*. https://blogs.sciencemag.org/pipeline/archives/2021/04/28/brazil-rejects-the-gamaleya-vaccine (accessed 2021-07-14).

(21) Marzio, G.; Kerkvliet, E.; Bogaards, J. A.; Koelewijn, S.; Groot, A. de; Gijsbers, L.; Weverling, G. J.; Vogels, R.; Havenga, M.; Custers, J.; Pau, M. G.; Guichoux, J. Y.; Lewis, J.; Goudsmit, J. A replication-competent adenovirus assay for E1-deleted Ad35 vectors produced in PER.C6 cells. *Vaccine* 2007, *25* (12), 2228–2237. DOI: 10.1016/j.vaccine.2006.12.011. Published Online: Dec. 28, 2006.

(22) Thomas, C. E.; Ehrhardt, A.; Kay, M. A. Progress and problems with the use of viral vectors for gene therapy. *Nature reviews. Genetics* 2003, *4* (5), 346–358. DOI: 10.1038/nrg1066.

(23) Akbarzadeh, A.; Rezaei-Sadabady, R.; Davaran, S.; Joo, S. W.; Zarghami, N.; Hanifehpour, Y.; Samiei, M.; Kouhi, M.; Nejati-Koshki, K. Liposome: classification, preparation, and applications. *Nanoscale research letters* 2013, *8* (1), 102. DOI: 10.1186/1556-276X-8-102. Published Online: Feb. 22, 2013.

(24) Bangham, A. D.; Standish, M. M.; Watkins, J. C. Diffusion of univalent ions across the lamellae of swollen phospholipids. *Journal of Molecular Biology* 1965, *13* (1), 238-IN27. DOI: 10.1016/S0022-2836(65)80093-6.

(25) Wagner, A.; Vorauer-Uhl, K. Liposome technology for industrial purposes. *Journal of drug delivery* 2011, *2011*, 591325. DOI: 10.1155/2011/591325.

(26) Schwendener, R. A. Liposomes in biology and medicine. *Advances in experimental medicine and biology* 2007, *620*, 117–128. DOI: 10.1007/978-0-387-76713-0_9.

(27) Bulbake, U.; Doppalapudi, S.; Kommineni, N.; Khan, W. Liposomal Formulations in Clinical Use: An Updated Review. *Pharmaceutics* 2017, *9* (4), 12. DOI: 10.3390/pharmaceutics9020012.

(28) Abuchowski, A.; van Es, T.; Palczuk, N. C.; Davis, F. F. Alteration of immunological properties of bovine serum albumin by covalent attachment of polyethylene glycol. *The Journal of biological chemistry* 1977, *252* (11), 3578–3581. DOI: 10.1016/S0021-9258(17)40291-2.

(29) Veronese, F. M.; Mero, A. The impact of PEGylation on biological therapies. *BioDrugs : clinical immunotherapeutics, biopharmaceuticals and gene therapy* 2008, *22* (5), 315–329. DOI: 10.2165/00063030-200822050-00004.

(30) Porche, D. J. Liposomal doxorubicin (Doxil®). *Journal of the Association of Nurses in AIDS Care* 1996, *7* (2), 55–59. DOI: 10.1016/S1055-3290(96)80016-1.

(31) Barenholz, Y. Doxil®--the first FDA-approved nano-drug: lessons learned. *Journal of controlled release : official journal of the Controlled Release Society* 2012, *160* (2), 117–134. DOI: 10.1016/j.jconrel.2012.03.020. Published Online: Mar. 29, 2012.

(32) Karn, P. R.; Cho, W.; Hwang, S.-J. Liposomal drug products and recent advances in the synthesis of supercritical fluid-mediated liposomes. *Nanomedicine (London, England)* 2013, *8* (9), 1529–1548. DOI: 10.2217/NNM.13.131.

(33) Cardarelli, F.; Digiacomo, L.; Marchini, C.; Amici, A.; Salomone, F.; Fiume, G.; Rossetta, A.; Gratton, E.; Pozzi, D.; Caracciolo, G. The intracellular trafficking mechanism of Lipofectamine-based transfection reagents and its implication for gene delivery. *Scientific reports* 2016, *6*, 25879. DOI: 10.1038/srep25879. Published Online: May. 11, 2016.

(34) Richner, J. M.; Himansu, S.; Dowd, K. A.; Butler, S. L.; Salazar, V.; Fox, J. M.; Julander, J. G.; Tang, W. W.; Shresta, S.; Pierson, T. C.; Ciaramella, G.; Diamond, M. S. Modified mRNA Vaccines Protect against Zika Virus Infection. *Cell* 2017, *168* (6), 1114-1125.e10. DOI: 10.1016/j.cell.2017.02.017.

(35) European Medicines Agency. *EMA recommends first COVID-19 vaccine for authorisation in the EU*. https://www.ema.europa.eu/en/news/ema-recommends-first-covid-19-vaccine-authorisation-eu (accessed 2021-07-13).

(36) European Medicines Agency. *EMA recommends COVID-19 Vaccine Moderna for authorisation in the EU*. https://www.ema.europa.eu/en/news/ema-recommends-covid-19-vaccine-moderna-authorisation-eu (accessed 2021-07-13).

(37) Woolston, C. How RNA therapies could be used to tackle the world's biggest killer. *Nature* 2019, *574* (7778), S13-S14. DOI: 10.1038/d41586-019-03073-7.

(38) Krienke, C.; Kolb, L.; Diken, E.; Streuber, M.; Kirchhoff, S.; Bukur, T.; Akilli-Öztürk, Ö.; Kranz, L. M.; Berger, H.; Petschenka, J.; Diken, M.; Kreiter, S.; Yogev, N.; Waisman, A.; Karikó, K.; Türeci, Ö.; Sahin, U. A noninflammatory mRNA vaccine for treatment of experimental autoimmune encephalomyelitis. *Science (New York, N.Y.)* 2021, *371* (6525), 145–153. DOI: 10.1126/science.aay3638.

(39) Marques, M. R. C.; Choo, Q.; Ashtikar, M.; Rocha, T. C.; Bremer-Hoffmann, S.; Wacker, M. G. Nanomedicines - Tiny particles and big challenges. *Advanced drug delivery reviews* 2019, *151-152*, 23–43. DOI: 10.1016/j.addr.2019.06.003.

(40) U.S. Department of Health and Human Services; Food and Drug Administration; Center for Drug Evaluation and Research. *Guidance for Industry*:*Liposome Drug Products*. Chemistry, Manufacturing, and Controls; Human, 2018.

(41) Committee for Human Medicinal Products. *Reflection paper on nanotechnology-based medicinal products for Human Use*:*EMEA/CHMP/79769/2006*.

(42) Committee for Human Medicinal Products. *Reflection paper on the data requirements for intravenous liposomal products developed with reference to an innovator liposomal product*:*EMA/CHMP/806058/2009/Rev. 02*.

(43) COMMISSION RECOMMENDATION of 18 October 2011 on the definition of nanomaterial (Text with EEA relevance):(2011/696/EU). *Official Journal of the European Union* 2011 (275), 38–40.

(44) *How to prepare registration dossiers covering nanoforms*:*October 2020*, First version; ECHA, 2020.

(45) European Chemicals Agency. *How to prepare registration dossiers covering nanoforms*:*ECHA-20-H-17-EN*.

(46) O'Hagan, D. T. The intestinal uptake of particles and the implications for drug and antigen delivery. *Journal of Anatomy* 1996, *189* (Pt 3), 477–482.

(47) Danaei, M.; Dehghankhold, M.; Ataei, S.; Hasanzadeh Davarani, F.; Javanmard, R.; Dokhani, A.; Khorasani, S.; Mozafari, M. R. Impact of Particle Size and Polydispersity Index on the Clinical Applications of Lipidic Nanocarrier Systems. *Pharmaceutics* 2018, *10* (2). DOI: 10.3390/pharmaceutics10020057. Published Online: May. 18, 2018.

(48) Elouahabi, A.; Ruysschaert, J.-M. Formation and intracellular trafficking of lipoplexes and polyplexes. *Molecular therapy : the journal of the American Society of Gene Therapy* 2005, *11* (3), 336–347. DOI: 10.1016/j.ymthe.2004.12.006.

(49) Tabatt, K.; Kneuer, C.; Sameti, M.; Olbrich, C.; Müller, R. H.; Lehr, C.-M.; Bakowsky, U. Transfection with different colloidal systems: comparison of solid lipid nanoparticles and liposomes. *Journal of controlled release : official journal of the Controlled Release Society* 2004, *97* (2), 321–332. DOI: 10.1016/j.jconrel.2004.02.029.

(50) Torchilin, V. Tumor delivery of macromolecular drugs based on the EPR effect. *Advanced drug delivery reviews* 2011, *63* (3), 131–135. DOI: 10.1016/j.addr.2010.03.011. Published Online: Mar. 18, 2010.

(51) Martínez-González, R.; Estelrich, J.; Busquets, M. A. Liposomes Loaded with Hydrophobic Iron Oxide Nanoparticles: Suitable T_2 Contrast Agents for MRI. *International journal of molecular sciences* 2016, *17* (8). DOI: 10.3390/ijms17081209. Published Online: Jul. 27, 2016.

(52) Cheng, Q.; Wei, T.; Farbiak, L.; Johnson, L. T.; Dilliard, S. A.; Siegwart, D. J. Selective organ targeting (SORT) nanoparticles for tissue-specific mRNA delivery and CRISPR-Cas gene editing. *Nature nanotechnology* 2020, *15* (4), 313–320. DOI: 10.1038/s41565-020-0669-6.

(53) Kedmi, R.; Ben-Arie, N.; Peer, D. The systemic toxicity of positively charged lipid nanoparticles and the role of Toll-like receptor 4 in immune activation. *Biomaterials* 2010, *31* (26), 6867–6875. DOI: 10.1016/j.biomaterials.2010.05.027.

(54) Rappolt, M. Chapter 9 The Biologically Relevant Lipid Mesophases as "Seen" by X-Rays. In *Advances in Planar Lipid Bilayers and Liposomes*:*Volume 5*; Advances in Planar Lipid Bilayers and Liposomes; Elsevier, 2006; pp 253–283. DOI: 10.1016/S1554-4516(06)05009-5.

(55) Koltover, I. An Inverted Hexagonal Phase of Cationic Liposome-DNA Complexes Related to DNA Release and Delivery. *Science (New York, N.Y.)* 1998, *281* (5373), 78–81. DOI: 10.1126/science.281.5373.78.

(56) Dittrich, M.; Heinze, M.; Wölk, C.; Funari, S. S.; Dobner, B.; Möhwald, H.; Brezesinski, G. Structure-function relationships of new lipids designed for DNA transfection. *Chemphyschem : a European journal of chemical physics and physical chemistry* 2011, *12* (12), 2328–2337. DOI: 10.1002/cphc.201100065.

(57) Leung, A. K. K.; Hafez, I. M.; Baoukina, S.; Belliveau, N. M.; Zhigaltsev, I. V.; Afshinmanesh, E.; Tieleman, D. P.; Hansen, C. L.; Hope, M. J.; Cullis, P. R. Lipid Nanoparticles Containing siRNA Synthesized by Microfluidic Mixing Exhibit an Electron-Dense Nanostructured Core. *The journal of physical chemistry. C, Nanomaterials and interfaces* 2012, *116* (34), 18440–18450. DOI: 10.1021/jp303267y.

(58) Szebeni, J. Complement activation-related pseudoallergy: a new class of drug-induced acute immune toxicity. *Toxicology* 2005, *216* (2-3), 106–121. DOI: 10.1016/j.tox.2005.07.023. Published Online: Sep. 2, 2005.

(59) Bleher, S.; Buck, J.; Muhl, C.; Sieber, S.; Barnert, S.; Witzigmann, D.; Huwyler, J.; Barz, M.; Süss, R. Poly(Sarcosine) Surface Modification Imparts Stealth-Like Properties to Liposomes. *Small (Weinheim an der Bergstrasse, Germany)* 2019, *15* (50), e1904716. DOI: 10.1002/smll.201904716.

(60) Nogueira, S.; Schlegel, A.; Maxeiner, K.; Weber, B.; Barz, M.; Schroer, M. A.; Blanchet, C. E.; Svergun, D.; Ramishetti, S.; Peer, D.; Langguth, P.; Sahin, U.; Haas, H. Polysarcosine-Functionalized Lipid Nanoparticles for Therapeutic mRNA Delivery. *ACS Appl. Nano Mater.* 2020. DOI: 10.1021/acsanm.0c01834.

(61) Sebastiani, F.; Yanez Arteta, M.; Lerche, M.; Porcar, L.; Lang, C.; Bragg, R. A.; Elmore, C. S.; Krishnamurthy, V. R.; Russell, R. A.; Darwish, T.; Pichler, H.; Waldie, S.; Moulin, M.; Haertlein, M.; Forsyth, V. T.; Lindfors, L.; Cárdenas, M. Apolipoprotein E Binding Drives Structural and Compositional Rearrangement of mRNA-Containing Lipid Nanoparticles. *ACS nano* 2021. DOI: 10.1021/acsnano.0c10064. Published Online: Mar. 23, 2021.

(62) Bros, M.; Nuhn, L.; Simon, J.; Moll, L.; Mailänder, V.; Landfester, K.; Grabbe, S. The Protein Corona as a Confounding Variable of Nanoparticle-Mediated Targeted Vaccine Delivery. *Frontiers in immunology* 2018, *9*, 1760. DOI: 10.3389/fimmu.2018.01760. Published Online: Aug. 2, 2018.

(63) Müller, L. K.; Simon, J.; Rosenauer, C.; Mailänder, V.; Morsbach, S.; Landfester, K. The Transferability from Animal Models to Humans: Challenges Regarding Aggregation and Protein Corona Formation of Nanoparticles. *Biomacromolecules* 2018, *19* (2), 374–385. DOI: 10.1021/acs.biomac.7b01472. Published Online: Jan. 12, 2018.

(64) Kowalski, P. S.; Rudra, A.; Miao, L.; Anderson, D. G. Delivering the Messenger: Advances in Technologies for Therapeutic mRNA Delivery. *Molecular therapy : the journal of the American Society of Gene Therapy* 2019, *27* (4), 710–728. DOI: 10.1016/j.ymthe.2019.02.012. Published Online: Feb. 19, 2019.

(65) Torchilin, V. P. Recent advances with liposomes as pharmaceutical carriers. *Nature reviews. Drug discovery* 2005, *4* (2), 145–160. DOI: 10.1038/nrd1632.

(66) Martens, T. F.; Remaut, K.; Demeester, J.; Smedt, S. C. de; Braeckmans, K. Intracellular delivery of nanomaterials: How to catch endosomal escape in the act. *Nano Today* 2014, *9* (3), 344–364. DOI: 10.1016/j.nantod.2014.04.011.

(67) Anselmo, A. C.; Mitragotri, S. Nanoparticles in the clinic: An update. *Bioengineering & translational medicine* 2019, *4* (3), e10143. DOI: 10.1002/btm2.10143. Published Online: Sep. 5, 2019.

(68) Heath, P. T.; Galiza, E. P.; Baxter, D. N.; Boffito, M.; Browne, D.; Burns, F.; Chadwick, D. R.; Clark, R.; Cosgrove, C.; Galloway, J.; Goodman, A. L.; Heer, A.; Higham, A.; Iyengar, S.; Jamal, A.; Jeanes, C.; Kalra, P. A.; Kyriakidou, C.; McAuley, D. F.; Meyrick, A.; Minassian, A. M.; Minton, J.; Moore, P.; Munsoor, I.; Nicholls, H.; Osanlou, O.; Packham, J.; Pretswell, C. H.; San Francisco Ramos, A.; Saralaya, D.; Sheridan, R. P.; Smith, R.; Soiza, R. L.; Swift, P. A.; Thomson, E. C.; Turner, J.; Viljoen, M. E.; Albert, G.; Cho, I.; Dubovsky, F.; Glenn, G.; Rivers, J.; Robertson, A.; Smith, K.; Toback, S.; for the 2019nCoV-302 Study Group. Safety and Efficacy of NVX-CoV2373 Covid-19 Vaccine. *The New England journal of medicine* 2021. DOI: 10.1056/NEJMoa2107659. Published Online: Jun. 30, 2021.

(69) European Medicines Agency. *EMA recommends Nuvaxovid for authorisation in the EU*, 2021.

(70) Mitchell, M. J.; Billingsley, M. M.; Haley, R. M.; Wechsler, M. E.; Peppas, N. A.; Langer, R. Engineering precision nanoparticles for drug delivery. *Nature reviews. Drug discovery* 2021, *20* (2), 101–124. DOI: 10.1038/s41573-020-0090-8. Published Online: Dec. 4, 2020.

(71) Uebbing, S.; Kreiß, M.; Scholl, F.; Häfner, A.-K.; Sürün, D.; Garscha, U.; Werz, O.; Basavarajappa, D.; Samuelsson, B.; Rådmark, O.; Suess, B.; Steinhilber, D. Modulation of microRNA processing by 5-lipoxygenase. *FASEB journal : official publication of the Federation of American Societies for Experimental Biology* 2021, *35* (2), e21193. DOI: 10.1096/fj.202002108R. Published Online: Nov. 17, 2020.

(72) Watts, J. K.; Corey, D. R. Silencing disease genes in the laboratory and the clinic. *The Journal of pathology* 2012, *226* (2), 365–379. DOI: 10.1002/path.2993. Published Online: Nov. 9, 2011.

(73) Lee, J. F.; Stovall, G. M.; Ellington, A. D. Aptamer therapeutics advance. *Current opinion in chemical biology* 2006, *10* (3), 282–289. DOI: 10.1016/j.cbpa.2006.03.015. Published Online: Apr. 18, 2006.

(74) Jinek, M.; Chylinski, K.; Fonfara, I.; Hauer, M.; Doudna, J. A.; Charpentier, E. A programmable dual-RNA-guided DNA endonuclease in adaptive bacterial immunity. *Science (New York, N.Y.)* 2012, *337* (6096), 816–821. DOI: 10.1126/science.1225829. Published Online: Jun. 28, 2012.

(75) The Royal Swedish Academy of Sciences. *The Nobel Prize in Chemistry 2020*, 2020.

(76) Babačić, H.; Mehta, A.; Merkel, O.; Schoser, B. CRISPR-cas gene-editing as plausible treatment of neuromuscular and nucleotide-repeat-expansion diseases: A systematic review. *PloS one* 2019, *14* (2), e0212198. DOI: 10.1371/journal.pone.0212198. Published Online: Feb. 22, 2019.

(77) Kim, Y.-K. RNA Therapy: Current Status and Future Potential. *Chonnam medical journal* 2020, *56* (2), 87–93. DOI: 10.4068/cmj.2020.56.2.87. Published Online: May. 25, 2020.

(78) Kulkarni, J. A.; Witzigmann, D.; Thomson, S. B.; Chen, S.; Leavitt, B. R.; Cullis, P. R.; van der Meel, R. The current landscape of nucleic acid therapeutics. *Nature nanotechnology* 2021, *16* (6), 630–643. DOI: 10.1038/s41565-021-00898-0. Published Online: May. 31, 2021.

(79) Magadum, A.; Kaur, K.; Zangi, L. mRNA-Based Protein Replacement Therapy for the Heart. *Molecular therapy : the journal of the American Society of Gene Therapy* 2019, *27* (4), 785–793. DOI: 10.1016/j.ymthe.2018.11.018. Published Online: Dec. 6, 2018.

(80) Gorzelany, J. A.; Souza, M. P. de. Protein replacement therapies for rare diseases: a breeze for regulatory approval? *Science Translational Medicine* 2013, *5* (178), 178fs10. DOI: 10.1126/scitranslmed.3005007.

(81) Akinc, A.; Maier, M. A.; Manoharan, M.; Fitzgerald, K.; Jayaraman, M.; Barros, S.; Ansell, S.; Du, X.; Hope, M. J.; Madden, T. D.; Mui, B. L.; Semple, S. C.; Tam, Y. K.; Ciufolini, M.; Witzigmann, D.; Kulkarni, J. A.; van der Meel, R.; Cullis, P. R. The Onpattro story and the clinical translation of nanomedicines containing nucleic acid-based drugs. *Nature nanotechnology* 2019, *14* (12), 1084–1087. DOI: 10.1038/s41565-019-0591-y.

(82) Dittrich, M.; Brauer, C.; Funari, S. S.; Dobner, B.; Brezesinski, G.; Wölk, C. Interactions of Cationic Lipids with DNA: A Structural Approach. *Langmuir : the ACS journal of surfaces and colloids* 2018, *34* (49), 14858–14868. DOI: 10.1021/acs.langmuir.8b01635.

(83) Torchilin, V. P.; Zhou, F.; Huang, L. pH-Sensitive Liposomes. *Journal of liposome research* 2008, *3* (2), 201–255. DOI: 10.3109/08982109309148213.

(84) Olden, B. R.; Cheng, E.; Cheng, Y.; Pun, S. H. Identifying key barriers in cationic polymer gene delivery to human T cells. *Biomaterials science* 2019, *7* (3), 789–797. DOI: 10.1039/c8bm01262h.

(85) Jayaraman, M.; Ansell, S. M.; Mui, B. L.; Tam, Y. K.; Chen, J.; Du, X.; Butler, D.; Eltepu, L.; Matsuda, S.; Narayanannair, J. K.; Rajeev, K. G.; Hafez, I. M.; Akinc, A.; Maier, M. A.; Tracy, M. A.; Cullis, P. R.; Madden, T. D.; Manoharan, M.; Hope, M. J. Maximizing the potency of siRNA lipid nanoparticles for hepatic gene silencing in vivo. *Angewandte Chemie (International ed. in English)* 2012, *51* (34), 8529–8533. DOI: 10.1002/anie.201203263.

(86) Patel, S.; Ashwanikumar, N.; Robinson, E.; Xia, Y.; Mihai, C.; Griffith, J. P.; Hou, S.; Esposito, A. A.; Ketova, T.; Welsher, K.; Joyal, J. L.; Almarsson, Ö.; Sahay, G. Naturally-occurring cholesterol analogues in lipid nanoparticles induce polymorphic shape and enhance intracellular delivery of mRNA. *Nature communications* 2020, *11* (1). DOI: 10.1038/s41467-020-14527-2.

(87) Muhl, C.; Conrad, M.; Unthan, D.; Barz, M. Synthesis and characterization of bisalkylated polysarcosine-based lipopolymers. *European Polymer Journal* 2019, *120*, 109223. DOI: 10.1016/j.eurpolymj.2019.109223.

(88) G. Alina, Z. Attala, J. Bakker, W. Bouwman, I. Breßler, P. Butler, K. Campbell, J-H. Cho, T. Cooper-Bennun, R. Cortes Hernandez, M. Doucet, C. Durniak, L. Forster, M. Gonzalez, R. Heenan, A. Jackson, G. Jensen, P. Kienzle, S. King, S. Kline, J. Krzywon, D. Mannicke, A. Nelson, T. Nielsen, M. Oakley, L. O'Driscoll, H. Park, P. Parker, W. Potrzebowski, S. Prescott, P. Rozyczko, T. Snow, A. Washington, R. Whitley, and J. Zhou. *SasView*. www.sasview.org (accessed 2021-04-13).

(89) SMITH, M. E.; SMITH, L. B. Piperazine dihydrochloride and glycylglycine as non-toxic buffers in distilled water and in sea water. *The Biological bulletin* 1949, *96* (3), 233–237.

(90) Romeis, B. *Mikroskopische Technik*, 16th ed.; R. Oldenbourg Verlag, 1968.

(91) Marchini, C.; Pozzi, D.; Montani, M.; Alfonsi, C.; Amici, A.; Amenitsch, H.; Candeloro De Sanctis, S.; Caracciolo, G. Tailoring lipoplex composition to the lipid composition of plasma membrane: a Trojan horse for cell entry? *Langmuir : the ACS journal of surfaces and colloids* 2010, *26* (17), 13867–13873. DOI: 10.1021/la1023899.

(92) Ziller, A.; Nogueira, S. S.; Huehn, E.; Funari, S. S.; Brezesinski, G.; Hartmann, H.; Sahin, U.; Haas, H.; Langguth, P. Incorporation of mRNA in lamellar lipid matrices for parenteral administration. *Molecular Pharmaceutics* 2018, *15* (2), 642–651. DOI: 10.1021/acs.molpharmaceut.7b01022.

(93) Massing, U.; Cicko, S.; Ziroli, V. Dual asymmetric centrifugation (DAC)--a new technique for liposome preparation. *Journal of controlled release : official journal of the Controlled Release Society* 2008, *125* (1), 16–24. DOI: 10.1016/j.jconrel.2007.09.010.

(94) Batzri, S.; Korn, E. D. Single bilayer liposomes prepared without sonication. *Biochimica et Biophysica Acta (BBA) - Biomembranes* 1973, *298* (4), 1015–1019. DOI: 10.1016/0005-2736(73)90408-2.

(95) Jeffs, L. B.; Palmer, L. R.; Ambegia, E. G.; Giesbrecht, C.; Ewanick, S.; MacLachlan, I. A scalable, extrusion-free method for efficient liposomal encapsulation of plasmid DNA. *Pharmaceutical research* 2005, *22* (3), 362–372.

(96) Abstiens, K.; Goepferich, A. M. Microfluidic manufacturing improves polydispersity of multicomponent polymeric nanoparticles. *Journal of Drug Delivery Science and Technology* 2019, *49*, 433–439. DOI: 10.1016/j.jddst.2018.12.009.

(97) Wagner, A.; Vorauer-Uhl, K.; Kreismayr, G.; Katinger, H. The crossflow injection technique: an improvement of the ethanol injection method. *Journal of liposome research* 2002, *12* (3), 259–270. DOI: 10.1081/LPR-120014761.

(98) <729> Globule Size Distribution in Lipid Injectable Emulsions. In *USP 36 - NF 31 The United States Pharmacopeia and National Formulary 2013*:*Main edition plus Supplements 1 and 2,* 1., neue Ausg; Deutscher Apotheker Verlag, 2012.

(99) Bhattacharjee, S. DLS and zeta potential - What they are and what they are not? *Journal of controlled release : official journal of the Controlled Release Society* 2016, *235*, 337–351. DOI: 10.1016/j.jconrel.2016.06.017.

(100) Einstein, A. Über die von der molekularkinetischen Theorie der Wärme geforderte Bewegung von in ruhenden Flüssigkeiten suspendierten Teilchen. *Ann. Phys.* 1905, *322* (8), 549–560. DOI: 10.1002/andp.19053220806.

(101) Santosh, M. S.; Bhat, D. K.; Bhat, A. S. Molecular Interactions in Glycylglycine−MnCl 2 Aqueous Solutions at (288.15, 293.15, 298.15, 303.15, 308.15, 313.15, and 318.15) K. *J. Chem. Eng. Data* 2009, *54* (10), 2813–2818. DOI: 10.1021/je800732f.

(102) HORIBA Ltd. *Z-Average Particle Size: An Explanation*. https://www.horiba.com/de/scientific/products/particle-characterization/education/sz-100/particle-size-by-dynamic-light-scattering-resources/what-is-z-average/ (accessed 2021-03-05).

(103) Wimedia Commons. *Diagram of zeta potential and slipping planeV2.svg*:*Diagram showing the ionic concentration and potential difference as a function of distance from the charged surface of a particle suspended in a dispersion medium.* https://commons.wikimedia.org/wiki/File:Diagram_of_zeta_potential_and_slipping_planeV2.svg (accessed 2021-03-08).

(104) Clogston, J. D.; Patri, A. K. Zeta potential measurement. In *Characterization of Nanoparticles Intended for Drug Delivery*; McNeil, S. E., Ed., Vol. 697; Humana Press, 2011; pp 63–70. DOI: 10.1007/978-1-60327-198-1_6.

(105) Molecular Probes, I. *Quant-iT™ RiboGreen® RNA Reagent and Kit*:*MP 11490*. https://www.thermofisher.com/document-connect/document-connect.html?url=https%3A%2F%2Fassets.thermofisher.com%2FTFS-Assets%2FLSG%2Fmanuals%2Fmp11490.pdf&title=UXVhbnQtaVQgUmlib0dyZWVuIFJOQSBSZWFnZW50IGFuZCBLaXQ=.

(106) Hayward, S. L.; Francis, D. M.; Kholmatov, P.; Kidambi, S. Targeted Delivery of MicroRNA125a-5p by Engineered Lipid Nanoparticles for the Treatment of HER2 Positive Metastatic Breast Cancer. *Journal of biomedical nanotechnology* 2016, *12* (3), 554–568. DOI: 10.1166/jbn.2016.2194.

(107) Heyes, J.; Palmer, L.; Bremner, K.; MacLachlan, I. Cationic lipid saturation influences intracellular delivery of encapsulated nucleic acids. *Journal of controlled release : official journal of the Controlled Release Society* 2005, *107* (2), 276–287. DOI: 10.1016/j.jconrel.2005.06.014.

(108) Thaler, M.; Ilsinger, B. Das Transmissionselektronenmikroskop. In *Grundlagen der Licht- und Elektronenmikroskopie*; Linnemann, A., Kühl, S., Eds.; UTB, Vol. 4864; Verlag Eugen Ulmer, 2018.

(109) Schnablegger, H.; Singh, Y. *The SAXS Guide*:*Getting acquainted with the principles*, 4th edition; Anton Paar GmbH, 2017.

(110) Deutsches Elektronen-Synchrotron DESY. *DESY - PETRA III*. https://petra3.desy.de/index_eng.html (accessed 2021-03-19).

(111) Agra-Kooijman, D. M.; Kumar, S. X-Ray Scattering Investigations of Liquid Crystals. In *Handbook of Liquid Crystals*; Goodby, J. W., Tschierske, C., Raynes, P., Gleeson, H., Kato, T., Collings, P. J., Eds.; Wiley-VCH Verlag GmbH & Co. KGaA, 2014; pp 1–38. DOI: 10.1002/9783527671403.hlc014.

(112) Blanchet, C. E.; Spilotros, A.; Schwemmer, F.; Graewert, M. A.; Kikhney, A.; Jeffries, C. M.; Franke, D.; Mark, D.; Zengerle, R.; Cipriani, F.; Fiedler, S.; Roessle, M.; Svergun, D. I. Versatile sample environments and automation for biological solution X-ray scattering experiments at the P12 beamline (PETRA III, DESY). *Journal of applied crystallography* 2015, *48* (Pt 2), 431–443. DOI: 10.1107/S160057671500254X.

(113) Yevick, D.; Yevick, H. *Fundamental Math and Physics for Scientists and Engineers*; Wiley, 2014. DOI: 10.1002/9781118979792.

(114) Harroun, T. A.; Wignall, G. D.; Katsaras, J. Neutron Scattering for Biology. In *Neutron Scattering in Biology: Techniques and Applications*; Fitter, J., Gutberlet, T., Katsaras, J., Eds.; Springer Berlin Heidelberg, 2006; pp 1–18. DOI: 10.1007/3-540-29111-3_1.

(115) Pabst, G.; Kucerka, N.; Nieh, M.-P.; Rheinstädter, M. C.; Katsaras, J. Applications of neutron and X-ray scattering to the study of biologically relevant model membranes. *Chemistry and physics of lipids* 2010, *163* (6), 460–479. DOI: 10.1016/j.chemphyslip.2010.03.010.

(116) Compton, A. H. A Quantum Theory of the Scattering of X-rays by Light Elements. *Phys. Rev.* 1923, *21* (5), 483–502. DOI: 10.1103/PhysRev.21.483.

(117) Birkholz, M.; Fewster, P. F. *Thin film analysis by X-Ray scattering*, 2nd reprint; Wiley-VCH, 2009.

(118) Schroer, M. A. *Small angle X-ray scattering studies on proteins under extreme conditions*.

(119) Li, N. Y. D.; Perutková, Š.; Iglič, A.; Rappolt, M. My first electron density map: A beginner's guide to small angle X-ray diffraction. *Elektrotehniski Vestnik* 2017, *84* (3), 69.

(120) Suryanarayana, C.; Norton, M. G. *X-Ray Diffraction*:*A Practical Approach*; Springer International Publishing, 20.

(121) Pedersen, J. S. Modelling of small-angle scattering data from colloids and polymer systems. In *Neutrons, X-rays and light*:*Scattering methods applied to soft condensed matter,* Transferred to digital print; Lindner, P., Ed.; North-Holland delta series; Elsevier, 2002; p 391.

(122) Chen, Y.; Pollack, L. SAXS studies of RNA: structures, dynamics, and interactions with partners. *Wiley interdisciplinary reviews. RNA* 2016, *7* (4), 512–526. DOI: 10.1002/wrna.1349.

(123) Breßler, I.; Kohlbrecher, J.; Thünemann, A. F. SASfit: a tool for small-angle scattering data analysis using a library of analytical expressions. *Journal of applied crystallography* 2015, *48* (Pt 5), 1587–1598. DOI: 10.1107/S1600576715016544.

(124) Bragg, W. H.; Bragg, W. L. The reflection of X-rays by crystals. *Proc. R. Soc. Lond. A* 1913, *88* (605), 428–438. DOI: 10.1098/rspa.1913.0040.

(125) Harper, P. E.; Mannock, D. A.; Lewis, R. N.A.H.; McElhaney, R. N.; Gruner, S. M. X-Ray Diffraction Structures of Some Phosphatidylethanolamine Lamellar and Inverted Hexagonal Phases*. *Biophysical Journal* 2001, *81* (5), 2693–2706. DOI: 10.1016/S0006-3495(01)75912-7.

(126) Pabst, G.; Koschuch, R.; Pozo-Navas, B.; Rappolt, M.; Lohner, K.; Laggner, P. Structural analysis of weakly ordered membrane stacks. *Journal of applied crystallography* 2003, *36* (6), 1378–1388. DOI: 10.1107/S0021889803017527.

(127) Nawroth, T.; Buch, P.; Buch, K.; Langguth, P.; Schweins, R. Liposome formation from bile salt-lipid micelles in the digestion and drug delivery model FaSSIF(mod) estimated by combined time-resolved neutron and dynamic light scattering. *Molecular Pharmaceutics* 2011, *8* (6), 2162–2172. DOI: 10.1021/mp100296w. Published Online: Nov. 16, 2011.

(128) *SAXS1 - LNLS*:*Overview*. https://www.lnls.cnpem.br/linhas-de-luz/saxs1-en/overview/ (accessed 2019-03-08).

(129) Radulescu, A.; Pipich, V.; Frielinghaus, H.; Appavou, M.-S. KWS-2, the high intensity / wide Q -range small-angle neutron diffractometer for soft-matter and biology at FRM II. *J. Phys.: Conf. Ser.* 2012, *351*, 12026. DOI: 10.1088/1742-6596/351/1/012026.

(130) Orlandini von Niessen, A. G.; Poleganov, M. A.; Rechner, C.; Plaschke, A.; Kranz, L. M.; Fesser, S.; Diken, M.; Löwer, M.; Vallazza, B.; Beissert, T.; Bukur, V.; Kuhn, A. N.; Türeci, Ö.; Sahin, U. Improving mRNA-Based Therapeutic Gene Delivery by Expression-Augmenting 3' UTRs Identified by Cellular Library Screening. *Molecular therapy : the journal of the American Society of Gene Therapy* 2019, *27* (4), 824–836. DOI: 10.1016/j.ymthe.2018.12.011. Published Online: Dec. 18, 2018.

(131) Bonner, W. A.; Hulett, H. R.; Sweet, R. G.; Herzenberg, L. A. Fluorescence activated cell sorting. *The Review of scientific instruments* 1972, *43* (3), 404–409. DOI: 10.1063/1.1685647.

(132) Ruiz, P.; Borowitz, M.; Tilahun, H.; Clarke, T.; Keyer, L.; Coxey, A. *Application Note*:*Productivity and Efficiency of 6-Color BD Multitest and BD Trucount Technologies for Enumeration of Lymphocyte Subsets*. https://static.bdbiosciences.com/documents/FACSCanto_II_app_note.pdf (accessed 2021-03-15).

(133) Taylor, J. R. *An introduction to error analysis*:*The study of uncertainties in physical measurements*, 2nd ed.; University Science Books, 1997.

(134) Vasavada, N. *Tutorial and Code for conducting Tukey HSD, Scheffe, Bonferroni and Holm multiple comparison in the R statistical package*. https://astatsa.com/OneWay_Anova_with_TukeyHSD/_Rcode_tutorial/ (accessed 2020-12-07).

(135) 7.4.7.3. Bonferroni's method. In *NIST/SEMATECH e-Handbook of Statistical Methods (NIST Handbook 151)*; National Institute of Standards and Technology, 2013.

(136) Malone, R. W.; Felgner, P. L.; Verma, I. M. Cationic liposome-mediated RNA transfection. *Proceedings of the National Academy of Sciences of the United States of America* 1989, *86* (16), 6077–6081.

(137) Ziller, A. Structural and functional characterisation of lipoplexes for tumour vaccination, Johannes Gutenberg-Universität Mainz, 2019.

(138) Hühn, E. Rational Design of Sustained Release Liposomal MRNA Formulations for Parenteral Administration and Image-Guided Assessment of in Vivo Performance, Johannes Gutenberg-Universität Mainz, 2013.

(139) Jacrot, B. The study of biological structures by neutron scattering from solution. *Nature* 1976, *39* (10), 911–953. DOI: 10.1088/0034-4885/39/10/001.

(140) Vitiello, G.; Luchini, A.; D'Errico, G.; Santamaria, R.; Capuozzo, A.; Irace, C.; Montesarchio, D.; Paduano, L. Cationic liposomes as efficient nanocarriers for the drug delivery of an anticancer cholesterol-based ruthenium complex. *Journal of materials chemistry. B* 2015, *3* (15), 3011–3023. DOI: 10.1039/C4TB01807A. Published Online: Mar. 5, 2015.

(141) Jousma, H.; Talsma, H.; Spies, F.; Joosten, J.G.H.; Junginger, H. E.; Crommelin, D.J.A. Characterization of liposomes. The influence of extrusion of multilamellar vesicles through polycarbonate membranes on particle size, particle size distribution and number of bilayers. *International journal of pharmaceutics* 1987, *35* (3), 263–274. DOI: 10.1016/0378-5173(87)90139-6.

(142) Jayaraman, M.; Ansell, S. M.; Mui, B. L.; Tam, Y. K.; Chen, J.; Du, X.; Butler, D.; Eltepu, L.; Matsuda, S.; Narayanannair, J. K.; Rajeev, K. G.; Hafez, I. M.; Akinc, A.; Maier, M. A.; Tracy, M. A.; Cullis, P. R.; Madden, T. D.; Manoharan, M.; Hope, M. J. Maximizing the Potency of siRNA Lipid Nanoparticles for Hepatic Gene Silencing In Vivo. *Angew. Chem.* 2012, *124* (34), 8657–8661. DOI: 10.1002/ange.201203263.

(143) Uebbing, L.; Ziller, A.; Siewert, C.; Schroer, M. A.; Blanchet, C. E.; Svergun, D. I.; Ramishetti, S.; Peer, D.; Sahin, U.; Haas, H.; Langguth, P. Investigation of pH-Responsiveness inside Lipid Nanoparticles for Parenteral mRNA Application Using Small-Angle X-ray Scattering. *Langmuir* 2020, *36* (44), 13331–13341. DOI: 10.1021/acs.langmuir.0c02446.

(144) Lee, D. K.; In, J.; Lee, S. Standard deviation and standard error of the mean. *Korean Journal of Anesthesiology* 2015, *68* (3), 220–223. DOI: 10.4097/kjae.2015.68.3.220.

(145) Cullis, P. R.; Hope, M. J. Lipid Nanoparticle Systems for Enabling Gene Therapies. *Molecular therapy : the journal of the American Society of Gene Therapy* 2017, *25* (7), 1467–1475. DOI: 10.1016/j.ymthe.2017.03.013.

(146) Guthrie, W. F. *NIST/SEMATECH e-Handbook of Statistical Methods (NIST Handbook 151)*. https://www.itl.nist.gov/div898/handbook/.

(147) Bernhardt, H. S.; Tate, W. P. Primordial soup or vinaigrette: did the RNA world evolve at acidic pH? *Biology direct* 2012, *7*, 4. DOI: 10.1186/1745-6150-7-4. Published Online: Jan. 20, 2012.

(148) Jarvinen, P.; Oivanen, M.; Lonnberg, H. Interconversion and phosphoester hydrolysis of 2',5'- and 3',5'-dinucleoside monophosphates: kinetics and mechanisms. *J. Org. Chem.* 1991, *56* (18), 5396–5401. DOI: 10.1021/jo00018a037.

(149) Wagner, A.; Platzgummer, M.; Kreismayr, G.; Quendler, H.; Stiegler, G.; Ferko, B.; Vecera, G.; Vorauer-Uhl, K.; Katinger, H. GMP production of liposomes—a new industrial approach. *Journal of liposome research* 2006, *16* (3), 311–319. DOI: 10.1080/08982100600851086.

(150) Evers, M. J. W.; Kulkarni, J. A.; van der Meel, R.; Cullis, P. R.; Vader, P.; Schiffelers, R. M. State-of-the-Art Design and Rapid-Mixing Production Techniques of Lipid Nanoparticles for Nucleic Acid Delivery. *Small Methods* 2018, *2* (9), 1700375. DOI: 10.1002/smtd.201700375.

(151) Belliveau, N. M.; Huft, J.; Lin, P. J.; Chen, S.; Leung, A. K.; Leaver, T. J.; Wild, A. W.; Lee, J. B.; Taylor, R. J.; Tam, Y. K.; Hansen, C. L.; Cullis, P. R. Microfluidic Synthesis of Highly Potent Limit-size Lipid Nanoparticles for In Vivo Delivery of siRNA. *Molecular therapy. Nucleic acids* 2012, *1*, e37. DOI: 10.1038/mtna.2012.28. Published Online: Aug. 14, 2012.

(152) Lowe, D. *Myths of Vaccine Manufacturing*. https://blogs.sciencemag.org/pipeline/archives/2021/02/02/myths-of-vaccine-manufacturing (accessed 2021-06-11).

(153) Rietwyk, S.; Peer, D. Next-Generation Lipids in RNA Interference Therapeutics. *ACS nano* 2017, *11* (8), 7572–7586. DOI: 10.1021/acsnano.7b04734.

(154) Kauffman, K. J.; Dorkin, J. R.; Yang, J. H.; Heartlein, M. W.; DeRosa, F.; Mir, F. F.; Fenton, O. S.; Anderson, D. G. Optimization of Lipid Nanoparticle Formulations for mRNA Delivery in Vivo with Fractional Factorial and Definitive Screening Designs. *Nano letters* 2015, *15* (11), 7300–7306. DOI: 10.1021/acs.nanolett.5b02497.

(155) Semple, S. C.; Akinc, A.; Chen, J.; Sandhu, A. P.; Mui, B. L.; Cho, C. K.; Sah, D. W. Y.; Stebbing, D.; Crosley, E. J.; Yaworski, E.; Hafez, I. M.; Dorkin, J. R.; Qin, J.; Lam, K.; Rajeev, K. G.; Wong, K. F.; Jeffs, L. B.; Nechev, L.; Eisenhardt, M. L.; Jayaraman, M.; Kazem, M.; Maier, M. A.; Srinivasulu, M.; Weinstein, M. J.; Chen, Q.; Alvarez, R.; Barros, S. A.; De, S.; Klimuk, S. K.; Borland, T.; Kosovrasti, V.; Cantley, W. L.; Tam, Y. K.; Manoharan, M.; Ciufolini, M. A.; Tracy, M. A.; Fougerolles, A. de; MacLachlan, I.; Cullis, P. R.; Madden, T. D.; Hope, M. J. Rational design of cationic lipids for siRNA delivery. *Nature biotechnology* 2010, *28* (2), 172–176. DOI: 10.1038/nbt.1602.

(156) Patil, Y. P.; Jadhav, S. Novel methods for liposome preparation. *Chemistry and physics of lipids* 2014, *177*, 8–18. DOI: 10.1016/j.chemphyslip.2013.10.011.

(157) Kremer, J. M. H.; van der Esker, M. W.; Pathmamanoharan, C.; Wiersema, P. H. Vesicles of variable diameter prepared by a modified injection method. *Biochemistry* 1977, *16* (17), 3932–3935. DOI: 10.1021/bi00636a033.

(158) Billingsley, M. M.; Singh, N.; Ravikumar, P.; Zhang, R.; June, C. H.; Mitchell, M. J. Ionizable Lipid Nanoparticle-Mediated mRNA Delivery for Human CAR T Cell Engineering. *Nano letters* 2020. DOI: 10.1021/acs.nanolett.9b04246.

(159) Vrieze, J. de. Pfizer's vaccine raises allergy concerns. *Science (New York, N.Y.)* 2021, *371* (6524), 10–11. DOI: 10.1126/science.371.6524.10.

(160) Allergic Reactions Including Anaphylaxis After Receipt of the First Dose of Moderna COVID-19 Vaccine - United States, December 21, 2020-January 10, 2021. *MMWR. Morbidity and mortality weekly report* 2021, *70* (4), 125–129. DOI: 10.15585/mmwr.mm7004e1. Published Online: Jan. 29, 2021.

(161) Ishida, T.; Masuda, K.; Ichikawa, T.; Ichihara, M.; Irimura, K.; Kiwada, H. Accelerated clearance of a second injection of PEGylated liposomes in mice. *International journal of pharmaceutics* 2003, *255* (1-2), 167–174. DOI: 10.1016/s0378-5173(03)00085-1.

(162) P. Garay, R. Immunogenicity of Polyethylene Glycol (PEG). *TOPROCJ* 2011, *2* (1), 104–107. DOI: 10.2174/2210289201102010104.

(163) Semple, S. C.; Harasym, T. O.; Clow, K. A.; Ansell, S. M.; Klimuk, S. K.; Hope, M. J. Immunogenicity and rapid blood clearance of liposomes containing polyethylene glycol-lipid conjugates and nucleic Acid. *The Journal of pharmacology and experimental therapeutics* 2005, *312* (3), 1020–1026. DOI: 10.1124/jpet.104.078113. Published Online: Nov. 3, 2004.

(164) Ishida, T.; Ichihara, M.; Wang, X.; Yamamoto, K.; Kimura, J.; Majima, E.; Kiwada, H. Injection of PEGylated liposomes in rats elicits PEG-specific IgM, which is responsible for rapid elimination of a second dose of PEGylated liposomes. *Journal of controlled release : official journal of the Controlled Release Society* 2006, *112* (1), 15–25. DOI: 10.1016/j.jconrel.2006.01.005. Published Online: Mar. 3, 2006.

(165) BioNTech SE. *Pipeline | Biontech*. https://biontech.de/de/science/pipeline (accessed 2021-08-02).

(166) Curevac AG. *Pipeline - Curevac*. https://www.curevac.com/pipeline/ (accessed 2021-08-02).

(167) Alnylam Pharmaceuticals, I. *Alnylam® Development Pipeline of Investigational RNAi Therapeutics*. https://www.alnylam.com/alnylam-rnai-pipeline/ (accessed 2021-08-02).

(168) ModernaTX. *Welcome to Moderna Clinical Trials*. https://trials.modernatx.com/ (accessed 2021-08-02).

(169) Wei, T.; Cheng, Q.; Min, Y.-L.; Olson, E. N.; Siegwart, D. J. Systemic nanoparticle delivery of CRISPR-Cas9 ribonucleoproteins for effective tissue specific genome editing. *Nature communications* 2020, *11* (1), 3232. DOI: 10.1038/s41467-020-17029-3. Published Online: Jun. 26, 2020.

(170) *Phosphat-Puffer nach Sörensen*. http://aeisner.de/rezepte/puffer2.html (accessed 2022-04-16).

7 | Appendix

7.1 List of Figures

7.2 List of Tables

7.3 List of Equations

7.4 Supplement

7.4.1 Mixing Ratios for the Preparation of pH Buffers

Volumes (%) of Na_2HPO_4 solution used for the preparation of pH buffers (2.2.2) in the range of pH 4.9 - pH 8.0 to be filled up to 100 vol% with KH_2PO_4 solution of the same molarity and adjusted with 0.1 M NaOH or HCl. For pH levels below 4.9 or above 8.0, only Na_2HPO_4 or KH_2PO_4 was used and adjusted to the wanted pH with 0.1 M NaOH or HCl. Table taken from [170].

pH	.0	.1	.2	.3	.4	.5	.6	.7	.8	.9
4.x	-	-	-	-	-	-	-	-	-	0.60
5.x	0.95	1.35	1.80	2.30	3.00	3.90	4.90	6.20	7.90	9.80
6.x	12.10	15.00	18.40	22.10	26.40	31.30	37.20	43.00	49.20	55.20
7.x	61.20	67.00	72.60	77.70	81.80	85.20	88.50	91.20	93.60	95.30
8.x	96.90	-	-	-	-	-	-	-	-	-

7.4.2 Exemplary Calculation of LNP Compositions and Preparation

Concentrations of the utilized stock solutions:

mRNA: 0.5 mg/mL
DOPE: 25 mg/mL
DODMA: 50 mg/mL
Cholesterol: 15 mg/mL
pSar (MC12-50): 25 mg/mL

Exemplary calculation of the composition and preparation of 1.0 mL LNP-04 (see Table 15) with a previously defined final mRNA concentration of 0.1 mg/mL:

$$\textbf{Volume}_{\textbf{mRNA stock}} = \frac{\text{total mass}_{\text{mRNA}}}{\text{concentration}_{\text{mRNA stock}}} = \frac{\text{sample volume} \cdot \text{final mRNA concentration}}{\text{concentration}_{\text{mRNA stock}}} = \frac{1\ \text{mL} \cdot 0.1\ \frac{\text{mg}}{\text{mL}}}{0.5\ \frac{\text{mg}}{\text{mL}}} = 0.2\ \text{mL}$$

$$\textbf{Volume}_{\textbf{buffer}} = \text{sample volume} - \text{volume}_{\text{mRNA stock}} = 0.8\ \text{mL}$$

$$\textbf{Total molar lipid concentration} = \frac{\text{final mRNA concentration} \cdot 100}{\text{mol\%}_{\text{mRNA}} \cdot 330\ \frac{\text{g}}{\text{mol}}} = \frac{0.1\ \frac{\text{mg}}{\text{mL}} \cdot 100}{8 \cdot 330\ \frac{\text{g}}{\text{mol}}} = 3.788 \cdot 10^{-3}\ \frac{\text{mmol}}{\text{mL}}$$

$$\textbf{Individual lipid concentration}\ \left[\frac{\textbf{mg}}{\textbf{mL}}\right] = \text{total molar lipid concentration} \cdot \frac{\text{lipid fraction [mol\%]}}{100} \cdot \text{lipid molecular weight}$$

$$\text{Concentration}_{\text{DOPE}} = 3.788 \cdot 10^{-3}\ \frac{\text{mmol}}{\text{mL}} \cdot \frac{10}{100} \cdot 744\ \frac{\text{g}}{\text{mol}} = 0.282\ \frac{\text{mg}}{\text{mL}}$$

$$\text{Concentration}_{\text{DODMA}} = 3.788 \cdot 10^{-3}\ \frac{\text{mmol}}{\text{mL}} \cdot \frac{40}{100} \cdot 620.01\ \frac{\text{g}}{\text{mol}} = 0.939\ \frac{\text{mg}}{\text{mL}}$$

$$\text{Concentration}_{\text{cholesterol}} = 3.788 \cdot 10^{-3}\ \frac{\text{mmol}}{\text{mL}} \cdot \frac{48}{100} \cdot 386.67\ \frac{\text{g}}{\text{mol}} = 0.703\ \frac{\text{mg}}{\text{mL}}$$

$$\text{Concentration}_{\text{pSar}} = 3.788 \cdot 10^{-3}\ \frac{\text{mmol}}{\text{mL}} \cdot \frac{2}{100} \cdot 3524.44\ \frac{\text{g}}{\text{mol}} = 0.267\ \frac{\text{mg}}{\text{mL}}$$

$$\textbf{Total lipid concentration}\ \left[\frac{\textbf{mg}}{\textbf{mL}}\right] = \sum \text{individual lipid concentrations} = 2.191\ \frac{\text{mg}}{\text{mL}}$$

$$\textbf{Volume}_{\textbf{individual lipid stock}} = \frac{\text{total mass}_{\text{lipid}}}{\text{concentration}_{\text{lipid stock}}} = \frac{\text{sample volume} \cdot \text{concentration}_{\text{lipid}}}{\text{concentration}_{\text{lipid stock}}}$$

$$\text{Volume}_{\text{DOPE stock}} = \frac{1\ \text{mL} \cdot 0.282\ \frac{\text{mg}}{\text{mL}}}{25\ \frac{\text{mg}}{\text{mL}}} = 11.28\ \mu\text{L}$$

$$\text{Volume}_{\text{DODMA stock}} = \frac{1\ \text{mL} \cdot 0.939\ \frac{\text{mg}}{\text{mL}}}{50\ \frac{\text{mg}}{\text{mL}}} = 18.78\ \mu\text{L}$$

$$\text{Volume}_{\text{cholesterol stock}} = \frac{1\ \text{mL} \cdot 0.703 \frac{\text{mg}}{\text{mL}}}{15 \frac{\text{mg}}{\text{mL}}} = 46.87\ \mu\text{L}$$

$$\text{Volume}_{\text{pSar stock}} = \frac{1\ \text{mL} \cdot 0.267 \frac{\text{mg}}{\text{mL}}}{25 \frac{\text{mg}}{\text{mL}}} = 10.68\ \mu\text{L}$$

$$\textbf{wt\%}_{\textbf{individual lipid}} = \frac{\text{individual lipid concentration}}{\text{total lipid concentration}} \quad \text{, e. g.:} \quad \text{wt\%}_{\text{DOPE}} = \frac{0.282 \frac{\text{mg}}{\text{mL}}}{2.191 \frac{\text{mg}}{\text{mL}}} = 12.9\%$$

Exemplary calculation of the composition and preparation of 1.0 mL LNP-04 with a **previously defined total lipid concentration of 1.0 mg/mL:**

$$\textbf{\textit{Total molar lipid concentration}} = \textit{total lipid concentration} \left[\frac{mg}{mL}\right] \div \sum \left(\frac{mol\%_{individual\ lipid}}{100} \cdot \textit{lipid molecular weight}\right)$$

$$= 1 \frac{mg}{mL} \div \left[\left(\frac{10}{100} \cdot 744 \frac{g}{mol}\right)_{DOPE} + \left(\frac{40}{100} \cdot 620.01 \frac{g}{mol}\right)_{DODMA} + \left(\frac{48}{100} \cdot 386.67 \frac{g}{mol}\right)_{cholesterol} + \left(\frac{2}{100} \cdot 3524.44 \frac{g}{mol}\right)_{pSar}\right]$$

$$= 1.729 \cdot 10^{-3} \frac{\text{mmol}}{\text{mL}}$$

$$\textbf{Individual lipid concentration} \left[\frac{\textbf{mg}}{\textbf{mL}}\right] = \text{total molar lipid concentration} \cdot \frac{\text{lipid fraction [mol\%]}}{100} \cdot \text{lipid molecular weight}$$

$$\text{Concentration}_{\text{DOPE}} = 1.729 \cdot 10^{-3} \frac{\text{mmol}}{\text{mL}} \cdot \frac{10}{100} \cdot 744 \frac{\text{g}}{\text{mol}} = 0.129 \frac{\text{mg}}{\text{mL}}$$

$$\text{Concentration}_{\text{DODMA}} = 1.729 \cdot 10^{-3} \frac{\text{mmol}}{\text{mL}} \cdot \frac{40}{100} \cdot 620.01 \frac{\text{g}}{\text{mol}} = 0.429 \frac{\text{mg}}{\text{mL}}$$

$$\text{Concentration}_{\text{cholesterol}} = 1.729 \cdot 10^{-3} \frac{\text{mmol}}{\text{mL}} \cdot \frac{48}{100} \cdot 386.67 \frac{\text{g}}{\text{mol}} = 0.321 \frac{\text{mg}}{\text{mL}}$$

$$\text{Concentration}_{\text{pSar}} = 1.729 \cdot 10^{-3} \frac{\text{mmol}}{\text{mL}} \cdot \frac{2}{100} \cdot 3524.44 \frac{\text{g}}{\text{mol}} = 0.122 \frac{\text{mg}}{\text{mL}}$$

$$\textbf{Volume}_{\textbf{individual lipid stock}} = \frac{\text{total mass}_{\text{lipid}}}{\text{concentration}_{\text{lipid stock}}} = \frac{\text{sample volume} \cdot \text{concentration}_{\text{lipid}}}{\text{concentration}_{\text{lipid stock}}}$$

$$\text{Volume}_{\text{DOPE stock}} = \frac{1\ \text{mL} \cdot 0.129 \frac{\text{mg}}{\text{mL}}}{25 \frac{\text{mg}}{\text{mL}}} = 5.16\ \mu\text{L}$$

$$\text{Volume}_{\text{DODMA stock}} = \frac{1\ \text{mL} \cdot 0.429 \frac{\text{mg}}{\text{mL}}}{50 \frac{\text{mg}}{\text{mL}}} = 8.58\ \mu\text{L}$$

$$\text{Volume}_{\text{cholesterol stock}} = \frac{1\ \text{mL} \cdot 0.321 \frac{\text{mg}}{\text{mL}}}{15 \frac{\text{mg}}{\text{mL}}} = 21.40\ \mu\text{L}$$

$$\text{Volume}_{\text{pSar stock}} = \frac{1\ \text{mL} \cdot 0.122 \frac{\text{mg}}{\text{mL}}}{25 \frac{\text{mg}}{\text{mL}}} = 4.88\ \mu\text{L}$$

$$\textbf{mRNA concentration} = \text{total molar lipid concentration} \cdot \frac{\text{mRNA fraction [mol\%]}}{100} \cdot \text{mRNA molecular weight}$$

$$= 1.729 \cdot 10^{-3} \frac{\text{mmol}}{\text{mL}} \cdot \frac{8}{100} \cdot 330 \frac{\text{g}}{\text{mol}} = 0.046 \frac{\text{mg}}{\text{mL}}$$

$$\textbf{Volume}_{\textbf{mRNA stock}} = \frac{\text{total mass}_{\text{mRNA}}}{\text{concentration}_{\text{mRNA stock}}} = \frac{\text{sample volume} \cdot \text{mRNA concentration}}{\text{concentration}_{\text{mRNA stock}}} = \frac{1\ \text{mL} \cdot 0.046 \frac{\text{mg}}{\text{mL}}}{0.5 \frac{\text{mg}}{\text{mL}}} = 91.27\ \mu\text{L}$$

$$\textbf{Volume}_{\textbf{buffer}} = \text{sample volume} - \text{volume}_{\text{mRNA stock}} = 908.73\ \mu\text{L}$$

7.4.3 R-script for Statistical Analysis

```
library("multcomp")

# FORMATING:
# Stack your input data into two columns:
# the first column is the numerical observation, the second column contains a character-string label
for the distinct category to which the observation belongs.
# The first row contains the column names with A_, B_, ... (important, since they are sorted
alphabetically in a later step)
# save as a tab-delimited text file ("importfile.txt")

# set your export directory:
setwd("example-path/R")

## Filename for Output File:
sink(file="Filename.txt", type = "output")

## Enter a description for your output file:
writeLines(c("-----------------------------------------","Description Line 1", "", "Description
Line 2 ", "-----------------------------------------"))

expt1 <- read.table("importfile.txt", header=T)
expt1$Formulation <- as.factor(expt1$Formulation)
writeLines(c("","","-----------------------------------------","Import:","-----------------------
------------------","",""))
expt1

writeLines(c("","","-----------------------------------------","ANOVA","--------------------------
---------------","",""))

#If evaluating Transfection per Formulation:
amod <- aov(Transfection~Formulation,data=expt1)
summary(amod)

writeLines(c("","","-----------------------------------------","Bonferroni / Holm ","-------------
-----------------------------","",""))

## Two sets of contrasts:
# (1) All pairs. (Here q=10)
# (2) Only pairs relative to A_, assuming A_ is control. (Here q= 5 v control)

# The Bonferroni method R multcomp procedure requires a Contrast Matrix, which is constructed below
for all pairs:
contrasts <- rbind(
  "B_ - A_"=c(-1,1,0,0,0,0),
  "C_ - A_"=c(-1,0,1,0,0,0),
  "D_ - A_"=c(-1,0,0,1,0,0),
  "E_ - A_"=c(-1,0,0,0,1,0),
  "F_ - A_"=c(-1,0,0,0,0,1),
  "C_ - B_"=c(0,-1,1,0,0,0),
  "D_ - B_"=c(0,-1,0,1,0,0),
  "E_ - B_"=c(0,-1,0,0,1,0),
  "F_ - B_"=c(0,-1,0,0,0,1),
  "D_ - C_"=c(0,0,-1,1,0,0),
  "E_ - C_"=c(0,0,-1,0,1,0),
  "F_ - C_"=c(0,0,-1,0,0,1),
  "E_ - D_"=c(0,0,0,-1,1,0),
  "F_ - D_"=c(0,0,0,-1,0,1),
  "F_ - E_"=c(0,0,0,0,-1,1)
)
contrasts

#Now invoke the R procedure to produce Bonferroni simultaneous multiple comparison for all pairs:
bmod <-glht(amod,linfct=mcp(Formulation=contrasts))
writeLines(c("-----------------------------------------","Bonferroni All Pairs","-----------------
-------------------------"))
summary(bmod,test=adjusted("bonferroni"))

#Now repeat Bonferroni comparison for fewer relevant pairs (Only pairs relative to column A, assuming
that column A represents the control)
#The Contrast Matrix is redefined as follows:
contrasts <- rbind(
  "B_ - A_"=c(-1,1,0,0,0,0),
  "C_ - A_"=c(-1,0,1,0,0,0),
  "D_ - A_"=c(-1,0,0,1,0,0),
  "E_ - A_"=c(-1,0,0,0,1,0),
  "F_ - A_"=c(-1,0,0,0,0,1)
)
contrasts

#Now invoke the R procedure to produce Bonferroni simultaneous multiple comparison for the relevant
q=4 pairs of contrasts relative to Std only.
bmod <-glht(amod,linfct=mcp(Formulation=contrasts))
writeLines(c("-----------------------------------------","Bonferroni vs Control Only","-----------
-------------------------------"))
summary(bmod,test=adjusted("bonferroni"))

sink()
```

7.4.4 Full Set of SANS Curves From 3.1.1.1

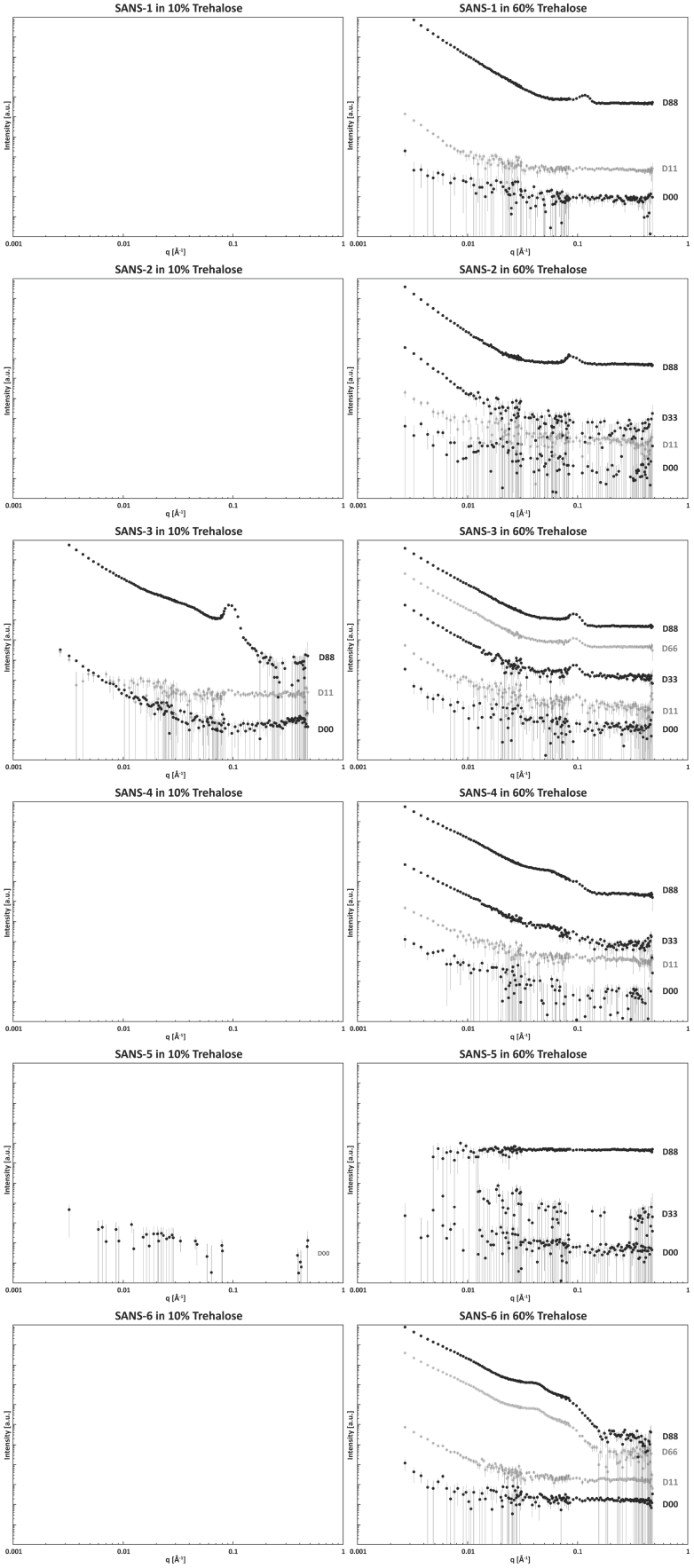

Suppl. Fig. 1. Full set of SANS curves from 3.1.1.1. The curves are shifted vertically for clarity.

7.4.5 Full Set of SAXS Curves From 3.1.2.2

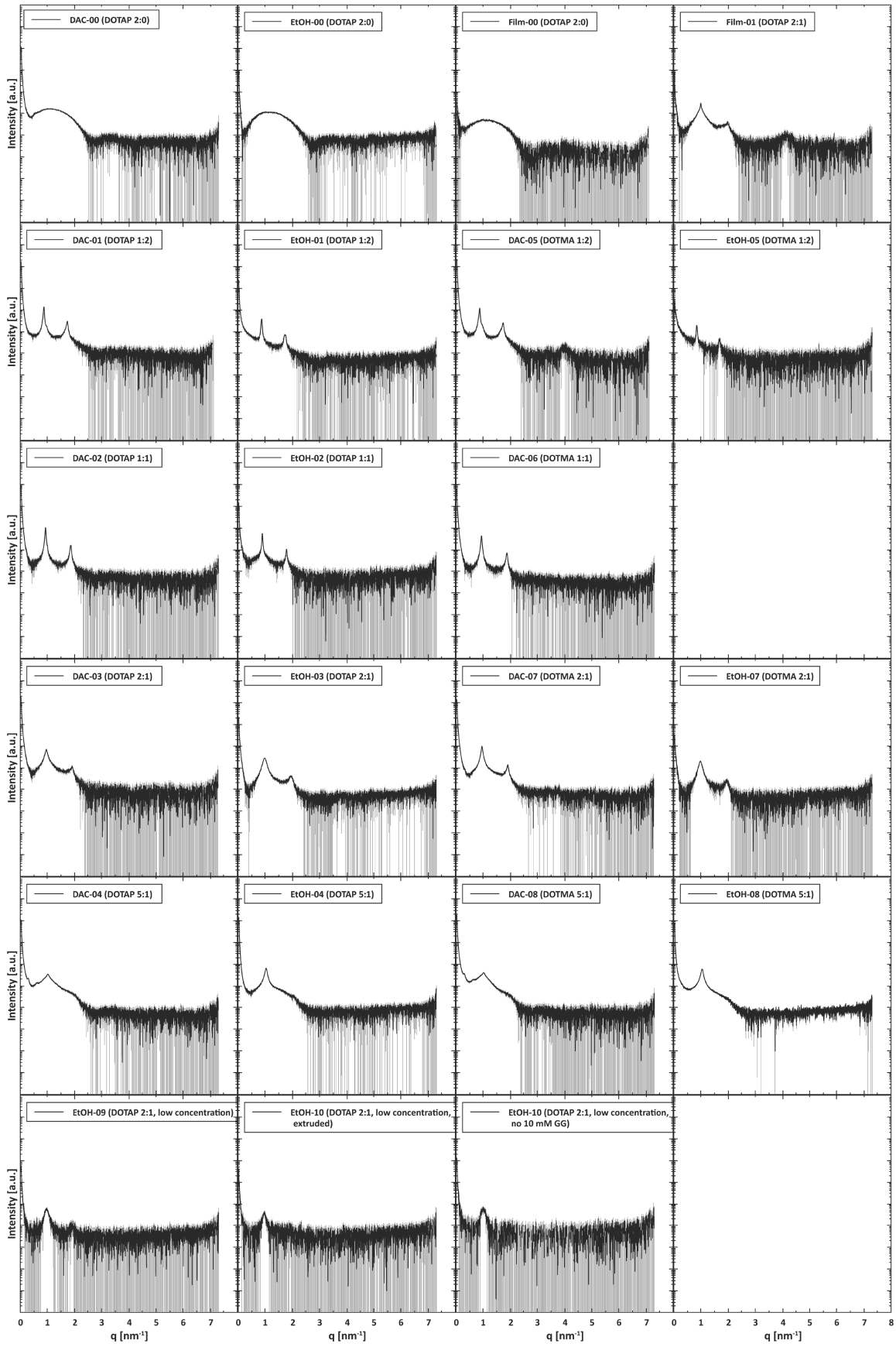

Suppl. Fig. 2. Full set of SAXS curves from 3.1.2.2.

7.4.6 Quantitative SAXS Data From pH-Responsive Lipoplexes (3.2.1.1.4)

pH	1st order peak position [nm^{-1}]	d-spacing [nm]	1st order peak width [nm^{-1}]	correlation length [nm]
		F-TMA-1:1		
8.0	0.86428±0.00002	7.26985±0.00017	0.02320±0.00006	270.8368±0.7004
7.5	0.86909±0.00005	7.22961±0.00042	0.04120±0.00018	152.5101±0.6663
7.0	0.86987±0.00002	7.22313±0.00017	0.03196±0.00007	196.6025±0.4306
6.5	0.87294±0.00004	7.19773±0.00033	0.02645±0.00011	237.5583±0.9880
6.0	0.87975±0.00002	7.14201±0.00016	0.02699±0.00005	232.8056±0.4313
5.5	0.87994±0.00004	7.14047±0.00032	0.02841±0.00012	221.1694±0.9342
5.0	0.87816±0.00002	7.15494±0.00016	0.02200±0.00006	285.6101±0.7789
4.5	0.88601±0.00000	7.09155±0.00000	0.01272±0.00001	270.8368±0.7004
		F-DMA-1:0		
8.0	0.93657±0.00081	6.70869±0.00581	0.08096±0.00294	77.6123±2.8214
7.5	0.91664±0.00125	6.85462±0.00938	0.12622±0.00560	49.7813±2.2073
7.0	0.91428±0.00072	6.87229±0.00542	0.10024±0.00278	62.6842±1.7413
6.5	0.85145±0.00091	7.37937±0.00791	0.19421±0.00451	32.3540±0.7516
6.0	0.82893±0.00083	7.57992±0.00755	0.17998±0.00379	34.9118±0.7345
5.5	0.80145±0.00306	7.83981±0.02994	0.17767±0.02135	35.3647±4.2488
5.0	0.81646±0.00143	7.69562±0.01348	0.26133±0.01098	24.0434±1.0102
4.5	0.75153±0.00249	8.36052±0.02765	0.27751±0.01560	22.6421±1.2732
		F-DMA-1:1		
8.0	0.80273±0.00005	7.82727±0.00049	0.03275±0.00017	191.8595±1.0126
7.5	0.83796±0.00010	7.49822±0.00091	0.05071±0.00033	123.9085±0.8148
7.0	0.86120±0.00015	7.29588±0.00126	0.04824±0.00075	130.2593±2.0159
6.5	0.88400±0.00106	7.10768±0.00850	0.06329±0.00405	99.2816±6.3584
6.0	0.88761±0.00011	7.07877±0.00089	0.03760±0.00131	167.1068±5.8268
5.5	0.89217±0.00014	7.04256±0.00112	0.03637±0.00064	172.7617±3.0473
5.0	0.89646±0.00008	7.00889±0.00066	0.06174±0.00025	101.7756±0.4179
4.5	0.89977±0.00008	6.98312±0.00062	0.05422±0.00024	191.8595±1.0126
		F-DMA-2:1		
8.0	0.81727±0.00029	7.68798±0.00270	0.02765±0.00081	227.2522±6.6686
7.5	0.86456±0.00004	7.26746±0.00031	0.03000±0.00073	209.4471±5.1137
7.0	0.91146±0.00019	6.89357±0.00146	0.04936±0.00055	127.3059±1.4259
6.5	0.93672±0.00026	6.70767±0.00183	0.04512±0.00030	139.2712±0.9340
6.0	0.94579±0.00011	6.64334±0.00075	0.05430±0.00032	115.7141±0.6846
5.5	0.94547±0.00012	6.64559±0.00087	0.05646±0.00038	111.2989±0.7458
5.0	0.94816±0.00016	6.62671±0.00109	0.06458±0.00046	97.2990±0.6902
4.5	0.96147±0.00020	6.53499±0.00138	0.06499±0.00068	227.2522±6.6686
		E-DMA-5:1		
7.93	0.77202±0.00112	8.13866±0.01186	0.10249±0.00574	61.3107±3.4368
7.57	0.81962±0.00053	7.66595±0.00496	0.08676±0.00214	72.4228±1.7868
7.06	0.87810±0.00042	7.15542±0.00343	0.08480±0.00143	74.1006±1.2511
6.55	0.93780±0.00032	6.69989±0.00226	0.08415±0.00110	74.6738±0.9794
6.06	0.98807±0.00106	6.35902±0.00683	0.09114±0.00365	68.9431±2.7636
5.54	1.00967±0.00034	6.22303±0.00210	0.09355±0.00136	67.1726±0.9764
5.12	1.01877±0.00057	6.16740±0.00347	0.09954±0.00228	63.1246±1.4481
4.59	1.02200±0.00053	6.14796±0.00320	0.10130±0.00263	61.3107±3.4368
		E-TAP-5:1		
7.93	1.04633±0.00339	6.00496±0.01947	0.08354±0.01819	4.1220±0.1773
7.57	1.03926±0.00511	6.04583±0.02974	0.11493±0.01662	89.2774±1.4598
7.06	1.03094±0.00531	6.09464±0.03138	0.13457±0.01687	93.7518±1.1452
6.55	1.03435±0.00537	6.07453±0.03156	0.14573±0.01774	95.4728±1.2286
6.06	1.04574±0.00268	6.00839±0.01542	0.16820±0.00877	87.0289±1.1738
5.54	1.03307±0.00425	6.08208±0.02502	0.12072±0.01346	85.2650±1.2892
5.12	1.04194±0.00297	6.03026±0.01717	0.09005±0.01004	86.6996±1.2179
4.59	1.04647±0.00341	6.00415±0.01957	0.08561±0.01857	4.1220±0.1773
		E-DAP-5:1		
7.93	0.85193±0.02236	7.37524±0.19357	1.52431±0.06557	75.2197±16.3803
7.57	0.75340±0.00035	8.33981±0.00386	0.07038±0.00115	54.6760±7.9083
7.06	0.81162±0.00025	7.74153±0.00239	0.06702±0.00082	46.6961±5.8557
6.55	0.87305±0.00026	7.19683±0.00217	0.06582±0.00085	43.1187±5.2495

6.06	0.92818±0.00027	6.76933±0.00198	0.07220±0.00097	37.3589±1.9487
5.54	0.96480±0.00030	6.51241±0.00203	0.07370±0.00111	52.0533±5.8058
5.12	0.98749±0.00028	6.36278±0.00181	0.07248±0.00102	69.7800±7.7764
4.59	0.99238±0.00032	6.33140±0.00205	0.07735±0.00119	75.2197±16.3803
		E-MC-2:1		
7.93	0.73639±0.00226	8.53237±0.02613	0.06181±0.00668	101.6622±10.9854
7.57	0.80914±0.00122	7.76528±0.01174	0.04882±0.00356	128.6990±9.3914
7.06	0.86359±0.00169	7.27569±0.01420	0.05536±0.00492	113.5118±10.0977
6.55	0.89728±0.00164	7.00249±0.01280	0.06037±0.00492	104.0902±8.4823
6.06	0.91616±0.00166	6.85819±0.01239	0.06235±0.00487	100.7804±7.8640
5.54	0.93049±0.00089	6.75259±0.00643	0.06858±0.00556	91.6301±7.4350
5.12	0.92698±0.00154	6.77811±0.01125	0.06007±0.00466	104.6017±8.1112
4.59	0.92397±0.00188	6.80020±0.01380	0.06579±0.00551	101.6622±10.9854
		E-MC-5:1		
7.93	0.75628±0.00334	8.30806±0.03664	1.00829±0.01415	6.2316±0.0875
7.57	0.77168±0.00588	8.14218±0.06207	0.39777±0.01609	12.1420±0.4913
7.06	0.82317±0.00291	7.63289±0.02699	0.31380±0.01292	20.0239±0.8243
6.55	0.92642±0.00135	6.78225±0.00990	0.24337±0.00587	25.8190±0.6222
6.06	0.98236±0.00120	6.39600±0.00780	0.23690±0.00545	26.5245±0.6102
5.54	1.03457±0.00742	6.07324±0.04355	0.16666±0.00113	37.7033±0.2560
5.12	1.04029±0.00190	6.03982±0.01103	0.17689±0.01289	35.5228±2.5892
4.59	1.04837±0.00180	5.99327±0.01026	0.17058±0.01175	36.8368±2.5374

7.4.7 Full Set of SAXS Curves From 3.2.1.2.2 and 3.2.1.3.3

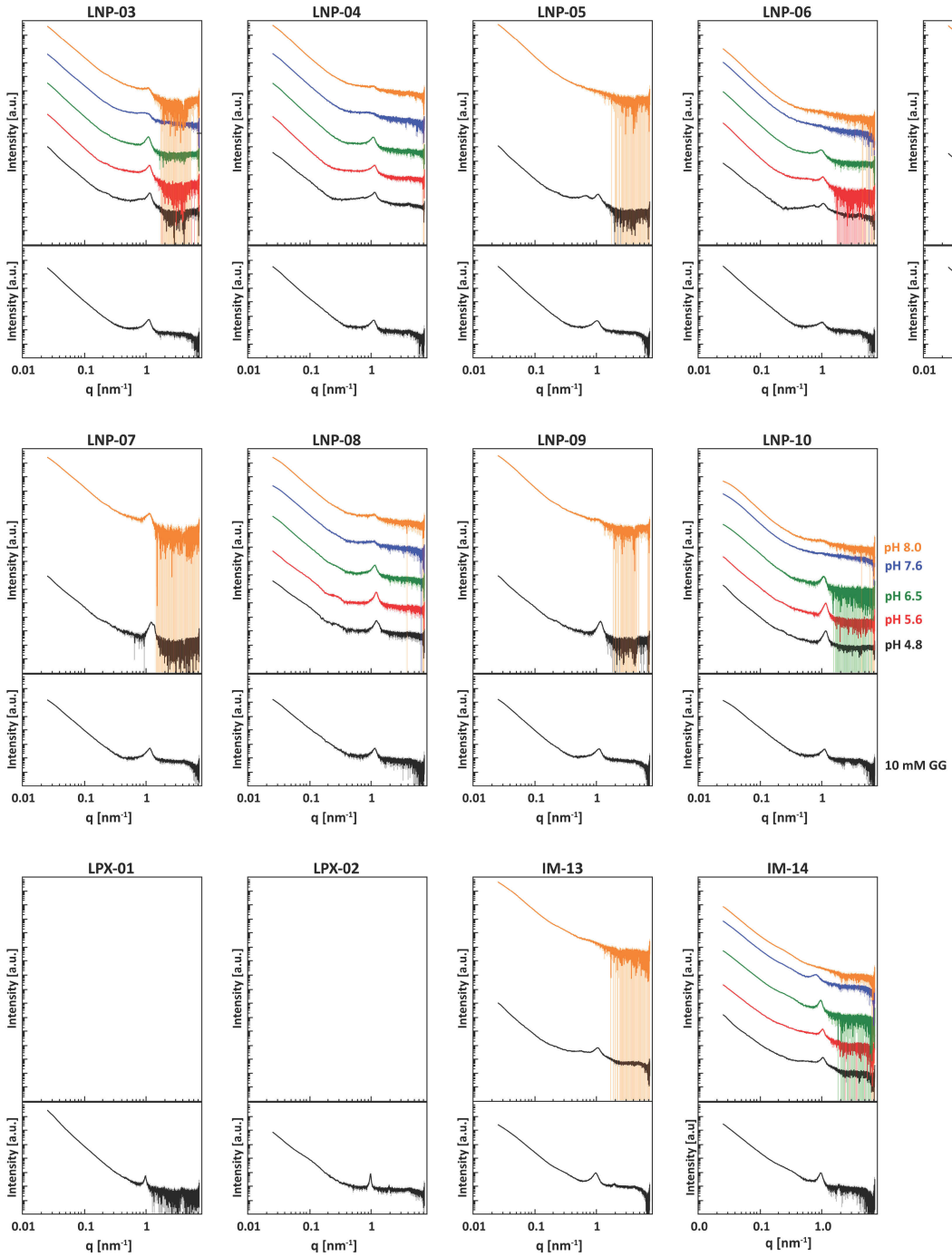

Suppl. Fig. 3. Full set of SAXS curves measured at 5 mg/mL in all media from 3.2.1.2.2 and 3.2.1.3.3. The curves are shifted vertically for clarity.

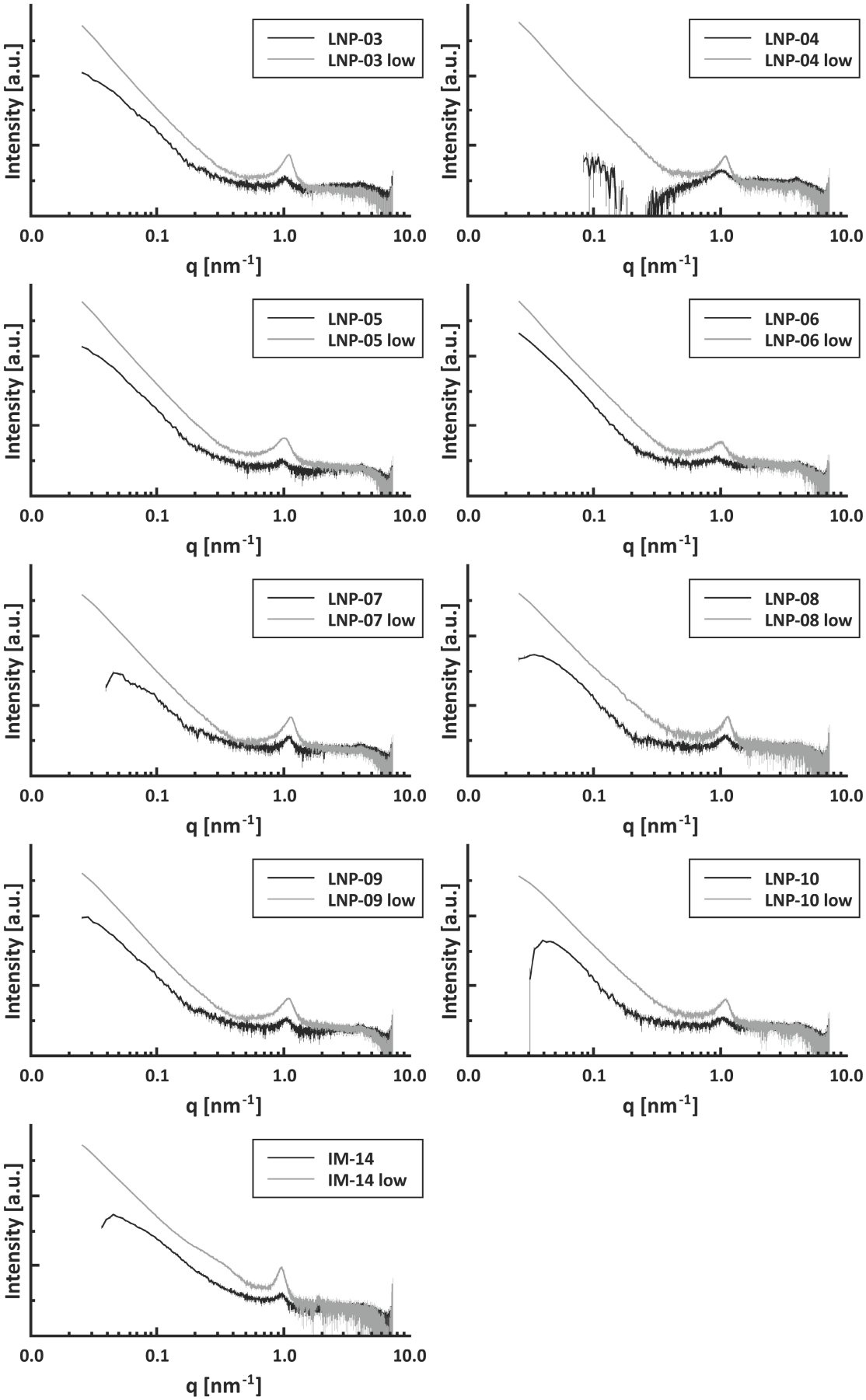

Suppl. Fig. 4. Comparison of SAXS curves measured at 5 mg/mL and at 1 mg/mL ("low") total lipid from chapter 3.2.1.3.3.

7.4.8 Quantitative SAXS Data From 3.2.1.4.2

Sample ID		Bragg Peak 1			Bragg Peak 2		
		Position [nm^{-1}]	Width [nm^{-1}]	Area [a.u.]	Position [nm^{-1}]	Width [nm^{-1}]	Area [a.u.]
DPL-14	001	0.6216±0.0013	0.1184±0.0043	44.1134±1.4376	1.0099±0.0013	0.0689±0.0055	16.7528±1.3929
	002	0.5839±0.0010	0.0930±0.0031	26.8459±0.7324	0.9909±0.0011	0.0864±0.0045	28.5505±2.1576
	003	0.5774±0.0009	0.1041±0.0028	28.9774±0.6689	1.0105±0.0012	0.0960±0.0036	32.6687±1.9625
	004	0.5628±0.0004	0.0704±0.0013	26.3123±0.3727	1.0145±0.0011	0.0949±0.0029	27.4024±1.1572
	005	0.5639±0.0006	0.0888±0.0020	21.0297±0.3871	1.0388±0.0022	0.0918±0.0047	18.4023±2.0842
	006	0.5718±0.0012	0.1248±0.0041	15.1015±0.4241	1.0537±0.0024	0.1132±0.0044	22.4129±1.9270
	007				0.7859±0.0053	0.3763±0.0173	54.8785±2.9261
	008				0.7494±0.0014	0.1989±0.0047	38.2527±0.8135
	009	0.6591±0.0494	0.5654±0.0761	42.8266±11.4883	0.7902±0.0015	0.1351±0.0119	27.6074±4.3738
	010	0.5577±0.0100	0.4365±0.0406	34.6712±3.7906	0.8119±0.0018	0.1964±0.0089	29.8851±2.0987
	011	0.5623±0.0056	0.2968±0.0210	24.9192±2.6041	0.8554±0.0048	0.3343±0.0311	34.4255±4.1683
	012	0.5832±0.0025	0.2604±0.0089	45.5437±1.3178			
	013				0.7197±0.0009	0.1307±0.0020	50.7411±0.7504
	014	0.4966±0.0113	0.2871±0.0661	10.2546±2.5270	0.7434±0.0018	0.2027±0.0069	34.2221±1.5791
	015	0.5208±0.0142	0.4381±0.0883	24.8252±6.0185	0.7898±0.0033	0.2203±0.0161	22.6447±2.7824
	016	0.5591±0.0075	0.3949±0.0303	30.7662±2.8042	0.9088±0.0149	0.3021±0.0613	16.3906±5.2166
	017	0.5529±0.0029	0.2612±0.0108	18.8285±0.7213	0.9973±0.0192	0.2673±0.0299	12.1768±3.2467
	018	0.5125±0.0029	0.2987±0.0116	21.1581±0.8030	0.9554±0.0259	0.1562±0.0841	1.0448±0.7569
	019				0.6655±0.0020	0.2598±0.0072	41.9770±1.0668
	020	0.6073±0.0085	0.4748±0.0183	54.5689±2.9001	0.7089±0.0019	0.0982±0.0107	7.8666±1.2350
	021	0.5302±0.0166	0.4381±0.0643	32.4163±6.3820	0.8673±0.0339	0.3602±0.1797	12.8738±10.4365
	022	0.5663±0.0107	0.2956±0.0397	15.2762±2.3204	0.8098±0.0022	0.1928±0.0099	28.3451±1.7728
	023	0.5363±0.0061	0.3636±0.0260	101.964±6.8010			
	024	0.4414±0.0105	0.3591±0.0322	124.815±11.0894			
DLin-MC3-DMA	025	0.6084±0.0010	0.1731±0.0055	66.5517±2.6254	1.0195±0.0010	0.0936±0.0054	18.0174±1.6284
	026	0.5917±0.0006	0.1325±0.0031	43.6638±1.1292	1.0152±0.0005	0.0650±0.0025	19.3317±1.0988
	027	0.5690±0.0005	0.0932±0.0021	30.4020±0.7169	1.0246±0.0008	0.0867±0.0024	26.5179±1.2611
	028	0.5523±0.0010	0.0902±0.0039	30.8149±1.2515	1.0704±0.0004	0.1261±0.0015	64.0622±0.7409
	029	0.5573±0.0008	0.0773±0.0029	20.0460±0.6785	1.0881±0.0003	0.1125±0.0013	53.3385±0.5532
	030	0.5631±0.0012	0.1040±0.0052	22.1278±1.1255	1.0995±0.0003	0.1048±0.0011	53.6249±0.4973
	031	0.5828±0.0074	0.1852±0.0264	4.7014±0.5999	0.9802±0.0054	0.3384±0.0103	40.6939±1.7953
	032	0.5577±0.0028	0.1171±0.0101	4.0223±0.3201	0.8860±0.0014	0.2416±0.0051	35.6979±0.7711
	033	0.5399±0.0071	0.3208±0.0345	9.3603±1.1671	0.9385±0.0010	0.2025±0.0041	42.0578±0.9627
	034	0.6046±0.0089	0.7037±0.0503	44.7704±3.5889	0.9773±0.0011	0.1719±0.0043	42.0544±1.4140
	035	0.5689±0.0028	0.3330±0.0131	27.4595±1.1435	0.9703±0.0045	0.2902±0.0099	39.8206±2.3379
	036	0.5763±0.0029	0.2836±0.0131	20.3945±1.0855	0.9886±0.0151	0.4696±0.0248	29.9334±2.3848
	037				0.9016±0.0009	0.1716±0.0028	50.6910±0.8154
	038	0.4717±0.0198	0.4404±0.0937	17.7053±3.5688	0.9083±0.0013	0.1608±0.0050	50.9428±1.6721
	039	0.5252±0.0112	0.5550±0.0807	57.8081±9.1830	0.9501±0.0048	0.2401±0.0170	60.3369±6.7266
	040	0.5440±0.0034	0.3380±0.0164	38.0868±1.7474	0.9550±0.0125	0.2824±0.0256	26.6833±4.8160
	041	0.5651±0.0046	0.2859±0.0196	17.8854±1.1713	0.9709±0.0420	0.3729±0.0521	13.2171±5.4098
	042	0.5170±0.0035	0.2925±0.0124	18.2489±0.6466	0.8035±0.0007	0.0034±0.0047	0.0797±0.0312
DODMA	043	0.5725±0.0003	0.0678±0.0008	25.5408±0.2365	1.0245±0.0003	0.0756±0.0011	27.2957±0.4228
	044	0.5937±0.0004	0.1127±0.0015	25.0872±0.2867	1.0569±0.0008	0.0697±0.0045	9.2613±1.0791
	045	0.5774±0.0007	0.1043±0.0024	29.0564±0.5729	1.0104±0.0010	0.0959±0.0031	32.4732±1.7201
	046	0.6110±0.0007	0.1083±0.0020	17.2555±0.2545	0.9962±0.0002	0.0656±0.0007	41.9861±0.558
	047	0.5905±0.0008	0.1171±0.0029	31.2103±0.7406	0.9920±0.0004	0.0509±0.0014	19.8522±0.5333
	048	0.6269±0.0019	0.2026±0.0129	11.3124±0.9817	1.0360±0.0007	0.0736±0.0023	5.8617±0.1465
	049				0.7902±0.0009	0.1490±0.0030	37.8073±0.7696
	050				0.8134±0.0007	0.1696±0.0024	45.1413±0.6069
	051	0.5423±0.0141	0.2542±0.0573	7.0197±1.5870	0.8367±0.0011	0.1948±0.0050	65.9634±1.8210
	052	0.5578±0.0058	0.3498±0.0253	25.0787±1.9048	0.8121±0.0006	0.1373±0.0027	44.5797±1.0095
	053	0.7851±0.0096	0.5709±0.0255	66.5884±4.2208	0.8216±0.0016	0.0920±0.0092	7.7288±1.1022
	054	0.6970±0.0035	0.4619±0.0146	52.5613±1.7526			
	055				0.7683±0.0002	0.1007±0.0005	38.7162±0.1724
	056	0.4970±0.0091	0.4150±0.0653	17.3243±2.9566	0.7931±0.0010	0.1969±0.0046	36.1458±1.1985
	057	0.4596±0.0193	0.5103±0.1628	45.5428±17.6235	0.7977±0.0041	0.2820±0.0233	45.6798±6.6842
	058	0.5546±0.0189	0.5225±0.0621	45.6420±9.6109	0.8287±0.0076	0.3707±0.0430	32.2202±7.9544
	059	0.6238±0.0191	0.4170±0.0411	37.7566±8.3685	0.8631±0.0288	0.3132±0.2034	10.6581±12.9176
	060	0.5763±0.0072	0.4468±0.0365	31.3895±2.3644	0.8649±0.0029	0.0110±0.0088	0.2024±0.1222
pH-Variation	071	0.4859±0.0051	0.1894±0.0278	10.1434±2.4416	0.8438±0.0080	0.3288±0.0462	28.9041±5.2644
	072	0.5079±0.0034	0.1818±0.0157	11.5951±1.3185	0.9638±0.0258	0.5482±0.0487	44.2678±5.0593
	073	0.5098±0.0115	0.0710±0.0427	1.1175±0.6267	0.9472±0.0238	0.5873±0.0447	46.3190±4.7858
	074	0.5896±0.0162	0.1693±0.0947	3.3369±2.6345	0.9545±0.0177	0.7641±0.0728	111.635±11.0174
	075	0.6728±0.0134	0.2356±0.0764	4.6461±2.8093	0.9135±0.0110	0.7696±0.0551	77.6359±6.9491
	076	0.7025±0.0107	0.2339±0.0579	6.7069±3.2005	0.8570±0.0185	0.4770±0.0700	32.3077±6.7711
	077	0.6532±0.0117	0.1372±0.0603	2.8803±2.0122	0.9454±0.0057	0.5315±0.0271	57.8356±5.0186
	081	0.7861±0.0042	0.5247±0.0179	53.3728±1.8285	1.1791±0.0004	0.1486±0.0018	72.7475±0.8789
	082	0.7791±0.0052	0.5382±0.0215	26.9545±1.1076	1.1777±0.0007	0.1726±0.0031	30.9952±0.6186
	083	0.7888±0.0063	0.5918±0.0265	30.9809±1.5227	1.1724±0.0007	0.1721±0.0032	33.8626±0.7198
	084	0.8273±0.0082	0.6937±0.0321	38.9181±2.3072	1.1482±0.0005	0.1527±0.0027	30.4700±0.6384
	085	0.8293±0.0089	0.6712±0.0274	46.2995±2.6898	1.1002±0.0006	0.1513±0.0029	33.7899±0.8299
	086	0.6635±0.0092	0.7709±0.0412	65.5471±4.4816	1.0336±0.0009	0.2023±0.0050	36.8434±1.2579
	087	0.5150±0.0035	0.4623±0.0189	52.4257±2.1058	0.9749±0.0012	0.2893±0.0048	51.1718±1.0135

Sample ID		Bragg Peak 3			Bragg Peak 4		
		Position [nm^{-1}]	Width [nm^{-1}]	Area [a.u.]	Position [nm^{-1}]	Width [nm^{-1}]	Area [a.u.]
DPL-14	001	1.1924±0.0085	0.5670±0.0340	103.2940±9.4346	1.6998±0.0032	0.3115±0.0182	37.0801±2.1820
	002	1.1027±0.0074	0.2179±0.0164	31.8119±3.6403	1.6770±0.0024	0.2959±0.0105	29.9044±1.0155
	003	1.1021±0.0043	0.1524±0.0092	25.8675±2.5431	1.6843±0.0031	0.3290±0.0139	30.5504±1.3089
	004	1.0967±0.0013	0.1023±0.0031	27.0495±1.1959	1.6708±0.0013	0.2428±0.0050	23.4927±0.5156
	005	1.0991±0.0021	0.1088±0.0034	30.3516±2.2216	1.6432±0.0029	0.2153±0.0112	15.0713±0.9379
	006	1.1181±0.0035	0.1022±0.0071	11.4461±1.8532	1.6210±0.0036	0.2804±0.0181	14.2776±1.0174
	007	1.0555±0.0019	0.1956±0.0068	39.4668±1.7419			
	008	1.0557±0.0011	0.2301±0.0039	58.3262±0.9823			
	009	1.0626±0.0013	0.1727±0.0072	47.9673±3.1710	1.3389±0.0579	0.8308±0.1773	31.8423±11.4545
	010	1.0687±0.0006	0.1587±0.0026	42.1359±0.7397	1.4769±0.0123	0.6654±0.0536	21.2685±2.2059
	011	1.0804±0.0009	0.1508±0.0041	34.6355±1.4117	1.5321±0.0096	0.4671±0.0478	11.9526±1.5519
	012	1.0854±0.0011	0.1874±0.0035	56.1756±0.8887	1.6601±0.0068	0.2126±0.0277	7.6106±0.9842
	013	1.0501±0.0007	0.1704±0.0026	56.0806±0.7886			
	014	1.0512±0.0007	0.1458±0.0025	33.3063±0.5396			
	015	1.0563±0.0008	0.1585±0.0031	33.1384±0.6805			
	016	1.0710±0.0018	0.1549±0.0076	25.3077±2.3680			
	017	1.0912±0.0063	0.1109±0.0371	2.9499±1.9599	1.5716±0.0236	0.1895±0.2656	2.8884±11.1538
	018	1.0984±0.0122	0.1813±0.0369	2.9795±0.8744	1.5895±0.0208	0.3429±0.1387	4.8600±2.2308
	019	1.0420±0.0010	0.1838±0.0039	42.4026±0.8473			
	020	1.0404±0.0008	0.1870±0.0034	45.2222±0.9544			
	021	1.0477±0.0017	0.1506±0.0089	30.4539±3.2903			
	022	1.0689±0.0009	0.1493±0.0032	38.0706±0.8222			
	023	1.0186±0.0069	0.2487±0.0293	39.9129±5.1663			
	024	0.9829±0.0123	0.2182±0.0502	20.0664±4.7388			
DLin-MC3-DMA	025	1.1369±0.0063	0.2783±0.0141	39.1933±3.3692	1.6993±0.0031	0.4097±0.0622	44.5327±14.3581
	026	1.1029±0.0034	0.1958±0.0078	35.8714±2.2307	1.7256±0.0018	0.2252±0.0218	19.4051±3.2756
	027	1.0999±0.0019	0.1269±0.0037	29.7131±1.5234	1.7545±0.0076	0.1024±0.0205	2.5404±0.8560
	028				1.7988±0.0039	0.0958±0.0146	2.2804±0.3697
	029				1.8323±0.0024	0.0751±0.0092	1.6356±0.1965
	030				1.8723±0.0044	0.0620±0.0178	0.8715±0.2563
	031	1.0660±0.0003	0.0877±0.0014	50.0375±1.1303			
	032	1.0776±0.0002	0.1078±0.0009	45.0040±0.4231	1.4208±0.0058	0.2107±0.0263	3.4459±0.4640
	033	1.1049±0.0004	0.1184±0.0014	39.0486±0.5716	1.4975±0.0046	0.2490±0.0281	6.1018±0.9116
	034	1.1044±0.0007	0.1144±0.0021	27.5942±0.7322	1.5582±0.0053	0.2791±0.0258	6.3730±0.7090
	035	1.0965±0.0008	0.1192±0.0041	23.5233±1.3888	1.6127±0.0085	0.3755±0.0406	6.5899±0.8707
	036	1.0999±0.0024	0.1666±0.0136	12.7348±2.0081	1.6492±0.0083	0.2735±0.0389	3.8777±0.6495
	037	1.0834±0.0008	0.1413±0.0025	38.3718±0.7039	1.3655±0.0053	0.3869±0.0249	20.5245±1.7822
	038	1.0771±0.0011	0.1273±0.0033	38.1060±1.0856	1.4847±0.0297	0.8894±0.1142	48.0453±8.9024
	039	1.0808±0.0014	0.1202±0.0059	36.7239±3.2211	1.4600±0.0532	1.1042±0.2124	51.4555±15.4189
	040	1.0790±0.0017	0.1412±0.0076	29.0289±3.1248	1.5143±0.0133	0.4609±0.0583	12.9255±1.9746
	041	1.0867±0.0068	0.1719±0.0358	8.6984±3.9557	1.5226±0.0245	0.6028±0.0992	11.0473±2.2364
	042	1.0563±0.0057	0.1675±0.0198	3.0385±0.3128	1.6307±0.0103	0.4979±0.0537	8.0778±1.0285
DODMA	043	1.1206±0.0007	0.1039±0.0020	24.3001±0.5021	1.7031±0.0010	0.1842±0.0038	18.0243±0.3565
	044	1.1108±0.0019	0.1837±0.0023	43.1119±1.4647	1.7236±0.0017	0.2866±0.0071	17.3407±0.4739
	045	1.1016±0.0038	0.1543±0.0079	26.3333±2.2330	1.6843±0.0029	0.3290±0.0131	30.5503±1.2271
	046	1.1037±0.0040	0.2499±0.0086	21.8791±1.1071	1.7039±0.0008	0.1688±0.0031	19.8756±0.3059
	047	1.1363±0.0050	0.4320±0.0203	49.8234±3.4799	1.7049±0.0017	0.1732±0.0067	17.5854±0.5832
	048	1.2989±0.0001	0.0342±0.0002	20.8025±0.0901	1.7715±0.0037	0.0648±0.0130	0.6971±0.1226
	049	1.0307±0.0008	0.2101±0.0033	74.7882±1.1339	1.3030±0.0065	0.1850±0.0209	6.3802±0.7641
	050	1.0556±0.0005	0.1603±0.0020	55.7843±0.6580	1.3306±0.0045	0.2482±0.0174	9.9134±0.7676
	051	1.0487±0.0010	0.1559±0.0038	46.9970±1.2462	1.3403±0.0058	0.2264±0.0243	9.7502±1.1439
	052	1.0403±0.0007	0.1764±0.0028	47.2627±0.7264	1.4621±0.0070	0.4650±0.0399	17.7509±2.051
	053	1.0545±0.0009	0.1443±0.0047	27.4755±1.3108			
	054	1.0523±0.0010	0.2006±0.0040	36.5069±0.8380			
	055	1.0385±0.0003	0.1871±0.0010	50.3389±0.2774	1.4269±0.0015	0.2171±0.0063	11.6657±0.3466
	056	1.0389±0.0005	0.1390±0.0017	30.7773±0.3594			
	057	1.0408±0.0010	0.1330±0.0036	33.6167±1.0494			
	058	1.0469±0.0004	0.1369±0.0022	37.4986±0.9327			
	059	1.0412±0.0048	0.2200±0.0155	29.3339±5.1882			
	060	1.0319±0.0083	0.2153±0.0318	6.5661±1.0214	1.7946±0.0076	0.0778±0.0310	1.0166±0.3927
pH-Variation	071	1.0695±0.0009	0.1381±0.0044	32.0453±1.4782			
	072	1.0887±0.0008	0.1110±0.0047	17.2526±1.1032			
	073	1.0897±0.0008	0.1118±0.0044	15.9968±0.9074			
	074	1.0539±0.0007	0.1066±0.0036	38.5490±1.7131			
	075	1.0452±0.0015	0.0881±0.0056	17.6685±1.2981	1.1138±0.0027	0.0446±0.0099	2.5101±0.6592
	076	1.0529±0.0008	0.1487±0.0061	32.6320±2.3806			
	077	1.0203±0.0015	0.0832±0.0069	6.6623±0.6816	1.1172±0.0014	0.0382±0.0058	1.7426±0.2490
	081	1.2949±0.0004	0.0428±0.0013	10.1799±0.3060			
	082	0.0003±0.0550	0.0011±10.0174	10.0174±0.2258			
	083	1.2990±0.0004	0.0586±0.0015	9.0252±0.2433			
	084	1.2975±0.0005	0.0570±0.0018	5.8399±0.1715			
	085						
	086						
	087	1.4253±0.0078	0.1758±0.0303	2.4507±0.4033			

Sample ID		Bragg Peak 5			Bragg Peak 6			Porod-Slope
		Position [nm^{-1}]	Width [nm^{-1}]	Area [a.u.]	Position [nm^{-1}]	Width [nm^{-1}]	Area [a.u.]	0.035-0.08 nm^{-1}
DPL-14	001				2.0016±0.0087	0.2302±0.0380	7.1563±1.5558	
	002				1.9800±0.0066	0.1653±0.0264	3.8228±0.6453	
	003				2.0397±0.0076	0.1766±0.0316	4.1785±0.8118	
	004				2.0428±0.0054	0.2691±0.0267	6.1306±0.7646	
	005	1.8039±0.0046	0.1117±0.0192	2.4650±0.5337	2.0754±0.0069	0.2564±0.0380	4.8795±0.9345	
	006	1.8063±0.0044	0.1016±0.0197	1.5690±0.3960	2.1027±0.0061	0.2216±0.0327	3.2451±0.6095	
	007							3.4614±0.0152
	008							3.5851±0.0144
	009							3.1655±0.0153
	010							3.4547±0.0060
	011							3.5770±0.0054
	012							3.6756±0.0053
	013							2.9963±0.0126
	014							3.5731±0.0083
	015							3.7033±0.0057
	016							3.5183±0.0044
	017	1.6666±0.7139	0.5620±0.5549	4.9614±21.0894	2.1451±0.0207	0.1811±0.1062	0.8776±0.7128	3.5558±0.0037
	018	1.7904±0.0117	0.1454±0.0619	1.2508±0.9113	2.1519±0.0238	0.3293±0.1233	1.6242±0.8123	3.4833±0.0031
	019							
	020							
	021							
	022							
	023							
	024							
DLin-MC3-DMA	025				1.9473±0.0087	0.4573±0.0377	24.2885±2.9013	
	026				1.9949±0.0031	0.2964±0.0171	12.9484±0.9190	
	027	1.6739±0.0066	0.1246±0.0198	4.6699±1.1750	2.0110±0.0050	0.4202±0.0360	19.6084±2.4927	
	028	1.6368±0.0017	0.1125±0.0075	6.9539±0.5229	2.0823±0.0062	0.0905±0.0304	0.8856±0.3325	
	029	1.6311±0.0013	0.1429±0.0054	8.8420±0.3723	2.1227±0.0027	0.2327±0.0176	6.5820±0.6817	
	030	1.6221±0.0017	0.1622±0.0083	10.5241±0.6819	2.1433±0.0046	0.2971±0.0438	8.8672±2.1348	
	031							3.6281±0.0161
	032							3.5268±0.0104
	033							3.8466±0.0074
	034							3.3109±0.0068
	035							3.3122±0.0048
	036							3.2281±0.0037
	037	1.7253±0.0217	0.6251±0.0684	19.494±3.1542				3.5944±0.0064
	038							3.3255±0.0142
	039							3.3383±0.0079
	040							3.5192±0.0044
	041							3.5646±0.0048
	042							3.4476±0.0037
DODMA	043	2.0408±0.0043	0.1442±0.0164	2.8443±0.3162				
	044	2.1049±0.0063	0.1081±0.0240	0.9418±0.1983				
	045	2.0397±0.0071	0.1767±0.0297	4.1786±0.7611				
	046	1.9810±0.0017	0.1569±0.0067	7.4671±0.3149				
	047	1.9829±0.0037	0.1236±0.0138	4.4227±0.4569				
	048							
	049							3.9904±0.0134
	050							3.9671±0.0113
	051							3.5669±0.0176
	052							3.3916±0.0072
	053							3.3852±0.0076
	054							3.8448±0.0036
	055							3.7086±0.0058
	056							3.0120±0.0070
	057							3.2666±0.0105
	058							4.1863±0.0028
	059							3.9237±0.0035
	060							3.6425±0.0066
pH-Variation	071							
	072							
	073							
	074							
	075							
	076							
	077							
	081							
	082							
	083							
	084							
	085							
	086							
	087							

7.4.9 Additional SAXS Curves and Figures From 3.2.1.4.2

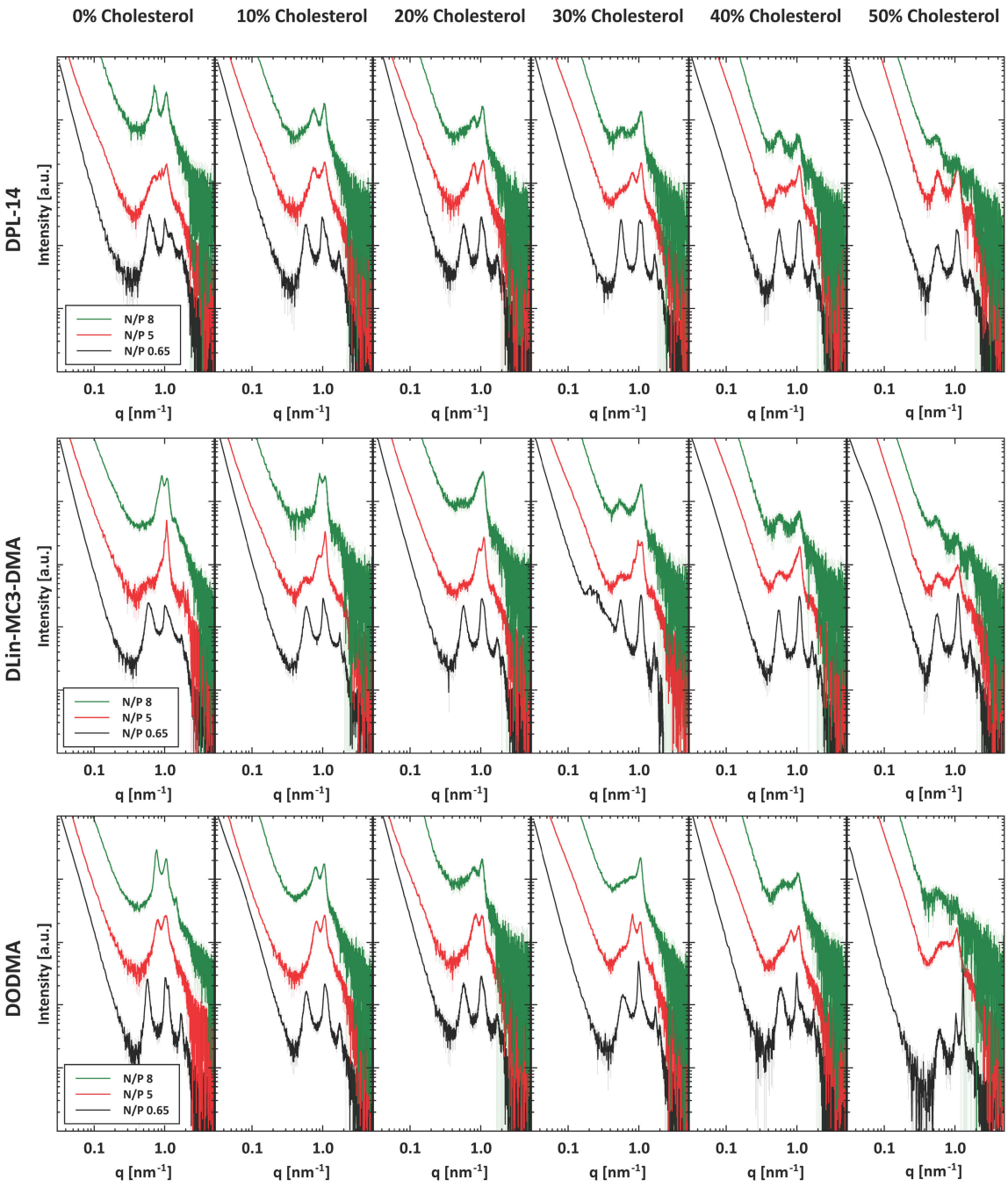

Suppl. Fig. 5. Alternative visualization of scattering curves from the cholesterol variation for lateral comparison. The curves are shifted vertically for clarity.

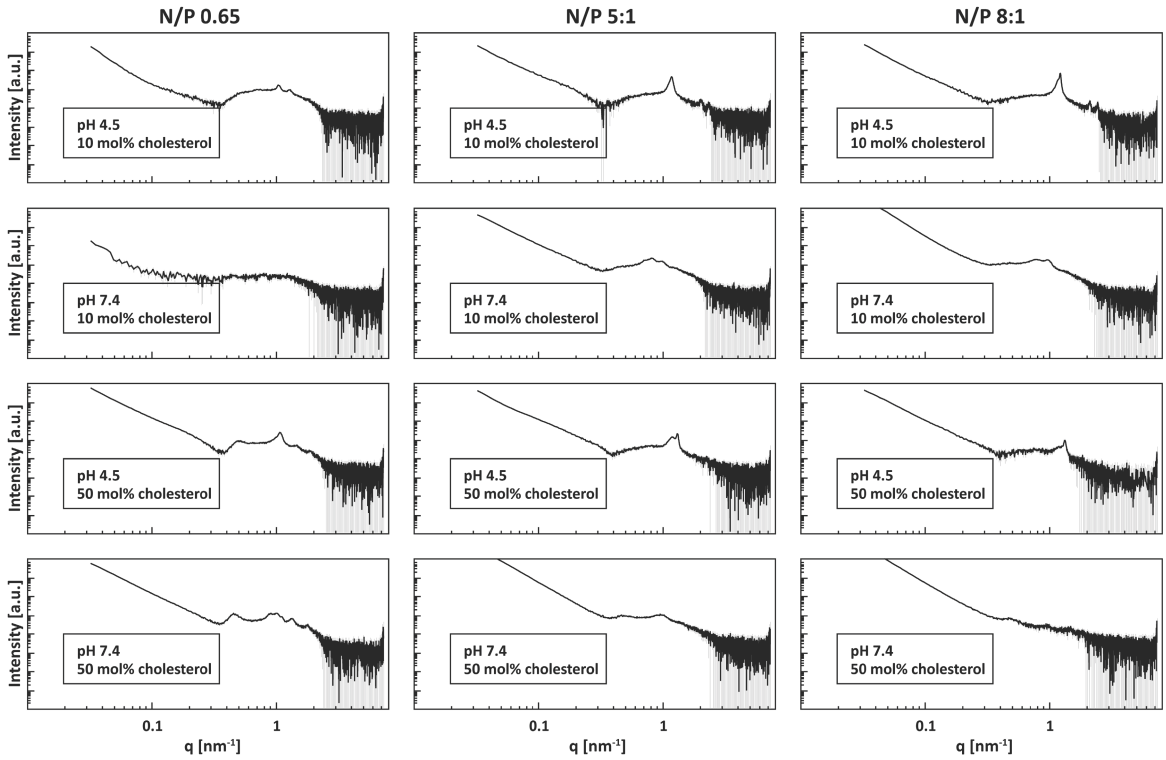

Suppl. Fig. 6. Scattering curves of LNPs comprising DPL-14 at 10 and 50 mol% cholesterol and pH 4.5 and 7.4 (pre-mixed).

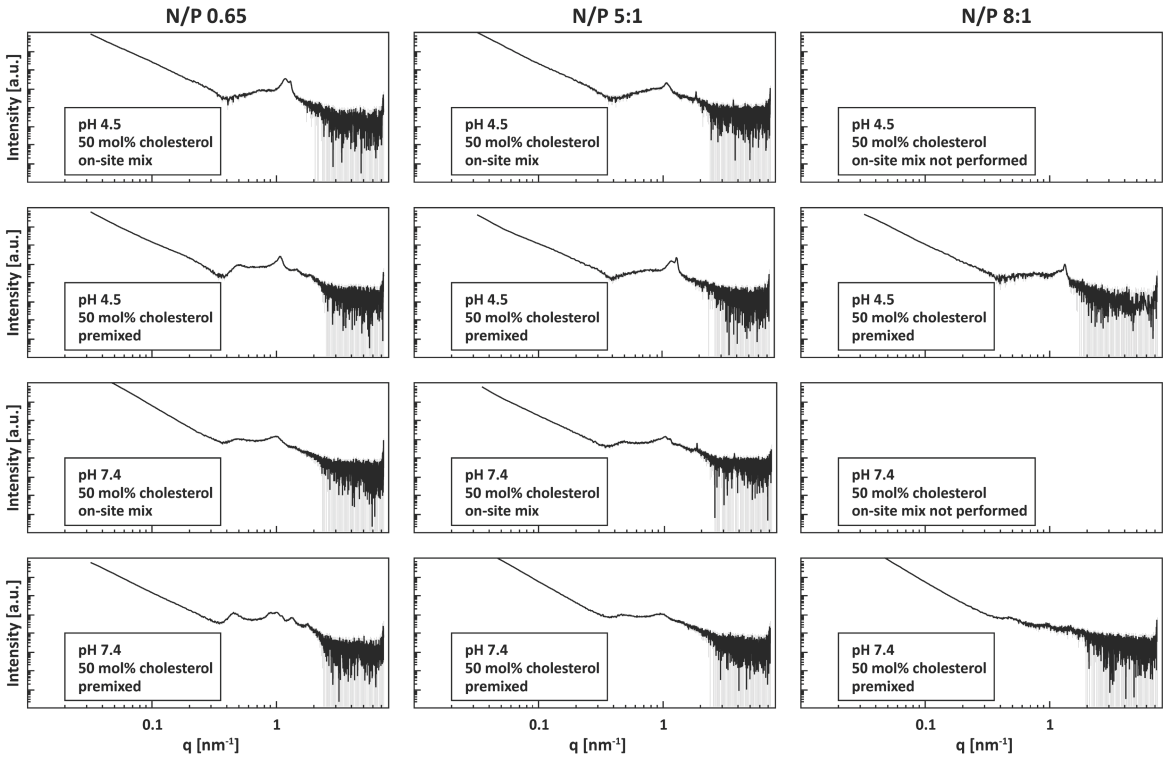

Suppl. Fig. 7. Scattering curves of LNPs at pH 4.5 and 7.4 mixed on-site vs premixed before shipping.

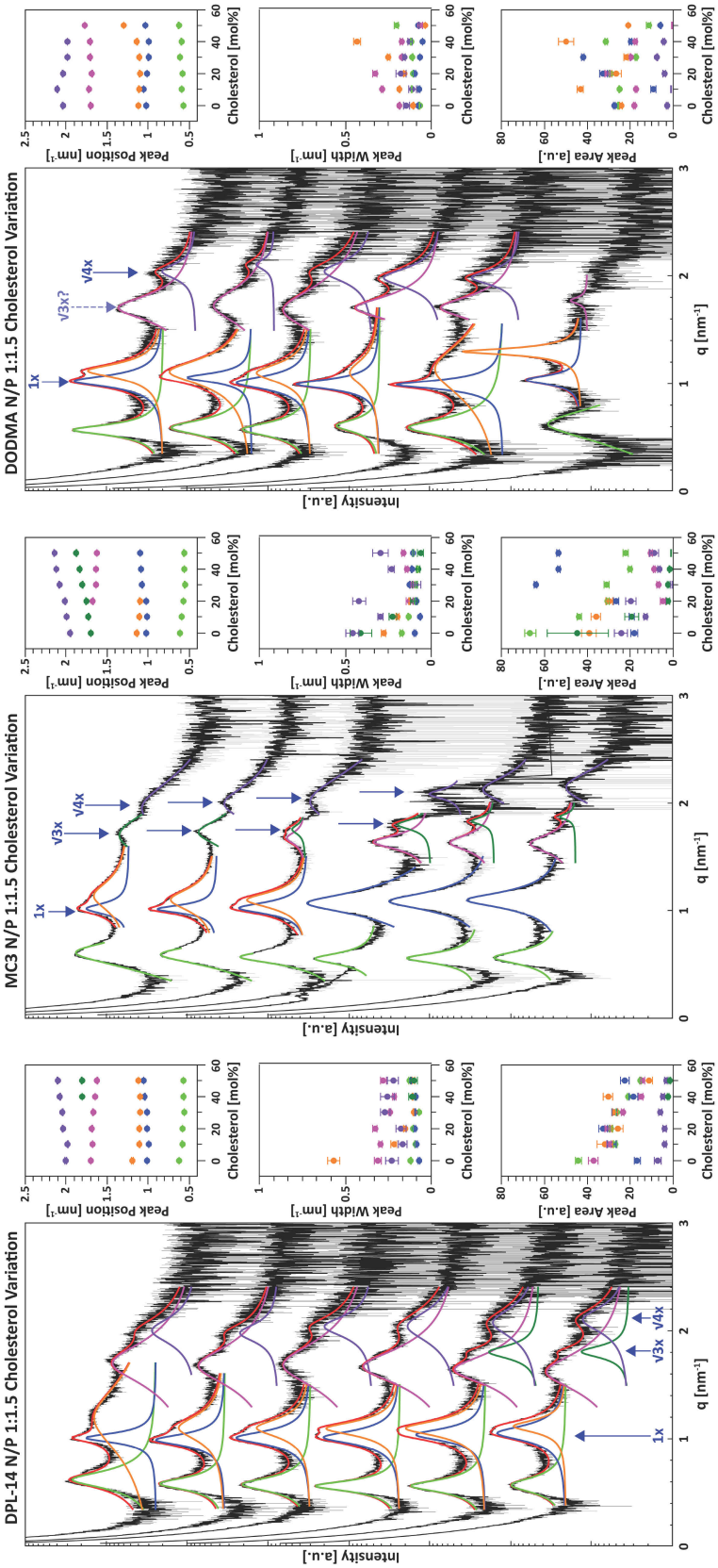

Suppl. Fig. 8. Detailed SAXS curves from the cholesterol- and N/P-variation experiments at an N/P ratio of 1:1.5 and their Bragg peak fits.
SAXS curves are shifted vertically for clarity (0% cholesterol at the top, 50% cholesterol at the bottom). Bragg peaks were either fitted as multi-peak Lorentzian (red curve = full function, other colors = single peaks) or single peaks, depending on their characteristics. The respective peak data (position, width, area) is shown in the adjacent panels in the peaks' colors. Error bars represent the error from the peak fitting process.

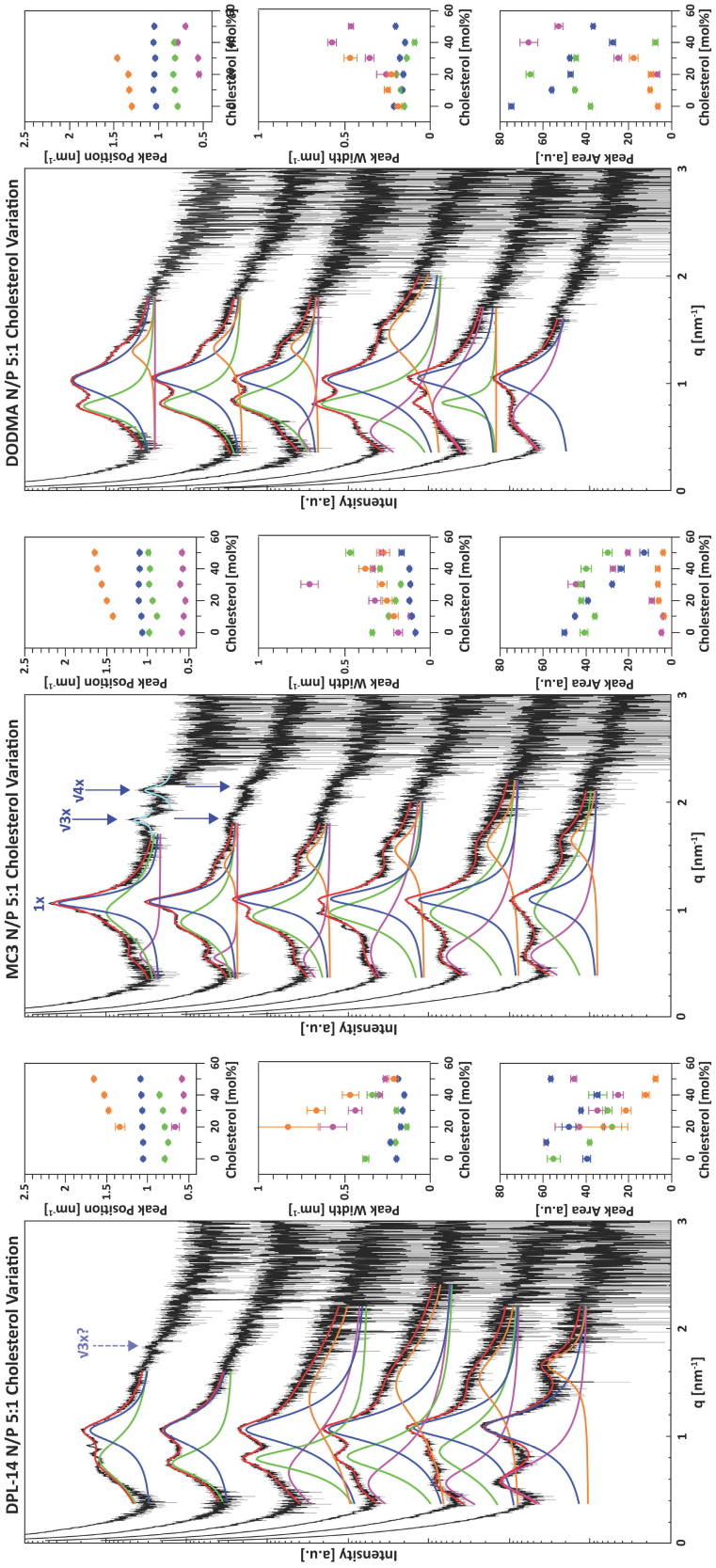

Suppl. Fig. 9. Detailed SAXS curves from the cholesterol- and N/P-variation experiments at an N/P ratio of 5:1 and their Bragg peak fits.
SAXS curves are shifted vertically for clarity (0% cholesterol at the top, 50% cholesterol at the bottom). Bragg peaks were either fitted as multi-peak Lorentzian (red curve = full function, other colors = single peaks) or single peaks, depending on their characteristics. The respective peak data (position, width, area) is shown in the adjacent panels in the peaks' colors. Error bars represent the error from the peak fitting process.

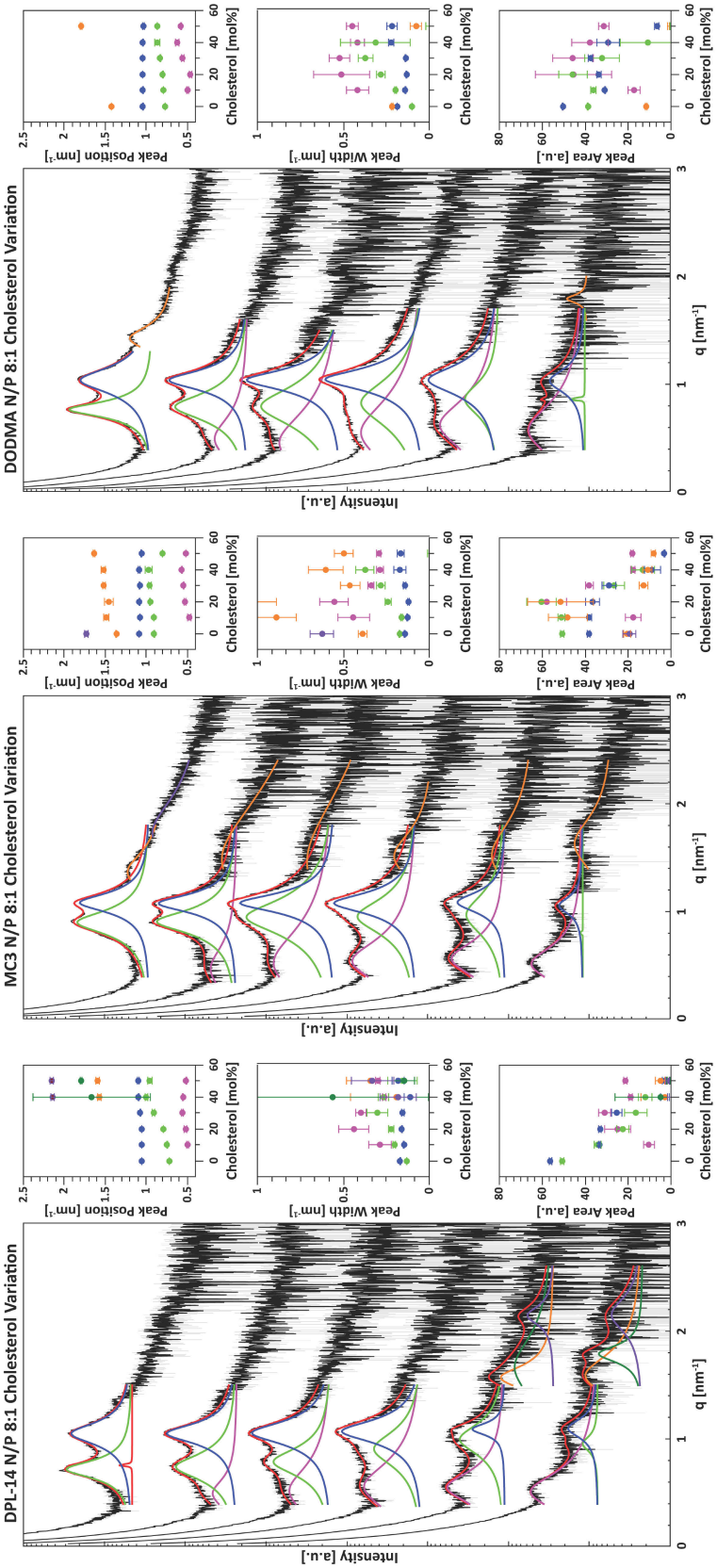

Suppl. Fig. 10. Detailed SAXS curves from the cholesterol- and N/P-variation experiments at an N/P ratio of 8:1 and their Bragg peak fits.
SAXS curves are shifted vertically for clarity (0% cholesterol at the top, 50% cholesterol at the bottom). Bragg peaks were either fitted as multi-peak Lorentzian (red curve = full function, other colors = single peaks) or single peaks, depending on their characteristics. The respective peak data (position, width, area) is shown in the adjacent panels in the peaks' colors. Error bars represent the error from the peak fitting process.

7.5 Curriculum Vitae